ADVANCED TECHNOLOGIES FOR MODELING, OPTIMIZATION AND CONTROL OF THE FUTURE DISTRIBUTION GRID

EDITED BY: Ningyi Dai, Yi Ding, Jiawei Wang and Dongdong Zhang

PUBLISHED IN: Frontiers in Energy Research

frontiers Research Topics

frontiers

ISSN 1664-8714
ISBN 978-2-88974-936-2
DOI 10.3389/978-2-88974-936-2

About Frontiers

Frontiers is more than just an open-access publisher of scholarly articles: it is a pioneering approach to the world of academia, radically improving the way scholarly research is managed. The grand vision of Frontiers is a world where all people have an equal opportunity to seek, share and generate knowledge. Frontiers provides immediate and permanent online open access to all its publications, but this alone is not enough to realize our grand goals.

Frontiers Journal Series

The Frontiers Journal Series is a multi-tier and interdisciplinary set of open-access, online journals, promising a paradigm shift from the current review, selection and dissemination processes in academic publishing. All Frontiers journals are driven by researchers for researchers; therefore, they constitute a service to the scholarly community. At the same time, the Frontiers Journal Series operates on a revolutionary invention, the tiered publishing system, initially addressing specific communities of scholars, and gradually climbing up to broader public understanding, thus serving the interests of the lay society, too.

Dedication to Quality

Each Frontiers article is a landmark of the highest quality, thanks to genuinely collaborative interactions between authors and review editors, who include some of the world's best academicians. Research must be certified by peers before entering a stream of knowledge that may eventually reach the public - and shape society; therefore, Frontiers only applies the most rigorous and unbiased reviews.
Frontiers revolutionizes research publishing by freely delivering the most outstanding research, evaluated with no bias from both the academic and social point of view. By applying the most advanced information technologies, Frontiers is catapulting scholarly publishing into a new generation.

What are Frontiers Research Topics?

Frontiers Research Topics are very popular trademarks of the Frontiers Journals Series: they are collections of at least ten articles, all centered on a particular subject. With their unique mix of varied contributions from Original Research to Review Articles, Frontiers Research Topics unify the most influential researchers, the latest key findings and historical advances in a hot research area! Find out more on how to host your own Frontiers Research Topic or contribute to one as an author by contacting the Frontiers Editorial Office: frontiersin.org/about/contact

ADVANCED TECHNOLOGIES FOR MODELING, OPTIMIZATION AND CONTROL OF THE FUTURE DISTRIBUTION GRID

Topic Editors:
Ningyi Dai, University of Macau, China
Yi Ding, Zhejiang University, China
Jiawei Wang, Technical University of Denmark, Denmark
Dongdong Zhang, Guangxi University, China

Citation: Dai, N., Ding, Y., Wang, J., Zhang, D., eds. (2022). Advanced Technologies for Modeling, Optimization and Control of the Future Distribution Grid. Lausanne: Frontiers Media SA. doi: 10.3389/978-2-88974-936-2

Table of Contents

frontiers in Energy Research

EDITORIAL
published: 25 March 2022
doi: 10.3389/fenrg.2022.885659

Editorial: Advanced Technologies for Modeling, Optimization and Control of the Future Distribution Grid

Ningyi Dai[1]*, *Yi Ding*[2], *Jiawei Wang*[3] and *Dongdong Zhang*[4]

[1]State Key Laboratory of Internet of Things for Smart City, University of Macau, Macau, China, [2]College of Electrical Engineering, Zhejiang University, Hangzhou, China, [3]Department of Electrical Engineering, DTU, Technical University of Denmark, Lyngby, Denmark, [4]School of Electrical Engineering, Guangxi University, Nanning, China

Keywords: Distribution energy resource, distribution grid, integrated energy system, microgrid, resilience

Editorial on the Research Topic

Advanced Technologies for Modeling, Optimization and Control of the Future Distribution Grid

Future power grids face various challenges due to a rapidly increasing share of renewable energy resources and increasing interplay with other energy sectors. Distributed energy resources (DERs) such as wind, solar, energy storage, combined heat and power plants, electric vehicles, and smart loads become prevalent. As shown in **Figure 1**, it has become an inevitable choice for the energy revolution to develop an integrated energy system that realizes the deep integration of new technologies with distributed energy and diversifies (cold, heat, electricity, gas, etc.) demand. Besides, we are moving towards an integrated energy system on an unprecedented scale. In the continuous development of integrated energy systems, the elements of participation and interaction are becoming more complex. The integration of variable sources and the efficient and synergistic utilization of these energies will be a key focus in the future development.

This issue contains ten research articles focusing on modeling and analysis methods for IES, advanced technologies for DERs and microgrid, active distribution network, impact of DERs interconnection on the distribution network, etc.

The paper by Cao et al. proposed the concept of shared ESS (Shared-ESS) for microgrid owner/operator and applied it to the economic optimal dispatch of a microgrid cluster. The microgrids can achieve the peer-to-peer (P2P) transaction among each other with the use of the Shared-ESS, which significantly improves the energy utilization efficiency. The numerical analysis shows that the Shared-ESS can significantly reduce the energy bills of microgrid owner/operator, shift the usage of energy during peak time, and facilitate the renewable energy consumption.

The orderly deregulation of planned electricity generation and consumption is an important measure for electricity market reform in several countries. Under the plan-market double-track mechanism (PMDM) implemented, a modified linear bidding function of generation companies was first proposed by He et al., and the unified clearing price of unilateral generation market is determined accordingly. Simulations based on data from a provincial electricity market in China illustrate that the market power can be reduced through a reasonable proportion of planned electricity designed by the power exchange.

The paper by Chen et al. discusses a passive sliding mode control strategy of MMC-UPFC to achieve the advantages of both the passive controller and sliding mode controller. An unbalanced grid treatment strategy is also presented with the series side of MMC-UPFC. Negative sequence components of the grid voltages are detected by the cross-decoupling method with second order

OPEN ACCESS

Edited and reviewed by:
ZhaoYang Dong,
University of New South Wales, Australia

Correspondence:
Ningyi Dai
nydai@um.edu.mo

Received: *28 February 2022*
Accepted: *09 March 2022*
Published: *25 March 2022*

Citation:
Dai N, Ding Y, Wang J and Zhang D (2022) Editorial: Advanced Technologies for Modeling, Optimization and Control of the Future Distribution Grid. Front. Energy Res. 10:885659. doi: 10.3389/fenrg.2022.885659

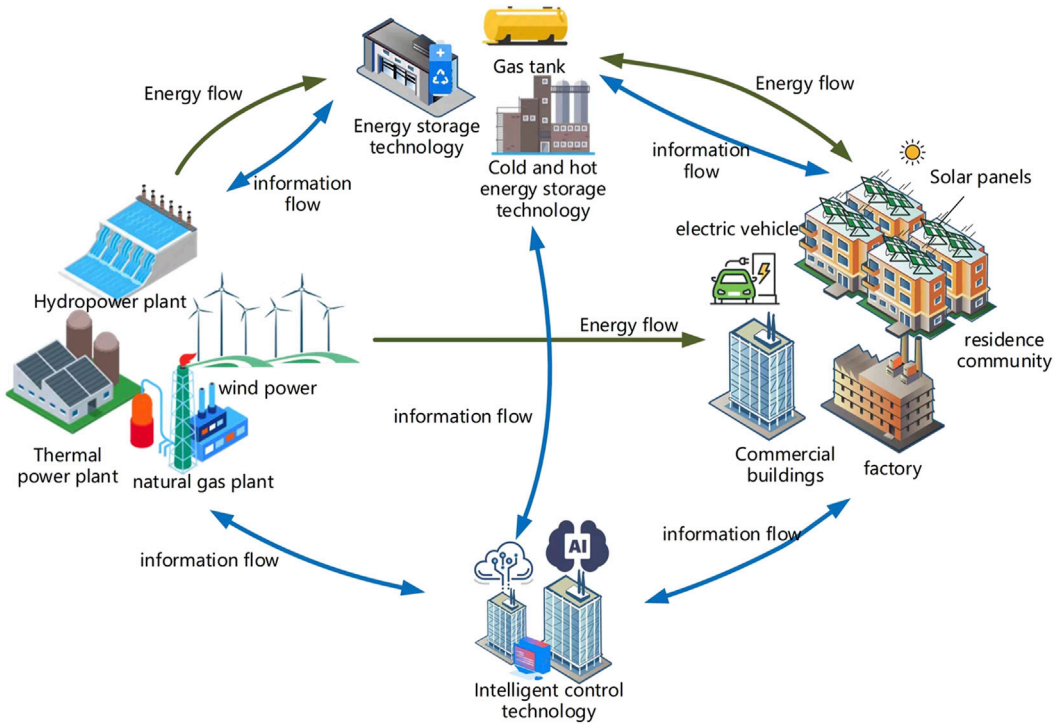

FIGURE 1 | Integrated energy system.

generalized integrator and then compensated by the series side of MMC-UPFC. The series side converter controls the power flow and treats unbalanced grid conditions simultaneously.

The article by Hu et al. is an assessment report meant to address the step-less, and low-cost reactive power to reduce the increasing risks of voltage violations in distribution networks (DNs). Firstly, reactive power compensation models of PVs and EV chargers are investigated and voltage deviation indexes of the regulation results are proposed. Moreover, kernel density estimation (KDE) and slice sampling are adopted to provide the PV output and EV charging demand samples. Then, the risk assessment is carried out with a voltage regulation model utilizing OLTCs, SCs, and available smart inverters.

One study, Wang et al. explored an optimal placement model of voltage sag monitor, which considers the sag economic loss weight, realizes the redundant coverage of important customers, and reduces the risk of sag loss of them. Compared with traditional methods, this method can reduce the risk of loss and ensure the economic benefits of important customers.

Frequency regulation is a critical issue in the islanded microgrids. Zhong et al. proposes an equivalent rotor speed compensation control scheme of PMSG for frequency support in the islanded microgrids. A new variable combining pitch angle and rotor speed is defined as the equivalent rotor speed. The inertia control scheme is optimized by adding a virtual compensation variable to the equivalent rotor speed to obtain the reference of the machine-side converter control loop.

Chen and Bai proposes a mixed-integer nonlinear programming (MINLP) model combining electrical, natural gas, and heating systems, as well as the coupling components, such as CHP and gas-fired generators. The second-order cone and linearized techniques are used to transform the non-convex fundamental matrix formulation of multi-energy network equations to a mixed-integer convex multi-energy flow model, which can improve the computational efficiency significantly.

One study Liu et al., focused on a weak-consistency–oriented collaborative strategy, which was proposed for the practical implementation of the large-scale distributed demand response. Using case studies with different information transmission error rates and other conditions, the proposed strategy is demonstrated to be an effective solution for the large-scale distributed demand response implementation, with a robust response capability under even remarkable transmission errors.

In another study Liu et al., a non-intrusive load disaggregation approach based on an enhanced neural network learning algorithm was proposed. The presented appliance enhances the flexibility and adaptability for diverse scenarios, leading to the improvement of disaggregation performance.

To manage a large scale of distributed energy resources (DERs) dispersed geographically and reduce the impact of DER uncertainties, Zheng et al. propose a distributed two-stage economic dispatch for a virtual power plant (VPP) to track a specified VPP schedule curve. The two-stage distributed optimization problems are solved by an improved

exact diffusion algorithm which is proved to be robust to local communication failure.

AUTHOR CONTRIBUTIONS

All authors listed have made a substantial, direct, and intellectual contribution to the work and approved it for publication.

Conflict of Interest: The authors declare that the research was conducted in the absence of any commercial or financial relationships that could be construed as a potential conflict of interest.

frontiers in Energy Research

HYPOTHESIS AND THEORY
published: 21 April 2021
doi: 10.3389/fenrg.2021.645017

Day-Ahead Economic Optimal Dispatch of Microgrid Cluster Considering Shared Energy Storage System and P2P Transaction

Siming Cao[1], *Hanlin Zhang*[2], *Kai Cao*[1], *Meng Chen*[1], *Yi Wu*[1] *and Suyang Zhou*[2]*

[1] *Yangzhou Power Supply Company, Jiangsu Electric Power Company, State Grid Cooperation of China, Yangzhou, China,*
[2] *School of Electrical Engineering, Southeast University, Nanjing, China*

With the increasing popularity of renewable energy, energy storage systems (ESSs) have now been used as an essential way to reduce energy bills and mitigate the impact of the uncertainty of renewable generators on the energy network. However, the high investment cost of ESS limits its application. This article proposes the concept of shared ESS (Shared-ESS) for microgrid owner/operator and applies it to the economic optimal dispatch of a microgrid cluster. In addition to the energy storage, the microgrids can achieve the peer-to-peer (P2P) transaction among each other with the use of the Shared-ESS, which significantly improves the energy utilization efficiency. The numerical analysis shows that the Shared-ESS can significantly reduce the energy bills of microgrid owner/operator, shift the usage of energy during peak time, and facilitate the renewable energy consumption.

Keywords: shared energy storage system, microgrid cluster, peer-to-peer transaction, economic optimal dispatch, global energy management

OPEN ACCESS

Edited by:
Yi Ding,
Zhejiang University, China

Reviewed by:
Yushuai Li,
University of Denver, United States
Yunfei Mu,
Tianjin University, China

***Correspondence:**
Suyang Zhou
suyang.zhou@seu.edu.cn

Specialty section:
This article was submitted to Smart Grids, a section of the journal Frontiers in Energy Research

Received: *22 December 2020*
Accepted: *29 March 2021*
Published: *21 April 2021*

Citation:
Cao S, Zhang H, Cao K, Chen M, Wu Y and Zhou S (2021) Day-Ahead Economic Optimal Dispatch of Microgrid Cluster Considering Shared Energy Storage System and P2P Transaction. Front. Energy Res. 9:645017. doi: 10.3389/fenrg.2021.645017

INTRODUCTION

To tackle the increasingly serious climate change, a number of countries have set their own targets on carbon emission reduction. Renewable energy is considered as an essential way to reduce the carbon emission, and correspondingly, the penetration of renewable energy has been increasing significantly in the past decade. The high penetration of renewable energy will bring challenges to network operator to balance the network due to their fluctuation characteristics (Borghetti et al., 2010; Denholm and Hand, 2011). Therefore, to mitigate the fluctuation and balance the network, new technologies need to be adopted urgently.

Some scholars focused on the distributed mechanism of network-connected microgrids. Zhou et al. (2020) developed a distributed secondary $H\infty$ consensus approach for DC microgrids. Full plug-and-play operation can be realized with the proposed strategy. Zhou et al. (2020a) studied an integrated hierarchical distributed coordinated control scheme for AC–DC microgrids interconnected by interlinking converters. Yushuai et al. (2020) established a distributed energy management model, which takes into consideration the maximum profits of overall energy generation and consumption and the minimum cost of energy delivery. Li et al. (2020) proposed a double-mode energy management model for multi microgrids, which include the island mode and the network-connected mode. A novel distributed dynamic event-triggered Newton–Raphson algorithm was adopted to solve the problem. Li et al. (2019) also used an

event-trigger-based distributed algorithm, which features distributed algorithm, asynchronous communication, and independent calculation to solve the established day-ahead and real-time energy management models.

Energy storage system (ESS) is also an effective way to deal with the uncertainty of renewable energy. Although the price of battery has dropped continuously, the price and lifetime of ESSs still cannot be ignored (Swierczyński et al., 2013). Thus, exploring the approach of efficiently using ESSs is necessary to accommodate the increasing renewable energy.

A number of research have been focused on the shared use of ESSs. Roberts et al. (2019) pointed out that there are clear financial benefits to the deployment of embedded networks with combined solar and shared ESS (Shared-ESS) for many sites. The addition of a Shared-ESS to an embedded network with Photovoltaic (PV) can increase self-consumption and self-sufficiency and reduce peak demand. Broering and Madlener (2017) studied the economic merit of Shared-ESS in three distinct households in Aachen, Germany, by analyzing three scenarios with different grid-use tariffs. The authors drew out that profits can indeed be made below a feed-in tariff of 10 €/kWh. Liu N. et al. (2018) proposed a concept of energy-sharing provider for PV prosumer cluster, and the neighboring PV prosumers can trade electricity with each other by direct sharing or buffered sharing using the ESS. Yan et al. (2020) developed a plug-and-play device for customer-side energy storage and an internet-based energy storage cloud platform, aiming to investigate the operating state and service life of energy storage devices. A kind of energy optimization and deployment strategy for stratified partition is designed to reduce the operating cost of the energy storage device. By means of MATLAB/Simulink, Biech et al. (2016) presented a simulation tool for the computation of amortization curves for the investment of local ESS. It enables the exploration of a wide search space by manipulating settings on the levels of entire neighborhoods that might want to share in local energy storage.

Some scholars have studied the service model and the operation mechanism of Share-ESS. Oh and Son (2019) proposed a shared energy storage service model for apartment-type factory buildings. The proposed model aims to maximize the profit of the service participants and the service provider. Liu et al. (2017) described the control and communication technologies as well as the business model that is required for the implementation of Shared-ESS. In this model, users can use the Shared-ESS just like their own energy storage facilities, while the Shared-ESS operator will invest and operate centralized batteries to provide energy storage services to the users. Based on the business model and operation mechanism of Shared-ESS, Chen et al. (2018) established the basic Shared-ESS operation model, according to the charging and discharging behavior of the users. Lombardi and Schwabe (2017) developed a business model based on the sharing economy principle. The authors investigated two scenarios: in the first one, a battery owner offers the service of his/her batteries to other users, and in the second one, an independent operator manages the battery.

The optimal capacity of the Shared-ESS is also one of the directions worth studying. Kim and Kim (2017) proposed a method that finds an optimal capacity of Shared-ESS and individual PV system minimizing the total energy cost, which consists of the expenses to buy electricity and to install the Shared-ESS. Wang et al. (2018) raised a new concept of "charging envelop," which can dynamically allocate the capacity of Shared-ESS between users and distribution network operators. Two goals can be achieved: minimizing the energy costs for users and releasing the distribution network constraints. Tushar et al. (2016) investigated the ownership sharing of ESS between residential units and multiple shared facility controllers. A modified auction-based mechanism is designed to determine the auction price and the allocation of energy storage shared by the residential units. Coincidentally, Zaidi et al. (2018) also applied the auction mechanism to carry out the capacity allocation of Shared-ESS. The households are allowed to submit bids in single bid format or in combinations of bids to the auctioneer to get storage capacity in Shared-ESS. The authors also presented a novel winner determination solution for combinatorial auctions, which combines the genetic algorithm with particle swarm optimization.

Besides, the service pricing of Shared-ESS is also of vital importance. Steriotis et al. (2019) presented a Shared-ESS real-time pricing model, which achieves an amazing tradeoff of the interest between the service provider and end users. In Zhang et al. (2020), the service price is determined by the marginal cost of the residential load aggregator, and the load dispatching is formulated as a fixed-point problem, which can better capture the marginal cost and the interaction between electricity and demand. Kim and Kim (2019) took the optimal capacity and service price of the Shared-ESS into consideration simultaneously and formulated a problem of optimal capacities of Shared-ESS for the residential users and an optimal unit price of Shared-ESS for the aggregator.

Plenty of research have paid attention to the energy management of Shared-ESS. Rahbar et al. (2016) proposed a shared energy storage management for high renewable penetrated smart grid. The profit allocation is determined by the profit coefficients of different users that were set by the system operator. AlSkaif et al. (2017) presented a centralized energy management system with a shared battery in microgrid. The proportion of energy in the shared battery is distributed based on the reputation function of the household users. Tascikaraoglu et al. (2019) proposed a direct load control approach for improving the electricity network using shared ESS and demand response of HVAC units. The shared ESS is controlled by the system operator to support the demand response event and maintain the comfort level of HVAC users. Carli and Dotoli (2017) presented a distributed control algorithm for the energy scheduling of a group of residential users. The algorithm is based on an iterative procedure combining parametric optimization. Dai and Charkhgard (2018) introduced three energy storage sharing strategies, namely, extreme free strategy, extreme fair strategy, and contract balance strategy, and developed a bi-objective mixed integer linear programming (MILP) model for each strategy. Taking into consideration the behavior uncertainty of the users, Hosseini et al. (2019) designed a tractable robust optimization scheme with a quadratic cost function, minimizing the total energy payment of each user. Also considering uncertainty, Zhu and Ouahada (2019a,b) described the energy

management problem as a constrained stochastic programming problem and designed a centralized real-time sharing control algorithm based on the Lyapunov optimization theory. Liu J. et al. (2018) accounted for the investment and operation decisions of both the Shared-ESS operator and the users and exploited the complementarity of the users as well as economies of scale. Taşcikaraoglu (2018) proposed a methodology that provides an energy credit to each household for the excess renewable energy. These energy credits are then used during peak periods, resulting in a virtual shift of excess energy to the periods with higher load demand. Chen et al. (2017) formulated the energy management problem as a bi-level mathematical model. The upper level model optimizes the allocation of energy storage among the distribution company and users, while the lower level model minimizes the electricity purchase costs of the distribution company and users. The bi-level model is transformed into a single-level mathematical program with the equilibrium constraints model.

However, the aforementioned research work mainly focuses on the control and pricing of the energy exchange between ESS and the energy users and the behind-meter trading among the users, though the commonly connected ESS is less considered. According to the modular bi-directional converter infrastructure proposed in Sickel et al. (2005), the trading among various users behind the meter can be achieved by using multiple individual AC/DC converter modules and shared DC/DC module, and a demonstration project is adopted in Malmo, Sweden (Fu et al., 2016). Therefore, benefiting from the power flow controllability of AC/DC modules, the power trading among the participants is controllable, and the billing of energy trading or selling/buying electricity to/from the ESS can be achieved behind the meter by adding metering unit on the AC/DC module. In this article, we proposed the concept of Shared-ESS for microgrid cluster, which enables the peer-to-peer (P2P) trading among participants and trading between participants and Shared-ESS. The proposed concept can bring benefits to both participants and the Shared-ESS operator.

The main contributions of this article are summarized below:

- Proposed the Shared-ESS concept that enables the behind-meter P2P trading among microgrids and the trading between microgrids and external grid.
- Introduced an optimized day-ahead operational scheduling approach for microgrids cluster with Shared-ESS.
- Performed a comprehensive analysis of Shared-ESS under different scenarios of microgrid clusters and evaluated the influence of Shared-ESS capacity and the number of microgrids to the cluster operation.

The remainder of this article is organized as follows. Section The Architecture of Microgrid Cluster With Shared-ESS presents the architecture of the proposed microgrid cluster with Shared-ESS. Section Problem Formulation and Optimization presents the problem formulation and optimization of the Shared-ESS in microgrid cluster. Section Comparative Performance Scenarios presents the evaluation of the proposed system performance under different scenarios, and the conclusion is drawn in section Conclusion.

THE ARCHITECTURE OF MICROGRID CLUSTER WITH SHARED-ESS

The general infrastructure of microgrid cluster with Shared-ESS is presented in **Figure 1**. The microgrid contains a number of electricity consumers and usually has the renewable generators like wind turbines and photovoltaic generators. The microgrid is able to buy/sell electricity from/to the external grid, store/buy electricity in/to the Shared-ESS, and buy/sell electricity from/to neighborhood microgrid through the common DC bus of Shared-ESS.

As the core equipment that helps micro-grid achieve P2P transaction and temporary energy storage, the infrastructure of Shared-ESS is given in **Figure 2**. The microgrid is connected to both external grid and the AC/DC module of the Shared-ESS. Each of the microgrid within the cluster will connect to one AC/DC module of Shared-ESS, and the DC terminal of AC/DC module is connected to the common DC bus, so that the microgrids can exchange energy flow through the common DC bus. In addition, if the surplus energy generated by renewable sources cannot be consumed by the microgrids, the surplus energy will be stored in the Shared-ESS during off-peak time unless the Shared-ESS is fully charged.

The advantages of adopting Shared-ESS for microgrid cluster are summarized below:

- During peak-time, Shared-ESS can reduce the amount of electricity bought from the grid by discharging the stored power to the microgrids.
- The Shared-ESS can reduce the fluctuation of electricity generation caused by renewable generations.
- The Shared-ESS enables the energy exchange by transmitting electricity through common DC bus rather than by charging/discharging the battery itself, which is not necessary to charge/discharge the battery frequently.

PROBLEM FORMULATION AND OPTIMIZATION

In this section, the objective function, mathematical models of core equipment, and constraints of the day-ahead microgrid cluster optimal dispatch problem are described. Taking the output of renewable generators and electric load of each microgrid and the electricity price of external grid as inputs, the optimal scheduling strategy can be obtained by solving the mathematical model to achieve the economic optimal operation of the microgrid cluster.

Objective Function

The objective function is to minimize the total cost of the microgrid cluster. The total cost includes the operation and maintenance cost of renewable generators, the cost of purchasing electricity from the grid, the cost of buying electricity from Shared-ESS, and the payoff of selling surplus electricity to the

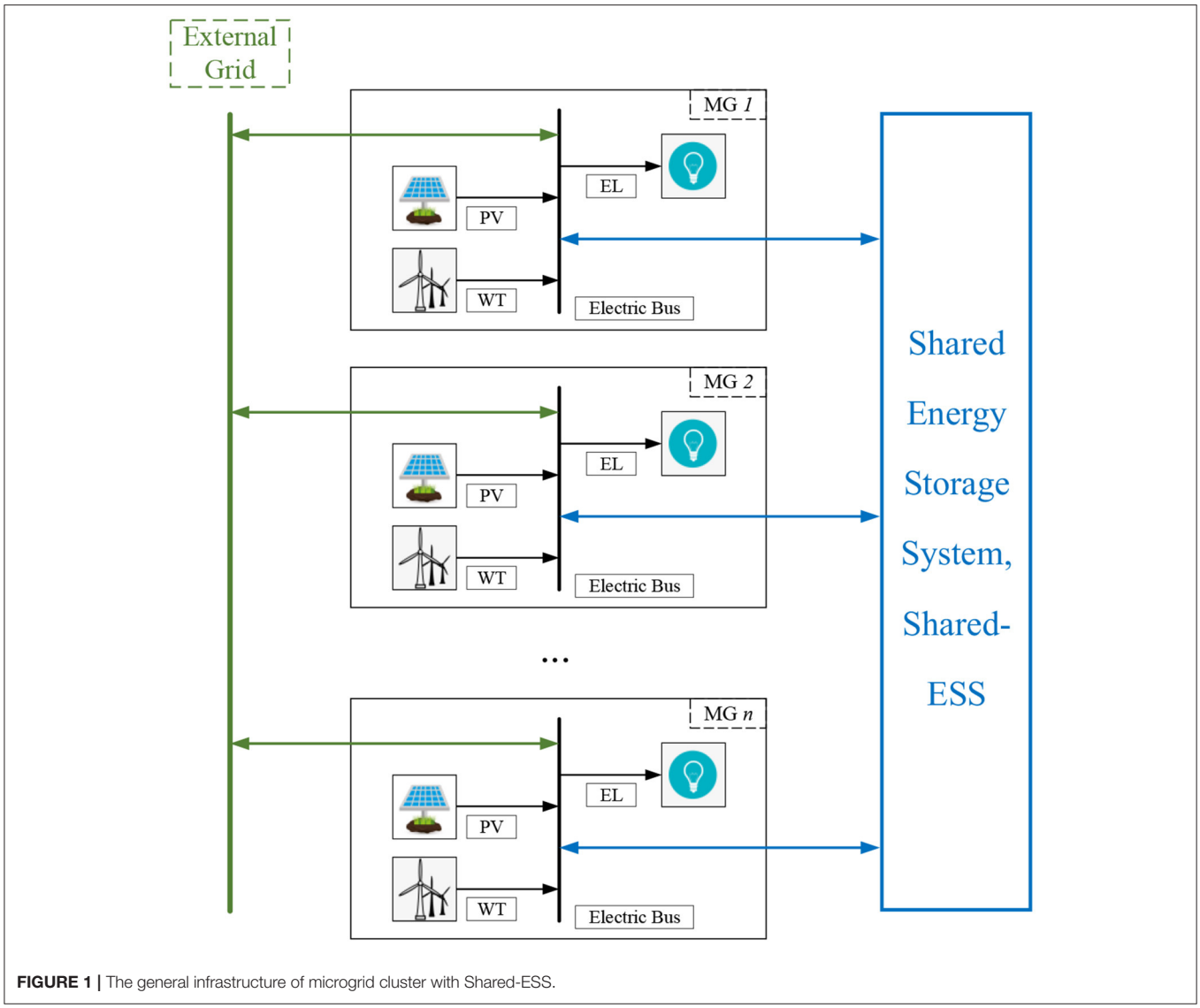

FIGURE 1 | The general infrastructure of microgrid cluster with Shared-ESS.

external grid and the Shared-ESS:

$$\min cost = \sum_{i=1}^{IMG} \left(C_{OM}^{i} + C_{ADN}^{i} + C_{ESS}^{i}\right) \quad (1)$$

$$C_{OM}^{i} = \sum_{t=1}^{T} \left(c_{PV}^{i,t} \cdot P_{PV}^{i,t} + c_{WT}^{i,t} \cdot P_{WT}^{i,t}\right) \cdot \Delta t \quad (2)$$

$$C_{ADN}^{i} = \sum_{t=1}^{T} \left(c_{b,ADN}^{i,t} \cdot P_{b,ADN}^{i,t} - c_{s,ADN}^{i,t} \cdot P_{s,ADN}^{i,t}\right) \cdot \Delta t \quad (3)$$

$$C_{ESS}^{i} = \sum_{t=1}^{T} \left(c_{b,ESS}^{i,t} \cdot P_{b,ESS,EX}^{i,t} - c_{s,ESS}^{i,t} \cdot P_{s,ESS,EX}^{i,t}\right) \cdot \Delta t \quad (4)$$

where the *Cost* represents the total operational cost of microgrid cluster; C_{OM}^{i} stands for the operation and maintenance cost of the renewable generators in microgrid *i*; C_{ADN}^{i}/C_{ESS}^{i} express the cost of exchanging power of microgrid *i* with the external grid and the Shared-ESS, respectively; *IMG* means the number of microgrids; *T* indicates the scheduling cycle; denotes the scheduling time resolution; $c_{PV}^{i,t}/c_{WT}^{i,t}$ represent the operation and maintenance cost factor of photovoltaic generators and wind turbines, respectively; $c_{b,ADN}^{i,t}/c_{s,ADN}^{i,t}/c_{b,ESS}^{i,t}/c_{s,ESS}^{i,t}$ are the $P_{PV}^{i,t}P_{WT}^{i,t}$ electricity prices at which microgrid *i* buy/sell electricity from/to external grid/Shared-ESS at time *t*, respectively; $P_{PV}^{i,t}/$ stand for the output power of photovoltaic generators and wind turbines in microgrid *i* at time *t*; and $P_{b,ADN}^{i,t}/P_{s,ADN}^{i,t}/P_{b,ESS,EX}^{i,t}/P_{s,ESS,EX}^{i,t}$ express the electric power that microgrid *i* buy/sell from/to extern grid/Shared-ESS at time *t*, respectively.

The purchase/sale electricity price of Shared-ESS is determined by Equations (5–7) based on the pricing methodology proposed in Zhou et al. (2020b):

$$c_{b,ESS}^{i,t} = c_{b,ESS,b}^{i,t} + b_{b,ESS,c} x_{s,ESS,c}^{i,t} \quad (5)$$

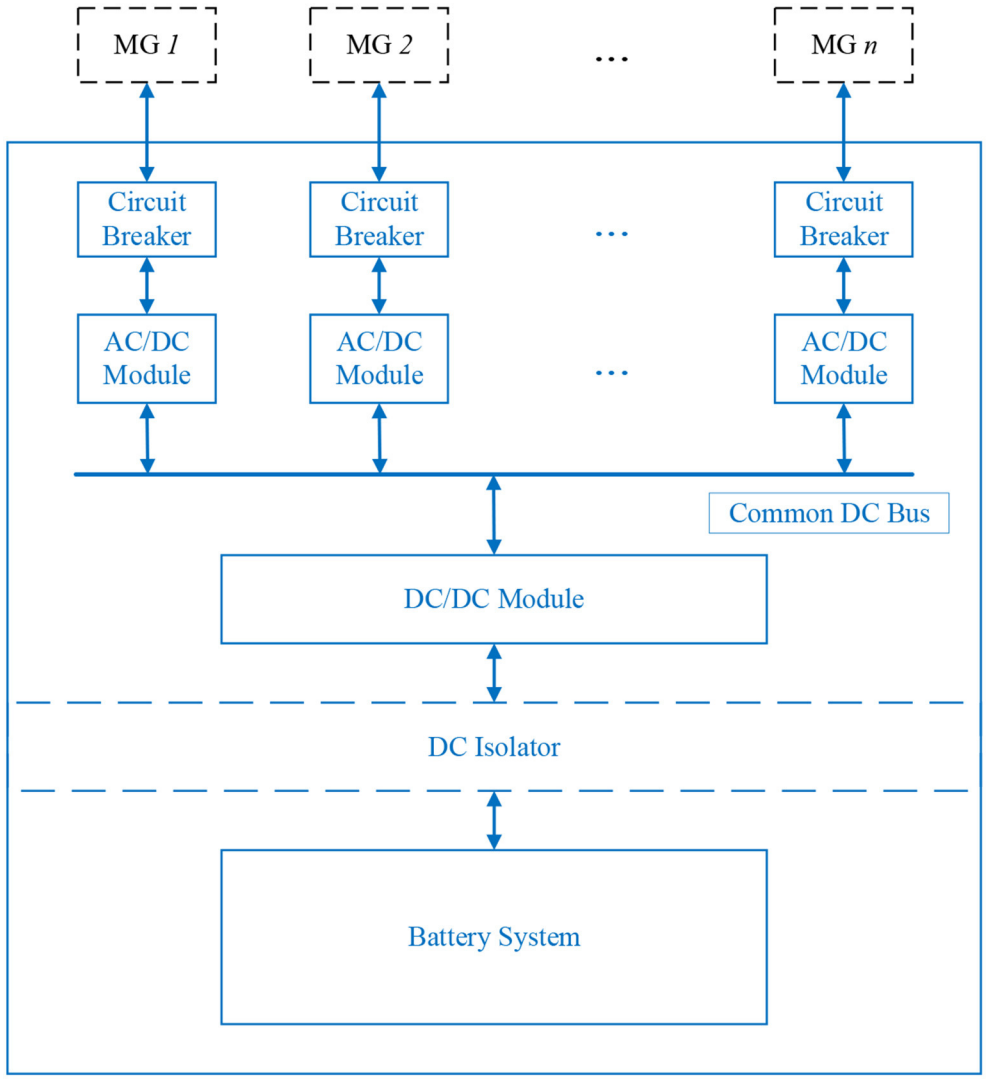

FIGURE 2 | The infrastructure of Shared-ESS.

$$c_{s,ESS}^{i,t} = c_{s,ESS,b}^{i,t} + b_{s,ESS,c} x_{s,ESS,c}^{i,t} \quad (6)$$

$$x_{ESS,c}^{i,t} = \frac{P_{EL}^{i,t}}{P_{PV}^{i,t} + P_{WT}^{i,t}} \quad (7)$$

where the $c_{b,ESS,b}^{i,t}/c_{s,ESS,b}^{i,t}$ mean the base electricity price at which microgrid i buy/sell electricity from/to Shared-ESS at time t; $P_{EL}^{i,t}$ indicates the power of electric load in microgrid i at time t; $x_{ESS,c}^{i,t}$ represents the ratio of electric load power to renewable energy power; and $x_{s,ESS,c}^{i,t}$ is the value of $x_{ESS,c}^{i,t}$ normalized to the interval $[-1, 1]$.

Constraints

Constraints on the Electric Power Balance of Microgrids

The electric power balance has to be met in each microgrid:

$$P_{PV}^{i,t} + P_{WT}^{i,t} + P_{b,ADN}^{i,t} + P_{b,ESS,EX}^{i,t} = P_{EL}^{i,t} + P_{s,ADN}^{i,t} + P_{s,ESS,EX}^{i,t} \quad (8)$$

Constraints on the Electric Power Balance of Common DC Bus in Shared-ESS

The electric power balance has to be met in the common DC bus inside Shared-ESS, as shown in (9). If there is a surplus in the power generated by renewable energy, the remaining power will be sold to other microgrids first. If there is still power remaining on the common DC bus, the battery of the Shared-ESS will be charged. Thus, though the common DC bus, the P2P transaction between the microgrids can be realized.

$$\sum_{i=1}^{IMG} P_{s,ESS,DC}^{i,t} + P_{ESS,dis,DC}^{t} = \sum_{i=1}^{IMG} P_{b,ESS,DC}^{i,t} + P_{ESS,ch,DC}^{t} \quad (9)$$

where the $P_{b,ESS,DC}^{i,t}/P_{s,ESS,DC}^{i,t}$ stand for the value of the electric power bought/sold from/to Shared-ESS transmitted to the common DC bus in microgrid i at time t and $P_{ESS,ch,DC}^{t}/P_{ESS,dis,DC}^{t}$

express the value of the charge/discharge power of the battery in Shared-ESS transmitted to the DC bus in microgrid i at time t.

Constraints on the Upper and Lower Limits of Electric Power Purchased/Sold From/to External Grid

Due to the capacity limitations of the transmission lines and transformers, the interaction power of each microgrid and external grid has upper and lower limits. Meanwhile, at each moment, the power purchase/sale behavior between microgrids and external grid cannot occur at the same time:

$$\begin{cases} 0 \le P_{b,ADN}^{i,t} \le I_{b,ADN}^{i,t} \cdot P_{b,ADN}^{\max} \\ 0 \le P_{s,ADN}^{i,t} \le I_{s,ADN}^{i,t} \cdot P_{s,ADN}^{\max} \\ 0 \le I_{b,ADN}^{i,t} + I_{s,ADN}^{i,t} \le 1 \end{cases} \tag{10}$$

where the $I_{b,ADN}^{i,t}/I_{s,ADN}^{i,t}$ are 0–1 variables, meaning that the microgrid i and external grid power buy/sale status at time t and $P_{b,ADN}^{\max}/P_{s,ADN}^{\max}$ indicate the upper limit of electric power bought/sold from/to external grid.

Constraints on Upper and Lower Limits of Electric Power Purchased/Sold From/to Shared-ESS

Due to the capacity limitations of the transmission lines and AC/DC converters, the interaction power of each microgrid and Shared-ESS has upper and lower limits. Meanwhile, at each moment, the power purchase/sale behavior between microgrids and Shared-ESS cannot occur at the same time:

$$\begin{cases} 0 \le P_{b,ESS,EX}^{i,t} \le I_{b,ESS}^{i,t} \cdot P_{b,ESS,EX}^{\max} \\ 0 \le P_{s,ESS,EX}^{i,t} \le I_{s,ESS}^{i,t} \cdot P_{s,ESS,EX}^{\max} \\ 0 \le I_{b,ESS}^{i,t} + I_{s,ESS}^{i,t} \le 1 \end{cases} \tag{11}$$

where the $I_{b,ESS}^{i,t}/I_{s,ESS}^{i,t}$ are 0–1 variables, representing that the microgrid i and Shared-ESS power buy/sale status at time t and $P_{b,ESS,EX}^{\max}/P_{s,ESS,EX}^{\max}$ are the upper limit of electric power bought/sold from/to Shared-ESS.

Constraints on Preventing the Transactions Between Shared-ESS and External Grid via Microgrids

In consideration of economy and safety, microgrids are not allowed to sell the electricity purchased from external grid to Shared-ESS or sell the electricity purchased from Shared-ESS to external grid at the same time:

$$\begin{cases} 0 \le I_{b,ADN}^{i,t} + I_{s,ESS}^{i,t} \le 1 \\ 0 \le I_{s,ADN}^{i,t} + I_{b,ESS}^{i,t} \le 1 \end{cases} \tag{12}$$

TABLE 1 | Introduction of different scenarios.

Scenario	The capacity of battery in Shared-ESS/(kWh)	Number of microgrids connected to Shared-ESS	Total cost/ RMB
Scenario 1	3,000	4	3360.8191
Scenario 2	0	4	4070.6475
Scenario 3	1,000	4	3564.7461
Scenario 4	5,000	4	3302.0391
Scenario 5	3,000	6	4962.4749
Scenario 6	0	6	5810.2365

TABLE 2 | Real-time trading price.

Period	Time	Price/[RMB/(kWh)]
Valley	23:00–07:00	0.47
Off-peak	07:00–08:00, 11:00–18:00	0.87
Peak	08:00–11:00, 18:00–23:00	1.09

TABLE 3 | Operational parameters of the microgrid cluster system.

Symbol	Value	Description
T	24	Scheduling cycle
Δt	1 h	Scheduling time resolution
	0.025 RMB/(kWh)	Operation and maintenance cost of photovoltaic generators
$c_{WT}^{i,t}$	0.029 RMB/(kWh)	Operation and maintenance cost of wind turbines
$P_{b,ADN}^{\max}$	500 kW	Maximum power bought by each microgrid from external grid
$P_{s,ADN}^{\max}$	500 kW	Maximum power sold by each microgrid to external grid
$P_{b,ESS,EX}^{\max}$	$0.1 \cdot Cap_{ESS}$	Maximum power bought by each microgrid from Shared-ESS
$P_{b,ESS,EX}^{\max}$	$0.1 \cdot Cap_{ESS}$	Maximum power sold by each microgrid to Shared-ESS
$P_{ESS,dis}^{\min}$	$0.02 \cdot Cap_{ESS}$	Minimum power discharged from the battery in Shared-ESS
$P_{s,ESS,EX}^{\max} P_{ESS,dis}^{\max}$	$0.25 \cdot Cap_{ESS}$	Maximum power discharged from the battery in Shared-ESS
$P_{ESS,ch}^{\min}$	$0.02 \cdot Cap_{ESS}$	Minimum power charged to the battery in Shared-ESS
$P_{ESS,ch}^{\max}$	$0.25 \cdot Cap_{ESS}$	Maximum power charged to the battery in Shared-ESS
$P_{ESS,cyc}^{\max}$	$4 \cdot Cap_{ESS}$	Maximum cycle power of the battery in Shared-ESS
$W_{ESS}^{\min}$	$0.025 \cdot Cap_{ESS}$	Lower limit of energy of the battery in Shared-ESS
$W_{ESS}^{\min}$	$0.975 \cdot Cap_{ESS}$	Upper limit of energy of the battery in Shared-ESS
σ_{ESS}	0.001	The self-discharge rate of the battery in Shared-ESS
$\eta_{ESS,DC,AC}$	0.95	The efficiency of DC/AC conversion in Shared-ESS
$\eta_{ESS,AC,DC}$	0.95	The efficiency of AC/DC conversion in Shared-ESS
$\eta_{ESS,ch}$	0.98	The efficiency of DC/DC conversion when the battery is charged
$\eta_{ESS,dis}$	0.98	The efficiency of DC/DC conversion when the battery is discharged

Constraints on the Charge and Discharge Power of the Battery in Shared-ESS

Due to the capacity limitations of the battery and the DC/DC converter, there is an upper limit on the charge and discharge power of the battery in Shared-ESS. Meanwhile, in order to prevent unnecessary battery loss, this power has a lower limit. In addition, the charge and discharge behavior of the battery cannot occur at the same time:

$$\begin{cases} I^t_{ESS,dis} \cdot P^{\min}_{ESS,dis} \le P^t_{ESS,dis} \le I^t_{ESS,dis} \cdot P^{\max}_{ESS,dis} \\ I^t_{ESS,ch} \cdot P^{\min}_{ESS,ch} \le P^t_{ESS,ch} \le I^t_{ESS,ch} \cdot P^{\max}_{ESS,ch} \\ 0 \le I^t_{ESS,dis} + I^t_{ESS,ch} \le 1 \end{cases} \tag{13}$$

where the $I^t_{ESS,ch}/I^t_{ESS,dis}$ are 0–1 variables, standing for the charge/discharge status of the battery in Shared-ESS at time t; $P^t_{ESS,ch}/P^t_{ESS,dis}$ express the charge/discharge power of the battery at time t; and $P^{\max}_{ESS,ch}/P^{\max}_{ESS,dis}/P^{\min}_{ESS,ch}/P^{\min}_{ESS,dis}$ mean the upper/lower limit of the charge/discharge power of the battery at time t.

Constraints on the Cycle Power of the Battery in Shared-ESS

In order to reduce the loss of the battery and thus ensure the service life of the battery, constraints on the charge and discharge cycle power of the battery have to be added:

$$\sum_{t=1}^{T} \left(P^t_{ESS,dis} + P^t_{ESS,ch} \right) \le P^{\max}_{ESS,cyc} \tag{14}$$

where the $P^{\max}_{ESS,cyc}$ indicates the maximum cycle power of the battery.

Constraints on the Energy of the Battery in Shared-ESS

In order to ensure the normal operation of the battery, the upper and lower limits of the energy of the battery in Shared-ESS should be set. In addition, the energy of the battery at each time has a certain relationship with the charge or discharge power of the previous time. Moreover, to ensure the sustainability of the scheduling strategy, the energy of the battery has to be made equal at the beginning and the end of each scheduling cycle:

$$\begin{cases} W^{\min}_{ESS} \le W^t_{ESS} \le W^{\max}_{ESS} \\ W^{t+1}_{ESS} = W^t_{ESS}\left(1 - \sigma_{ESS}\right) + \left(P^t_{ESS,ch} - P^t_{ESS,dis} \right) \cdot \\ \qquad \Delta t, \ (t = 0, \cdots, T-1) \\ W^T_{ESS} = W^0_{ESS} \end{cases} \tag{15}$$

where the W^t_{ESS} represents the energy of the battery in Shared-ESS at time t; $W^{\min}_{ESS}/W^{\max}_{ESS}$ are the lower/upper limit of the energy of the battery; and σ_{ESS} stands for the self-discharge rate of the battery.

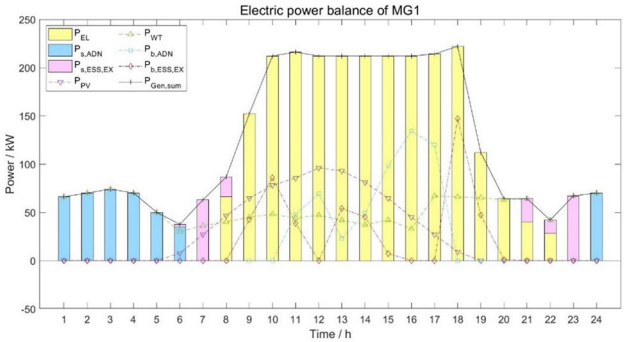

A Electric power balance of microgrid 1 in scenario 1

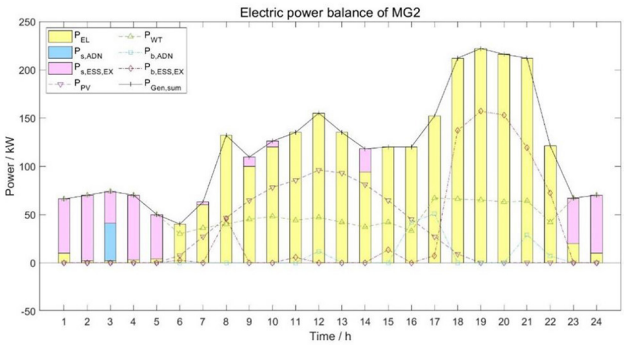

B Electric power balance of microgrid 2 in scenario 1

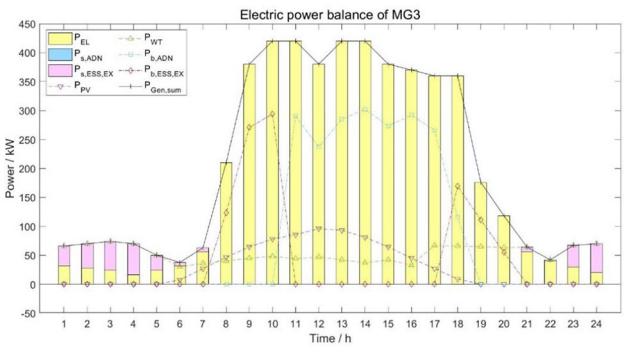

C Electric power balance of microgrid 3 in scenario 1

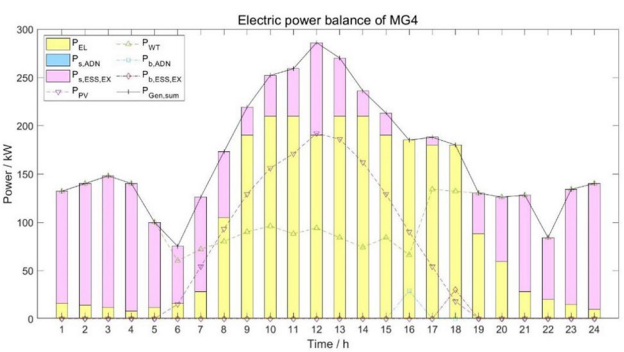

D Electric power balance of microgrid 4 in scenario 1

FIGURE 3 | Electric power balance of microgrids in scenario 1. **(A)** Electric power balance of microgrid 1 in scenario 1. **(B)** Electric power balance of microgrid 2 in scenario 1. **(C)** Electric power balance of microgrid 3 in scenario 1. **(D)** Electric power balance of microgrid 4 in scenario 1.

Constraints on the Efficiency of Energy Conversion in Shared-ESS

Because of the power loss of bidirectional converters in Shared-ESS, the efficiency constraints of each device should be added:

$$\begin{cases} P^{i,t}_{b,ESS,EX} = \eta_{ESS,DC,AC} \cdot P^{i,t}_{b,ESS,DC} \\ P^{i,t}_{s,ESS,DC} = \eta_{ESS,AC,DC} \cdot P^{i,t}_{s,ESS,EX} \\ P^{t}_{ESS,dis,DC} = \eta_{ESS,dis} \cdot P^{t}_{ESS,dis} \\ P^{t}_{ESS,ch} = \eta_{ESS,ch} \cdot P^{t}_{ESS,ch,DC} \end{cases} \tag{16}$$

where the $\eta_{ESS,DC,AC}$ expresses the efficiency of DC/AC converters to convert electricity from DC to AC; $\eta_{ESS,AC,DC}$ means the efficiency of DC/AC converters to convert electricity from AC to DC; $\eta_{ESS,dis}$ indicates the efficiency of DC/DC converter when the battery is discharge$\eta_{ESS,DC,AC}$d; and $\eta_{ESS,ch}$ denotes the efficiency of DC/DC converter when the battery is charged.

COMPARATIVE PERFORMANCE SCENARIOS

To evaluate the performance of the proposed Shared-ESS in microgrid cluster, a number of case studies have been performed in this section. The power exchanged among the microgrids, the charging/discharging actions of shared-ESS, and the influence of the capacity of the battery in Shared-ESS to the whole system operation in different scenarios are discussed in this section as well. The modeling, solving, and analysis of the numerical analysis are programmed based on MATLAB R2018b, and the IBM ILOG CPLEX Optimization Studio is used as the solver to find the optimal day-ahead scheduling of the proposed model.

The six scenarios used for evaluating the Shared-ESS are listed in **Table 1**. The microgrid models are of three types: (1) commercial type, (2) domestic type, and (3) industrial type. The Time of Use (TOU) tariff is adopted for purchasing

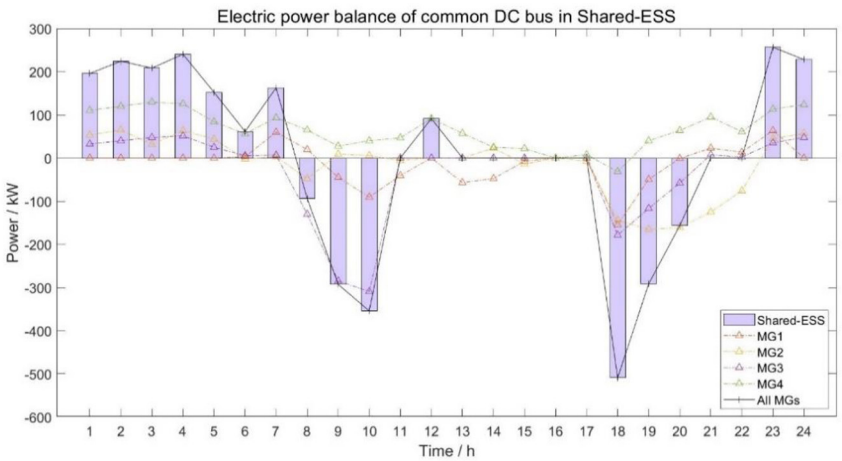

A Electric power balance of common DC bus in Shared-ESS in scenario 1

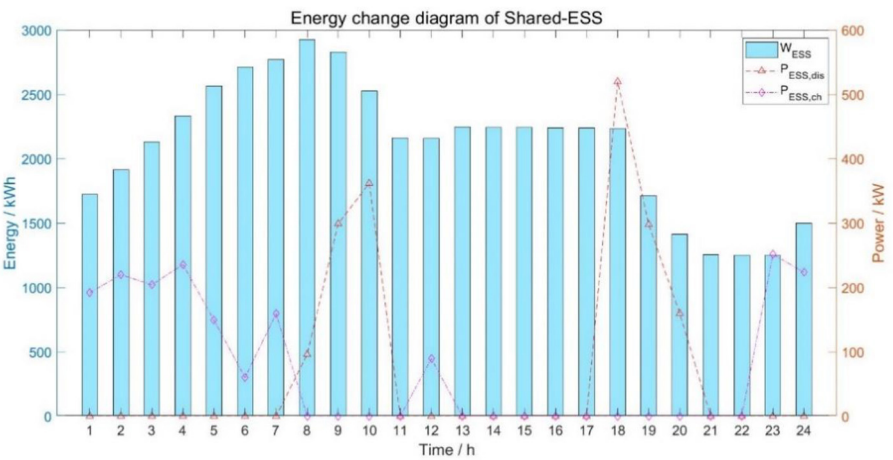

B Energy change diagram of Shared-ESS in scenario 1

FIGURE 4 | The operating status of Shared-ESS in scenario 1. **(A)** Electric power balance of common DC bus in Shared-ESS in scenario 1. **(B)** Energy change diagram of Shared-ESS in scenario 1.

electricity from external grid by microgrid. The peak time duration is between 08:00–11:00 and 18:00–23:00; the off-peak time duration is between 07:00–08:00 and 11:00–18:00; and the valley time duration is between 23:00 and 07:00. The real-time trading electricity price is shown in **Table 2**. The feed-in tariff of export renewable generation to external grid is set as 0.34 RMB/(kWh).

The operational parameters for the system are listed in **Table 3**.

Basic Scenario

The basic scenario refers to scenario 1 in **Table 1**, the capacity of Shared-ESS is 3,000 kWh, and the microgrid cluster contains 4 microgrids. The operational performance of the microgrid cluster is shown in **Figures 3–5**.

Operation Overview

According to **Figure 3**, it can be found that electricity demand can be satisfied by purchasing electricity from Shared-ESS rather than from the external grid during most of the peak time; during the off-peak time duration, the microgrids will purchase the inexpensive electricity from the external grid to feed the demand gap that the renewable generator cannot support; during the valley time, the surplus electricity generated by wind turbines will be stored into the Shared-ESS rather than selling to the external grid, which bring extra benefits to the microgrids.

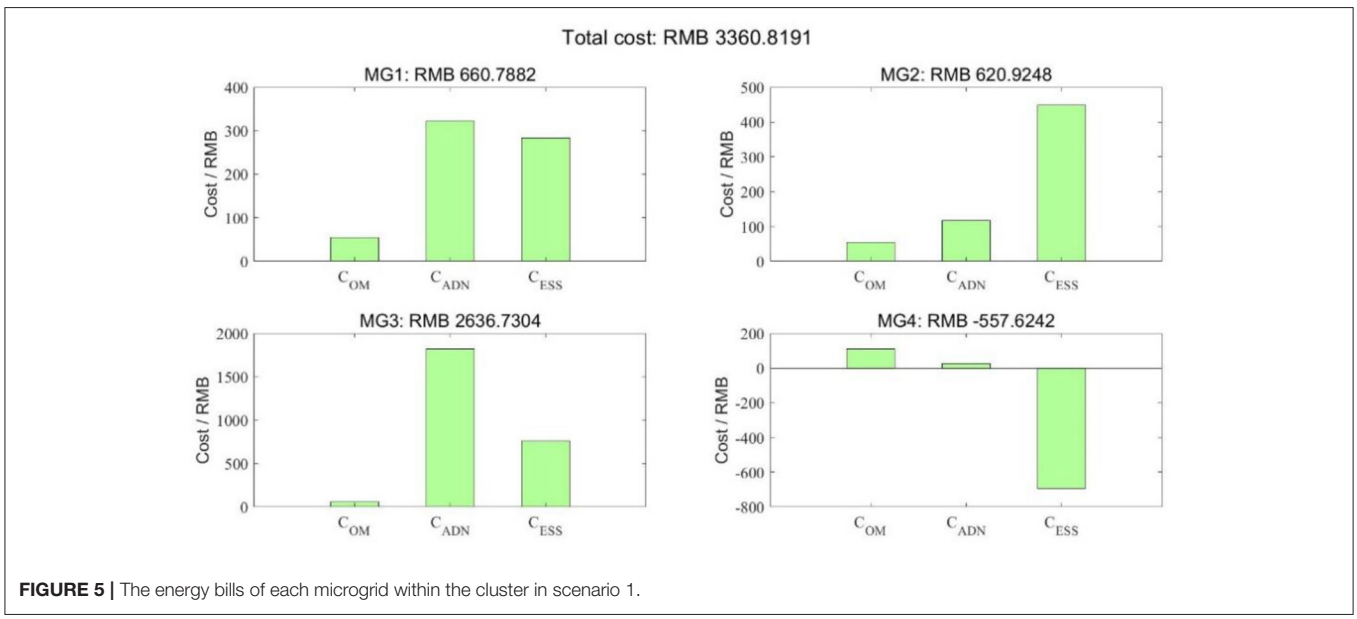

FIGURE 5 | The energy bills of each microgrid within the cluster in scenario 1.

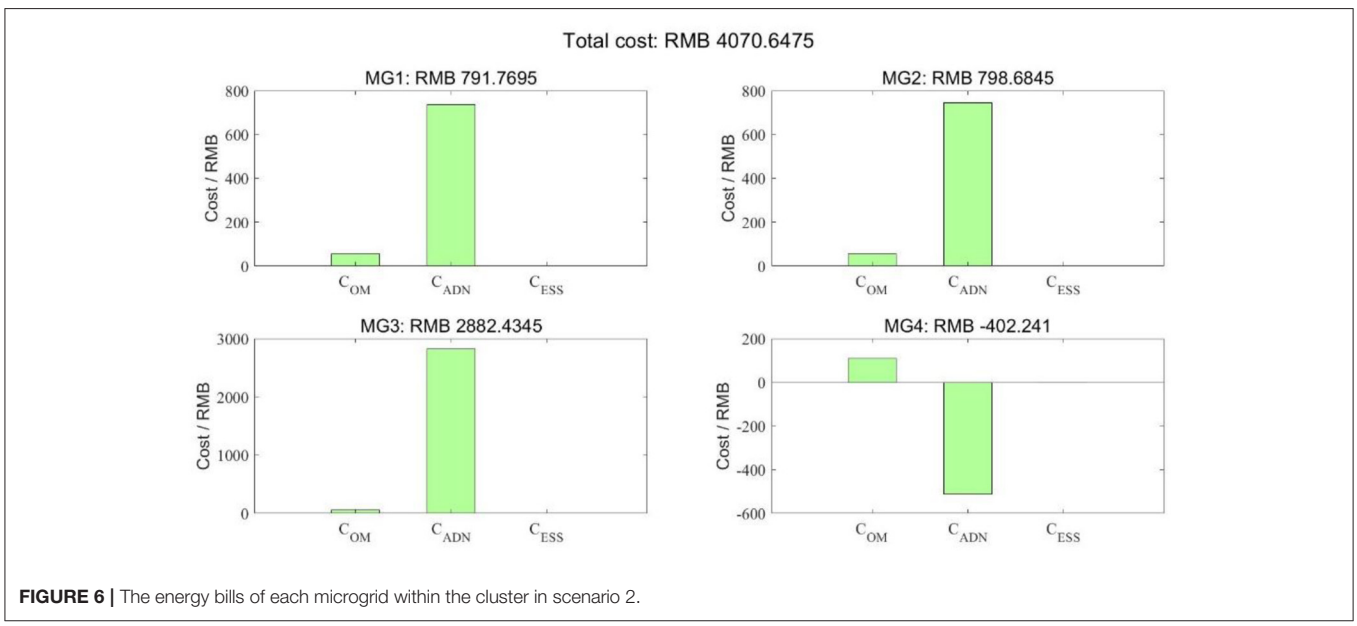

FIGURE 6 | The energy bills of each microgrid within the cluster in scenario 2.

However, due to the limited capacity of the battery in Shared-ESS, a considerable portion of the surplus power in microgrid 1 is sold to the external grid. The reason why the electricity of microgrid 1 is sold instead of other microgrids is because during this period, microgrid 1 has the lowest electricity price to Shared-ESS. Therefore, microgrid 1 sells surplus power to the external grid, so that the entire microgrid group can obtain the maximum economic benefits.

Power Exchange Among Microgrids

During 13:00–16:00 and 21:00–23:00, since the renewable energy of microgrid 4 generates more electricity, the power needs to be sold to meet the power balance of microgrid 4. However, other microgrids are still unable to make ends meet. At this time, it is not necessary to choose to sell electricity to the external grid with a low feed-in-tariff, and it is also not necessary to charge the battery in Shared-ESS. Electricity can be sold to microgrid 2 and microgrid 1 indirectly through the common DC bus inside Shared-ESS. In this way, the energy transmission efficiency is improved, the battery loss is reduced, and the cost of electricity is reduced too. Similarly, as for the selection of the microgrid, the algorithm will automatically choose to make microgrid 4 interact with the microgrid with the lowest cost of purchasing power from Shared-ESS.

Economic Benefit Analysis

The energy bills of each microgrid within the cluster are presented in **Figure 5**. It can be seen that the microgrid 3 with a higher electric load purchases more electricity from the external grid, so the cost is higher; and the microgrid 4 with more

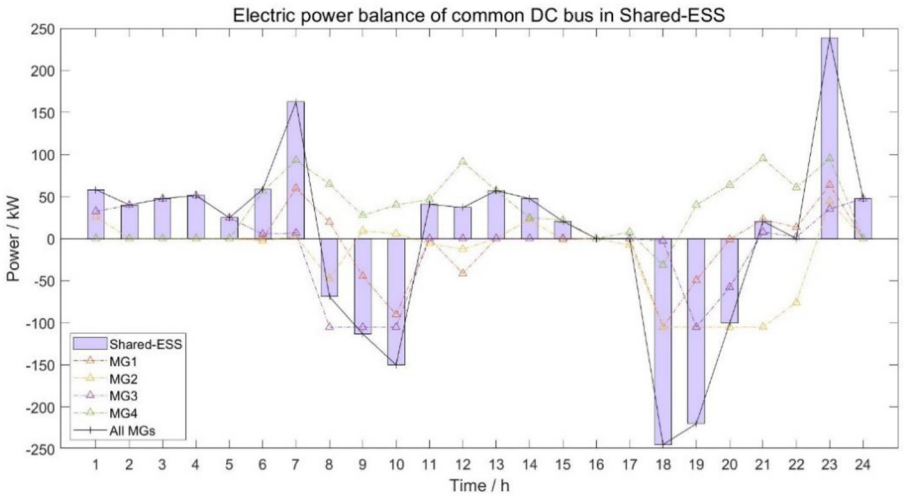

A Electric power balance of common DC bus in Shared-ESS in scenario 3

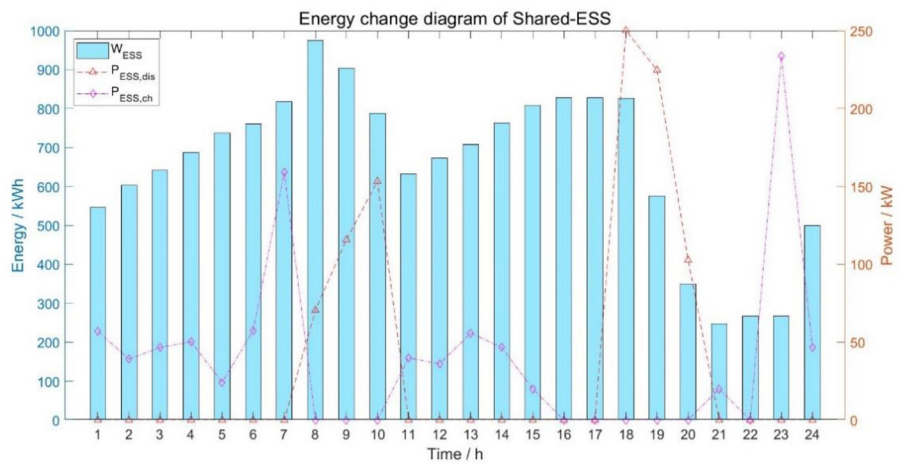

B Energy change diagram of Shared-ESS in scenario 3

FIGURE 7 | The operating status of Shared-ESS in scenario 3. **(A)** Electric power balance of common DC bus in Shared-ESS in scenario 3. **(B)** Energy change diagram of Shared-ESS in scenario 3.

renewable energy sources sells more electricity to Shared-ESS, so as to obtain more profits.

As shown in **Figure 4**, during the period when the renewable energy generation of microgrids exceed the electric load (23:00–7:00 the next day), the battery in Shared-ESS is charged; and during the period when the electricity price of external grid is very high (08:00–11:00 and 18:00–21:00), the battery in Shared-ESS is discharged. It can be seen that the use of Shared-ESS can not only play a role in shifting the usage of energy during peak time but also achieve the consumption of renewable energy.

Non-Shared-ESS Scenario

The non-Shared-ESS scenario refers to scenario 2 in **Table 1**. It has no Shared-ESS, and the load profile of the microgrid cluster is the same as scenario 1. The energy bills of each microgrid within the cluster are presented in **Figure 6**.

Operation Overview

Since there are no Shared-ESS in this scenario, the microgrid can only sell surplus electricity to the external grid and purchase the electricity from the external grid when necessary, which will result in compressed profit margins.

Economic Benefit Analysis

The daily electricity bill of the microgrid cluster without Shared-ESS is 4,070.6475RMB, which is 699.8284RMB higher than the cost of scenario 1. For the high renewable penetrated microgrid 4, the payoff is reduced from 557.6242RMB to 402.2410RMB (38.63% lower).

In general, compared with the microgrid cluster without Shared-ESS, the cluster equipped with Shared-ESS can reduce the total cost of purchasing electricity from the grid and improve the profitability of the microgrid that acts as a prosumer in the cluster.

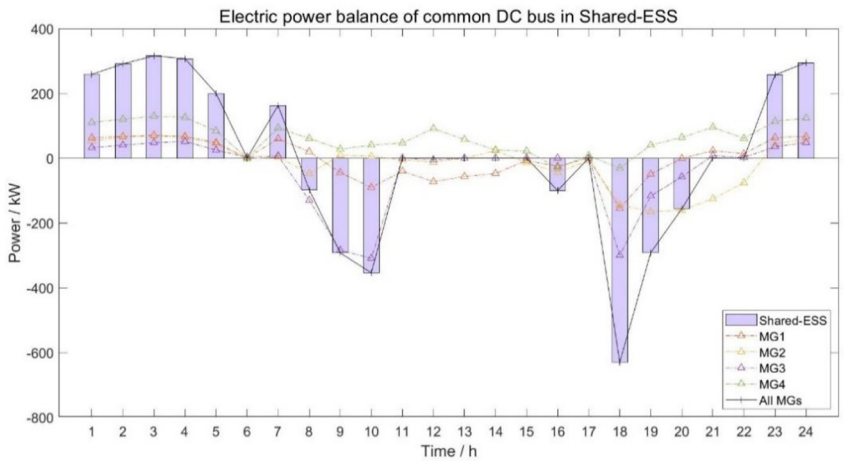

A Electric power balance of common DC bus in Shared-ESS in scenario 4

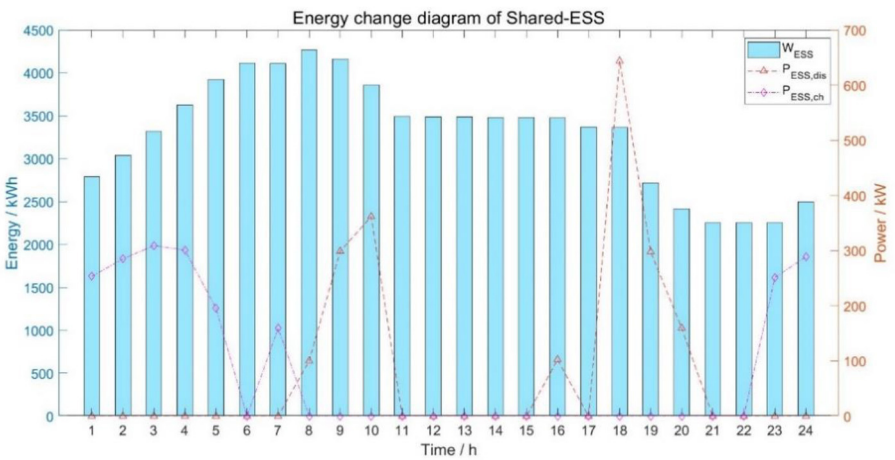

B Energy change diagram of Shared-ESS in scenario 4

FIGURE 8 | The operating status of Shared-ESS in scenario 4. **(A)** Electric power balance of common DC bus in Shared-ESS in scenario 4. **(B)** Energy change diagram of Shared-ESS in scenario 4.

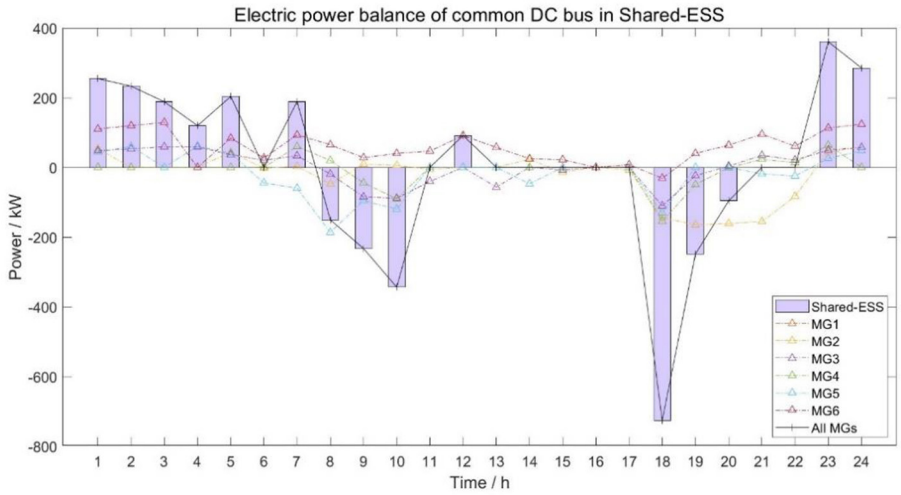

A Electric power balance of common DC bus in Shared-ESS in scenario 5

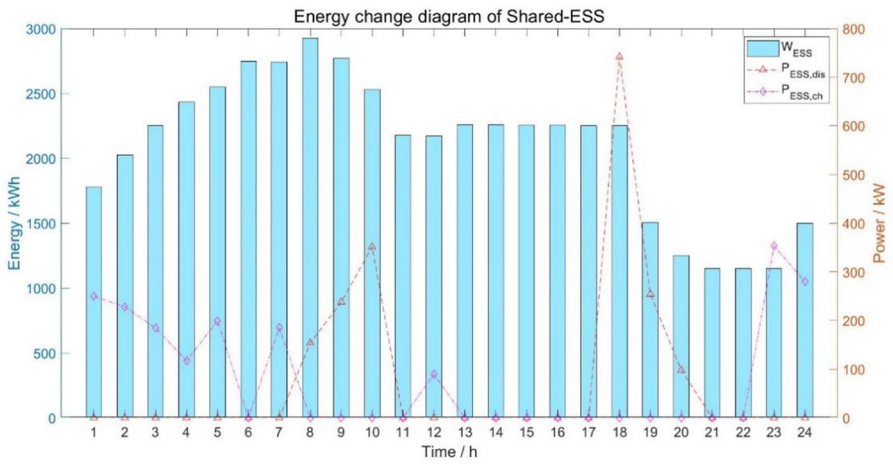

B Energy change diagram of Shared-ESS in scenario 5

FIGURE 9 | The operating status of Shared-ESS in scenario 5. **(A)** Electric power balance of common DC bus in Shared-ESS in scenario 5. **(B)** Energy change diagram of Shared-ESS in scenario 5.

Influence of the Capacity of the Battery in Shared-ESS to Microgrid Cluster

Larger capacity of Shared-ESS can correspondingly improve the flexibility of microgrid clusters. However, larger Shared-ESS means higher investment toward the physical equipment. In this part, various capacities (1,000 and 5,000 kWh) of the battery in Shared-ESS are evaluated and compared to scenario 1. These scenarios refer to scenario 3 and cenario 4 in **Table 1**. The operational results are given in **Figures 7**, **8**.

Operation Overview

When the capacity of the battery in Shared-ESS is 1,000 kWh, due to the insufficient battery capacity, a considerable part of the energy generated by renewable energy is not stored in the battery but is sold to the external grid due to lower feed-in-tariff. As a result of the power limitation of the AC/DC converters, during the peak period of power consumption, the demand of the load could not be met when the Shared-ESS reached the upper limit of the power sold to the microgrids. Therefore, it is still necessary to purchase electricity from the external grid at a high price. In fact, even if the power limitation of the AC/DC converter is not considered, the ESS still could not meet the load demand during the peak period of power consumption, because the battery capacity is so small that the stored energy is not enough.

When the capacity of the battery in Shared-ESS is 5,000 kWh, almost all the output of renewable energy is stored into Shared-ESS. During the period when the electricity price is high, most of the load demand is satisfied by Shared-ESS. There is still a small part that needs to be purchased from the external grid, because

the battery of Shared-ESS needs to keep the energy equal to the beginning after the end of a scheduling cycle.

Power Exchange Among Microgrids

For scenario 3, as the renewable energy output of microgrid 4 is relatively large, a part of the energy still needs to be sold to other microgrids through the common DC bus, but this part of energy reduces a lot, for the battery of Shared-ESS needs to be charged at noon to meet the electricity demand in the evening.

For scenario 4, the situation in which the microgrid 4 with more renewable energy output supplies energy to other microgrids through the common DC bus is not much different from the basic scenario.

Economic Benefit Analysis

When the capacity of the battery in Shared-ESS is reduced from 3,000 to 1,000 kWh, the total electricity cost of the microgrid cluster increases from 3,360.8191RMB to 3,564.7461RMB, which is 203.927RMB higher. According to the different electric load, the cost of microgrids 1–3 increases to a different extent. It can be seen that, in this situation, reducing the capacity of the battery in Shared-ESS is inconducive not only to shift the usage of energy during peak time but also to significantly increase the cost of electricity.

When the capacity of the battery in Shared-ESS is increased from 3,000 to 5,000 kWh, the total electricity cost of the microgrid cluster reduces from 3,360.8191RMB to

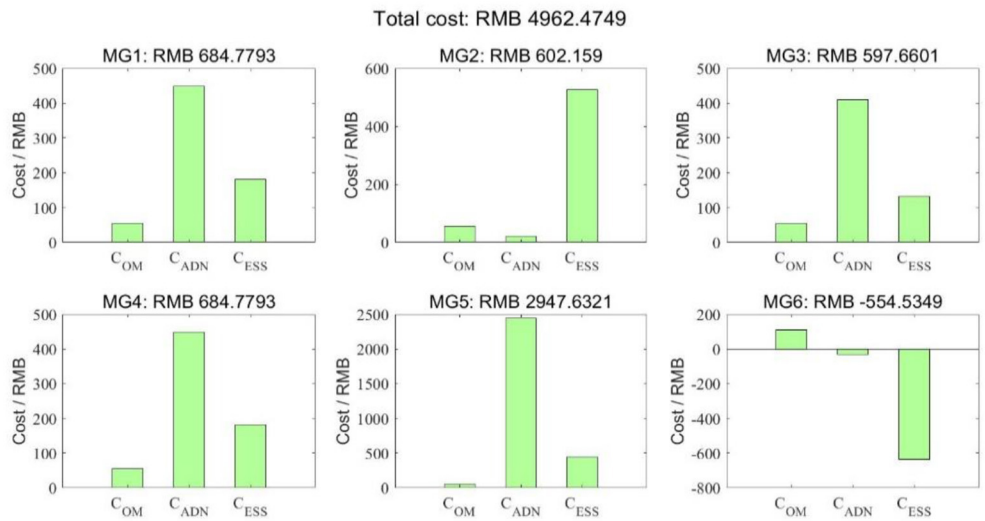

FIGURE 10 | The energy bills of each microgrid within the cluster in scenario 5.

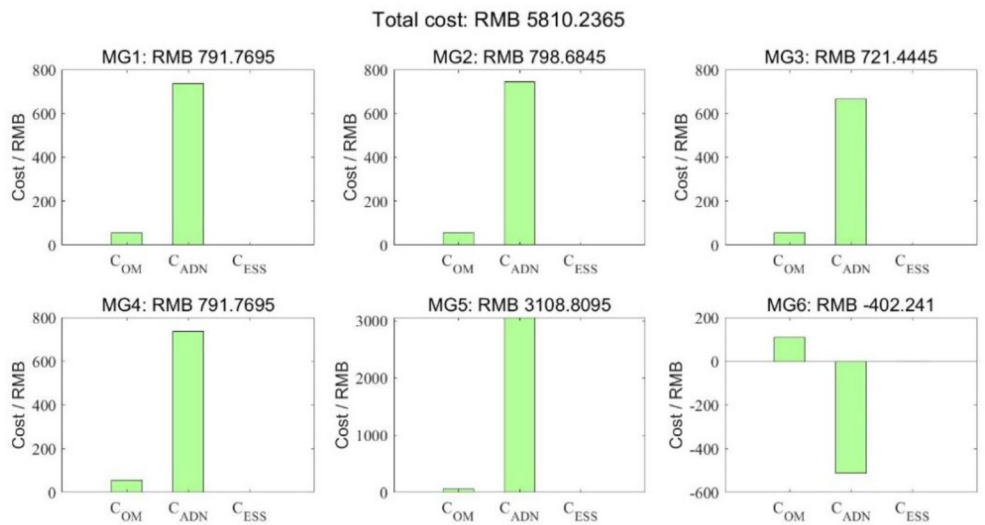

FIGURE 11 | The energy bills of each microgrid within the cluster in scenario 6.

3,302.0391RMB, which is 58.78RMB lower. Each microgrid has a slight decrease in cost or increase in profit, but not significantly. It can be seen that, in this situation, increasing the capacity of the battery in Shared-ESS does not play an important role, and the cost reduction is very small. Obviously, this reduction is not worth the additional investment costs.

In summary, about 3,000 kWh is an ideal capacity for the battery in Shared-ESS.

Influence of the Number of Microgrids to Microgrid Cluster

This case corresponds to scenarios 5 and 6 in **Table 1**. The battery in Shared-ESS has a capacity of 3,000 kWh, and 6 microgrids in the microgrid cluster are connected to Shared-ESS. The results of the optimization are shown in **Figures 9–11**.

Operation Overview

When the number of the microgrids increases to 6, the 3,000 kWh battery capacity is not enough. At this time, some of the renewable generation output could not be stored in the battery in Shared-ESS, but is sold to the external grid. And during the peak period of power consumption, a considerable part of electric load is satisfied by purchasing electricity from the external grid (of course, microgrids with higher electricity purchase prices from Shared-ESS at this time are chosen to buy electricity from the external grid).

However, when the number of microgrids is larger, the battery in Shared-ESS and microgrids with more renewable energy generation can choose microgrids for energy trading more freely at different time. Therefore, the algorithm will choose the microgrid with the lowest electricity purchase price from Shared-ESS, thereby saving more electricity cost for the microgrid cluster.

Power Exchange Among Microgrids

The microgrid 6 with more renewable energy generation sells electricity to microgrid 5, microgrid 3, and microgrid 2 at different time, depending on which microgrid has a lower electric purchase price. Under this circumstance, there are more opportunities for energy transactions between microgrids, and more economical transaction ways will be selected, thereby achieving better economic benefits.

Economic Benefit Analysis

When the number of microgrids is 6, the saved electricity cost is 847.7616RMB, which is much more than the 699.8284RMB when the number of microgrids is 4. It can be seen that when the number of microgrids increases, for the microgrid cluster with Shared-ESS, it facilitates reducing the total energy cost of the system.

CONCLUSION

This article proposes an economic optimal scheduling method for microgrid clusters with Shared-ESS. The global energy optimization management of the microgrid cluster can be achieved based on the established model and the optimization method. The microgrids can realize bidirectional energy flow with Shared-ESS through the common connected DC bus, thereby achieving energy storage and P2P transaction among each other. Case studies show that after equipping with the Shared-ESS, the microgrid cluster can save up to 17.23% of the total electricity cost, which is quite significant. For this microgrid cluster system, 3,000 kWh is a relatively reasonable battery capacity, based on the evaluations of different sizes of the Shared-ESS. The greater the number of microgrids connected to Shared-ESS, the more the electricity consumption costs can be saved, benefiting from the better power exchange among the microgrids. It can be concluded that the Shared-ESS effectively facilitates the consumption of renewable energy, plays an important role in shifting the usage of energy during peak time, improves energy utilization efficiency, and reduces electricity costs. Therefore, by optimizing the charge and discharge status and the power of the battery in Shared-ESS, and the purchase and sale strategy of the microgrids, the operating cost of the microgrid cluster system can be significantly reduced, and the day-ahead economic optimal dispatch of the microgrid cluster can be achieved.

DATA AVAILABILITY STATEMENT

The raw data supporting the conclusions of this article will be made available by the authors, without undue reservation.

AUTHOR CONTRIBUTIONS

SC and SZ conceptualized the study and contributed to the investigation. HZ and MC contributed to the study methodology. YW contributed to the software. KC and SZ contributed to the validation and writing—review and editing. HZ and SZ contributed to the formal analysis and visualization. SC and HZ contributed to the writing—original draft preparation. MC and SC contributed to the supervision. KC, YW, MC, and SC contributed to the funding acquisition. All authors have read and agreed to the published version of the manuscript.

FUNDING

The authors declare that this study received funding from Science and Technology Project of Jiangsu Electric Power Company "Key Technologies and Research of Smart Energy Service for City-Scale Energy Internet" under the grand number J2019089. The funder was not involved in the study design, collection, analysis, interpretation of data, the writing of this article or the decision to submit it for publication.

ACKNOWLEDGMENTS

The authors would like to thank the sponsorship of Science and Technology Project of Jiangsu Electric Power Company.

REFERENCES

AlSkaif, T., Luna, A. C., Zapata, M. G., Guerrero, J. M., and Bellalta, B. (2017). Reputation-based joint scheduling of households appliances and storage in a microgrid with a shared battery. *Energy Build.* 138, 228–239. doi: 10.1016/j.enbuild.2016.12.050

Biech, M., Bigdon, T., Dielitz, C., Fromme, G., and Remke, A. (2016). "A smart neighbourhood simulation tool for shared energy storage and exchange," in *Analytical and Stochastic Modelling Techniques and Applications. ASMTA 2016. Lecture Notes in Computer Science*. eds S. Wittevrongel and T. Phung-Duc (Cham: Springer), 76–91. doi: 10.1007/978-3-319-43904-4_6

Borghetti, A., Bosetti, M., Grillo, S., Massucco, S., Nucci, C. A., Paolone, M., et al. (2010). Short-term scheduling and control of active distribution systems with high penetration of renewable resources. *IEEE Syst. J.* 4, 313–322. doi: 10.1109/JSYST.2010.2059171

Broering, H., and Madlener, R. (2017). Simulation and evaluation of the economic merit of cloud energy storage for prosumers: the case of Germany. *Energy Proc.* 105, 3507–3514. doi: 10.1016/j.egypro.2017.03.804

Carli, R., and Dotoli, M. (2017). Cooperative distributed control for the energy scheduling of smart homes with shared energy storage and renewable energy source. *IFAC Papers Online* 50, 8867–8872. doi: 10.1016/j.ifacol.2017.08.1544

Chen, H., Cheng, H., Xu, G., Zhou, W., Zhang, X., and Sang, D. (2018). "Research on consumer side energy storage optimization configuration based on cloud energy storage," in *2018 3rd International Conference on Smart City and Systems Engineering* (Xiamen: ICSCSE; IEEE). doi: 10.1109/ICSCSE.2018.00102

Chen, H., Yu, Y., Hu, Z., Luo, H., Tan, C., and Rajagopal, R. (2017). "Energy storage sharing strategy in distribution networks using bi-level optimization approach," in *2017 IEEE Power & Energy Society General Meeting* (Chicago, IL). doi: 10.1109/PESGM.2017.8274595

Dai, R., and Charkhgard, H. (2018). Bi-objective mixed integer linear programming for managing building clusters with a shared electrical energy storage. *Comput. Oper. Res.* 96, 173–187. doi: 10.1016/j.cor.2018.01.002

Denholm, P., and Hand, M. (2011). Grid flexibility and storage required to achieve very high penetration of variable renewable electricity. *Energy Policy* 39, 1817–1830. doi: 10.1016/j.enpol.2011.01.019

Fu, H., Wu, Z., Li, J., Zhang, X., and Brandt, J. (2016). A configurable VPP with managed energy services: a malmo western harbour case. *IEEE Power Energy Technol. Syst. J.* 3, 166–178. doi: 10.1109/JPETS.2016.2596779

Hosseini, S. M., Carli, R., and Dotoli, M. (2019). "Robust energy scheduling of interconnected smart homes with shared energy storage under quadratic pricing," in *2019 IEEE 15th International Conference on Automation Science and Engineering* (Vancouver, BC: CASE). doi: 10.1109/COASE.2019.8843230

Kim, I., and Kim, D. (2017). "Optimal capacity of shared energy storage and photovoltaic system for cooperative residential customers," in *2017 International Conference on Information and Communications* (Hanoi: ICIC). doi: 10.1109/INFOC.2017.8001682

Kim, I., and Kim, D. (2019). "Pricing-based shared energy storage optimization for residential users with photovoltaic generation system and demand-side load management," in *2019 Eleventh International Conference on Ubiquitous and Future Networks* (Zagreb: ICUFN). doi: 10.1109/ICUFN.2019.8806069

Li, Y., Gao, D. W., Gao, W., Zhang, H., and Zhou, J. (2020). Double-mode energy management for multi-energy system via distributed dynamic event-triggered newton-raphson algorithm. *IEEE Trans. Smart Grid* 11, 5339–5356. doi: 10.1109/TSG.2020.3005179

Li, Y., Zhang, H., Liang, X., and Huang, B. (2019). Event-triggered-based distributed cooperative energy management for multienergy systems. *IEEE Trans. Smart Grid* 4, 2008–2022. doi: 10.1109/TII.2018.2862436

Liu, J., Zhang, N., Kang, C., Kirschen, D., and Xia, Q. (2017). Cloud energy storage for residential and small commercial consumers: a business case study. *Appl. Energy* 188, 226–236. doi: 10.1016/j.apenergy.2016.11.120

Liu, J., Zhang, N., Kang, C., Kirschen, D. S., and Xia, Q. (2018). Decision-making models for the participants in cloud energy storage. *IEEE Trans. Smart Grid* 9, 5512–5521. doi: 10.1109/TSG.2017.2689239

Liu, N., Cheng, M., Yu, X., Zhong, J., and Lei, J. (2018). Energy-sharing provider for pv prosumer clusters: a hybrid approach using stochastic programming and stackelberg game. *IEEE Trans. Ind. Electron. cs* 65, 6740–6750. doi: 10.1109/TIE.2018.2793181

Lombardi, P., and Schwabe, F. (2017). Sharing economy as a new business model for energy storage systems. *Appl. Energy* 188, 485–496. doi: 10.1016/j.apenergy.2016.12.016

Oh, E., and Son, S. (2019). Shared electrical energy storage service model and strategy for apartment-type factory buildings. *IEEE Access* 7, 130340–130351. doi: 10.1109/ACCESS.2019.2939406

Rahbar, K., Moghadam, M. R. V., Panda, S. K., and Reindl, T. (2016). "Shared energy storage management for renewable energy integration in smart grid," in *2016 IEEE Power & Energy Society Innovative Smart Grid Technologies Conference* (Minneapolis, MN: ISGT). doi: 10.1109/ISGT.2016.7781230

Roberts, M. B., Bruce, A., and MacGill, I. (2019). Impact of shared battery energy storage systems on photovoltaic self-consumption and electricity bills in apartment buildings. *Appl. Energy* 245, 78–95. doi: 10.1016/j.apenergy.2019.04.001

Sickel, R., Vetters, D., Mehlich, H., Bodach, M., Bocklisch, T., and Lutz, J. (2005). "Modular converter for fuel cell systems with buffer storage," in *2005 European Conference on Power Electronics and Applications* (Dresden: IEEE). doi: 10.1109/EPE.2005.219721

Steriotis, K., Tsaousoglou, G., Efthymiopoulos, N., Makris, P., and Varvarigos, E. (2019). Real-time pricing in environments with shared energy storage systems. *Energy Effic.* 12, 1085–1104. doi: 10.1007/s12053-018-9723-8

Swierczyński, M., Stroe, D. I., Stan, A. I., and Teodorescu, R. (2013). "Primary frequency regulation with Li-ion battery energy storage system: a case study for Denmark," in *2013 IEEE ECCE Asia Downunder* (Melbourne, VIC: IEEE). doi: 10.1109/ECCE-Asia.2013.6579141

Taşcikaraoglu, A. (2018). Economic and operational benefits of energy storage sharing for a neighborhood of prosumers in a dynamic pricing environment. *Sustain. Cities Soc.* 38, 219–229. doi: 10.1016/j.scs.2018.01.002

Tascikaraoglu, A., Paterakis, N. G., Erdinc, O., and Catalao, J. P. S. (2019). Combining the flexibility from shared energy storage systems and DLC-based demand response of HVAC units for distribution system operation enhancement. *IEEE Trans. Sustain. Energy* 10, 137–148. doi: 10.1109/TSTE.2018.2828337

Tushar, W., Chai, B., Yuen, C., Huang, S., Smith, D. B., Poor, H. V., et al. (2016). Energy storage sharing in smart grid: a modified auction-based approach. *IEEE Trans. Smart Grid* 7, 1462–1475. doi: 10.1109/TSG.2015.2512267

Wang, Z., Gu, C., and Li, F. (2018). Flexible operation of shared energy storage at households to facilitate PV penetration. *Renew. Energy* 116, 438–446. doi: 10.1016/j.renene.2017.10.005

Yan, T., Liu, J., Niu, Q., Chen, J., Xu, S., Niu, M., et al. (2020). Distributed energy storage node controller and control strategy based on energy storage cloud platform architecture. *Glob. Energy Interconnect.* 3, 166–174. doi: 10.1016/j.gloei.2020.05.008

Yushuai, L., Gao, W., Gao, W., Zhang, H., and Zhou, J. (2020). A distributed double-newton descent algorithm for cooperative energy management of multiple energy bodies in energy internet. *IEEE Trans. Ind. Inform.* 8:1. doi: 10.1109/TII.2020.3029974

Zaidi, B. H., Bhatti, D. M. S., and Ullah, I. (2018). Combinatorial auctions for energy storage sharing amongst the households. *J. Energy Stor.* 19, 291–301. doi: 10.1016/j.est.2018.08.010

Zhang, W., Wei, W., Chen, L., Zheng, B., and Mei, S. (2020). Service pricing and load dispatch of residential shared energy storage unit. *Energy* 202, 117543. doi: 10.1016/j.energy.2020.117543

Zhou, J., Xu, Y., Sun, H., Li, Y., and Chow, M. (2020). Distributed power management for networked ac–dc microgrids with unbalanced microgrids. *IEEE Trans. Ind. Inform.* 16, 1655–1667. doi: 10.1109/TII.2019.2925133

Zhou, J., Xu, Y., Sun, H., Wang, L., and Chow, M. (2020a). Distributed event-triggered H∞ consensus based current sharing control of DC microgrids considering uncertainties. *IEEE Trans. Ind. Inform.* 16, 7413–7425. doi: 10.1109/TII.2019.2961151

Zhou, S., Zou, F., Wu, Z., Gu, W., Hong, Q., and Booth, C. (2020b). A smart community energy management scheme considering user dominated demand side response and P2P trading. *Int. J. Electr. Power Energy Syst.* 114:105378. doi: 10.1016/j.ijepes.2019.105378

Zhu, H., and Ouahada, K. (2019a). "Cost minimization energy storage sharing management," in *2019 IEEE International Conference on Communications, Control, and Computing Technologies for Smart Grids* (Beijing: SmartGridComm; IEEE). doi: 10.1109/SmartGridComm.2019.8909720

Zhu, H., and Ouahada, K. (2019b). Credit-based distributed real-time energy storage sharing management. *IEEE Access* 7, 185821–185838. doi: 10.1109/ACCESS.2019.2961389

Conflict of Interest: SC, KC, MC, and YW was employed by Yangzhou Power Supply Company, Jiangsu Electric Power Company, State Grid Cooperation of China.

The remaining authors declare that the research was conducted in the absence of any commercial or financial relationships that could be construed as a potential conflict of interest.

frontiers in Energy Research

ORIGINAL RESEARCH
published: 15 June 2021
doi: 10.3389/fenrg.2021.679365

Optimal Planned Electricity Allocation Model for Power Exchange Under the Plan-Market Double-Track Mechanism

Chuan He[1,2], Jiajun Tang[3], Weishi Zhang[1,2], Zhi Zhang[3], Zhemin Lin[1,2], Yating Li[3], Hanhan Qian[1,2], Hailong Jiang[1,2], Zhenzhi Lin[3,4] and Li Yang[3]*

[1]State Grid Anhui Electric Power Co., Ltd., Hefei, China, [2]Anhui Power Exchange Center Company, Hefei, China, [3]College of Electrical Engineering, Zhejiang University, Hangzhou, China, [4]College of Electrical Engineering, Shandong University, Jinan, China

The orderly deregulation of planned electricity generation and consumption is an important measure for electricity market reform in several countries (such as China), and a reasonable proportion of planned electricity in the total energy consumption is conducive to the smooth transition from the regulation mode to the market mode. Under the plan-market double-track mechanism (PMDM) implemented, a modified linear bidding function of generation companies (GCs) is first proposed, and the unified clearing price of unilateral generation market is determined accordingly. Second, considering the robust bidding strategies of generation companies, a bi-level optimal planned electricity allocation model for power exchange (PX) is constructed. In the upper level, the proportion of planned electricity is optimized by PX to minimize the CVaR of Lerner Index (LI), so as to maintain the market power at a low level. In the lower level, based on the robust optimization theory and the prediction of rival bidding, the bidding strategy of a GC is optimized by solving a specified max–min problem. Simulations based on data from a provincial electricity market in China illustrate that the market power can be reduced through a reasonable proportion of planned electricity designed by the PX. In addition, when more GCs tend to avoid a market risk, the proportion of planned electricity can be increased accordingly.

Keywords: plan-market double-track mechanism, planned electricity, conditional value at risk, robust optimization, lerner index

OPEN ACCESS

Edited by:
Ningyi Dai,
University of Macau, China

Reviewed by:
Amirreza Naderipour,
University of Technology Malaysia, Malaysia
Haibo Li,
Tsinghua University, China

****Correspondence:***
Zhenzhi Lin
linzhenzhi@zju.edu.cn

Specialty section:
This article was submitted to Smart Grids, a section of the journal Frontiers in Energy Research

Received: *11 March 2021*
Accepted: *21 May 2021*
Published: *15 June 2021*

Citation:
He C, Tang J, Zhang W, Zhang Z, Lin Z, Li Y, Qian H, Jiang H, Lin Z and Yang L (2021) Optimal Planned Electricity Allocation Model for Power Exchange Under the Plan-Market Double-Track Mechanism. Front. Energy Res. 9:679365. doi: 10.3389/fenrg.2021.679365

INTRODUCTION

Electricity market reform is a task that many countries are facing or will face, the key point of which is to ensure the smooth transition from regulation to deregulation (National Development and Reform Commission National Energy Administration, 2017). In the past, due to low load demand and low risk of reform at the initial stage of electricity market construction, it took only a short time for many countries or regions to complete the transition, and the liberalization of these electricity markets is achieved by gradually easing market access. For example, it took only 5 months for ERCOT electricity market in Texas, the United States, to realize the transition from the pilot stage to the full liberalization of electricity market users (Sioshansi, 2013). All eligible users are allowed to participate in the transaction at the early stage of electricity market reform in Norway, which is the predecessor of Nord Pool (Woo et al., 2003). However, the rapid liberalization of the electricity

market may also lead to many problems in the early stage of electricity market reform. Among them, the market power issue is the most concern of the PX. For example, the rotational and large-scale blackouts in California from 2000 to 2001, which led to direct economic losses of as much as US $40 billion, were partly caused by GCs using market power to manipulate market prices (Budhraja, 2001). In 2006, the economic withholding of GCs in the capacity market in New York caused a total loss of US $160 million (Antitrust, 2010). Even in a period of low load demand and little influence of market power, huge economic losses have been caused by the rapid liberalization of market. Nowadays, electricity market reform is underway in China and the load demand is much higher than 20 years ago, thus it is necessary to pay more attention to the market power in the transition from the regulation mode to the market mode.

Electricity market reform had been carried out in some areas of China several years ago. For example, the generation side market bidding transaction was implemented in Northeast China in the last electricity market reform. However, because of the full liberalization of market in the early stage of the reform, the generation and consumption plans are highly mismatching. In May 2006, Northeast Power Grid Company lost a total of 3.2 billion CNY within 16 days as GCs improved their bidding price together (International Energy Agency, 2006). Therefore, in the current electricity market reform, in order to ensure the stability of the market, China gradually allows users to participate in the electricity market according to the voltage level or annual electricity consumption, which is similar to the mode of the British electricity market reform (Sioshansi, 2013). The plan-market double-track mechanism (PMDM) is put forward in the electricity market reform since 2016, which means that only some of the qualified electricity users participate in the market, and correspondingly, GCs have both planned electricity and market electricity. The PMDM is also an effective mechanism that can be used in electricity market reforms for other countries. The key task of PMDM is to determine the reasonable proportion of planned electricity in total consumption.

Under this background, an appropriate method to determine the proportion of planned electricity in total electricity consumption is needed by PX, so as to set the market access conditions and ensure the smooth progress of electricity market reform. In a study by Jiang et al. (2004), the economic allocation of planned electricity and market electricity is realized considering the unit operation and network congestion constraints. In a study by Sun et al. (2020), an intraday planned electricity rolling model aiming at fairness is established to deal with the uncertainty of wind power generation. Obviously, the existing researches focus on the allocation and scheduling of planned and market electricity for specified units in time series, but few on the proportion of planned electricity in the total consumption. Therefore, to make up for the lack of previous research, an optimal planned electricity allocation model for PX is established, with the bidding strategy of GCs under PMDM considered.

The bidding strategy of generators has been studied. In the study by Bompard et al. (2008), the optimal bidding strategy of generators is obtained by analyzing the residual demand curve, and the stable state of the market is studied by iteration. In the study by Park et al. (2001), the bidding behaviors of generators under complete information market is modeled and analyzed based on the Nash equilibrium game theory. In other studies, probability statistics or fuzzy mathematics are introduced to model the uncertainty of market price and rival biddings, so as to optimize the bidding strategy of GCs. In a study by Wen and David (2001), the linear bidding model of generators under incomplete information is constructed, and the prediction of competitors' bidding strategies is simulated by the probability density function of joint normal distribution. In a study by Ansari and Rahimi-Kian (2015), considering the uncertainty of market demand, a bidding model of generators is established which takes variance of profit as the risk measurement. In the study by Pousinho et al. (2013), the prediction of market demand and competitors' bidding strategies is reflected by the residual demand curve in multi-scenarios, and the conditional value at risk is used to measure the profit risk of market, and then the sectional bidding model of generators is constructed. The bidding model of microgrid based on robust optimization is constructed in the study by Liu et al. (2016), and the uncertainty of its own output and market price is simulated by the scenario based on prediction data. However, the bidding strategies of GCs are influenced by the planned electricity under PMDM. In order to model the bidding behavior of GCs under the special market mechanism, a modified linear bidding function is proposed in this study, and an optimal bidding strategy model of power generation companies based on robust optimization is further constructed.

The contributions of this work are presented as follows:

(1) The optimal planned electricity allocation model for PX is built in the study to formulate a reasonable proportion of planned electricity in total consumption, so as to reduce the risk of transition from regulation to deregulation. Considering that the existing studies rarely focus on the proportion of planned electricity and related market power issues in the transition of electricity market, this study provides effective support for the PX to operate the market.
(2) A modified linear bidding function of generators is proposed in the study due to the traditional linear bidding function is not suitable for PMDM. By comparison, since the impact of planned electricity is considered, the bidding strategies of GCs under PMDM are better reflected by the modified linear bidding function, which further supports PX to determine the proportion of planned electricity.

The rest of this article is as follows. The modified linear bidding function of generators is analyzed in *Modified Linear Bidding Function of Generation Companies under Plan-Market Double-Track Mechanism*. The planned electricity allocation bi-level model for PX is constructed in *Bi-level Optimal Planned Electricity Allocation Model Considering Generation Companies' Robust Bidding Strategies*. The effectiveness of the model is analyzed by the market data of a province in China in *Case Study*, and the main research results of the study are summarized in *Conclusion*.

MODIFIED LINEAR BIDDING FUNCTION OF GENERATION COMPANIES UNDER PLAN-MARKET DOUBLE-TRACK MECHANISM

Under PMDM in China, the total electricity generation is divided into planned electricity and market electricity by PX, planned electricity is allocated according to the generation capacity of GCs and settled at regulated prices, while the market-oriented generation is allocated according to the bidding of each generating unit. The market electricity on the consumption side is determined by the types of electricity users and market access conditions of each province. For example, in 2017, it was only large industrial enterprises with annual electricity consumption of more than 80 million kWh, commercial users with consumption of more than 50 million kWh, and some designated enterprises or users that were allowed to participate in the electricity market in the Guangdong Province of China (Guangdong Economic and Information Commission et al., 2017); and in 2020, industrial/commercial enterprises with annual electricity consumption of more than four million kWh are allowed to participate in the transaction (Guangdong Electric Power Exchange Center Co., Ltd, 2020). Let Q^P and Q^M represent planned electricity and market electricity, respectively. Thus, the total electricity consumption Q^U is expressed as follows:

$$Q^U = Q^P + Q^M. \tag{1}$$

The planned electricity for the year Y + 1 is announced by PX at the end of the year Y and allocated to GCs according to the ratio of the generation capacity. After allocation, GCs participate in the electricity market of the year Y + 1 based on their residual generation capacity. Therefore, in order to give priority to meeting the planned demand for electricity, part of the capacity of GCs in a certain period of time is occupied, and the rest is involved in market transactions. Considering the increasing marginal generation cost of units, the occupied capacity will increase the cost of the market electricity of GC, which should be fully considered in market bidding.

Generally, quadratic function is introduced to model the relationship between generation cost and generation capacity, and expressed as follows (Dagoumas, 2019):

$$C_i = \frac{1}{2}a_i Q_i + b_i Q_i + c_i, \tag{2}$$

where a_i, b_i, and c_i represent the inherent generation cost coefficients of the GC i, which can be obtained by fitting the historical data. Q_i represents the total generation of the GC i. Then, the marginal generation cost C_i^M can be obtained by deriving the generation cost of the GC i, and expressed as follows:

$$C_i^M = a_i Q_i + b_i, \tag{3}$$

Linear bidding function is a common form of cost-based bidding strategy for GCs, which can be expressed as follows:

$$P_i^{bid,nor} = k_i^{nor} Q_i + b_i, \tag{4}$$

where b_i is the fixed generation cost coefficient. k_i^{nor} is the optimization variable; each different k_i^{nor} represents a bidding strategy for generation company i.

The marginal generation cost of GC is positively related to the total generation, and planned electricity increases the marginal cost of the market electricity, which is not considered in the bidding function in **Eq. 4**. Let $\overline{Q_i}$ represents the maximum generation capacity of the GC i and Q_i^P represents the planned electricity of the GC i, then the latter can be expressed as follows:

$$Q_i^p = Q^p \frac{\overline{Q_i}}{\sum_{j=1}^{n} \overline{Q_j}}, \tag{5}$$

where n is the total number of GCs.

As shown in **Figure 1**, the bidding function curve of GCs (in green) is higher than the marginal generation cost (in yellow) without planned electricity. But under PMDM in China, as part of the generating capacity of GCs is occupied by the planned electricity, and the traditional linear bidding function (in blue) of GCs is lower than the marginal generation cost within a certain range (i.e., the shadow part). For rational GCs, the linear bidding function under PMDM should be modified, as shown by the red curve in **Figure 1**. On the premise that the allocated planned electricity is known to GC in advance, its quotation in the market will be higher than or equal to the corresponding marginal cost. Thus, the modified bidding function can be expressed as follows:

$$P_i^{bid,*} = k_i^* \left(Q_i - Q_i^P\right) + a_i Q_i^P + b_i \ , \ \ k_i^* \geq a_i, \tag{6}$$

where $P_i^{bid,*}$ is the bidding function of the GC i. k_i^* is the modified quotation coefficient. $a_i Q_i^P$ represents the marginal generation cost increment resulting from the allocated planned electricity.

For a generation side quotation market with n generation companies, the unified clearing price P^{MCP} can be expressed as follows:

$$P^{MCP} = k_i^* Q_i^M + a_i Q_i^P + b_i \ , \ \ i = 1, 2, \cdots, n. \tag{7}$$

Here, Q_i^M is the market electricity of GC i, which meets the following equation:

$$\sum_{i=1}^{n} Q_i^M = Q^M. \tag{8}$$

By solving the **Eqs 1**, **5**, **7**, and **8** simultaneously, the unified clearing price of the electricity market under PMDM is obtained, which can be expressed as follows (Wen and David, 2001):

$$P^{MCP} = \frac{Q^U - Q^P + \sum_{i=1}^{n} \frac{a_i \overline{Q_i} Q^P + b_i \sum_{j=1}^{n} \overline{Q_j}}{k_i^* \sum_{j=1}^{n} \overline{Q_j}}}{\sum_{i=1}^{n} \frac{1}{k_i^*}}. \tag{9}$$

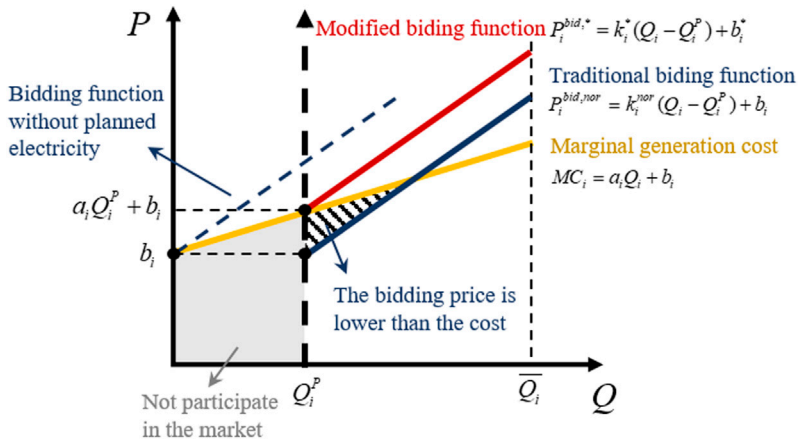

FIGURE 1 | The bidding function of GCs under the PMDM.

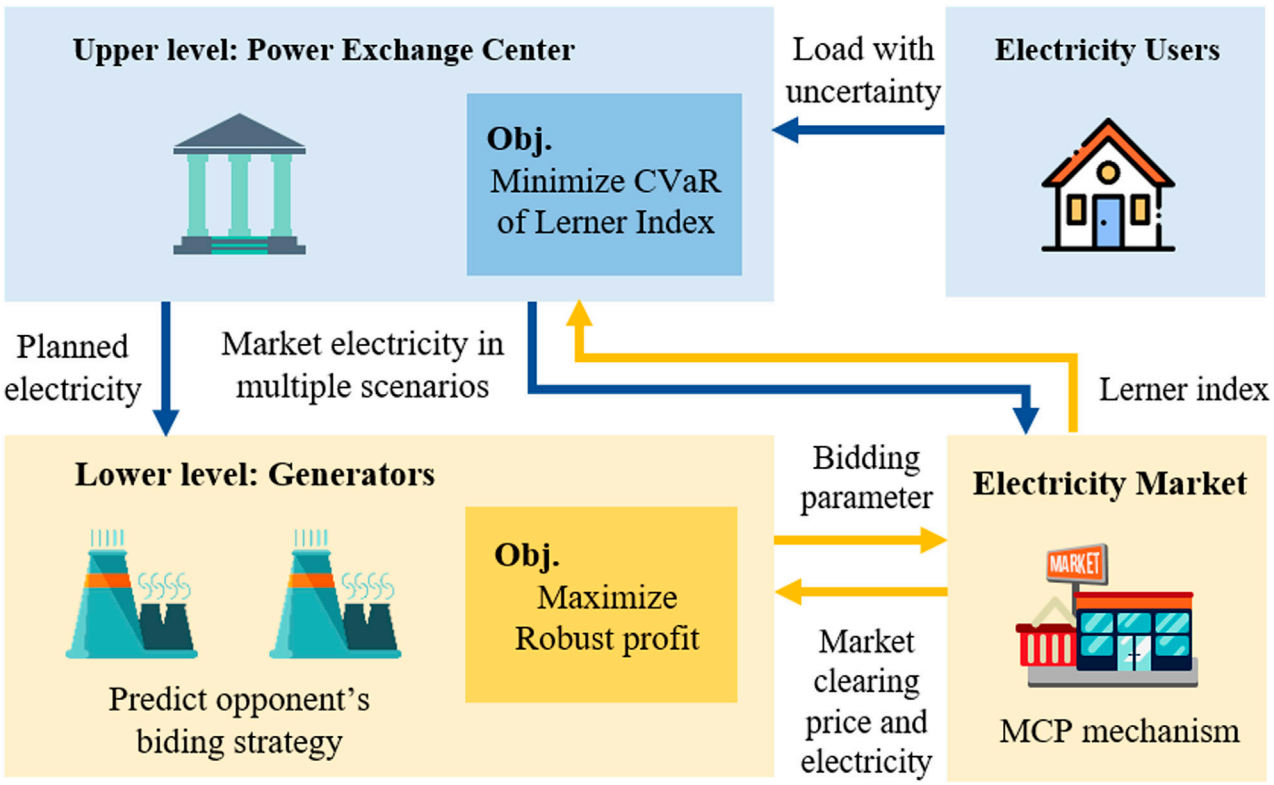

FIGURE 2 | Schematic diagram of the bi-level model of planned electricity allocation.

THE BI-LEVEL OPTIMAL PLANNED ELECTRICITY ALLOCATION MODEL CONSIDERING GENERATION COMPANIES' ROBUST BIDDING STRATEGIES

In order to ensure the stable operation of the electricity market in reform, it is important to allocate planned electricity and market electricity reasonably. The impact of the planned electricity on the market behavior of GCs should be fully considered by PX when determining the planned electricity. Under this background, a bi-level model of planned electricity allocation considering the robust bidding strategy of GCs is constructed in this section, and the schematic diagram of the model is shown in **Figure 2**. In the upper level, the planned electricity is optimized by PX to minimize the CVaR of Lerner index in multiple scenarios,

considering the uncertainty of the load demand. In the lower level, the bidding coefficient is optimized by GCs to maximize the robust profit under a certain confidence level considering the uncertainty of the competitors' bidding strategies. The decision variable of the upper level model will affect the earnings of GCs in the lower level model, which in turn affect their bidding strategies; the bidding strategies of GCs determine the price of the market, which affects the Lerner index in the upper target function. More details on the objectives and variables of the upper and lower level models are presented in *Robust Bidding Strategies and The Lower Level Model: An Optimal GC's Bidding Strategy Model Based on Robust Optimization Theory* and *The Upper Level Model: Optimal Planned Electricity Allocation Model Based on CVaR*, respectively.

Bi-level nonlinear optimization is a relatively complex optimization problem. Common solving algorithms include the penalty method by Dault and Shanker (2015), tabu search by Wu and Soto (2020), the genetic algorithm by Silva et al. (2019), the neural network by Zarco and Froese (2018)., etc. The proportion of planned electricity consumption is related to user structure, while the latter is related to market access conditions. In fact, the relevant parameters of market access conditions are usually discrete points in a limited range, so that the solution of the model does not need to be globally optimal and accurate. The genetic algorithm (GA) has good global search capability, and it is suitable for solving the optimal planned electricity. Thus, in this study, GA is used to solve the upper level model and the fmincon function in MATLAB is used to solve the lower level model.

The Lower Level Model: An Optimal Generation Companies Bidding Strategy Model Based on Robust Optimization Theory

With the implementation of PMDM, the revenue of GCs includes planned electricity revenue and market electricity revenue. The planned electricity and the corresponding regulated price are determined in advance in the previous year, while the market electricity quantity and the unified price are obtained according to the clearing results of the electricity market. The revenue of GC i under PMDM can be expressed as follows:

$$R_i = R_i^P + R_i^M - C_i, \tag{10}$$

$$R_i^P = Q_i^P P^P, \tag{11}$$

$$R_i^M = Q_i^M P^{MCP}. \tag{12}$$

Here, R_i^P and R_i^M represent the electricity sales revenue of planned electricity and market electricity, respectively. P^P is the regulated price of planned electricity that is estimated by the government and fixed during a settlement cycle.

In fact, the bidding strategies of GCs is carried out in a market with limited information. The bidding coefficients of other companies are unknown to a particular GC, but the uncertainty set of their bidding coefficients can be calculated based on the historical bidding data. For GC i, the predicted uncertainty set of its rival's quotation coefficient is $[k_i^{low}, k_i^{high}]$.

Due to the uncertainty of competitors' bidding, the market quotation of power generation companies is a kind of risk decision. According to the robust optimization theory, risk-averse GCs are usually more concerned about the highest revenue they can earn in the worst case while meeting a certain degree of confidence conditions in the decision-making (Annamraju and Nandiraju, 2019). The theory has been applied in many fields such as power system planning (Chowdhury et al. 2020) and dispatching (Choi et al. 2018). Based on robust optimization theory, the model is established to maximize the lowest possible profit $R_i^{RB}(k_i^*)$, and the objective function can be expressed as follows:

$$\max\ R_i^{RB}(k_i^*) = \min\ R_i\left(k_i^*, \widehat{k}_i\right), \tag{13}$$

where the decision variable k_i^* represents the bidding coefficient of the GC i. The random variable $\widehat{k}_i$ represents the uncertain counterparty's bidding strategy.

In order to solve the problem, $\psi_i(k_i^*, \alpha)$ is defined as the probability that the GC's profit is not less than a certain critical value α, and expressed as follows:

$$\psi_i(k_i^*, \alpha) = \int_{R_i\left(k_i^*, \widehat{k}_i\right) \geq \alpha} p\left(\widehat{k}_i\right) d\widehat{k}_i, \tag{14}$$

where $p(\widehat{k}_i)$ is the probability density function of competitor's bidding coefficient. According to robust optimization theory, $R_i^{RB}(k_i^*)$ can be obtained by solving the following models (Zhang et al., 2020):

$$\max\ \alpha, \tag{15}$$

$$\text{s.t.}\quad \psi_i(k_i^*, \alpha) \geq \varepsilon. \tag{16}$$

Here, ε is a given confidence level.

In addition, the constraints of the bidding model of GCs are as follows:

$$0 \leq Q_i^M \leq \overline{Q_i} - Q_i^P\ ,\quad i = 1, 2, \cdots, n. \tag{17}$$

The Upper Level Model: An Optimal Planned Electricity Allocation Model Based on CVaR

As a nonprofit organization, the goal of PX is to improve social benefits through reasonable planned electricity allocation. In an immature electricity market, due to the oligopoly of the generation side, some generation companies may have great market power. Therefore, market power supervision is one of the key tasks for PX to promote the reform of electricity market (Hakam et al., 2020).

The commonly used market power indicators include the Herfindahl–Hirschman index (HHI), must run ratio (MRR), the Lerner index (LI), etc. HHI and MRR are static index which reflect the capacity concentration of the market participants (Hajiabadi and Samadi 2019) and the possibility of market power based on market share (Wang et al. 2004), respectively. By contrast, LI reflects the degree of market monopoly by measuring the deviation between market clearing price and marginal cost, and is a market power index used to analyze the performance of electricity market afterward (Razmi et al., 2021). Therefore, LI is used to reflect the market power under PMDM in this section.

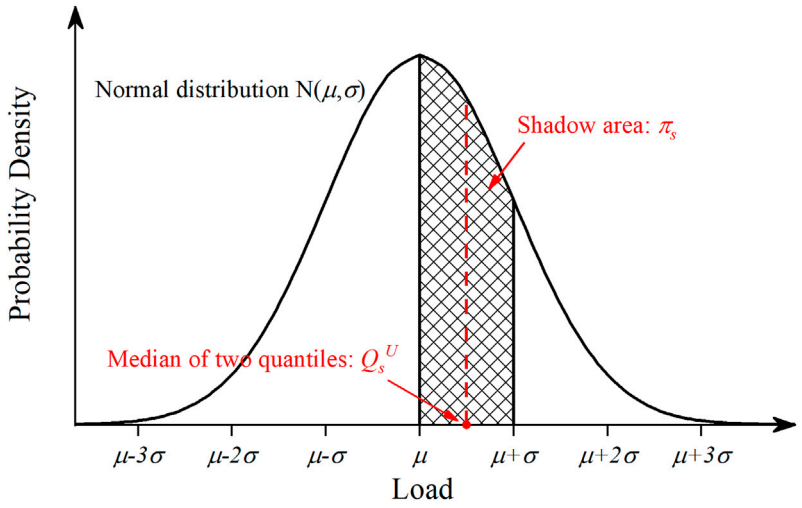

FIGURE 3 | The method of sample user load based on normal distribution quantile.

Considering that the LI of the market is influenced by the load demand, the load on the user side is assumed to obey the normal distribution N (μ, σ^2) in this study. The scenario set $\boldsymbol{S}$ of load demand can be obtained by sampling user load through quantiles of normal distribution (Soranzo and Epure, 2014), as shown in **Figure 3**. The median of two quantiles is taken as the sampling value and the shadow area is the probability of the sampling value.

Because the load demand is uncertain, LI is subject to a probability distribution rather than a certain value. Furthermore, as the market power cannot be avoided, the LI in adverse conditions is more concerned by PX than the expectation of LI. CVaR measures the average loss when the loss exceeds the value at risk (VaR) in a certain confidence level. For the PX, CVaR of the LI indicates the expected value when the LI is higher than the critical value (Yin and Zhao, 2018). Therefore, the objective function of the upper model is to minimize the CVaR of LI, and expressed as follows:

$$\min \ I_{CVaR}(\gamma) = \sum_{L_s > I_{VaR}(\gamma), s \in \boldsymbol{S}} \pi_s L_s, \tag{18}$$

where π_s is the probability of scenario s. $I_{CVaR}(\gamma)$ and $I_{VaR}(\gamma)$ represent the CVaR and the VaR of LI in confidence level γ, respectively. L_s is the LI in scenario s, which can be expressed as follows:

$$L_s = \frac{\overline{P_s} - \overline{C_s^M}}{\overline{P_s}}, \tag{19}$$

$$\overline{P_s} = \frac{Q^P P^P + Q_s^M P_s^{MCP}}{Q_s^U}, \tag{20}$$

$$\overline{C_s^M} = \frac{\sum_{i=1}^{n} \overline{Q_i} C_{i,s}^M}{\sum_{i=1}^{n} \overline{Q_i}}. \tag{21}$$

TABLE 1 | Generation costs and bidding parameters.

Name of GC	$\overline{Q_i}$(billion kWh)	a_i	b_i	c_i	$[k_i^{low}, k_i^{high}]$
HN	20	0.073	307	1,000	[0.021, 0.063]
DT	50	0.064	286	5,000	[0.022, 0.068]
GT	75	0.057	271	9,000	[0.024, 0.072]
GD	100	0.048	264	14,000	[0.025, 0.075]
WN	125	0.039	258	18,000	[0.027, 0.081]

The optimization results of the bi-level planned electricity allocation model.

Here, $\overline{P_s}$ and $\overline{C_s^M}$ represent the average electricity price and the average marginal cost of GCs in scenario s, respectively. P_s^{MCP} is the unified market clearing price in scenario s. $C_{i,s}^M$ is the marginal generation cost of GC i in scenario s. Q_s^U and Q_s^M represent the total electricity demand and market electricity demand on the user side in scenario s, respectively.

The constraint of the planned electricity allocation model is the upper and lower limit of the electricity, which can be expressed as follows:

$$0 \le Q^P \le \min_{s \in \boldsymbol{S}} \{Q_s^U\}. \tag{22}$$

CASE STUDY

The data of a provincial electricity market in China are served for demonstrating the proposed planned electricity allocation model for PX. The generation cost and bidding parameters of the five major large power generation companies in the province are shown in **Table 1**. The original planned electricity in the province is set at 250 billion kWh, and the regulated price of planned electricity generation is 0.384 CNY/kWh. The normal distribution obeyed by load demand is N (300,225). The confidence level ε and γ are 0.9 and 0.8, respectively.

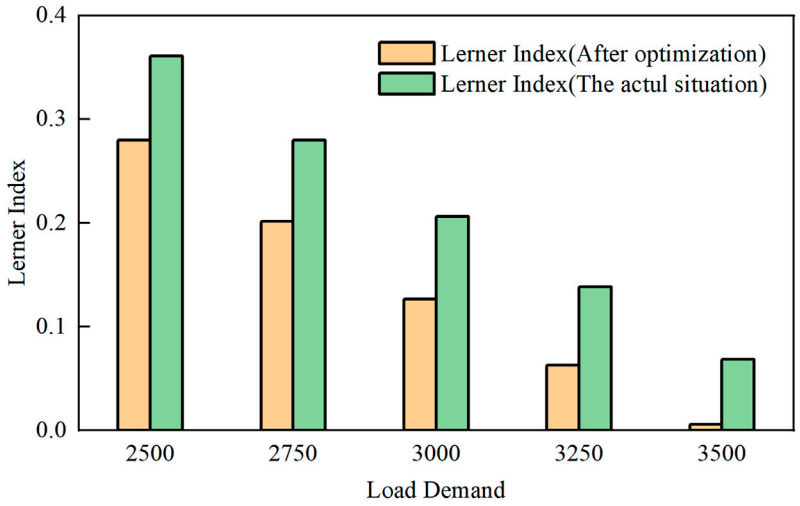

FIGURE 4 | The Lerner Index of electricity market in actual situation and after optimization.

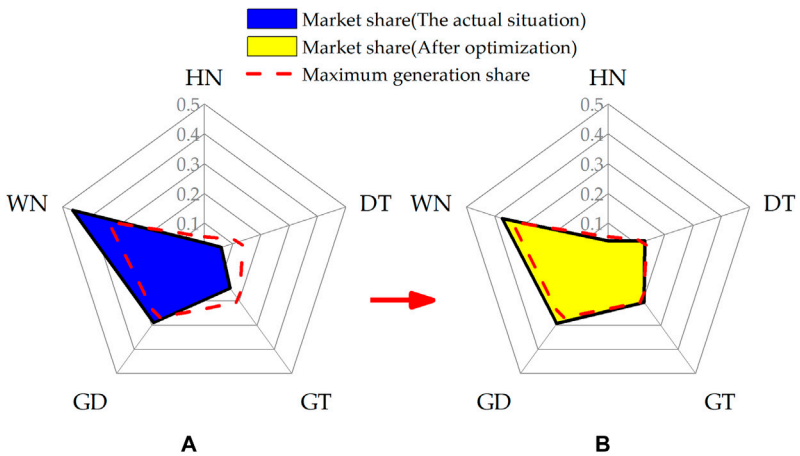

FIGURE 5 | The market shares and maximum generation shares of GCs: **(A)** in actual situation; **(B)** after optimization.

By solving the above bi-level model, the optimal planned electricity allocation is 93 billion kWh (the proportion is about 31%). Compared with original planned electricity (250 billion kWh), the CVaR of LI decreases from 0.2015 to 0.1344, that is, a decrease of 33.3%. The LI of electricity market under different load demand is shown in **Figure 4**, and the LI is obviously decreased after optimization. The main reason for the decrease of LI is the reduction of average electricity price. As the regulated price of planned electricity is much higher than that of the market, the reduction of planned electricity means the decrease of the average electricity price. However, as can be inferred from **Eq. 9**, when the market electricity increases, the supply and demand ratio decreases and the market unified clearing price increases correspondingly, which leads to a higher LI. Therefore, it is necessary to maintain a certain amount of planned electricity under a given constant supply side conditions.

For the 5 GCs, when the planned electricity is 250 billion kWh and the load demand is equal to the expected value of 300 billion kWh, their market electricity are 3.95 billion kWh, 25.67 billion kWh, 40.78 billion kWh, 58.20 billion kWh, and 74.27 billion kWh, respectively. It can be seen from the **Figure 5A** that the market electricity shares of generation companies HN, GD, GT, DT, and HN are 3.4, 6.0, 14.7, 28.9, and 46.4%, respectively, and the shares allocated in proportion to their maximum generation capacity are 5.4, 13.5, 20.3, 27.0, and 33.8%, respectively. The market shares of HN, GD, and GT are less than their maximum generation shares, while the market electricity shares of DT and HN are higher than that of maximum generation. This is mainly because the market share of each GCs is determined by their cost-based bidding strategies. The larger the generation scale of the company, the smaller the power generation cost and the bidding coefficient, and the stronger its competitiveness in the electricity market. As a result, GCs with larger capacity can gain more

TABLE 2 | The annual electricity consumption and market electricity of various users.

Electricity user	Annual electricity consumption (billion kWh)	The consumption accessed in the market (billion kWh)	The market access conditions
Large industrial enterprises	123.53	31.47	The voltage level is above 10kV and the annual electricity consumption is above 50 million kWh
General industrial enterprises	43.24	3.9	
Commercial users	45.07	4.63	
Resident	55.26	0	Not allowed
Others	22.9	0	Not allowed

The influence of uncertainty of load and rival bidding strategy on optimal planned electricity allocation.

market electricity than small GCs, which improves the market power.

The market share of each GC under the optimized proportion of planned electricity is shown in **Figure 5B**. By comparison, it can be found that in the case of optimized planned electricity allocation, the GCs acquired reasonable market share based on maximum generation share. When planned electricity is 250 billion kWh and market electricity is low, most of the market electricity is won by low-cost companies. On the other hand, when the market electricity is high, the market electricity of large GCs is limited by the increasing generation costs. Take the generation company WN as an example, the market share decreases from 46.4 to 37.4%, which shows that the optimization result of the bi-level model can effectively reduce the excessive market share of large-scale GCs and significantly decrease the market power.

The annual electricity consumption of various users of this province is shown in **Table 2**. In the original situation (the planned electricity is 250 billion kWh), some of the large industrial enterprises, general industrial enterprises, and commercial users are accessed to the electricity market according to their voltage level or annual electricity consumption. The market access conditions and the lists of market users are decided by PX. In order to reduce the planned electricity from 250 billion kWh to 93 billion kWh, the market access conditions should be changed correspondingly. For example, when industrial enterprises and commercial users with consumption of more than five million kWh are allowed to participate in the electricity market, the total consumption accessed in the market is about 190 billion kWh and the planned electricity is about 110 billion kWh which is close to the optimal result of the model. As for the generation side, PX only needs to reduce GCs' planned electricity.

There are two uncertain factors in the bi-level model constructed in this study, that is, the uncertain load demand in the upper model and the uncertain bidding coefficients of competitors in the lower model. In the upper model, the uncertainty of load demand is represented by the standard deviation of the normal distribution, the greater the standard deviation, the greater the uncertainty of load. The relationship among the optimal allocation of planned electricity, the CVaR of LI, and the uncertainty of load is shown in **Figure 6**. It can be seen from **Figure 6** that both the quantity of the planned electricity and the CVaR of LI are proportional to the standard deviation. When the standard deviation of load forecast is five billion kWh, the optimal planned electricity is 63.2 billion kWh and the CVaR of LI is 0.1270. Both of them are the least among five standard deviations. This is mainly because the CVaR of LI measures the expectation of LI when it exceeds the critical value. The smaller the volatility of the load demand is, the more stable the LI of the market is, and the smaller the CVaR value is.

In the lower level model, the uncertainty of generation companies' bidding strategies can be reflected by the interval size of competitors' bidding coefficient. The larger the interval, the greater the uncertainty of the bidding coefficient. Taking generation company WN as an example, the relationship between its bidding coefficient and the uncertain of rival bidding strategy is shown in **Figure 7** with planned electricity set at 93 billion kWh and the load demand set at 300 billion kWh. It can be seen from **Figure 7** that the bidding coefficient is inversely proportional to the uncertainty of rival bidding strategy. When the predicted interval of rival bidding coefficient is 0.037 and 0.071, the bidding coefficient of WN is 0.0831 and the LI is 0.1287. When the predicted interval is 0.017 and 0.091 whose size is the largest, the bidding coefficient of WN is least (0.0676) and the corresponding LI is also the smallest (0.1238). The main reason is that GCs aim to maximize their revenue in the worst case. Thus, the more uncertain the rival bidding strategy is, the greater the fluctuation range of GC revenue is, and the lower the revenue in the worst case is, which makes GCs more inclined to adopt bidding strategies close to the cost.

The Influence of the Risk Aversion Degree of Generation Companies on Optimal Planned Electricity Allocation

The confidence level ε in the lower level model indicates the risk aversion degree of GCs. The larger the ε, the higher the degree of risk aversion of GCs. **Figure 8** shows the optimal allocation results of planned electricity under different risk aversion degrees of GCs, and **Table 3** shows the market clearing results and LI under the corresponding optimal planned electricity allocation. It can be seen from **Figure 8** that the higher the risk aversion degree of GCs is, the lower the allocation value of planned electricity is,

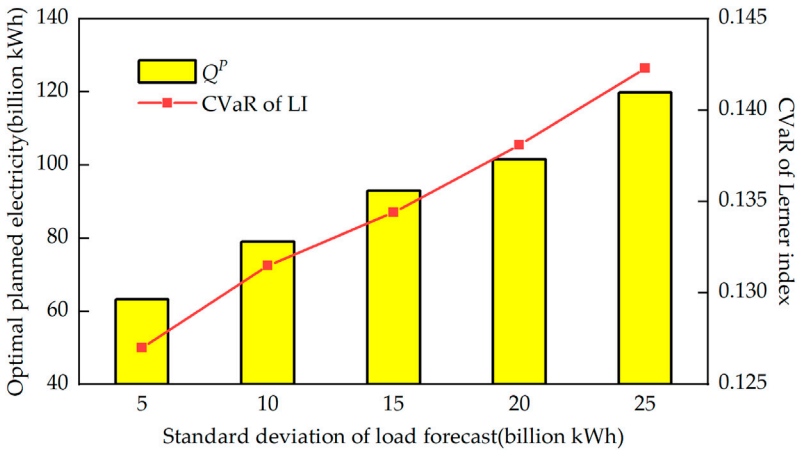

FIGURE 6 | The relationship between optimization results and uncertainty of load demand.

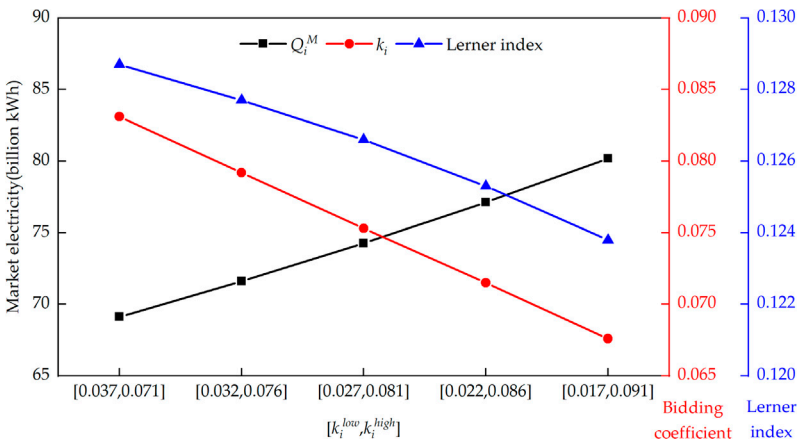

FIGURE 7 | The relationship between the bidding strategy of generation company WN and the uncertainty of rival bidding.

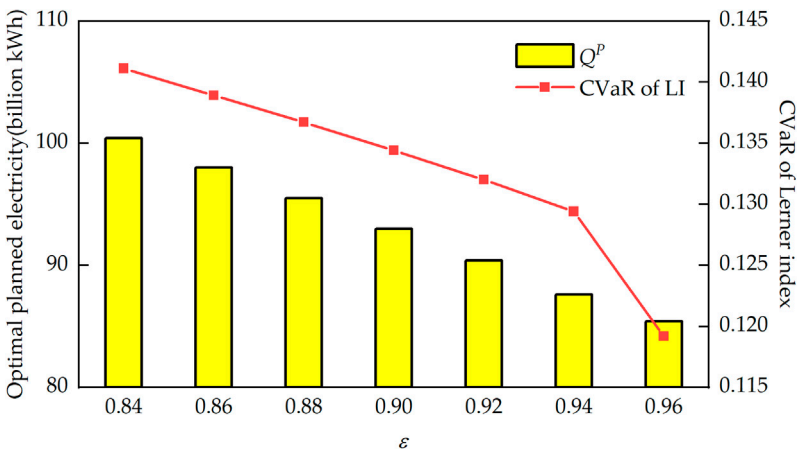

FIGURE 8 | Optimal allocation of planned electricity under different risk aversion degrees of GCs.

TABLE 3 | Market-clearing results under different risk aversion degrees of GCs.

ε	Q^P(billion kWh)	P^{MCP}(CNY/kWh)	*LI*
0.84	100.4	0.3267	0.1331
0.86	98.0	0.3262	0.1310
0.88	95.5	0.3256	0.1288
0.90	93.0	0.3250	0.1266
0.92	90.4	0.3244	0.1242
0.94	87.6	0.3238	0.1216
0.96	85.4	0.3231	0.1198

and the smaller the CVaR of LI is. GCs who tend to avoid risk are willing to adopt conservative bidding strategies with low-bidding coefficients. According to **Table 3**, as ε increases from 0.84 to 0.96, the unified clearing price decreases from 0.3267°CNY/kWh to 0.3131°CNY/kWh, and the LI decreases from 0.1331 to 0.1198, that is, a decrease of 10.0%. For PX, its objective function is to minimize the CVaR of the LI. The decline of market clearing price enables the PX to allocate more market electricity, reducing the optimal allocation value of planned electricity.

CONCLUSION

An optimal planned electricity allocation model considering the robust bidding strategy of GCs is constructed under PMDM for PX to determine the proportion of planned electricity in the total energy consumption. The Lerner Index is used to reflect the level of market power. The impact of planned electricity on the market electricity generation cost of GCs under PMDM is considered in the lower level model. Considering the bidding strategies of GCs, the planned electricity quantity is optimized in the upper level model with the objective of minimizing the CVaR of LI. The validity of the model is analyzed by taking the market data of a province in China and the main conclusions are as follows:

1) The market power in the electricity market is effectively decreased under the optimization results of the proposed model. PX can reduce market power by setting a reasonable proportion of planned electricity.
2) The optimal planned electricity decreases with the reduction of the uncertainty of the load demand. PX should improve the load forecasting accuracy and avoid reducing the planned electricity when the load demand fluctuates greatly.
3) The market power is related to the risk aversion degree of GCs. The more the GCs tend to avoid market risks, the lower the market power. For PX, it is necessary to evaluate the risk aversion degree of GCs in the process of orderly deregulation of planned electricity generation and consumption.

In the future, the research on the bidding strategies of GCs or the market methods of PX can be more complicated and comprehensive.

DATA AVAILABILITY STATEMENT

The original contributions presented in the study are included in the article/Supplementary Material, and further inquiries can be directed to the corresponding author.

AUTHOR CONTRIBUTIONS

CH, LY, and ZL conceptualized the study; JT, WZ, and ZZ performed the analysis; JT, HQ, and HJ performed investigations; JT and CH acquired resources; CH, WZ, ZL, HQ, and HJ acquired funding; CH wrote the original draft; JT, ZZ, and YL reviewed and edited the manuscript. All authors agree to be accountable for the content of the work.

FUNDING

This work was supported by State Grid Anhui Electric Power Co., Ltd. Science and Technology Project (B31200200006) and National Key R&D Program of China (No. 2016YFB0901100).

REFERENCES

Annamraju, A., and Nandiraju, S. (2019). Robust Frequency Control in a Renewable Penetrated Power System: an Adaptive Fractional Order-Fuzzy Approach. *Prot. Control. Mod. Power Syst.* 4 (1), 1–15. doi:10.1186/s41601-019-0130-8

Ansari, B., and Rahimi-Kian, A. (2015). A Dynamic Risk-Constrained Bidding Strategy for Generation Companies Based on Linear Supply Function Model. *IEEE Syst. J.* 9 (4), 1463–1474. doi:10.1109/JSYST.2015.2427374

Antitrust, D. (2010). *United States V. Keyspan Corporation, Public Comments and Response on Proposed Final Judgment*. Available at: https://www.federalregister.gov/documents/2010/07/20/2010-16321/united-states-v-keyspan-corporation-public-comments-and-response-on-proposed-final-judgment (Accessed March 8, 2021)

Bompard, E., Carpaneto, E., Ciwei, G., Napoli, R., Benini, M., Gallanti, M., et al. (2008). A Game Theory Simulator for Assessing the Performances of Competitive Electricity Markets. *Electric Power Syst. Res.* 78 (2), 217–227. doi:10.1016/j.epsr.2007.02.007

Budhraja, V. (2001). *California's Electricity Crisis*. Vancouver, BC: Power Engineering Society Summer Meeting. doi:10.1109/pess.2001.970051

Choi, S.-H., Hussain, A., and Kim, H.-M. (2018). Adaptive Robust Optimization-Based Optimal Operation of Microgrids Considering Uncertainties in Arrival and Departure Times of Electric Vehicles. *Energies*. 11 (10), 2646. doi:10.3390/en11102646

Chowdhury, N., Pilo, F., and Pisano, G. (2020). Optimal Energy Storage System Positioning and Sizing with Robust Optimization. *Energies* 13 (3), 512. doi:10.3390/en13030512

Dagoumas, A. (2019). Impact of Bilateral Contracts on Wholesale Electricity Markets: in a Case where a Market Participant Has Dominant Position. *Appl. Sci.* 9 (3), 382. doi:10.3390/app9030382

Dault, D., and Shanker, B. (2015). An interior Penalty Method for the Generalized Method of Moments. *IEEE Trans. Antennas Propagat.* 63 (8), 3561–3568. doi:10.1109/TAP.2015.2430876

Guangdong Economic and Information CommissionGuangdong Development and Reform CommissionNational Energy Administration Southern Supervision Bureau (2017). *Notice on Matters Related to Power Users Participating in Market Transactions in 2017*. Available at: http://gdii.gd.gov.cn/dlny/content/post_942834.html (Accessed March 8, 2021).

Guangdong Electric Power Exchange Center Co., Ltd (2020). *Guangdong Electricity Market Half-Year Report 2020*. Available at: https://pm.gd.csg.cn/views/page/xwzxCont-10589.html (Accessed March 8, 2021)

Hajiabadi, M. E., and Samadi, M. (2019). Locational Marginal price Share: a New Structural Market Power index. *J. Mod. Power Syst. Clean. Energ.* 7 (6), 1709–1720. doi:10.1007/s40565-019-0532-7

Hakam, D. F., Wiyono, S. K., and Hariyanto, N. (2020). Competition in Power Generation: Ex-Ante Analysis of Indonesia's Electricity Market. *Energies*. 13 (24), 6741. doi:10.3390/en13246741

International Energy Agency (2006). *China's Power Sector Reforms: Where to Next*. Paris: OECD Publishing

Jiang, D., Liu, X., and Li, Q. (2004). Economically Distributing Strategies for Daily Generation Scheduling in a Power System under Power Market Environment. *Proc. Chin. Soc. Electr. Eng.* 24 (7), 94–98. doi:10.13334/j.0258-8013.pcsee.2004.07.017

Liu, G., Xu, Y., and Tomsovic, K. (2016). Bidding Strategy for Microgrid in Day-Ahead Market Based on Hybrid Stochastic/robust Optimization. *IEEE Trans. Smart Grid*. 7 (1), 227–237. doi:10.1109/TSG.2015.2476669

National Development and Reform Commission National Energy Administration (2017). *Notice on Orderly Releasing Plans of Power Generation and Power Utilization*. Available at: http://www.gov.cn/xinwen/2017-04/11/content_5184607.htm (Accessed March 8, 2021)

Park, k. J., Kim, B., Kim, J., Jung, M., and Park, J. (2001). A Continuous Strategy Game for Power Transactions Analysis in Competitive Electricity Markets. *IEEE Trans. Power Syst.* 16 (4), 847–855. doi:10.1109/59.962436

Pousinho, H. M. I., Contreras, J., Bakirtzis, A. G., and Catalao, J. P. S. (2013). Risk-constrained Scheduling and Offering Strategies of a price-maker Hydro Producer under Uncertainty. *IEEE Trans. Power Syst.* 28 (2), 1879–1887. doi:10.1109/TPWRS.2012.2229473

Razmi, P., Oloomi Buygi, M., and Esmalifalak, M. (2021). A Machine Learning Approach for Collusion Detection in Electricity Markets Based on Nash Equilibrium Theory. *J. Mod. Power Syst. Clean. Energ.* 9 (1), 170–180. doi:10.35833/MPCE.2018.000566

Silva, F. T., Silva, M. X., and Belchior, J. C. (2019). A New Genetic Algorithm Approach Applied to Atomic and Molecular Cluster Studies. *Front. Chem.* 7, 707. doi:10.3389/fchem.2019.00707

Sioshansi, F. (2013). *Evolution of Global Electricity Markets: New Paradigms, New Challenges, New Approaches*. USA: Academic Press

Soranzo, A., and Epure, E. (2014). Very Simply Explicitly Invertible Approximations of normal Cumulative and normal Quantile Function. *ams*. 8 (87), 4323–4341. doi:10.12988/ams.2014.45338

Sun, L., Zhang, N., Li, N., Liu, X., and Li, W. (2020). An Intra-day Rolling Scheduling Considering Energy Equity Based on Gini Coefficient. *Power Sys. Techno*. 44 (1), 340–347. doi:10.13335/j.1000-3673.pst.2019.1459

Wang, P., Xiao, Y., and Ding, Y. (2004). Nodal Market Power Assessment in Electricity Markets. *IEEE Trans. Power Syst.* 19 (3), 1373–1379. doi:10.1109/TPWRS.2004.831695

Wen, F., and David, A. (2001). Optimal Bidding Strategies and Modeling of Imperfect Information Among Competitive Generators. *IEEE Trans. Power Syst.* 16 (1), 15–21. doi:10.1109/59.910776

Woo, C.-K., Lloyd, D., and Tishler, A. (2003). Electricity Market Reform Failures: UK, Norway, Alberta and California. *Energy Policy*. 31 (11), 1103–1115. doi:10.1016/S0301-4215(02)00211-2

Wu, K., and García de Soto, B. (2020). Spatiotemporal Modeling of Lifting Task Scheduling for tower Cranes with a Tabu Search and 4-D Simulation. *Front. Built Environ.* 6, 79. doi:10.3389/fbuil.2020.00079

Yin, J., and Zhao, D. (2018). Fuzzy Stochastic Unit Commitment Model with Wind Power and Demand Response under Conditional Value-At-Risk Assessment. *Energies*. 11 (2), 341. doi:10.3390/en11020341

Zarco, M., and Froese, T. (2018). Self-optimization in Continuous-Time Recurrent Neural Networks. *Front. Robot. AI* 5, 96. doi:10.3389/frobt.2018.00096

Zhang, Q., Zhang, S., Wang, X., Li, X., and Wu, L. (2020). Conditional-robust-profit-based Optimization Model for Electricity Retailers with Shiftable Demand. *Energies*. 13 (6), 1308. doi:10.3390/en13061308

Conflict of Interest: CH, JT, WZ, ZL, HQ, and HJ were employed by State Grid Anhui Electric Power Co., Ltd. and Anhui Power Exchange Center Company.

The remaining authors declare that the research was conducted in the absence of any commercial or financial relationships that could be construed as a potential conflict of interest.

frontiers in Energy Research

ORIGINAL RESEARCH
published: 06 July 2021
doi: 10.3389/fenrg.2021.713510

Assessment for Voltage Violations considering Reactive Power Compensation Provided by Smart Inverters in Distribution Network

Jindi Hu[1], Weibin Yin[2], Chengjin Ye[1], Weidong Bao[3], Jiajia Wu[3] and Yi Ding[1]*

[1]College of Electrical Engineering, Zhejiang University, Hangzhou, China, [2]State Grid Jiaxing Power Supply Company, Jiaxing, China, [3]State Grid Yiwu Power Supply Company, Yiwu, China

Due to the high proportion of renewable energies, traditional voltage regulation methods such as on-load tap changers (OLTCs) and switching capacitors (SCs) are currently facing the challenge of providing fast, step-less, and low-cost reactive power to reduce the increasing risks of voltage violations in distribution networks (DNs). To meet such increasing demand for voltage regulation, smart inverters, including photovoltaics (PVs) and electric vehicle (EV) chargers, stand out as a feasible approach for reactive power compensation. This paper aims to assess the voltage violation risks in DNs considering the reactive power response of smart inverters. Firstly, reactive power compensation models of PVs and EV chargers are investigated and voltage deviation indexes of the regulation results are proposed. Moreover, kernel density estimation (KDE) and slice sampling are adopted to provide the PV output and EV charging demand samples. Then, the risk assessment is carried out with a voltage regulation model utilizing OLTCs, SCs, and available smart inverters. Numerical studies demonstrate that the reactive power support from smart inverters can significantly mitigate the voltage violation risks and reduce the switching and cost of OLTCs and capacitors in DNs.

Keywords: distribution network, reactive power compensation, risk assessment, electric vehicle charger, photovoltaic

OPEN ACCESS

Edited by:
Yang Li,
Northeast Electric Power University, China

Reviewed by:
Huaiyuan Wang,
Fuzhou University, China
Gengfeng Li,
Xi'an Jiaotong University, China
Yunfei Mu,
Tianjin University, China

****Correspondence:***
Chengjin Ye
yechenjing@zju.edu.cn

Specialty section:
This article was submitted to Smart Grids, a section of the journal Frontiers in Energy Research

Received: *23 May 2021*
Accepted: *21 June 2021*
Published: *06 July 2021*

Citation:
Hu J, Yin W, Ye C, Bao W, Wu J and Ding Y (2021) Assessment for Voltage Violations considering Reactive Power Compensation Provided by Smart Inverters in Distribution Network. Front. Energy Res. 9:713510. doi: 10.3389/fenrg.2021.713510

1 INTRODUCTION

The development of power electronics in distribution networks (DNs) brings prosperity for distributed photovoltaics (PVs), electric vehicle (EV) chargers, and other devices with AC-DC inverters. However, DNs are more prone to voltage violation problems nowadays because of the uncertainty of PV outputs and the load impact of EV charging (Kekatos et al., 2015). Traditional reactive power compensation facilities such as on-load tap changers (OLTCs) and switching capacitors (SCs) are only able to provide step-wise and high-delay reactive power at the feeder head, which limits the regulation effect (Kekatos et al., 2015), while the high cost of Distribution Static Synchronous Compensators (D-STATCOMs) restricts its application in DNs (Chen et al., 2018). Therefore, it is of vital importance to implement step-less compensation facilities at the feeder terminal.

Meanwhile, the two-way reactive power ability of smart inverters (i.e., PVs and EV chargers in this paper) enables these terminal end power electronics in DNs to participate in voltage regulation. There have already been some investigations to achieve reactive power delivery from smart inverters.

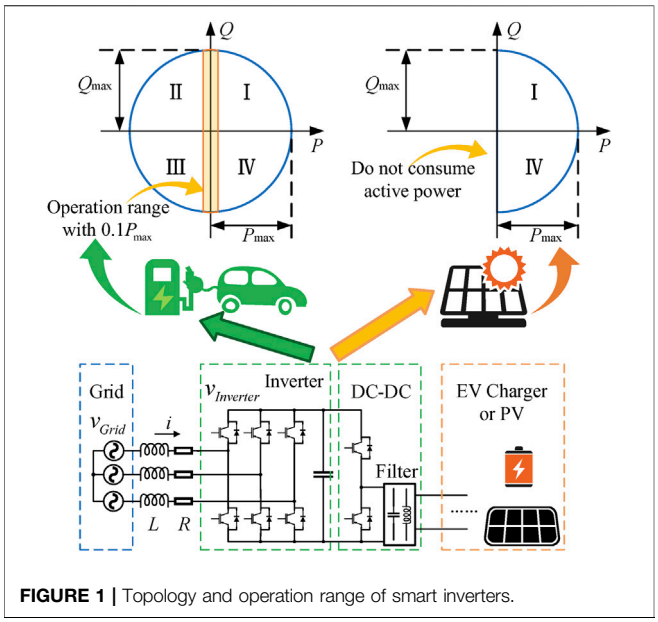

FIGURE 1 | Topology and operation range of smart inverters.

Sharma and Das (2020) and Feng et al. (2018) extend the reactive power exchange for PV inverters and help to balance the active and reactive power transmission of each phase. Buja et al. (2017) analyze and validate the reactive power compensation abilities of EV chargers theoretically and experimentally. Moreover, Varma and Siavashi (2018), Abeywardana et al. (2018), and Kesler et al. (2014) point out that the reactive power compensation process of PVs and EV chargers does not intervene in the active power delivery or cause damage to EV batteries, which expands the implementation of EV chargers to a large extent. To integrate these flexible power electronics, Varma and Siavashi (2018) present a novel smart inverter PV-STATCOM which controls PV inverters as a dynamic reactive power compensator. Furthermore, Singh et al. (2019) achieve voltage regulation through smart inverters of PVs and EV charging stations in the global as well as local domain. Smart inverters have been well investigated and developed to compensate reactive power (Ustun et al., 2020; Gush et al., 2021). Therefore, it is feasible to resort to smart inverters for accurate and fast voltage regulation in DNs.

The application of smart inverters to regulate voltage quality has been investigated. Zeraati et al. (2019) develop a distributed voltage regulation scheme to utilize the reactive power capability of PV inverters. Quirós-Tortós et al. (2016) and Singh et al. (2019) achieve reactive power control in DNs with the support of EV chargers and PVs. However, the voltage regulation techniques using smart inverters are still under research and need practical implementations. Therefore, it is essential to assess the voltage regulation effects of smart inverters to provide references for the market price of their reactive power compensation.

To assess the reliability of power systems, the Monte Carlo simulation is usually utilized to sample from the target distribution when considering the uncertainty of renewable energies or power demands (Zhou et al., 2016). It is applicable for common Monte Carlo methods, such as importance sampling (Tómasson and Sö) and acceptance-rejection sampling (Hu et al., 2017), to sample from a standard target distribution. However, the irregular PV outputs and EV loads require non-parametric estimation techniques to acquire their probability density functions (PDFs) and more universal sampling methods suitable for any non-standard PDF (Huang et al., 2020). Slice sampling is an advanced method of Markov Chain Monte Carlo (MCMC) simulation (Neal, 2003). It is feasible for PV outputs and EV loads owing to its ability to sample from irregular PDFs efficiently.

Based on the above analysis, this paper proposes a voltage violation assessment model considering the participation of smart inverters. Samples of PV outputs and EV loads are generated. The voltage violation assessment is carried out to evaluate the performance of smart inverters. The main contributions of this paper can be summarized as two-fold:

1. The quantitative compensation ability assessment of smart inverters is proposed with the available reactive power capacities under active power constraints. The optimization model for voltage regulation is established considering both traditional reactive power compensation facilities and smart inverters.
2. The voltage violation assessment under the uncertainty of PV outputs and EV behaviors is achieved based on the proposed voltage deviation indexes, non-parametric kernel density estimation (KDE), and slice sampling. The non-standard PDFs of PVs and EVs are fitted accurately by KDE. Besides, the automated step width selection for slice

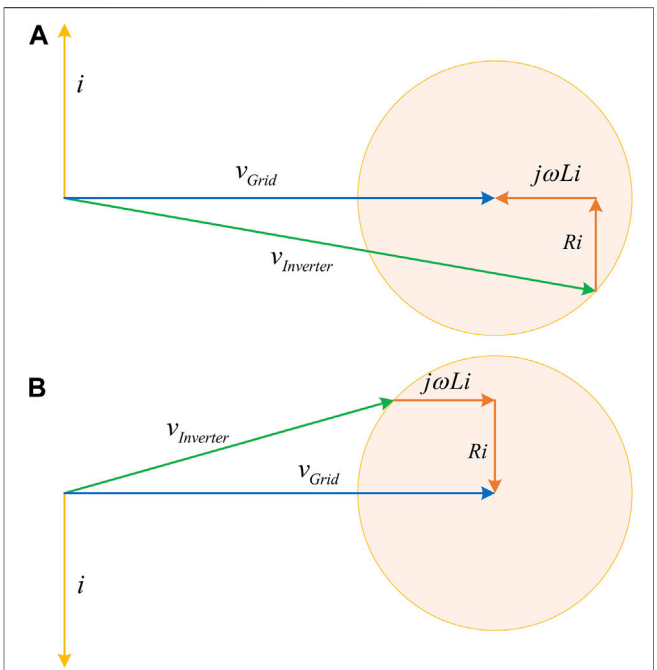

FIGURE 2 | Voltage vector diagrams of two typical operation modes **(A)** is the capacitive mode **(B)** is the inductive mode.

sampling is adopted to efficiently generate samples from the obtained PDFs. The results demonstrate that smart inverters have better voltage regulation effects and are able to reduce the operation cost of OLTCs and SCs.

The remaining of this paper is organized as follows. **Section 2** describes the basic models and voltage deviation indexes for voltage regulation. KDE and slice sampling are introduced in **Section 3**. **Section 4** illustrates the risk assessment process for voltage violations. Numerical studies are presented in **Section 5**. Finally, **Section 6** concludes this paper.

2 BASIC MODELS

2.1 Reactive Power Compensation Mechanism of Smart Inverters

The AC-DC inverters of EV chargers and PVs are composed of controllable power electronics with a three-phase six-pulse topology. The equivalent smart inverter models are depicted in **Figure 1**. This structure provides these smart inverters with the flexibility to operate their output voltages. By changing the amplitude and phase angle of the output voltage, the inverter can adjust its active and reactive power transmission. To illustrate the reactive power compensation mechanism of smart inverters, **Figure 2** shows two typical operation modes, which provide pure capacitive or inductive reactive power to the grid.

As shown in **Figure 2**, the reactive power compensation modes are determined by the voltage of smart inverters. The yellow circle range in **Figure 2** is drawn based on the limitation of the rated current, which protects the inverter from over-loading. As the inverter voltage varies within this yellow circle, the current changes accordingly. Then, the inverter gives out both active power P and reactive power Q according to the current and the grid voltage. The operation range of P and Q of smart inverters is thus further determined as illustrated in **Figure 1** (Kisacikoglu et al., 2013; Su et al., 2014). However, EV chargers and PVs have different operation ranges. EV chargers can operate in four quadrants, which can absorb or give out both P and Q, while PVs do not consume any active power. Therefore, the operation range can be expressed as:

$$P^2 + Q^2 \le S_{\max}^2 \tag{1}$$

$$\begin{cases} P_{\max}^{EV} \ge P^{EV} \ge P_{\min}^{EV} \\ P^{PV} = P_{output}^{PV} \end{cases} \tag{2}$$

where $S_{\max}$ is the maximum value of the inverter capacity; P^{EV} and P^{PV} are the active power of EV chargers and PVs respectively; $P_{\max}^{EV}$ and $P_{\min}^{EV}$ denote the maximum and minimum allowed active charging power for EV chargers respectively; P_{output}^{PV} is the active power generated by PVs.

Eq. 1 indicates that when chargers and PVs are idle, these smart inverters are capable of providing considerable reactive power compensation. This advantage is illustrated by the orange rectangle in **Figure 1**, where the inverter has a vast operation range under low active power level.

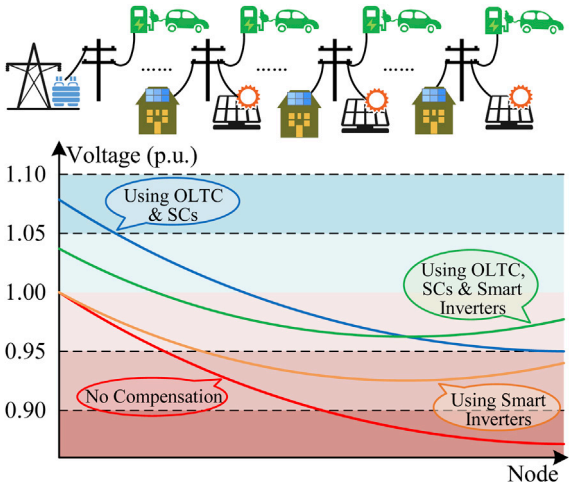

FIGURE 3 | Voltage diagrams of different compensation strategies.

2.2 Models of On-Load Tap Changers and Switching Capacitors

OLTCs and SCs are fundamental voltage regulation resources in DNs, which are usually equipped at the transformer substation. The reactive power compensation mechanism for OLTCs is to change the turn ratio by adjusting the tap position. The model of the OLTCs can be expressed as (Wu et al., 2017)

$$k_{ij} = k_{ij}^{\min} + tap_{ij} \cdot \Delta k_{ij}, 0 \le tap_{ij} \le \overline{tap_{ij}} \tag{3}$$

where k_{ij} is the turns ratio of the transformer between node i and node j; $k_{ij}^{\min}$ is the minimum turns ratio; tap_{ij} is the tap position of the OLTC; $\overline{tap_{ij}}$ is the maximum value of the tap position; Δk_{ij} is the ratio change per tap.

SCs provide capacitive reactive power to maintain the voltage level. According to the capacity of each SC connected to the grid, the model of SCs can be described as

$$Q_{SC} = \sum_{i=1}^{N_{SC}} (Q_i^{SC} \cdot n_i^{SC}), 0 \le n_i^{SC} \le \overline{n_i^{SC}} \tag{4}$$

where Q_{SC} is the total reactive power provided by SCs; N_{SC} is the total number of the SC types; Q_i^{SC} and n_i^{SC} are the capacity and the number of SCs that belong to type i; $\overline{n_i^{SC}}$ is the maximum value of n_i^{SC}.

2.3 Comparisons of Different Compensation Strategies

Since OLTCs and SCs are commonly located in the transformer substation, traditional compensation methods regulate the voltage levels by injecting reactive power at the head of the feeders, resulting in the difficulty of balancing the voltage of

the whole feeder line. **Figure 3** illustrates the effect of different compensation strategies. When the voltage violation occurs, the voltage profile with no compensation adopted drops seriously at the feeder terminal. Although the OLTC and SCs are able to raise the voltage profile as shown in the blue line, they cause over-voltage at the head of feeders because of too much reactive power injection.

Smart inverters can regulate the voltages at the demand side in a local way, as they are distributed close to terminal users in DNs. Therefore, smart inverters are capable of compensating reactive power locally as the orange line in **Figure 3** depicts. However, in severe voltage violations, smart inverters may not be able to raise all voltages above the safe line due to the limited capacities of demand-side power electronics.

The green line in **Figure 3** illustrates that by using both traditional compensation resources and smart inverters, a satisfactory compensation effect can be achieved without causing over-compensation or being constrained by capacities, which is feasible for voltage regulation in DNs.

2.4 Voltage Deviation Indexes

To further evaluate the voltage deviation, the voltage violation probability P_{vio} and the expected comprehensive deviation of voltage violations E_{dev} are proposed in this paper. The definition of voltage violations in this paper is the scenario where any nodal voltage exceeds the safe range, which is set as 0.95 p. u. to 1.05 p. u. In MCMC simulation analysis, P_{vio} can be expressed as the proportion of voltage violation scenarios in all simulated scenarios:

$$P_{vio} = \frac{1}{N_{sim}} \sum_{i=1}^{N_{sim}} L_i^{vio} \tag{5}$$

$$L_i^{vio} = \begin{cases} 1\,, \text{ the voltage violation happens} \\ 0\,, \text{ no voltage violation happens} \end{cases} \tag{6}$$

where N_{sim} is the number of all simulated scenarios and L_i^{vio} marks the simulation result in the i^{th} scenario.

E_{dev} describes the deviation degree of the voltage violation. The expression of E_{dev} is

$$E_{dev} = \frac{1}{N_{sim}} \sum_{i=1}^{N_{sim}} D_i \tag{7}$$

$$D_i = \sqrt{\frac{\sum_{j=1}^{N_{node}} \left[V_j(i) - V^{ref} \right]^2}{N_{node}}} \tag{8}$$

where D_i is the comprehensive voltage deviation of the i^{th} scenario; N_{node} is the number of nodes in the DN; $V_j(i)$ is the nodal voltage of node j in the i^{th} scenario; V^{ref} is the reference nodal voltage, which is set to 1 p. u. in this paper.

3 SIMULATION METHODS FOR VOLTAGE VIOLATION ASSESSMENT

3.1 Kernel Density Estimation of Electric Vehicle Loads and Photovoltaics Outputs

The KDE method is utilized to model the PDFs of EV loads and PV outputs. Its basic idea is to treat each sample as a kernel function and sum these functions to form an overall PDF. Several load samples and the normal distribution kernel function are selected in **Figure 4** to illustrate the mechanism of KDE.

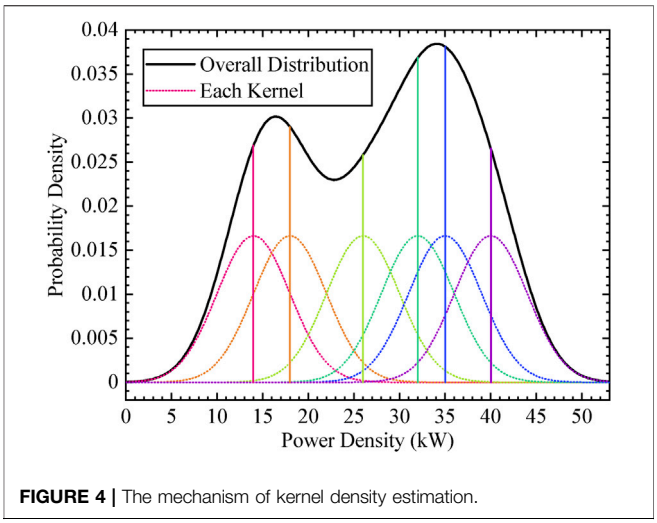

FIGURE 4 | The mechanism of kernel density estimation.

Different kernel functions create different PDFs of the sample data. With the kernel function defined as $K(\cdot)$, the PDF estimated by KDE is (Bowman and Azzalini, 1997)

$$\tilde{f}(x) = \frac{1}{N_{sam}h} \sum_{i=1}^{N_{sam}} K\left(\frac{x - X_i}{h}\right) \tag{9}$$

where N_{sam} is the number of sample data; h is the bandwidth; $X_1, X_2, \ldots, X_n$ are the sample data from the target distribution.

The standard normal distribution kernel function is adopted in this paper. Hence, **Eq. 9** can be specified as

$$\tilde{f}(x) = \frac{1}{N_{sam}h} \sum_{i=1}^{N_{sam}} \frac{1}{\sqrt{2\pi}} e^{\frac{(x-X_i)^2}{2h^2}} \tag{10}$$

To avoid over-smooth or under-smooth in KDE, the bandwidth h is determined according to the formula provided by Silverman (2018).

$$h = \left(\frac{4}{3N_{sam}}\right)^{1/5} \sigma \tag{11}$$

where σ is the standard deviation of the sample data.

3.2 Slice Sampling for Voltage Violation Assessment

It is essential to accurately sample from the PDF obtained by KDE to generate adequate data for MCMC simulation. Slice sampling is an efficient method for handling the continuous PDF with an irregular shape and is mainly composed of two procedures as illustrated in **Figure 5** (Neal, 2003).

The first procedure is defined as the step-out process in **Figure 5A**. Assume x_k is the previous sampling result and y_k is an auxiliary variable randomly drawn from $U[0, \tilde{f}(x_k)]$. The step-out process is to extend the slice range from the initial point

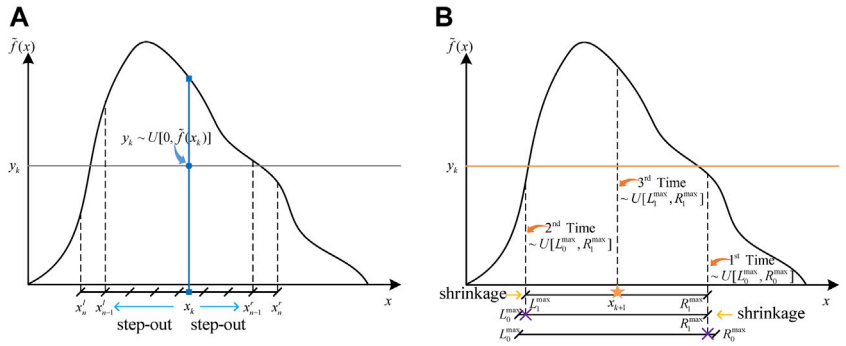

FIGURE 5 | Procedures of slice sampling **(A)** is the step-out process **(B)** is the shrinkage process.

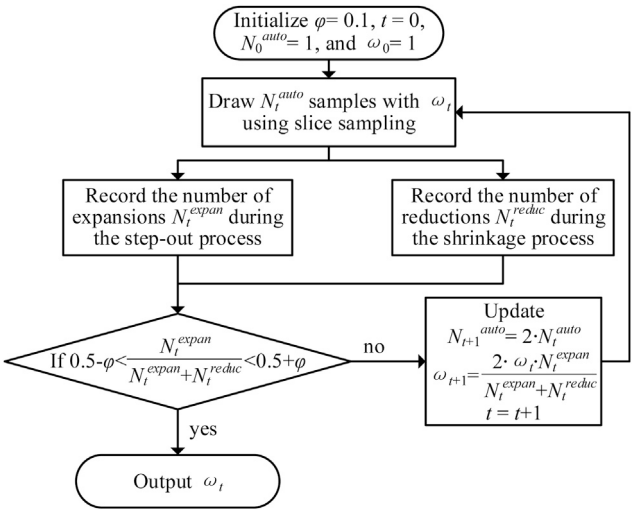

FIGURE 6 | Flow chart of the step width selection.

of x_k step by step in a step width of ω until the probability densities of both ends are all below y_k. Therefore, the eventual slice range completely contains the PDF range which is above y_k.

Then, the shrinkage process is carried out to obtain the next sample x_{k+1} that satisfies $\tilde{f}(x_{k+1}) \geq y_k$. In **Figure 5B**, $L_0^{\max}$ and $R_0^{\max}$ are the initial values of the left end and the right end of the slice range respectively. The first sample is drawn from $U[L_0^{\max}, R_0^{\max}]$ with its corresponding PDF value calculated. If the value is below y_k, the new slice range boundary will be updated and the next sample will be drawn according to the new range until the sample satisfies $\tilde{f}(x_{k+1}) \geq y_k$. The step-out and shrinkage procedures continue to provide samples until the simulation converges.

3.3 Automated Step Width Selection for Slice Sampling

The inappropriate value of the step width ω can decrease the sampling efficiency significantly. Therefore, the automated selection mechanism is introduced in this paper to find the optimal ω (Tibbits et al., 2014).

The selection algorithm is shown in **Figure 6**. This algorithm helps to minimize the effort of step-out and shrinkage operations with several pre-sampling iterations. In each iteration, the numbers of step-out and shrinkage operations are recorded to optimize ω until the tuning iteration converges. After that, the optimal ω is utilized in slice sampling to accelerate the MCMC simulation.

4 RISK ASSESSMENT FOR VOLTAGE VIOLATION

In this section, the tap position of the OLTC and the reactive power from smart inverters and SCs are regarded as manipulated variables to regulate voltage violations in DNs. As different EV loads and PV outputs are sampled from the slice sampling methods, these manipulated variables are optimized to minimize the voltage deviations in each simulation. P_{vio} and E_{dev} are also calculated during the simulation. When P_{vio} and E_{dev} converge, the MCMC simulation stops and outputs the final risk assessment results.

4.1 Voltage Regulation Models

The voltage regulation models proposed in this paper only utilize the remaining reactive power capacities of smart inverters. The total reactive power compensation provided from node i is

$$Q_i = \sum_{j=1}^{N_i^{SI}} Q_i^j \tag{12}$$

where Q_i^j is the reactive power by the j^{th} smart inverter of node i and N_i^{SI} is the number of smart inverters in node i.

Besides, the tap position and n_i^{SC} of SCs are also controlled in the voltage regulation. Their models are expressed in **Eq. 3** and **Eq. 4**. Based on the above equations, the power flow model is (Saadat, 2011)

$$\begin{cases} \Delta P_i = -P_i^{load} - V_i \sum_{j=1}^{N_{node}} V_j \left(G_{ij} \cos\theta_{ij} + B_{ij} \sin\theta_{ij} \right) = 0 \\ \Delta Q_i = Q_i - Q_i^{load} - V_i \sum_{j=1}^{N_{node}} V_j \left(G_{ij} \sin\theta_{ij} - B_{ij} \cos\theta_{ij} \right) = 0 \end{cases} \tag{13}$$

where P_i^{load} and Q_i^{load} are the active and reactive power consumed by loads in node i respectively; V_i is the nodal

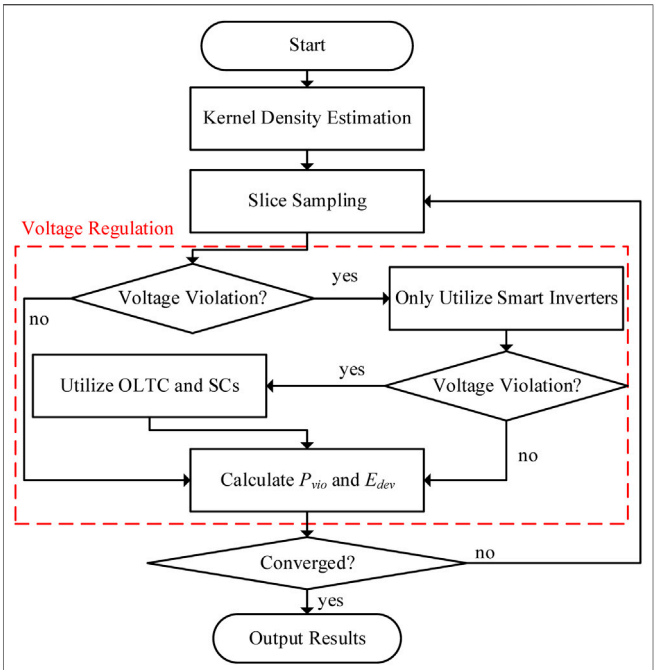

FIGURE 7 | Flow chart of the risk assessment.

voltage of node i; θ_{ij} is the voltage phase angle difference of node i and node j; G_{ij} and B_{ij} are the conductance and susceptance of the nodal admittance matrix elements in row i and column j respectively.

4.2 Voltage Regulation Constraints

Eq. 3 and **Eq. 4** show the operational constraints of the OLTC and SCs. The operation range of smart inverters is

$$-\sqrt{\left(S_i^{j,max}\right)^2-\left(P_i^j\right)^2}<Q_i^j<\sqrt{\left(S_i^{j,max}\right)^2-\left(P^j{}_i\right)^2} \tag{14}$$

where $\left(S_i^{j,max}\right)^2$ is the maximum capacity of the j^{th} smart inverter of node i and P_i^j is the active power from the j^{th} smart inverter of node i.

Apart from constraints of reactive power compensation resources, the voltage regulation model is also limited by voltage amplitude constraints and transmission capacity constraints:

$$\underline{V_i}<V_i<\overline{V_i} \tag{15}$$

$$\underline{S_{ij}}<S_{ij}<\overline{S_{ij}} \tag{16}$$

$$S_{ij}=P_{ij}+Q_{ij} \tag{17}$$

where $\underline{V_i}$ and $\overline{V_i}$ are the minimum and maximum allowed nodal voltages respectively; S_{ij}, P_{ij}, and Q_{ij} are the line apparent power, active power, and reactive power between node i and node j respectively; $\underline{S_{ij}}$ and $\overline{S_{ij}}$ are the minimum and maximum allowed line capacity between node i and node j respectively.

The voltage regulation aims to minimize the nodal voltage deviation of all nodes with reactive power resources, which can be expressed as

$$\min J=\sum_{i=1}^{N_{node}}\left(V_i-V^{ref}\right)^2 \tag{18}$$

4.3 Risk Assessment Process

With the models and methods mentioned above, the risk assessment process is proposed and shown in **Figure 7**. Firstly, the KDE is carried out to derive the PDFs of EV loads and PV outputs. Then, these PDFs are utilized by the slice sampling with automated width selection to produce data samples for voltage regulation. During the voltage regulation, smart inverters are considered the first choice to reduce the operation cost of OLTCs and SCs. Moreover, voltage deviation indexes are calculated to describe the performance of regulation and estimate the convergence of MCMC simulation. If the convergence requirements are not met, the slice sampling will continue to provide samples for risk assessment.

The convergence requirements are satisfied when the accuracy indexes $\sigma(F)$ of both P_{vio} and E_{dev} are below the threshold $\underline{\sigma}$ (Green et al., 2010):

$$\sigma(F)=\frac{\sqrt{\mathrm{var}(F)}}{F},F=P_{vio},E_{dev} \tag{19}$$

where $\mathrm{var}(F)$ is the variance calculation function of F.

5 CASE STUDIES

In this section, the proposed risk assessment is carried out in a modified IEEE 33-bus distribution system (Baran and Wu, 1989). Seven charging stations and 6 PVs are randomly installed along the feeder as **Figure 8** shows. Besides, the OLTC and SCs are equipped at the head of the feeder. The capacity of each smart inverter is 550 kVA and the total capacity of SCs is 5 Mvar in this case study.

5.1 Kernel Density Estimation Results

The EV loads and PV output measurements are derived from Huang et al. (2020) and UK Power Networks (2017) respectively. The data are normalized and estimated by KDE to obtain the PDFs of EV loads and PV outputs.

Figure 9 illustrates the estimation results of KDE. To examine the goodness-of-fit, the chi-square test is performed with the significant level set at 0.05 and the degree of freedom at 49 (Su et al., 2020). The test results of the EV and PV are 23.53 and 42.40 respectively, which are both below the critical value 66.34 and validate the accuracy of KDE.

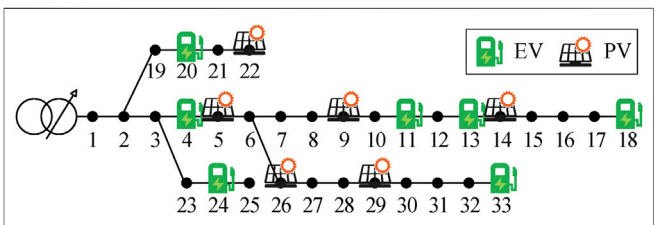

FIGURE 8 | The test feeder topology.

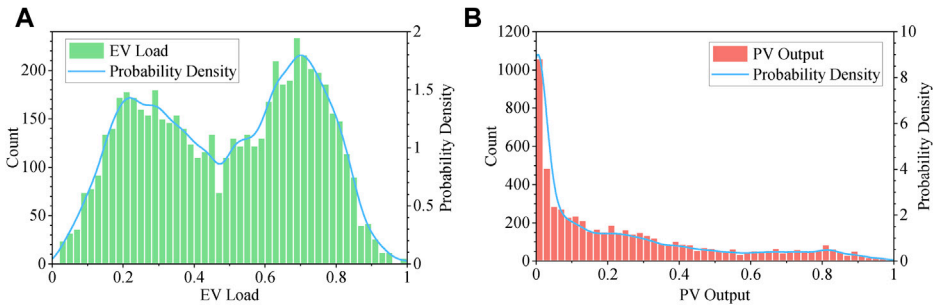

FIGURE 9 | Results of KDE **(A)** is the KDE result of EV loads with *h* as 0.02485 **(B)** is the KDE result of PV outputs with *h* as 0.02486.

TABLE 1 | Comparison of slice sampling and Monte Carlo.

Method	P_{vio}	E_{dev}	Iterations	Time (min)
Slice sampling	0.00470	0.02162	42,513	89.1
Monte Carlo	0.00465	0.02157	43,673	310.4

TABLE 2 | Voltage regulation under different cases.

Case	P_{vio}	E_{dev} (p.u.)	p_{SC}^{OLTC} (%)[a]
Only OLTC and SCs	0.96160	0.03597	100
Only smart inverters	0.17768	0.02364	0
Using above together	0.00470	0.02162	18.00

[a] p_{SC}^{OLTC} *stands for the proportion of scenarios where OLTC and SCs are utilized.*

5.2 Performance of Slice Sampling

To compare the sampling efficiency of slice sampling and the classic Monte Carlo simulation (Zhao et al., 2009), both methods are tested on an i5-4590T 2.00 GHz CPU computer through Matlab R2020a and MATPOWER 7.1 (Zimmerman et al., 2011; Zimmerman and Murillo-Sánchez, 2020). The convergence threshold is 0.01. The optimal step widths ω of EV PDF and PV PDF for slice sampling are 0.761 and 0.343 respectively. The simulation results are listed in **Table 1**.

The slice sampling only consumes 28.7% of the time of the Monte Carlo method to accomplish almost the same number of iterations and the same results of indexes. It takes more time for the classic Monte Carlo method to complete the iterations because this method rejects many unqualified samples during simulation. By contrast, no samples are discarded in slice sampling, which improves the sampling efficiency.

Table 2 illustrates three typical cases where only the OLTC and SCs, only smart inverters, and all these facilities are respectively utilized in voltage regulation. Compared with OLTC and SCs, and E_{dev} by using smart inverters decrease 81.52 and 34.28% respectively, which shows that it is more effective to compensate reactive power along the feeder *via* smart inverters. With the OLTC, SCs, and smart inverters all adopted, P_{vio} drops significantly to almost 0 and E_{dev} also gets mitigated. Besides, p_{SC}^{OLTC} in **Table 2** demonstrates that smart inverters are capable of reducing the utilization of the OLTC and SCs, which help to save the operation cost of these traditional compensation facilities.

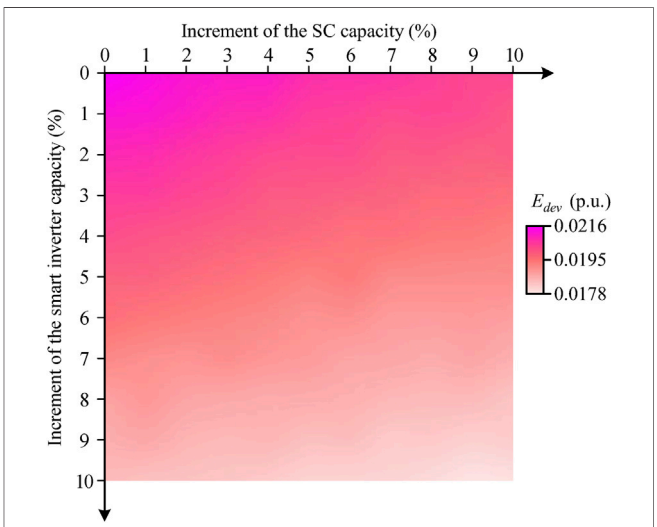

FIGURE 10 | Sensitivity analysis.

5.3 Sensitivity Analysis

In the sensitivity analysis, the capacities of smart inverters and SCs are set to increase 10% of the original value respectively. **Figure 10** depicts E_{dev} under different increments of smart inverters and SCs. P_{vio} is not illustrated since its value approximates zero and rarely varies during the simulation. If the capacity of smart inverters increases 10%, E_{dev} drops by 14.24%, while E_{dev} only drops by 5.52% if the SCs increases 10%. It can be concluded from **Figure 10** that under the same increment of capacities, smart inverters perform better in voltage regulation than SCs.

6 CONCLUSION

This paper establishes a voltage violation assessment model considering the support provided by smart inverters. With the active power samples from KDE and slice sampling, the reactive power compensation process is modeled and implemented to minimize the voltage deviation. Based on the voltage deviation indexes proposed in this paper, the case studies demonstrate that

slice sampling takes less time to converge than the Monte Carlo method. Besides, while OLTCs, SCs, and smart inverters are all essential to avoid voltage violations, smart inverters are more effective than the traditional facilities, which can save the operation cost of these facilities as well. Moreover, the sensitivity analysis shows that it is more beneficial to develop smart inverters than SCs, which validates the prospect of smart inverters for voltage regulation.

In future works, the cooperative control strategies of smart inverters for voltage regulation will be studied. The integration of both active and reactive power deliveries will be considered to further implement the four-quadrant operation characteristic of smart inverters.

DATA AVAILABILITY STATEMENT

The original contributions presented in the study are included in the article/Supplementary Material, further inquiries can be directed to the corresponding author.

AUTHOR CONTRIBUTIONS

The paper was a collaborative effort among the authors. JH designed the voltage violation assessment model. CY proposed the original idea and established the framework. WY made the case studies. WB and JW contributed to the introduction. YD contributed to the supervision and editing.

FUNDING

This work was supported in part by the National Natural Science Foundation of China under Grant 51807173, in part by the Fundamental Research Funds for the Central Universities under Grant 2021QNA4012, and in part by the Science and technology project of State Grid Zhejiang Electric Power Co., Ltd with No. 5211JX1900CV. The funders were not involved in the study design, collection, analysis, interpretation of data, the writing of this article, or the decision to submit it for publication. All authors declare no other competing interests.

REFERENCES

Abeywardana, W. D. B., Acuna, P., Hredzak, B., Aguilera, R. P., and Agelidis, V. G. (2018). Single-Phase Boost Inverter-Based Electric Vehicle Charger with Integrated Vehicle to Grid Reactive Power Compensation. *IEEE Trans. Power Electron.* 33, 3462–3471. doi:10.1109/TPEL.2017.2700944

Baran, M. E., and Wu, F. F. (1989). Network Reconfiguration in Distribution Systems for Loss Reduction and Load Balancing. *IEEE Trans. Power Deliv.* 4, 1401–1407. doi:10.1109/61.25627

Bowman, A. W., and Azzalini, A. (1997). *Applied Smoothing Techniques for Data Analysis: The Kernel Approach with S-Plus Illustrations*. Oxford and New York: Clarendon Press and Oxford University Press.

Buja, G., Bertoluzzo, M., and Fontana, C. (2017). Reactive Power Compensation Capabilities of V2G-Enabled Electric Vehicles. *IEEE Trans. Power Electron.* 32, 9447–9459. doi:10.1109/TPEL.2017.2658686

Chen, H., Prasai, A., and Divan, D. (2018). A Modular Isolated Topology for Instantaneous Reactive Power Compensation. *IEEE Trans. Power Electron.* 33, 975–986. doi:10.1109/TPEL.2017.2688393

Feng, J., Wang, H., Xu, J., Su, M., Gui, W., and Li, X. (2018). A Three-phase Grid-Connected Microinverter for AC Photovoltaic Module Applications. *IEEE Trans. Power Electron.* 33, 7721–7732. doi:10.1109/TPEL.2017.2773648

Green, R. C., Lingfeng Wang, L., and Singh, C. (2010). "State Space Pruning for Power System Reliability Evaluation Using Genetic Algorithms," in IEEE PES General Meeting, Minneapolis, MN, July 25–29, 2010 (Minneapolis: IEEE), 1–6. doi:10.1109/PES.2010.5590205

Gush, T., Kim, C.-H., Admasie, S., Kim, J.-S., and Song, J.-S. (2021). Optimal Smart Inverter Control for PV and BESS to Improve PV Hosting Capacity of Distribution Networks Using Slime Mould Algorithm. *IEEE Access* 9, 52164–52176. doi:10.1109/ACCESS.2021.3070155

Hu, B., Li, Y., Yang, H., and Wang, H. (2017). Wind Speed Model Based on Kernel Density Estimation and its Application in Reliability Assessment of Generating Systems. *J. Mod. Power Syst. Clean. Energ.* 5, 220–227. doi:10.1007/s40565-015-0172-5

Huang, S., Ye, C., Liu, S., Zhang, W., Ding, Y., Hu, R., et al. (2020). Data-driven Reliability Assessment of an Electric Vehicle Penetrated Grid Utilizing the Diffusion Estimator and Slice Sampling. *Csee Jpes*, 1–9. doi:10.17775/CSEEJPES.2020.01030

Kekatos, V., Wang, G., Conejo, A. J., and Giannakis, G. B. (2015). Stochastic Reactive Power Management in Microgrids with Renewables. *IEEE Trans. Power Syst.* 30, 3386–3395. doi:10.1109/TPWRS.2014.2369452

Kesler, M., Kisacikoglu, M. C., and Tolbert, L. M. (2014). Vehicle-to-Grid Reactive Power Operation Using Plug-In Electric Vehicle Bidirectional Offboard Charger. *IEEE Trans. Ind. Electron.* 61, 6778–6784. doi:10.1109/TIE.2014.2314065

Kisacikoglu, M. C., Ozpineci, B., and Tolbert, L. M. (2013). EV/PHEV Bidirectional Charger Assessment for V2G Reactive Power Operation. *IEEE Trans. Power Electron.* 28, 5717–5727. doi:10.1109/TPEL.2013.2251007

Neal, R. M. (2003). Slice Sampling. *Ann. Statist.* 31, 705–767. doi:10.1214/aos/1056562461

Quirós-Tortós, J., Ochoa, L. F., Alnaser, S. W., and Butler, T. (2016). Control of EV Charging Points for Thermal and Voltage Management of LV Networks. *IEEE Trans. Power Syst.* 31, 3028–3039. doi:10.1109/TPWRS.2015.2468062

Saadat, H. (2011). *Power System Analysis*. Third edn. United States: PSA Publishing LLC), 228–295.

Sharma, R., and Das, A. (2020). Extended Reactive Power Exchange with Faulty Cells in Grid-Tied Cascaded H-Bridge Converter for Solar Photovoltaic Application. *IEEE Trans. Power Electron.* 35, 5683–5691. doi:10.1109/TPEL.2019.2950336

Silverman, B. W. (2018). *Density Estimation for Statistics and Data Analysis*. Boca Raton: Routledge.

Singh, S., Pamshetti, V. B., and Singh, S. P. (2019). Time Horizon-Based Model Predictive Volt/VAR Optimization for Smart Grid Enabled CVR in the Presence of Electric Vehicle Charging Loads. *IEEE Trans. Ind. Applicat.* 55, 5502–5513. doi:10.1109/TIA.2019.2928490

Su, N., An, X., Yan, C., and Ji, S. (2020). Incremental Attribute Reduction Method Based on Chi-Square Statistics and Information Entropy. *IEEE Access* 8, 98234–98243. doi:10.1109/ACCESS.2020.2997013

Su, X., Masoum, M. A. S., and Wolfs, P. J. (2014). Optimal PV Inverter Reactive Power Control and Real Power Curtailment to Improve Performance of Unbalanced Four-Wire LV Distribution Networks. *IEEE Trans. Sustain. Energ.* 5, 967–977. doi:10.1109/TSTE.2014.2313862

Tibbits, M. M., Groendyke, C., Haran, M., and Liechty, J. C. (2014). Automated Factor Slice Sampling. *J. Comput. Graphical Stat.* 23, 543–563. doi:10.1080/10618600.2013.791193

Tómasson, E., and Söder, L. (2017). Improved Importance Sampling for Reliability Evaluation of Composite Power Systems. *IEEE Trans. Power Syst.* 32, 2426–2434. doi:10.1109/TPWRS.2016.2614831

UK Power Networks (2017). *Photovoltaic (PV) Solar Panel Energy Generation Data*. London, United Kingdom: London Datastore. Available at: https://data.london.gov.uk/dataset/photovoltaic–pv–solar-panel-energy-generation-data.

Ustun, T. S., Aoto, Y., Hashimoto, J., and Otani, K. (2020). Optimal PV-INV Capacity Ratio for Residential Smart Inverters Operating under Different Control Modes. *IEEE Access* 8, 116078–116089. doi:10.1109/ACCESS.2020.3003949

Varma, R. K., and Siavashi, E. M. (2018). PV-STATCOM: A New Smart Inverter for Voltage Control in Distribution Systems. *IEEE Trans. Sustain. Energ.* 9, 1681–1691. doi:10.1109/TSTE.2018.2808601

Wu, W., Tian, Z., and Zhang, B. (2017). An Exact Linearization Method for OLTC of Transformer in Branch Flow Model. *IEEE Trans. Power Syst.* 32, 2475–2476. doi:10.1109/TPWRS.2016.2603438

Zeraati, M., Golshan, M. E. H., and Guerrero, J. M. (2019). Voltage Quality Improvement in Low Voltage Distribution Networks Using Reactive Power Capability of Single-phase PV Inverters. *IEEE Trans. Smart Grid* 10, 5057–5065. doi:10.1109/TSG.2018.2874381

Zhao, Y., Zhang, X.-F., and Zhou, J.-Q. (2009). Load Modeling Utilizing Nonparametric and Multivariate Kernel Density Estimation in Bulk Power System Reliability Evaluation. *Proc. CSEE* 29, 27–33.

Zhou, P., Jin, R. Y., and Fan, L. W. (2016). Reliability and Economic Evaluation of Power System with Renewables: A Review. *Renew. Sustain. Energ. Rev.* 58, 537–547. doi:10.1016/j.rser.2015.12.344

Zimmerman, R. D., and Murillo-Sánchez, C. E. (2020). *MATPOWER*. Genève, Switzerland: Zenodo. doi:10.5281/zenodo.4074135 Available at: https://zenodo.org/record/4074135#.YKB4HqgzaUk (Accessed October 8, 2020).

Zimmerman, R. D., Murillo-Sánchez, C. E., and Thomas, R. J. (2011). MATPOWER: Steady-State Operations, Planning, and Analysis Tools for Power Systems Research and Education. *IEEE Trans. Power Syst.* 26, 12–19. doi:10.1109/TPWRS.2010.2051168

Conflict of Interest: The author WY was employed by State Grid Jiaxing Power Supply Company and authors WB and JW were employed by State Grid Yiwu Power Supply Company.

The remaining authors declare that the research was conducted in the absence of any commercial or financial relationships that could be construed as a potential conflict of interest.

frontiers in Energy Research

ORIGINAL RESEARCH
published: 27 July 2021
doi: 10.3389/fenrg.2021.712397

Passive Sliding Mode Controlled UPFC and its Treatment Strategy of Unbalanced Grid Conditions

Yang Chen, Han Wang, Miao Zhu, Ming Liu, Jianjun Ma and Xu Cai*

Key Laboratory of Control of Power Transmission and Conversion, Ministry of Education, Shanghai Jiao Tong University, Shanghai, China

Modular multilevel converter based unified power flow controller (MMC-UPFC) can provide flexible power regulation and plays an important role in the smart grid and future distribution networks. PI controller is widely adopted in the Unified power flow controller (UPFC) control. However, it is often difficult to figure out a pair of stable control parameters with good dynamic performance. A passive sliding mode control strategy of MMC-UPFC is proposed in this paper to achieve the advantages of both the passive controller and sliding mode controller. The proposed passive sliding mode control strategy has a fast response speed and is not sensitive to system parameter variation. Since unbalance grid voltage conditions are common in the modern distribution networks, an unbalanced grid treatment strategy is also presented with the series side of MMC-UPFC. Negative sequence components of the grid voltages are detected by the cross-decoupling method with second order generalized integrator and then compensated by the series side of MMC-UPFC. The series side converter controls the power flow and treats unbalanced grid conditions simultaneously. The efficiency of the general device is increased thus. A 27-level MMC-UPFC simulation system is built based on the Shanghai UPFC Project and validate the proposed approach.

Keywords: unified power flow controller, modular multilevel converter, passive control, sliding mode control, unbalanced grid condition treatment

OPEN ACCESS

Edited by:
Ningyi Dai,
University of Macau, China

Reviewed by:
Fujin Deng,
Southeast University, China
Xiaoqiang Guo,
Yanshan University, China

****Correspondence:***
Miao Zhu
miaozhu@sjtu.edu.cn

Specialty section:
This article was submitted to Smart Grids, a section of the journal Frontiers in Energy Research

Received: *20 May 2021*
Accepted: *31 May 2021*
Published: *27 July 2021*

Citation:
Chen Y, Wang H, Zhu M, Liu M, Ma J and Cai X (2021) Passive Sliding Mode Controlled UPFC and its Treatment Strategy of Unbalanced Grid Conditions. Front. Energy Res. 9:712397. doi: 10.3389/fenrg.2021.712397

INTRODUCTION

Modern flexible AC transmission systems (FACTS) devices are the key components in the smart grid and the future energy internet. FACTS devices leverage the potential of the power grid and enable the smarter power grid in the future energy network (Peng, 2017). Unified power flow controller (UPFC) is one of the most powerful power conditioners in the FACTS device family (Gyugyi et al., 1995).

A typical UPFC often consists of two back-to-back connected shunt- and series-connected AC-DC converters. Transmission line power flow can be controlled by the series side converter and the inner DC bus voltage can be regulated by the shunt side. Due to the development of modular multilevel converter (MMC) technologies (Akagi, 2017; Haque et al., 2020), UPFC has enjoyed a new research and construction boom in recent years. Several MMC-UPFC projects have been put into operation in China recently. The UPFC for 220 kV Nanjing Western-Ring Grid launched in 2015 is the first MMC-UPFC in the world (Li, et al., 2016). The first urban MMC-UPFC is launched for Shanghai distribution network in 2017. The 500 kV UPFC in southern Jiangsu Province is playing an important role in the power flow regulation of Suzhou grid.

Classical dual-loop control strategy can be applied to the cascaded AC-DC converters in the UPFC. PI controllers are widely used in the dual-loop control, which can achieve good steady-state performances with certain parameters. However, there may be steady state error and the dynamic performance will be affected when system parameters change. To improve the dynamic response, nonlinear control strategies such as model predictive control (MPC) (Guo et al., 2018; Ramirez et al., 2020), passive control (Yang, et al., 2018), and sliding mode control (SMC) (Yang et al., 2019; Feng et al., 2020) are proposed for MMC-UPFC. However, MPC requires precise system modeling and the computation amount increases with the increased number of switches in the converter. Passive control is another non-linear control strategy from the system energy attributes which provides a faster step response and better transient dynamics due to the injected extra system damping. A passive control scheme for multi-terminal VSC-HVDC is investigated in (Yang et al., 2018), which can achieve a reliable and effective renewable energy integration. However, passive control requires precise system modeling. Thus the wider application of passive control is limited significantly. SMC is an efficient tool to design robust controllers which has been widely used in the converter controller designing (Ma et al., 2019; Feng et al., 2020). An observer based sliding mode frequency control strategy is proposed for multi-machine power systems with high renewable energy (Tummala et al., 2018). A fractional-order sliding mode control is proposed for a D-STATCOM to compensate the low power distribution system (Ahmed et al., 2021). An adaptive sliding mode reactive power control strategy is proposed in (Mi et al., 2019) to eliminate system parameter uncertainties or disturbances and improve the system stability. The integration of passive control and sliding mode control is proved to be an efficient approach for MMC-UPFC control (Ke et al., 2019). The inherent chattering problem can be solved by adopting integral sliding surface.

On the other side, the unbalanced grid condition is one of the most severe power quality issues. Shunt connected FACTS devices often deal with power quality problems by inserting currents to the bus. Several research works have been done on power quality treatment with shunt side converters of UPFC as well. However, there was rare work on the series side compensation. Meanwhile, plenty of researches have been done on VSC and MMC operation under unbalanced grid conditions (Li et al., 2018; Shang et al., 2019; Kryonidis et al., 2021). The multiple objective control method (Stefanov and Stankovic, 2002), modeling and operation analysis of UPFC with unbalanced conditions (Yang et al., 2020), the methods of the fault ride improvement of MMC-UPFC (Santos et al., 2014) have been discussed widely. An arm current balancing control and capacitor voltage reduction method for MMC-UPFC under unbalanced grid conditions are proposed in (Li et al., 2019) and (Wang et al., 2019) respectively. The controllable regions of MMC-UPFC under unbalanced grid conditions are investigated and a voltage limit control is given accordingly in (Hao et al., 2017). The influence of UPFC in grid fault scenarios are analyzed in (Akter et al., 2020) and (Chatterjee and Sudipta, 2020). As mentioned above, most researches focused on the operation of UPFC under unbalanced grid voltage conditions. As the most powerful FACTS device, both sides of UPFC can take part in the treatment of unbalanced grid conditions as well.

To improve the performance of MMC-UPFC, a passive sliding mode control (P-SMC) strategy is proposed and discussed firstly in this paper. The dependence of passive control on precise modeling is overcome by the adoption of sliding mode control. The integral sliding mode is introduced to solve the chattering problem of the classical sliding mode control. The proposed passive sliding mode control strategy is easy to implement with fast response.

The treatment strategy for unbalanced grid conditions is provided using the series side of MMC-UPFC afterwards. The negative sequence components of the grid currents are detected via the cross-decoupling strategy with second order generalized integrator. The negative sequence voltages are inserted by the series side of MMC-UPFC to compensate the grid negative sequence voltage. The grid currents return to symmetry and the power quality can be improved.

Mathematical modeling, theoretical analysis, and simulation results of a 27 level MMC-UPFC system are provided in the paper and validate the proposed P-SMC strategy and unbalanced condition treatment strategy.

GENERAL WORKING PRINCIPLES AND THE EULER-LAGRANGE MODEL OF MODULAR MULTILEVEL CONVERTER-UNIFIED POWER FLOW CONTROLLER

MMC-UPFCs usually contain two back-to-back MMC-structured converters. A Typical layout of MMC-UPFC in the power grid is shown in **Figure 1**.

The shunt side MMC of UPFC obtains power from the bus to keep the DC link voltage V_{dc} constant and injects reactive power to the AC bus. The series side MMC employs a voltage source v_{se} series connected in the transmission line. By changing the amplitude and phase angle of the inserted series voltage v_{se}, active and reactive power through the transmission line can be controlled. The series side MMC performs like the Static Synchronous Series Compensator (SSSC) but has higher flexibility due to the stable DC link voltage provided by the shunt side MMC.

As shown in **Figure 1**, both shunt and series sides of the MMC-UPFC share the same modular multilevel converter topology. Thus the Euler-Lagrange model of the general MMC is deduced in this part for the further controller design in the next section. The equivalent circuit of MMC is provided in **Figure 2**. The mathematic model of the grid connected MMC can be expressed as **Eq. 1**.

$$\begin{cases} \dfrac{V_{dc}}{2} - R_0 i_{jp} - L_0 \dfrac{di_{jp}}{dt} - v_{jp} = v_{gj} + R_g i_j + L_g \dfrac{di_j}{dt} \\ -\dfrac{V_{dc}}{2} + R_0 i_{jp} + L_0 \dfrac{di_{jp}}{dt} + v_{jp} = v_{gj} + R_g i_j + L_g \dfrac{di_j}{dt} \end{cases} \tag{1}$$

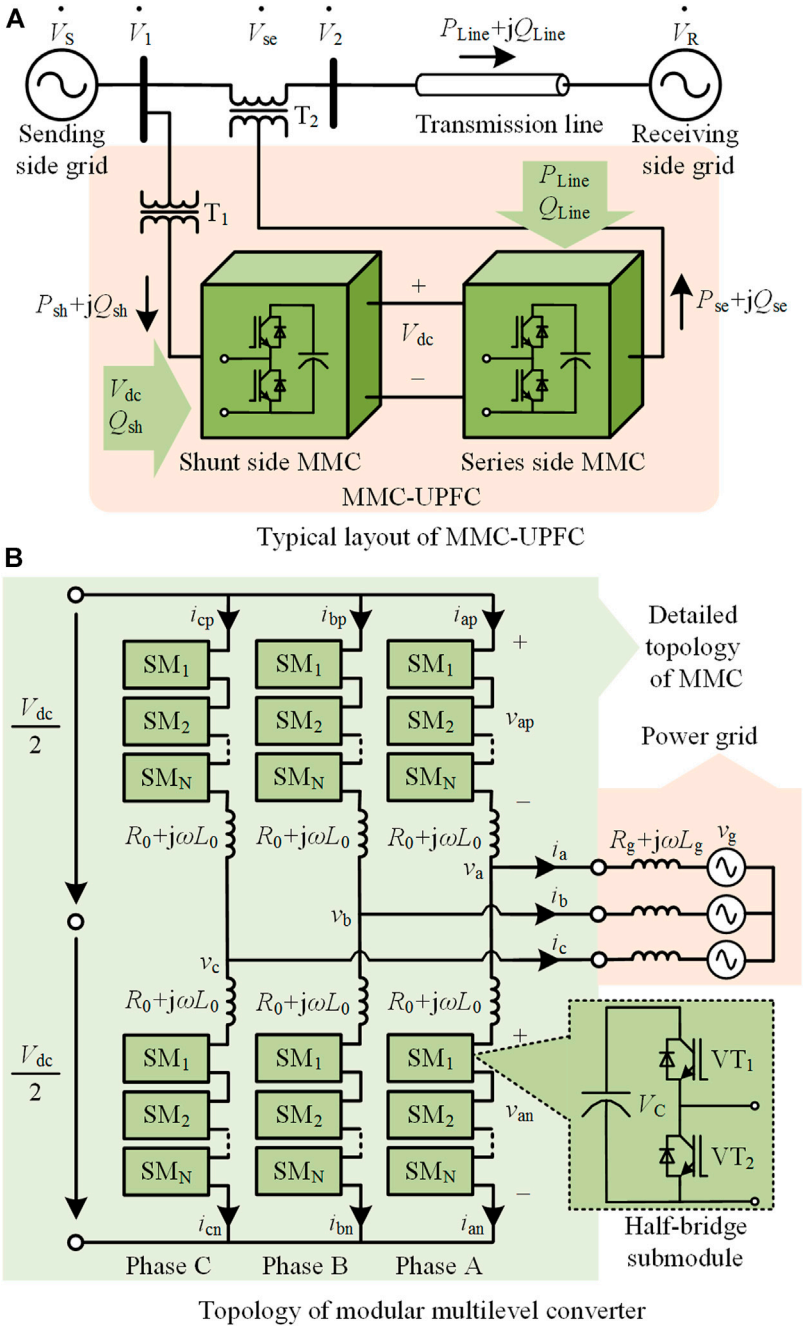

FIGURE 1 | Typical topology and application of MMC-UPFC in power grid.

Here in **Eq. 1**, j = a, b, c. The dynamic model of MMC with differential- and common-mode components in the static *abc* frame can be deduced as follows from **Eq. 1**.

$$\begin{cases} \left(\frac{R_0}{2}+R_g\right)i_j+\left(\frac{L_0}{2}+L_g\right)\frac{di_j}{dt}=v_{jdiff}-v_{gj} \\ R_0 i_{jcir}+L_0\frac{di_{jcir}}{dt}=\frac{v_{dc}}{2}-v_{jcom} \end{cases} \tag{2}$$

The differential- and common-mode voltages and currents mentioned in **Eq. 2** are defined as follows.

$$\begin{cases} v_{jdiff}=\frac{1}{2}\left(v_{jn}-v_{jp}\right) \\ v_{jcom}=\frac{1}{2}\left(v_{jn}+v_{jp}\right) \end{cases} \tag{3}$$

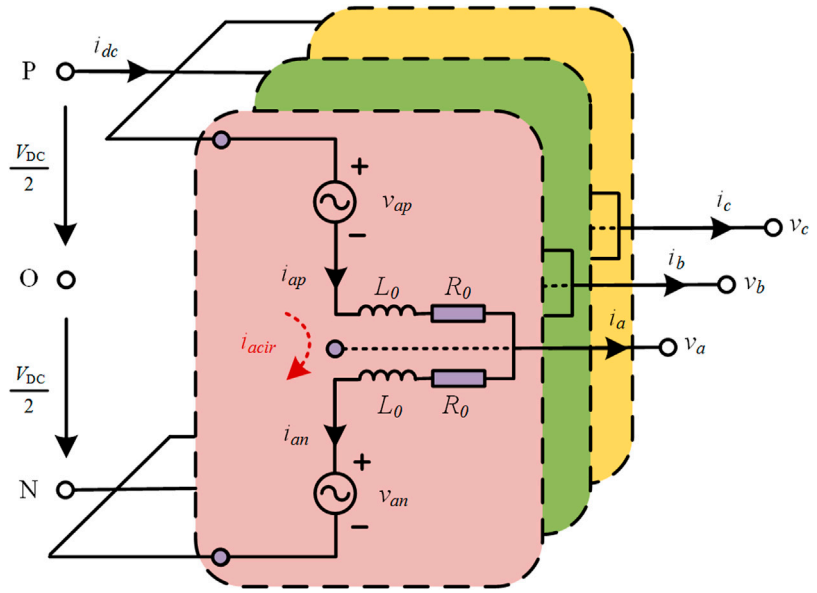

FIGURE 2 | Equivalent circuit of MMC.

$$\begin{cases} i_j = i_{jp} - i_{jn} \\ i_{jcir} = \frac{1}{2}\left(i_{jp} + i_{jn}\right) \end{cases} \tag{4}$$

Here in **Eq. 3** and **Eq. 4**, v_{jn} and v_{jp} are composed of submodule capacitor voltages and they are adjusted by changing submodule states. The differential voltage component v_{jdiff} is equivalent to the output AC voltage v of MMC. Thus v_{jdiff} is replaced by v in the following modeling. $R_0/2 + j\omega L_0/2$ is equivalent to the cascaded impedance of MMC. The equivalent grid impedance $R_g + j\omega L_g$ and the equivalent converter impedance $R_0/2 + j\omega L_0/2$ are replaced by a general impedance $R + j\omega L$ in the following modeling as well.

When the unbalanced grid condition occurs in the power grid, the grid voltage and current can be separated into positive, negative, and zero sequence components by the symmetrical components method. The zero sequence current can be eliminated by setting proper transformer winding connection mode in the high voltage transmission system. The unbalanced grid condition treatment strategy is another topic of this paper. Thus the control of positive and negative components are the focus of this paper. The positive and negative sequence EL model of MMC are deduced in the remaining of this section.

The universal positive and negative sequence models of MMC in *dq* frames are shown in **Eq. 5** and **Eq. 6**.

$$R\begin{pmatrix} i_d^+ \\ i_q^+ \end{pmatrix} + L\begin{pmatrix} \frac{di_d^+}{dt} \\ \frac{di_q^+}{dt} \end{pmatrix} + L\begin{pmatrix} 0 & -\omega \\ \omega & 0 \end{pmatrix}\begin{pmatrix} i_d^+ \\ i_q^+ \end{pmatrix} = \begin{pmatrix} v_d^+ \\ v_q^+ \end{pmatrix} - \begin{pmatrix} v_{gd}^+ \\ v_{gq}^+ \end{pmatrix} \tag{5}$$

$$R\begin{pmatrix} i_d^- \\ i_q^- \end{pmatrix} + L\begin{pmatrix} \frac{di_d^-}{dt} \\ \frac{di_q^-}{dt} \end{pmatrix} + L\begin{pmatrix} 0 & \omega \\ -\omega & 0 \end{pmatrix}\begin{pmatrix} i_d^- \\ i_q^- \end{pmatrix} = \begin{pmatrix} v_d^- \\ v_q^- \end{pmatrix} - \begin{pmatrix} v_{gd}^- \\ v_{gq}^- \end{pmatrix} \tag{6}$$

According to **Eq. 5** and **Eq. 6**, MMC has the same output model with traditional three-phase inverters. Thus, the classical decoupled dual-loop control can be applied for MMC control as well.

The positive and negative sequence models of MMC in **Eq. 5** and **Eq. 6** can be rewritten in the form of Euler-Lagrange (EL) model as shown in **Eq. 7** and **Eq. 8**.

$$M\dot{x}^+ + J^+x^+ + Rx^+ = u^+ \tag{7}$$

$$M\dot{x}^- + J^-x^- + Rx^- = u^- \tag{8}$$

The meanings and basic features of each matrix in **Eq. 7** and **Eq. 8** are explained as follows:

- x^+ and x^- are the state variable of the system.

$$x^+ = \begin{pmatrix} i_d^+ \\ i_q^+ \end{pmatrix}, x^- = \begin{pmatrix} i_d^- \\ i_q^- \end{pmatrix} \tag{9}$$

- u^+ *and* u^- are the energy exchanges between the system and the external environment.

$$u^+ = \begin{pmatrix} v_d^+ - v_{gd}^+ \\ v_q^+ - v_{gq}^+ \end{pmatrix}, u^- = \begin{pmatrix} v_d^- - v_{gd}^- \\ v_q^- - v_{gq}^- \end{pmatrix} \tag{10}$$

- M is the positive definite diagonal matrix.

$$M = \begin{pmatrix} L & 0 \\ 0 & L \end{pmatrix} \tag{11}$$

- J^+ and J^- are the antisymmetric matrix of the positive and negative sequence system respectively. The two matrixes satisfy $J^+ = {}^-J^{+T}$ and $J^-= -J^{-T}$ with consideration of the interconnection structure of the system.

$$J^+ = \begin{pmatrix} 0 & -\omega L \\ \omega L & 0 \end{pmatrix}, J^- = \begin{pmatrix} 0 & \omega L \\ -\omega L & 0 \end{pmatrix} \tag{12}$$

- R is the positive definite matrix which represents the dissipative characteristics of the system.

$$R = \begin{pmatrix} R & 0 \\ 0 & R \end{pmatrix} \tag{13}$$

Note that the shunt and series sides of the MMC-UPFC in **Figure 1** share the same mathematical model form since they have the same MMC topology. Then the passive sliding mode control will be proposed in the following section on the basis of the EL models here.

PASSIVE SLIDING MODE CONTROL STRATEGY FOR MODULAR MULTILEVEL CONVERTER-UNIFIED POWER FLOW CONTROLLER

The passive sliding mode control is proposed in the inner current loop of both the shunt and series sides of the MMC-UPFC instead of the traditional PI controller, which provides easier parameter design and better dynamic performance for the proposed MMC-UPFC. The design of the passive sliding mode control strategy of the MMC positive sequence system is discussed in this section.

Fundamental Passive Control Design

The passive control redistributes the energy of the system and injects nonlinear damping to the system. It can help the system energy track the pre-set energy function and make the state variable of the system gradually converges to the set value. Then the system can finally reach the specified control target. Here the positive sequence system of MMC is taken to show the whole controller design process.

When the grid voltage is unbalanced, the expected stable balance point of the positive sequence system is **Eq. 14**.

$$x_{ref}^+ = \begin{pmatrix} x_{1ref}^+ \\ x_{2ref}^+ \end{pmatrix} = \begin{pmatrix} i_{dref}^+ \\ i_{qref}^+ \end{pmatrix} \tag{14}$$

Here in **Eq. 14**, $i + dref$ is the expected stable value of the state variable $i + d$, which is the d frame component current and it controls the output active power. $i + qref$ is the expected stable value of the state variable $i + q$, which is the q frame component current and it controls the output reactive power.

The error component of the MMC positive sequence system is **Eq. 15**.

$$x_e^+ = x^+ - x_{ref}^+ = \begin{pmatrix} i_d^+ - i_{dref}^+ \\ i_q^+ - i_{qref}^+ \end{pmatrix} \tag{15}$$

The EL error model of the MMC positive sequence system can be obtained as **Eq. 16** from the EL mathematical model of MMC given in **Eq. 7**.

$$M\dot{x_e^+} + J^+x_e^+ + Rx_e^+ = u^+ - M\dot{x_{ref}^+} - J^+x_{ref}^+ - Rx_{ref}^+ \tag{16}$$

The damping injection method is applied to accelerate the energy dissipation of the system and make the system converge to the expected point faster. Thus, the system conversion can quickly reach the expected point. The new damping dissipation term is **Eq. 17** with the newly added positive definite matrix of injected damping $R+ a$.

$$R_dx_e^+ = \left(R + R_a^+\right)x_e^+ \tag{17}$$

Here in **Eq. 17**, the newly injected damping $R+ a$ is **Eq. 18**.

$$R_a^+ = \begin{pmatrix} R_a^+ & 0 \\ 0 & R_a^+ \end{pmatrix} \tag{18}$$

In order to realize the decoupling control, the original EL error model **Eq. 7** is rewritten. The new EL error model of the MMC positive sequence system with the newly injected damping $R+ a$ is **Eq. 19**.

$$\begin{aligned} Q^+ &= M\dot{x_e^+} + R_d^+x_e^+ = u^+ - \left(M\dot{x_{ref}^+} + J^+\left(x_{ref}^+ + x_e^+\right) + Rx_{ref}^+ - R_a^+x_e^+\right) \\ &= u^+ - \left(M\dot{x_{ref}^+} + J^+x^+ + Rx_{ref}^+ - R_a^+x_e^+\right) \end{aligned} \tag{19}$$

If Q^+ is 0, the steady-state error will be eliminated and the decoupling control can be achieved. Thus the passive control law of the positive sequence system is selected as **Eq. 20**.

$$u^+ = M\dot{x_{ref}^+} + J^+x^+ + Rx_{ref}^+ - R_a^+x_e^+ \tag{20}$$

Thus the passive controller of the MMC positive sequence system in dq frame can be derived as follows.

$$\begin{cases} v_{dref}^+ = v_{gd}^+ - \omega Li_q^+ + Ri_{dref}^+ + R_a^+\left(i_d^+ - i_{dref}^+\right) \\ v_{qref}^+ = v_{gq}^+ + \omega Li_d^+ + Ri_{qref}^+ + R_a^+\left(i_q^+ - i_{qref}^+\right) \end{cases} \tag{21}$$

The stability of the passive controller can be proved by the Lyapunov stability theory. The energy function of the MMC positive sequence system V^+ is selected as **Eq. 22**. Due to the positive definiteness of matrix M, V^+ is always positive.

$$V^+ = \frac{1}{2}x_e^{+T}Mx_e^+ \tag{22}$$

The derivative of the above energy function V^+ can be calculated by **Eq. 23**.

$$\dot{V}^+ = x_e^{+T}M\dot{x_e^+} = x_e^{+T}\left(Q^+ - J^+x_e^+ - R_d^+x_e^+\right) = x_e^{+T}Q^+ - x_e^{+T}R_d^+x_e^+ \tag{23}$$

Since the terminal value of Q^+ is 0, the derivative of V^+ is **Eq. 24** and it is obviously negative.

$$\dot{V}^+ = -x_e^{+T} R_d^+ x_e^+ < 0 \tag{24}$$

The conclusion can be drawn that V^+ is always positive while the derivative of V^+ is negative. The system is proved to be asymptotically stable according the Lyapunov stability theory.

Developed Passive Sliding Mode Control Design

The passive control theory requires precise system parameters to achieve higher dynamic performance. However, several system parameters cannot be measured directly and precisely. There may be parameter perturbation during the long operating process as well. System parameters will change when the grid operation mode changes. These will lead to the change of the system balancing point in the passive controller above.

The sliding mode control has good performance facing system parameter variation. Therefore, the sliding mode control is integrated in the proposed passive controller to acquire the advantages of the two control strategies.

It is known that there is often a steady-state error in the linear sliding mode control of MMC-UPFC. An integrator is introduced in the control loop to eliminate the steady state error of sliding mode control. The positive sequence system sliding surfaces $s + d$and $s + q$ in the dq frame are selected as **Eq. 25**.

$$\begin{cases} s_d^+ = k_{pd}^+ e_d^+ + k_{id}^+ \int e_d^+ & e_d^+ = i_{dref}^+ - i_d^+ \\ s_q^+ = k_{pq}^+ e_q^+ + k_{iq}^+ \int e_q^+ & e_q^+ = i_{qref}^+ - i_q^+ \end{cases} \tag{25}$$

Here in **Eq. 25**, k_{pd}^+, $\mathrm{k}_{\mathrm{id}}^+$, k_{pq}^+, *and* $\mathrm{k}_{\mathrm{iq}}^+$ are the control parameters of the sliding faces. The ubiquitous high frequency chattering problem of traditional sliding mode control can be solved by choosing the exponential reaching law with saturated function *sat* (·) instead of the ideal symbolic function *sgn* (·). The proposed exponential reaching law is presented in **Eq. 26**.

$$\begin{cases} \dot{s}_d^+ = -\varepsilon_d^+ sat\left(s_d^+\right) - k_d^+ s_d^+ & \varepsilon_d^+ > 0, k_d^+ > 0 \\ \dot{s}_d^+ = -\varepsilon_d^+ sat\left(s_d^+\right) - k_d^+ s_d^+ & \varepsilon_q^+ > 0, k_q^+ > 0 \end{cases} \tag{26}$$

Here in **Eq. 26** ε_d^+, $\varepsilon_{\mathrm{q}}^+$, $k_{\ d}^+$, $\mathrm{k}_{\mathrm{q}}^+$ are the reaching law parameters and they are all positive. This ensures the product of the sliding face s and its derivative $\dot{s}$ to be negative, and the sliding mode control requirements can be satisfied.

The saturated function *sat* (·) is shown in **Eq. 27**, which gives the system a boundary layer Δ. The exponential reaching law is applied outside the boundary layer. Thus the tracking error can be reduced fast. When it comes into the boundary layer, the linear approach law is applied to slow down the reaching speed and the chattering phenomenon can be reduced.

$$sat(x) = \begin{cases} 1 & x > \Delta \\ kx & |x| \le \Delta, \quad k = \dfrac{1}{\Delta} \\ -1 & x < -\Delta \end{cases} \tag{27}$$

The general passive sliding mode controller of the positive sequence system can be derived as **Eq. 28** by combining **Eq. 21**, **Eq. 25**, and **Eq. 26**.

$$\begin{cases} v_{dref}^+ = v_{gd}^+ - \omega L i_q^+ + R i_{dref}^+ - \dfrac{R_a L\left(\varepsilon_d^+ sat\left(s_d^+\right) + k_d^+ s_d^+\right)}{k_{pd}^+ (R_a + R) - k_{id}^+ L} \\ v_{qref}^+ = v_{gq}^+ + \omega L i_d^+ + R i_{qref}^+ - \dfrac{R_a L\left(\varepsilon_q^+ sat\left(s_q^+\right) + k_q^+ s_q^+\right)}{k_{pq}^+ (R_a + R) - k_{iq}^+ L} \end{cases} \tag{28}$$

The stability of the passive sliding mode controller can be proved by selecting as^2 ($a > 0$) as the energy function according to the Lyapunov stability theory.

The passive sliding mode controllers mentioned above serve as the inner current loop in the dual-loop control strategy. The output power is controlled by the outer loop. Power calculation for output power control is shown as **Eq. 29** in the grid voltage vector oriented dq frame.

$$\begin{cases} P = \dfrac{3}{2} v_d^+ i_d^+ \\ Q = -\dfrac{3}{2} v_q^+ i_q^+ \end{cases} \tag{29}$$

Active and reactive power related controls are decoupled according to **Eq. 29**. The inner d component current i_{d} loop provides active power related control abilities. The inner q component current i_{q} loop provides reactive power related control abilities. As shown in **Figure 3**, the main control target of the shunt side of MMC-UPFC contains two main parts. One is the DC voltage control which provides a stable DC bus voltage V_{dc} with i_{d} current loop while the other is the reactive power control with the i_{q} current loop. They provide the AC voltage reference v_{jdiff} together. Thus the reference values of each bridge arm v_{jpref} and v_{jnref} are calculated by **Eq. 30** according to **Eq. 3**.

$$\begin{cases} v_{jpref} = v_{jcomref} - v_{jdiffref} \\ v_{jnref} = v_{jcomref} + v_{jdiffref} \end{cases} \tag{30}$$

PASSIVE SLIDING MODE CONTROL FOR UNBALANCED GRID TREATMENT

Unbalanced grid condition is a common power quality problem in the modern power system. The unbalanced grid phasors can be resolved into three sets of sequence components according to the method of symmetrical components. They are positive sequence components, negative sequence components, and zero sequence components. The zero sequence components in the power grid can be eliminated by choosing the proper transformer connection method. Thus, the negative sequence components are the main problem to be dealt with in the unbalanced condition treatment.

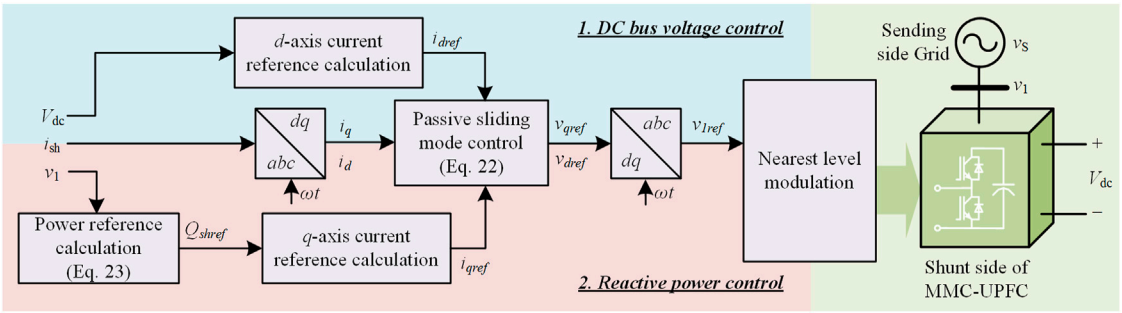

FIGURE 3 | General control diagram of the shunt side of MMC-UPFC.

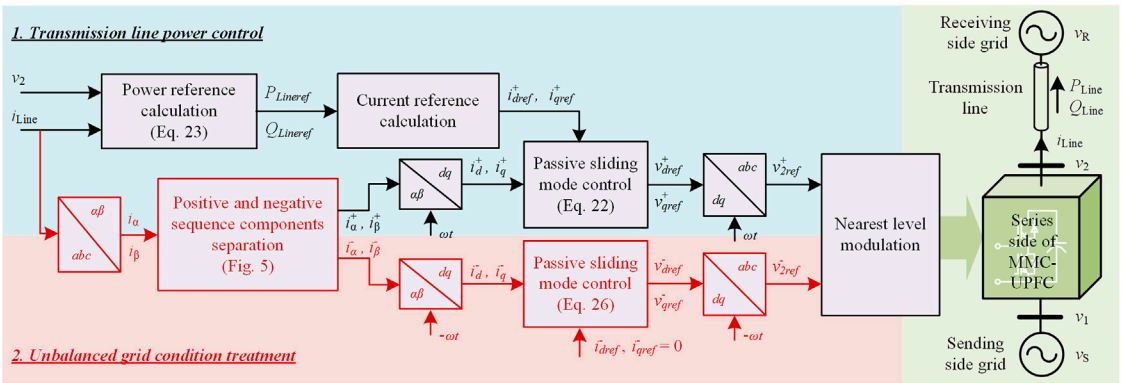

FIGURE 4 | General control diagram of the series side of MMC-UPFC with unbalanced grid condition treatment strategy.

The shunt side of UPFC performs as a current source and it is suitable for unbalanced local load compensation which has been well discussed in the existing works. A typical UPFC consists of two back-to-back connected converters and the series side of UPFC can deal with the unbalanced condition in the power grid networks such as unbalanced grid voltage and unbalanced line impedance as well.

Controller Design for Modular Multilevel Converter-Unified Power Flow Controller With Unbalanced Grid Condition Treatment Strategy

The general treatment strategy is to provide negative sequence voltages by the series side of MMC-UPFC and compensate the negative components of the grid voltage so that the transmission line current can return to symmetry. Thus, the negative component controller is needed besides the regular control discussed in the previous section.

A detailed control diagram of the series side is shown in **Figure 4** with unbalanced grid treatment. As shown in the red part, the control diagram of the series side has an additional negative sequence control loop which provides unbalanced grid condition treatment besides the similar power control loop in **Figure 3**.

A cross-decoupling positive and negative components separation method is proposed with the second-order generalized integrator (SOGI) firstly as shown in **Figure 5**. The positive and negative sequence components can be separated precisely. The positive sequence components help to control the transmission line power while the negative sequence components are to be eliminated according to the unbalanced grid condition treatment strategy.

According to the negative sequence mathematic model given in **Eq. 8**, the model of the negative sequence passive controller in the *dq* frame can be derived as **Eq. 31**.

$$\begin{cases} v_d^- = v_{gd}^- + \omega L i_q^- + R i_{dref}^- - R_a^-\left(i_d^- - i_{dref}^-\right) \\ v_q^- = v_{gq}^- - \omega L i_d^- + R i_{qref}^- - R_a^-\left(i_q^- - i_{qref}^-\right) \end{cases} \tag{31}$$

Combining the sliding mode control strategy to improve the performance of system parameter variation, the passive sliding mode control law of the negative sequence system is deduced in **Eq. 32**.

$$\begin{cases} v_{dref}^- = v_{gd}^- + \omega L i_q^- + R i_{dref}^- - \dfrac{R_a L\left(\varepsilon_d^- sat\left(s_d^-\right) + k_d^- s_d^-\right)}{k_{pd}^-\left(R_a + R\right) - k_{id}^- L} \\ v_{qref}^- = v_{gq}^- - \omega L i_d^- + R i_{qref}^- - \dfrac{R_a L\left(\varepsilon_q^- sat\left(s_q^-\right) + k_q^- s_q^-\right)}{k_{pq}^-\left(R_a + R\right) - k_{iq}^- L} \end{cases} \tag{32}$$

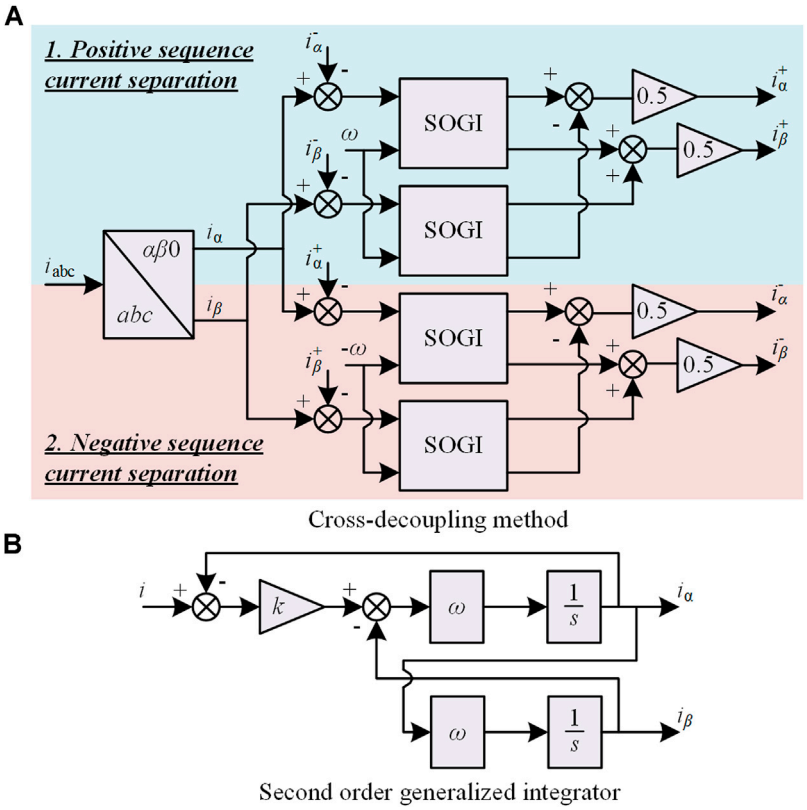

FIGURE 5 | Positive and negative sequence separation method with SOGI.

Power Flow Regulating Range Change of Modular Multilevel Converter-Unified Power Flow Controller With Unbalanced Grid Condition Treatment Strategy

The power flow through the transmission line is regulated by the series side of MMC-UPFC. The natural power flow without the inserted voltage by MMC-UPFC can be calculated by **Eq. 33**.

$$\begin{cases} P_{Line0} = \dfrac{\omega L_{Line} F_1(\varphi_R) + R_{Line} F_2(\varphi_R)}{R_{Line}^2 + (\omega L_{Line})^2} \\ Q_{Line0} = \dfrac{R_{Line} F_1(\varphi_R) - \omega L_{Line} F_2(\varphi_R)}{R_{Line}^2 + (\omega L_{Line})^2} \end{cases} \tag{33}$$

Here in **Eq. 33**, F_1 (φ_R) and F_2 (φ_R) are as follows.

$$\begin{cases} F_1(\varphi_R) = -V_1 V_R \sin\varphi_R \\ F_2(\varphi_R) = V_1^2 - V_1 V_R \cos\varphi_R \end{cases} \tag{34}$$

After the MMC-UPFC is enabled, the new power flow can be calculated by **Eq. 35**.

$$\begin{cases} P_{Line1} = \dfrac{\omega L_{Line} H_1(\varphi_{UPFC}) + R_{Line} H_2(\varphi_{UPFC})}{R_{Line}^2 + (\omega L_{Line})^2} \\ Q_{Line1} = \dfrac{R_{Line} H_1(\varphi_{UPFC}) - \omega L_{Line} H_2(\varphi_{UPFC})}{R_{Line}^2 + (\omega L_{Line})^2} \end{cases} \tag{35}$$

Here in **Eq. 35**, H_1 (φ_{UPFC}) and H_2 (φ_{UPFC}) are as follows.

$$\begin{cases} H_1(\varphi_{UPFC}) = V_{UPFC} V_R \sin(\varphi_R - \varphi_{UPFC}) - V_1 V_R \sin\varphi_R \\ H_2(\varphi_{UPFC}) = V_1^2 + V_{UPFC}^2 + 2V_1 V_{UPFC} \cos\varphi_{UPFC} \\ \qquad\qquad - V_{UPFC} V_R \cos(\varphi_R - \varphi_{UPFC}) - V_1 V_R \cos\varphi_R \end{cases} \tag{36}$$

The power flow change with the inserted $\dot{V}_{UPFC}$ in **Figure 1** can be calculated by **Eq. 37**.

$$\begin{cases} \Delta P_{Line} = P_{Line1} - P_{Line0} = \dfrac{\omega L_{Line} T_1(\varphi_{UPFC}) + R_{Line} T_2(\varphi_{UPFC})}{R_{Line}^2 + (\omega L_{Line})^2} \\ \Delta Q_{Line} = Q_{Line1} - Q_{Line0} = \dfrac{R_{Line} T_1(\varphi_{UPFC}) - \omega L_{Line} T_2(\varphi_{UPFC})}{R_{Line}^2 + (\omega L_{Line})^2} \end{cases} \tag{37}$$

Here in **Eq. 37**, T_1 (φ_{UPFC}) and T_2 (φ_{UPFC}) are as follows.

$$\begin{cases} T_1(\varphi_{UPFC}) = V_{UPFC} V_R \sin(\varphi_R - \varphi_{UPFC}) \\ T_2(\varphi_{UPFC}) = V_{UPFC}^2 + 2V_1 V_{UPFC} \cos\varphi_{UPFC} \\ \qquad\qquad - V_{UPFC} V_R \cos(\varphi_R - \varphi_{UPFC}) \end{cases} \tag{38}$$

If the resistive component R_{Line} is neglected, **Eq. 37** can be simplified as **Eq. 39**.

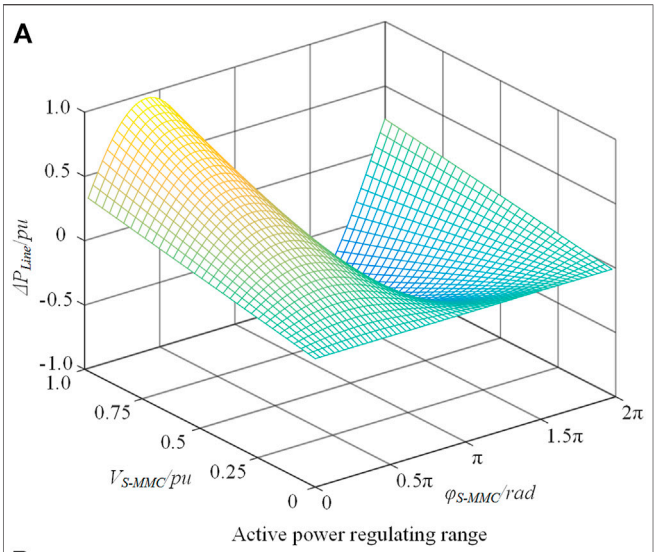

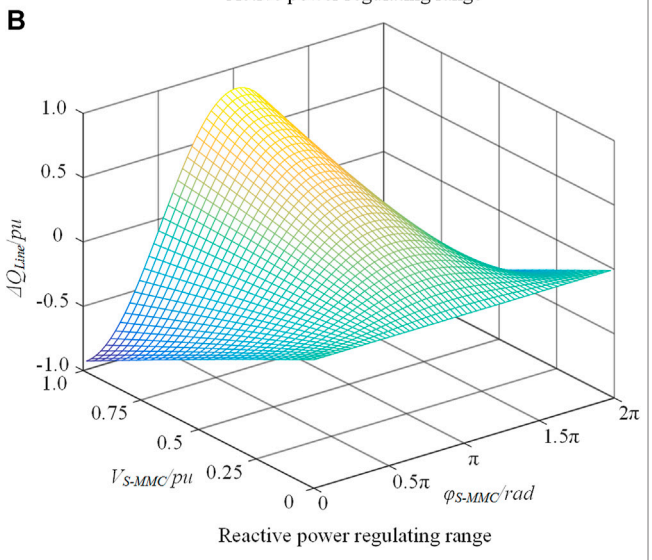

FIGURE 6 | Ideal power flow regulating range in balanced power grid.

$$\begin{cases} \Delta P_{Line} = \dfrac{V_{UPFC} V_R \sin(\varphi_R - \varphi_{UPFC})}{\omega L_{Line}} \\ \Delta Q_{Line} = \dfrac{V_{UPFC}(V_R \cos(\varphi_R - \varphi_{UPFC}) - 2V_1 \cos\varphi_{UPFC} - V_{UPFC})}{\omega L_{Line}} \end{cases} \tag{39}$$

The power calculation equations in **Eq. 39** have similar structures to the power formulae of the high voltage power grid, but the variation of the active power and reactive power flow are not decoupled. This is because both V_{UPFC} and φ_{UPFC} can be regulated widely and freely. The ideal power flow regulating range without an unbalanced grid treatment strategy is shown in **Figure 6**.

Due to the inserted negative sequence voltages for unbalanced grid compensation, the output voltages of the series side of MMC-UPFC are unbalanced as well. The general phasor diagram of

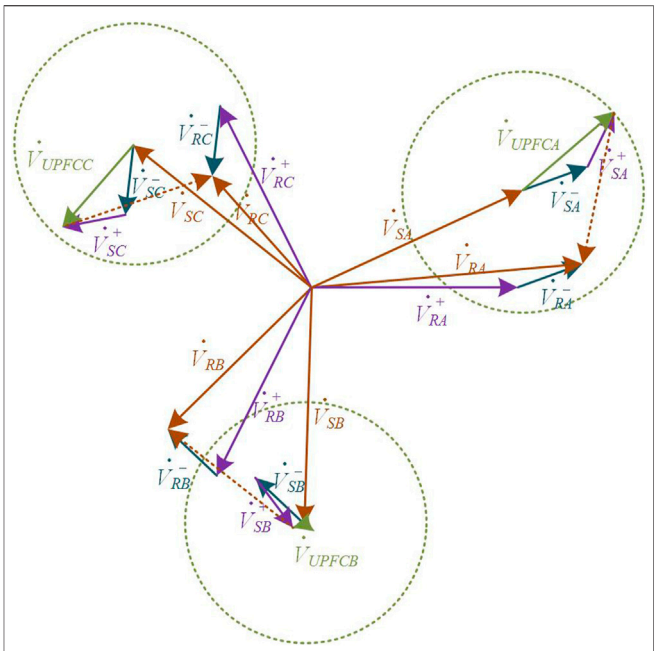

FIGURE 7 | Phasor diagram of UPFC with unbalanced grid condition treatment.

UPFC with unbalanced grid condition treatment is shown in **Figure 7**.

Here in **Figure 7**, the brown solid lines are the sending and receiving side grid voltages V_{S} and V_{R}, respectively. The receiving side voltages $V_{\mathrm{RA/B/C}}$ are unbalanced, and they can be solved to the positive and negative components of $V_{\mathrm{RA/B/C}}$, which are represented by purple and dark green arrows, respectively. The negative components bring unbalanced transmission line currents. The output voltages $V_{\mathrm{UPFCA/B/C}}$ of MMC-UPFC are represented by light green arrows, and they can be solved to the positive and negative components as well. The negative components $V_{\mathrm{SA/B/C}}^{-}$ of UPFC compensate the receiving side negative sequence voltages $V_{\mathrm{RA/B/C}}^{-}$. The positive components $V_{\mathrm{SA/B/C}}^{+}$ of UPFC provides active power flow control.

The insert voltage amplitude range of the MMC-UPFC is shown as the light green circle in **Figure 7**. The positive sequence voltage of UPFC cannot reach the boundary from the start point with the same amplitude freely as that in the balanced grid condition. Thus, the power flow regulating range is influenced by the negative sequence voltage. The additional voltage limit control in **Figure 7** is necessary, and the power flow regulating range is narrowed down accordingly.

SIMULATION RESULTS

A 27-level MMC-UPFC simulation system, based on the recent UPFC project in Shanghai of China, is built in MATLAB/Simulink to verify the proposed control strategy. The main circuit is the same as **Figure 1**. The specific parameters of the system are shown in **Table 1**.

TABLE 1 | Parameters of the simulation system.

System parameters	Value
Rated power of transmission line	400 MW
Rated power of MMC-UPFC	50 (×2) MW
Rated grid voltage	220 kV
Rated AC voltage of MMC-UPFC	19.2 kV
Rated current of MMC-UPFC	1.5 kA
Rated voltage on DC-side of MMC-UPFC	±20.8 kV
Shunt-side transformer ratio	220/19.2 (u_k = 5%)
Series-side transformer ratio	19.2/6.5 (u_k = 5%)
Bridge arm impedance	0.4 + j2.2Ω
Submodule capacitance	10 mF
Submodule capacitor voltage	1.6 kV
Number of bridge arm submodules	26

TABLE 2 | Power references in different time period.

Time (s)	0.2–0.6	0.6–0.7	0.7–0.9	0.9–1.2	1.2–1.5	1.5–2.0
Pref (MW)	350	300	270	370	330	330
Qref (Mvar)	50	20	30	30	0	100

The general power flow control performance of MMC-UPFC is given in this section firstly. Then the performance of unbalanced grid treatment is presented. Two scenarios are discussed separately. One is the unbalanced grid voltages while the other is the asymmetrical transmission lines. Simulation results verify the proposed control strategy and treatment strategy.

Performance of Modular Multilevel Converter-Unified Power Flow Controller With the Proposed Passive Sliding Mode Control Strategy

Simulation results of the steady and dynamic state performances of the proposed P-SMC strategy are presented in this part and then compared with the traditional PI controller to verify the performance improvement of the proposed control strategy.

Steady and Dynamic Performance of Passive-Sliding Mode Control

According to the parameters given in **Table 1**, the initial power flow without UPFC is approximately 327 + j51MVA. During the time from 0.2 to 2 s, the active power and reactive power are set as different values. The power references at different times are provided in **Table 2**.

The performance of MMC-UPFC with the proposed passive sliding mode control strategy during power flow regulation is shown in **Figure 8**.

At the series side of MMC-UPFC: The output active and reactive power follow the power references well as shown in **Figure 8A**. The dynamic response at 0.9 s is provided in **Figures 8B,C**. The inserted voltages by the series side of MMC-UPFC respond to the change of power reference immediately as shown in

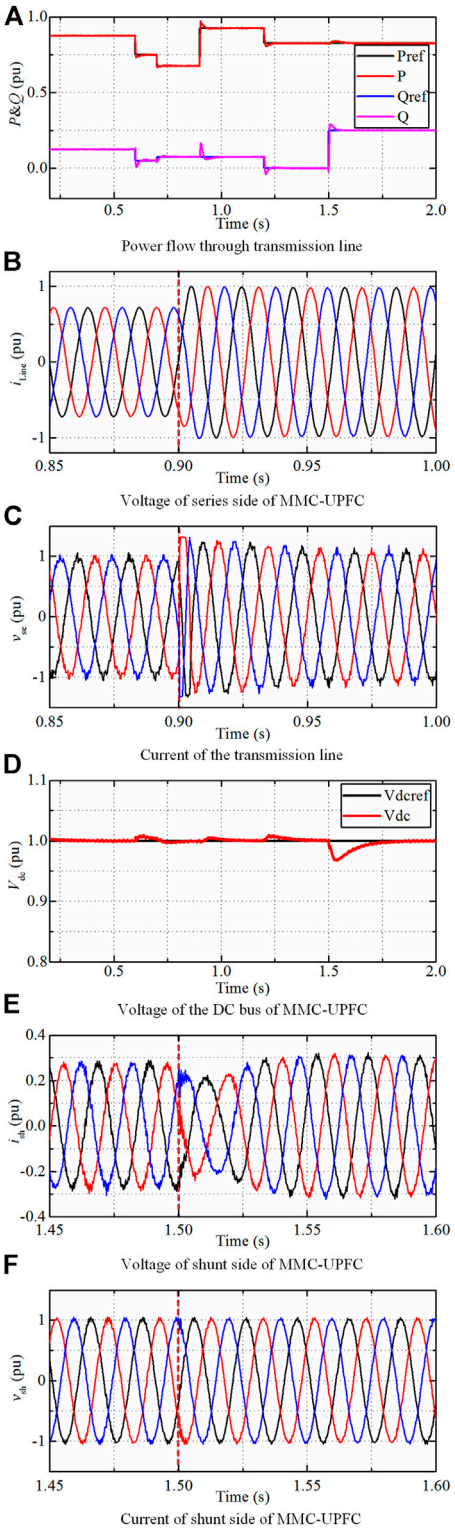

FIGURE 8 | Simulation results of the proposed passive-sliding mode control strategy.

TABLE 3 | Main control parameters.

Outer power control loop	
Active power	kp = 0.05, ki = 50
Reactive power	kp = 0.1, ki = 100
Inner current loop	
Traditional PI controller	d-axis: kp = 100, ki = 10,000 q-axis: kp = 200, ki = 20,000
Proposed P-SMC controller	Injected damping: Ra = 100 Integral sliding surface: kp = 5, ki = 10 Reaching law: Δ = 0.1, ε = 100, k = 1,000

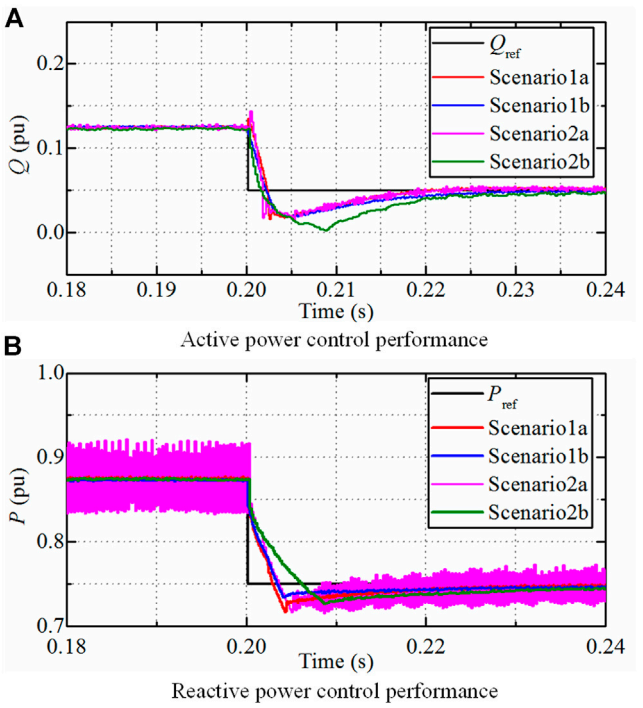

FIGURE 9 | Treatment strategy performance under unbalanced grid voltage.

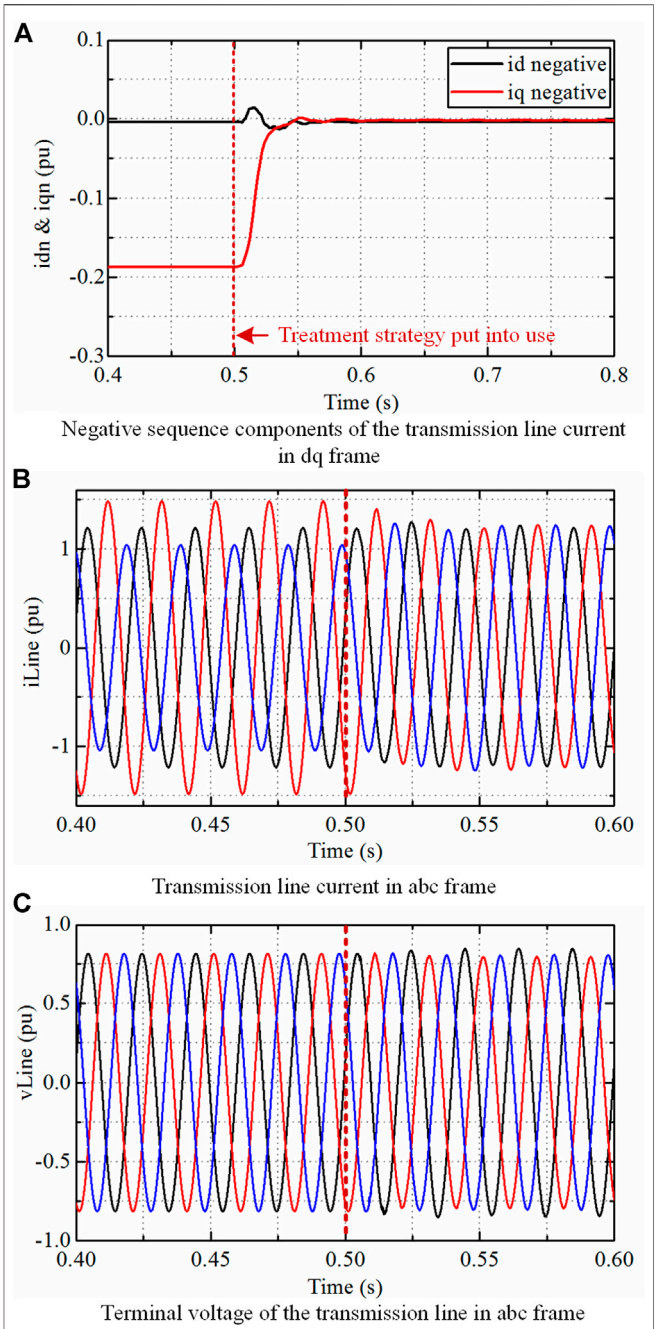

FIGURE 10 | Treatment strategy performance under unbalanced grid voltage condition.

Figure 8B. The transmission line current is changed accordingly in **Figure 8C** to regulate the transmission line power.

At the shunt side of MMC-UPFC: The dynamic response at 1.5 s is provided in **Figures 8D–F**. The voltage of the DC bus is maintained stable as shown in **Figure 8D** due to the shunt side of MMC-UPFC whose dynamic responses are provided in **Figures 8E,F**.

The power flow through the transmission line follows the reference values well due to the regulation by the series side of MMC-UPFC. The DC link voltage maintains stable due to the regulation by the shunt side of MMC-UPFC. The proposed passive sliding mode control strategy is validated by the simulation results.

Dynamic Performance Comparison Between Traditional PI Control and Proposed Passive-Sliding Mode Control

In this scenario, the grid impedance fluctuation and control delay are considered disturbing items. The power flow control performances are presented. The same PI controllers are adopted in the outer power control loop while the inner current loops with PI controller and P-SMC controller are adopted respectively. Main control parameters are provided in **Table 3**.

The *P* and *Q* reference values are changed from 0.875/0.125 to 0.75/0.05 at 0.20 s. The performance comparison is provided in **Figure 9**. The meaning of each scenario are:

Scenario 1: 10^{-4}s control delay and normal transmission line impedance. **1)** PI control; **2)** P-SMC.
Scenario 2: 2×10^{-4}s control delay and 0.9 times as normal transmission line impedance. **1)** PI control; **2)** P-SMC.

The control parameters are designed and optimized for scenario 1. As can be seen in **Figure 9**, the proposed P-SMC has similar dynamic performance with PI controller in scenario 1, and both control strategies have fast and precise dynamic performances. However, when the system parameters change in scenario 2, the P-SMC performance is still fast and precise while the PI control results are fluctuating with the same control parameters scenario 1 and 2.

The comparison results show that the proposed P-SMC provides fast and robust performances than traditional PI controllers when facing system disturbances.

Performance of the Proposed Unbalanced Grid Treatment Strategy

Simulation results of MMC-UPFC under unbalanced grid voltage conditions and asymmetrical line conditions are presented in this part to verify the proposed treatment strategy.

Treatment Performance Under Unbalanced Grid Voltage Condition

In this scenario, the negative sequence voltages with the amplitude of 0.04 pu are added at the receiving side grid. The unbalanced grid treatment strategy is put into use at 0.5 s. The whole process of unbalanced condition treatment of MMC-UPFC is shown in **Figure 10**.

The transmission line current is asymmetrical before the unbalanced treatment strategy is enabled at 0.5 s. The negative sequence voltages are separated precisely by the proposed cross-decoupling method with SOGI. The negative sequence components of transmission line current are reduced to nearly zero as shown in **Figure 10A**. The unbalance factor of line currents is reduced from about 36 to 0.7% quickly. The terminal voltages of the transmission line in **Figure 10C** are asymmetrical from 0.5 s due to the inserted negative sequence voltage from the series side of MMC-UPFC. Simulation results in this scenario well validate the proposed unbalanced treatment strategy.

Treatment Performance Under Asymmetrical Line Condition

In this scenario, the transmission line between the sending side grid and the receiving side grid is set to be asymmetrical. The transmission line impedance of Phase A is 1.1 times that of Phase B and C. The whole process of unbalanced condition treatment of MMC-UPFC is shown in **Figure 11**.

The transmission line current is asymmetrical before the unbalanced treatment strategy is enabled. The negative sequence voltages are separated precisely by the proposed cross-decoupling method with SOGI. The negative sequence components of transmission line current are reduced to nearly zero and the unbalance factor of currents is reduced from about 16 to 0.5% quickly. The terminal voltages of the transmission line are slightly asymmetrical from 0.5 s due to the inserted negative sequence voltage from the series side of MMC-UPFC. Simulation results in this scenario well validate the proposed unbalanced treatment strategy.

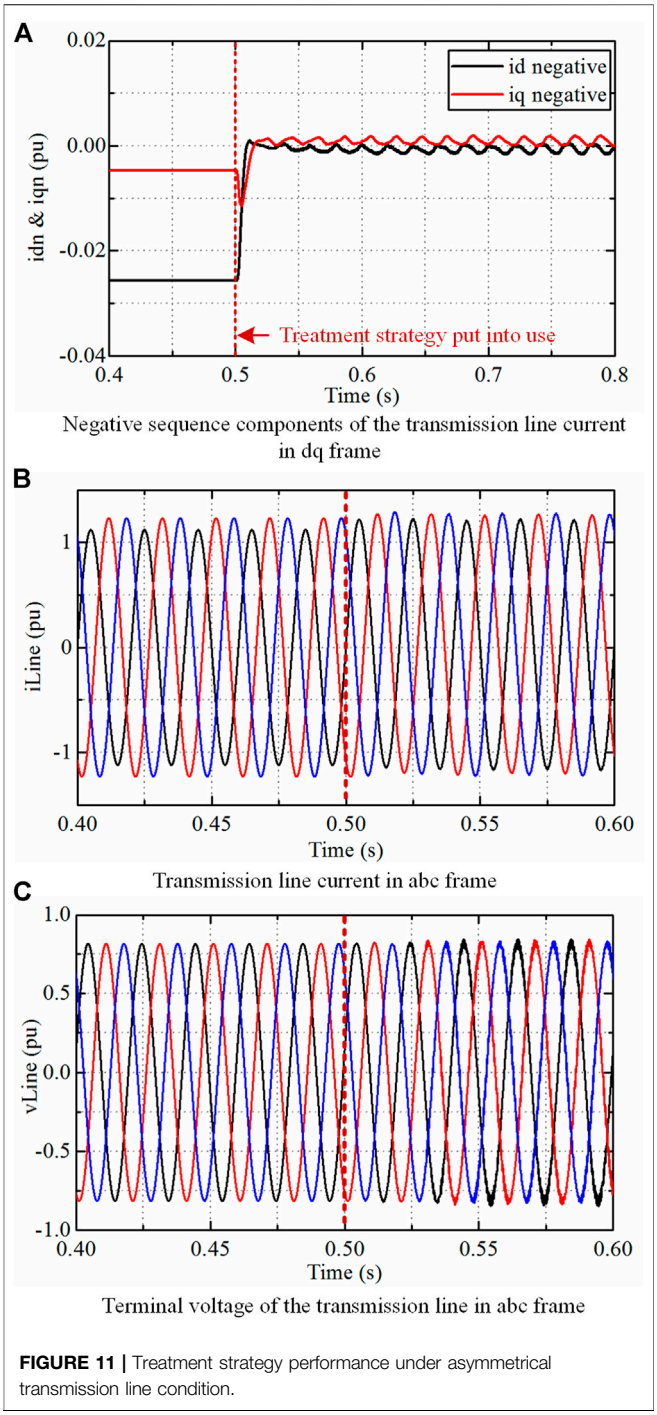

FIGURE 11 | Treatment strategy performance under asymmetrical transmission line condition.

CONCLUSION

A passive sliding mode control strategy is proposed and discussed in this paper providing fast and precise control for MMC-UPFC.

The unbalanced grid condition treatment strategy for distribution networks is then proposed with the series side of MMC-UPFC. The proposed approach is validated by simulation results based on a 27 level MMC-UPFC. Conclusions are drawn as below.

1) The detailed passive sliding mode controller of the MMC-UPFC design from the energy attributes system provides fast, precise, and robust transmission line power flow control and enables more control flexibility for the smart grid.
2) The proposed unbalanced grid condition treatment strategy with the series side of MMC-UPFC reduces line current unbalance factor and improves power quality effectively. The adoption of the series side of MMC-UPFC in the treatment strategy increases the efficiency of the whole device.
3) The deduced power flow regulating range changing due to the unbalanced grid treatment leads to the additional voltage limit control and enables the high operation quality of MMC-UPFC.

DATA AVAILABILITY STATEMENT

The original contributions presented in the study are included in the article/Supplementary Material, further inquiries can be directed to the corresponding author.

AUTHOR CONTRIBUTIONS

YC: analysis, modeling, method, verification and writing. HW and ML: conceptualization and methodology. JM: simulation and verification. MZ and XC: advising, supervision, writing-reviewing and editing.

FUNDING

This work was supported by the Program of Shanghai Academic Research Leader (19XD1422000).

REFERENCES

Ahmed, T., Waqar, A., Elavarasan, R. M., Imtiaz, J., Premkumar, M., and Subramaniam, U. (2021). Analysis of Fractional Order Sliding Mode Control in a D-STATCOM Integrated Power Distribution System. *IEEE Access* 9, 70337–70352. doi:10.1109/ACCESS.2021.3078608

Akagi, H. (2017). Multilevel Converters: Fundamental Circuits and Systems. *Proc. IEEE* 105 (11), 2048–2065. doi:10.1109/JPROC.2017.2682105

Akter, S., Biswal, S., Rathore, N. S., Das, P., and Abdelaziz, A. Y. (2020). Amplitude Based Directional Relaying Scheme for UPFC Compensated Line during Single Pole Tripping. *Electric Power Syst. Res.* 184, 106290. doi:10.1016/j.epsr.2020.106290

Chatterjee, B., and Debnath, S. (2020). Sequence Component Based Approach for Fault Discrimination and Fault Location Estimation in UPFC Compensated Transmission Line. *Electric Power Syst. Res.* 180, 106155. doi:10.1016/j.epsr.2019.106155

Feng, F., Yu, J., Dai, W., Yang, Z., Zhao, X., Kamel, S., et al. (2021). Operational Reliability Model of Hybrid MMC Considering Multiple Time Scales and Multi-State Submodule. *J. Mod. Power Syst. Clean Energ.* 9, 648–656. doi:10.35833/MPCE.2019.000227

Feng, X., Tao, Y., Cui, X., Shao, K., and Wang, Y. (2020). Sliding Mode and Predictive Current Control Strategy of the Three-phase Vienna Rectifier. *J. Power Electron.* 20, 743–753. doi:10.1007/s43236-020-00055-1

Guo, P., He, Z., Yue, Y., Xu, Q., Huang, X., Chen, Y., et al. (2019). A Novel Two-Stage Model Predictive Control for Modular Multilevel Converter with Reduced Computation. *IEEE Trans. Ind. Electron.* 66 (3), 2410–2422. doi:10.1109/TIE.2018.2868312

Gyugyi, L., Schauder, C. D., Williams, S. L., Rietman, T. R., Torgerson, D. R., and Edris, A. (1995). The Unified Power Flow Controller: a New Approach to Power Transmission Control. *IEEE Trans. Power Deliv.* 10 (2), 1085–1097. doi:10.1109/61.400878

Hao, Q., Man, J., Gao, F., and Guan, M. (2018). Voltage Limit Control of Modular Multilevel Converter Based Unified Power Flow Controller under Unbalanced Grid Conditions. *IEEE Trans. Power Deliv.* 33 (3), 1319–1327. doi:10.1109/TPWRD.2017.2736562

Haque, M. M., Ali, M. S., Wolfs, P., and Blaabjerg, F. (2020). A UPFC for Voltage Regulation in LV Distribution Feeders with a DC-Link Ripple Voltage Suppression Technique. *IEEE Trans. Ind. Applicat.* 56 (6), 6857–6870. doi:10.1109/TIA.2020.3023068

Ke, S., Zhu, M., Chen, Y., Zheng, C., and Hu, C. (2019). Passive Sliding Mode Variable Structure Control for MMC-UPFC. Proceedings of the 2019 IEEE Innovative Smart Grid Technologies-Asia, Chengdu, China, May 21, 2019. ISGT Asia, 2184–2189. doi:10.1109/ISGT-Asia.2019.8881777

Kryonidis, G. C., Malamaki, K.-N. D., Gkavanoudis, S. I., Oureilidis, K. O., Kontis, E. O., Mauricio, J. M., et al. (2021). Distributed Reactive Power Control Scheme for the Voltage Regulation of Unbalanced LV Grids. *IEEE Trans. Sustain. Energ.* 12 (2), 1301–1310. doi:10.1109/TSTE.2020.3042855

Li, J., Konstantinou, G., Wickramasinghe, H. R., and Pou, J. (2019). Operation and Control Methods of Modular Multilevel Converters in Unbalanced AC Grids: A Review. *IEEE J. Emerg. Sel. Top. Power Electron.* 7 (2), 1258–1271. doi:10.1109/JESTPE.2018.2856505

Li, J., Konstantinou, G., Wickramasinghe, H. R., Townsend, C. D., and Pou, J. (2020). Capacitor Voltage Reduction in Modular Multilevel Converters under Grid Voltages Unbalances. *IEEE Trans. Power Deliv.* 35 (1), 160–170. doi:10.1109/TPWRD.2019.2919788

Li, P., Lin, J., Kong, X., and Wang, Y. (2016). Application of MMC-UPFC and its Performance Analysis in Nanjing Western Grid. Proceedings of the 2016 IEEE PES Asia-Pacific Power and Energy Engineering Conference, Xian, China, October 25, 2016. APPEEC), 2601–2605. doi:10.1109/APPEEC.2016.7779960

Ma, F., Zhu, Z., Min, J., Yue, Y., and He, X. (2019). Model Analysis and Sliding Mode Current Controller for Multilevel Railway Power Conditioner under the V/v Traction System. *IEEE Trans. Power Electron.* 34 (2), 1243–1253. doi:10.1109/TPEL.2018.2835570

Mi, Y., Song, Y., Fu, Y., and Wang, C. (2020). The Adaptive Sliding Mode Reactive Power Control Strategy for Wind-Diesel Power System Based on Sliding Mode Observer. *IEEE Trans. Sustain. Energ.* 11 (4), 2241–2251. doi:10.1109/TSTE.2019.2952142

Peng, F. Z. (2017). Flexible AC Transmission Systems (FACTS) and Resilient AC Distribution Systems (RACDS) in Smart Grid. *Proc. IEEE* 105 (11), 2099–2115. doi:10.1109/JPROC.2017.2714022

Ramirez, D., Zarei, M. E., Gupta, M., and Serrano, J. (2020). Fast Model-Based Predictive Control (FMPC) for Grid Connected Modular Multilevel Converters (MMC). *Int. J. Electr. Power Energ. Syst.* 119, 105951. doi:10.1016/j.ijepes.2020.105951

Santos, N. M. R., Silva, J. F., Verveckken, J., Pires, V. M. F., and Castro, R. M. G. (2014). Enhancing the Ride-Through Capability of DC-link Voltage in NPC Multilevel Unified Power-Flow Controllers. *IEEE Trans. Power Deliv.* 29 (4), 1542–1550. doi:10.1109/TPWRD.2014.2326774

Shang, L., Hu, J., Yuan, X., and Huang, Y. (2019). Improved Virtual Synchronous Control for Grid-Connected VSCs under Grid Voltage Unbalanced Conditions. *J. Mod. Power Syst. Clean. Energ.* 7 (1), 174–185. doi:10.1007/s40565-018-0388-2

Stefanov, P. C., and Stankovic, A. M. (2002). Modeling of UPFC Operation under Unbalanced Conditions with Dynamic Phasors. *IEEE Trans. Power Syst.* 17 (2), 395–403. doi:10.1109/TPWRS.2002.1007909

Tummala, A. S. L. V., Inapakurthi, R., and Ramanarao, P. V. (2018). Observer Based Sliding Mode Frequency Control for Multi-Machine Power Systems with

High Renewable Energy. *J. Mod. Power Syst. Clean. Energ.* 6 (3), 473–481. doi:10.1007/s40565-017-0363-3

Wang, J., Tang, Y., and Liu, X. (2020). Arm Current Balancing Control for Modular Multilevel Converters under Unbalanced Grid Conditions. *IEEE Trans. Power Electron.* 35 (3), 2467–2479. doi:10.1109/TPEL.2019.2932003

Yang, B., Jiang, L., Yu, T., Shu, H. C., Zhang, C.-K., Yao, W., et al. (2018). Passive Control Design for Multi-Terminal VSC-HVDC Systems via Energy Shaping. *Int. J. Electr. Power Energ. Syst.* 98, 496–508. doi:10.1016/j.ijepes.2017.12.028

Yang, Q., Ding, T., He, H., Chen, X., Tao, F., Zhou, Z., et al. (2020). Model Predictive Control of MMC-UPFC under Unbalanced Grid Conditions. *Int. J. Electr. Power Energ. Syst.* 117, 105637. doi:10.1016/j.ijepes.2019.105637

Yang, Q., Saeedifard, M., and Perez, M. A. (2019). Sliding Mode Control of the Modular Multilevel Converter. *IEEE Trans. Ind. Electron.* 66 (2), 887–897. doi:10.1109/TIE.2018.2818657

Conflict of Interest: The authors declare that the research was conducted in the absence of any commercial or financial relationships that could be construed as a potential conflict of interest.

frontiers in Energy Research

METHODS
published: 29 July 2021
doi: 10.3389/fenrg.2021.718151

Multi-Energy Flow Calculation Considering the Convexification Network Constraints for the Integrated Energy System

*Danlei Chen and Xiaoqing Bai **

Key Laboratory of Power System Optimization and Energy Saving Technology, Guangxi University, Nanning, China

To alleviate environmental pollution and improve the energy efficiency of end-user utilization, the integrated energy systems (IESs) have become an important direction of energy structure adjustment over the world. The widespread application of the coupling units, such as gas-fired generators, gas-fired boilers, and combined heat and power (CHP), increases the connection among electrical, natural gas, and heating systems in IESs. This study proposes a mixed-integer nonlinear programming (MINLP) model combining electrical, natural gas, and heating systems, as well as the coupling components, such as CHP and gas-fired generators. The proposed model is applicable for either the radial multi-energy network or the meshed multi-energy network. Since the proposed MINLP model is difficult to be solved, the second-order cone and linearized techniques are used to transform the non-convex fundamental matrix formulation of multi-energy network equations to a mixed-integer convex multi-energy flow model, which can improve the computational efficiency significantly. Moreover, the potential convergence problem of the original model can also be avoided. A simulation of IEEE 14-node electrical system, 6-node natural gas system, and 23-node heating system are studied to verify the accuracy and computational rapidity of the proposed method.

Keywords: combined heat and power, convexification, coupling units, integrated energy systems, multi-energy flow

OPEN ACCESS

Edited by:
Jiawei Wang,
Technical University of Denmark, Denmark

Reviewed by:
Yayu Peng,
Electric Power Research Institute (EPRI), United States
Guifu Du,
Soochow University, China

***Correspondence:**
Xiaoqing Bai
baixq@gxu.edu.cn

Specialty section:
This article was submitted to Smart Grids, a section of the journal Frontiers in Energy Research

Received: *31 May 2021*
Accepted: *25 June 2021*
Published: *29 July 2021*

Citation:
Chen D and Bai X (2021) Multi-Energy Flow Calculation Considering the Convexification Network Constraints for the Integrated Energy System. Front. Energy Res. 9:718151. doi: 10.3389/fenrg.2021.718151

INTRODUCTION

With the rapid development of the economy, energy and environmental problems have become increasingly prominent. How to achieve clean and efficient use of energy has become the focus of research in recent years. The integrated energy system (IES) (Jia et al., 2015; OMalley and Kroposki, 2013) incorporates the production, transmission, distribution, conversion, storage, and consumption of many kinds of energy; can realize the comprehensive management and economic dispatching of electricity, heat, gas, *etc.*; and provides an essential solution for learning the total utilization of energy. The energy efficiency of natural gas–based combined heat and power (CHP) units (Yang et al., 2010) is more than 80%. It is an efficient and environmentally friendly energy supply mode and has become an integral coupling unit among electric, gas, and heating networks. Under the IES, all kinds of energy conversion equipment, such as CHP, gas turbine, and gas boiler, make electricity, heat, and nature closely coupled and realize the interaction and conversion of multi-energy. The integrated energy system recognizes the exchange and transformation of thermal/electric/gas energy, but the

coupling of the three energy sources has dramatically changed the system's trend. How to effectively calculate the distribution of multi-energy flow (multi-energy flow, MEF) (Pan et al., 2016) is of great significance to guide the investment planning and operation decision of IESs.

At present, aiming at the problems related to MEF, the research at home and abroad is mainly focused on the joint analysis of electricity/gas or electricity/heat energy networks. In the study by Zhang (2005), a sequential solution of hybrid power flow is proposed by combining the existing natural gas hydraulic calculation method with the power system power flow calculation method, and the energy concentrator model is established in the study by Geidl and Andersson (2007), Arnold et al. (2008), Geidl (2007). The centralized optimization algorithm and distributed optimization algorithm are used to solve the electric/gas hybrid optimal power flow, respectively.

From the point of view of the reliability of energy supply, the transmission delay and compressibility of natural gas are considered, and the optimal short-term operation of the electricity/gas coupling system is studied in reference Correa-Posada and Sanchez-Martin (2015). In reference Gu et al. (2015), an optimization model of the electro-thermal energy integrated system considering the constraints of power network and thermal network is established, and the benefit of wind power heating is studied. The research significance, application prospect, and critical technologies of the electric heating combined system with large capacity heat storage are reviewed in reference Xu et al. (2014). Considering the internal coupling of MEF, the decomposition algorithm of electric/thermal/gas hybrid optimal power flow based on energy hub is proposed in reference Moeini-Aghtaie et al. (2014), Shabanpour-Haghighi and Seifi (2015), but the method cannot guarantee the optimal global solution. In reference Xu et al. (2015), a hierarchical energy management model of the regionally integrated energy system is established by considering timescale and network constraints, but the consideration of thermal part is limited to adjustable heat load.

The above research shows that MEF computing under IESs has been widely concerned, but there are still the following problems:

1) Most of the research objects are electricity/gas systems or electricity/thermal systems, and there is a lack of research on electricity/gas/thermal interconnection systems.
2 In the steady natural flow model, the velocity at the inlet and outlet of the gas pipeline is the same, and there is a quadratic Weymouth function relationship between the velocity of the natural gas pipeline and the pressure difference of the gas pipeline. However, the Weymouth equation is non-convex and nonlinear, which brings difficulties to the MEF calculation.
3) The original heating network power flow equation is a nonlinear equation. The coupling relationship between temperature and flow is strong and contains an exponential equation, making the computational complexity high so that the numerical stability is difficult to be guaranteed.
4) At present, the research on IESs is mainly focused on the distribution of energy in the system, and there is a lack of research on the coupling interaction of electricity/heat/gas systems.

TABLE 1 | Different node types with their known and unknown variables.

System type	Node type	Known	Unknown
Electric system	Slack	V,θ	P,Q
	PQ	P,Q	V,θ
	PV	P,V	Q,θ
Heat system1	Slack	T_s	T_r,ϕ,m
	ϕT_s	T_s,ϕ	T_r,m
	ϕT_r	T_r,ϕ	T_s,m
Natural gas system	Slack	π	f
	Load (source)	f	π

In order to solve the above problems, the MEF calculation method of IESs with electricity, heat, and gas is studied in this article. First, the modeling of many kinds of electro-thermal coupling units such as CHP and the gas turbine is studied, and the mathematical models of subsystems and coupling links in IESs are established, and the Weymouth equation is linearized reasonably by making use of the characteristic of short pipeline in the natural gas network. The traditional method of solving power flow in a power system is improved to establish a model which is easier to solve. As for the heating system, a method based on Taylor's second-order expansion is implemented to avoid the nonlinear equation in this article. Considering different operation modes of CHP units, two models of cogeneration are established, including the backpressure model and the pumping model. On this basis, the multi-energy flow solution model of the joint electric/heating/gas network is established, and the practicability and rapidity of the method proposed in this article are proven by practical examples.

SYSTEM MODELING

The integrated energy system with electricity, gas, and heat is composed of a power system, thermal system, natural gas systems, and the coupling units such as CHP, gas turbine, and gas boilers.

The power system mainly includes generator, electric load, and transmission line; the thermal system mainly comprises a heat source, heat load, supply, and reflux pipeline; and the natural gas system includes explicitly gas source, gas load, and gas transmission pipeline.

The classification and variables of each system node are shown in **Table 1**.

For electrical networks, P, Q, V, and θ are the active power, reactive power, voltage amplitude, and phase angle of the power system nodes, respectively. In the natural gas network, f and π are the natural gas injection flow and pressure of the nodes, respectively. T_s, T_r, ϕ, and m are the supply temperature,

reflux temperature, heat power, and water flow of the heat source or heat load of the thermal system, respectively.

Heating Network

The steady-state power flow calculation model of the heating network is divided into two parts: hydraulic model and thermodynamic model (Liu, 2013).

Hydraulic Model

The flow of hot water in the network should meet the fundamental law of the network: the flow of each pipeline should satisfy the flow continuity equation at each node, that is, the injection flow at the node is equal to the outflow; in a closed-loop composed of pipes, the sum of the head loss of water flowing in each pipeline is 0, that is,

$$\begin{cases} A_s m = m_q \\ B_h h_f = 0 \end{cases}, \tag{1}$$

where A_s is the node-branch correlation matrix of the heating network, m is the flow of each pipeline, m_q is the flow out of each node, B_h is the loop-branch correlation matrix of the heating network, h_f is the head loss vector, and its calculation method is as follows:

$$h_f = Km|m|, \tag{2}$$

where K is the resistance coefficient matrix of the pipeline.

Thermodynamic Model

For each heat load node, the heating temperature T_s represents the temperature before the hot water is injected into the load node, the output temperature T_o represents the temperature when the hot water flows out of the load node, and the heat recovery temperature T_r represents the temperature after the hot water from the load node is mixed with the water of other pipes at the pipe node.

The thermodynamic model is as follows:

$$\Phi = C_p m_q (T_s - T_o), \tag{3}$$

$$T_{end} = (T_{start} - T_a) e^{-\frac{\lambda L}{C_p m}} + T_a, \tag{4}$$

$$\left(\sum m_{out}\right) T_{out} = \sum m_{in} T_{in}. \tag{5}$$

Equation 3 is the expression of the node thermal power Φ of the thermal network, and C_p is the specific heat capacity of water; **Eq. 4** represents the relationship between the temperature at the end of the pipe T_{end} and the temperature T_{start} at the beginning, T_a is the ambient temperature, λ is the heat conduction coefficient of the pipe, and L is the length of the pipe; **Eq. 5** represents the temperature relationship before and after the hot water is mixed at the node, and $m_{out}, T_{out}, m_{in}, T_{in}$ represent the flow rate and temperature of the water flowing out and into the pipe, respectively.

Natural Gas Network

A natural gas system can be specified by several equations related to various elements of this system, including pipelines, compressors, sources, and loads. The input–output flow balance of each node should be considered for a feasible operational condition. The amount of gas flow through a pipeline connected between nodes i and j in standard cubic meter per hour (SCM/h) can be expressed by (De Wolf and Smeers, 2000) the following:

$$f_{ij} = C_{ij} sign(\pi_i, \pi_j) \left[sign(\pi_i, \pi_j) * (\pi_i^2 - \pi_j^2) \right]^{0.5}, \tag{6}$$

$$C_{ij} = 96.074830 \times 10^{-15} \frac{D_{ij}}{\lambda_{ij} z T L_{ij} \delta}, \tag{7}$$

$$\lambda_{ij} = \left[2 \log\left(\frac{3.7 D_{ij}}{\varepsilon_g} \right) \right]^{-2}, \tag{8}$$

where π_i and π_j are pressures at the nodes i and j, respectively. $sign(\pi_i, \pi_j)$ is a sign function of pressures where its value is +1 if $\pi_i > \pi_j$ and −1 otherwise. The pipeline constant can be computed by **Eq. 7**, where z is the gas compressibility factor, T is the gas temperature, and δ is the density of gas relative to air. D_{ij} and L_{ij} are the interior diameter and length of the pipeline, respectively. λ_{ij} is the friction factor of the gas pipeline. It is computed by **Eq. 8**, where ε_g is absolute rigidity of the pipe.

The node flow balance equation of the natural gas network is as follows:

$$\Delta f = f_l - f_s + \sum f_{ij}, \tag{9}$$

where f_l is the natural gas flow consumed by the natural gas load, including gas turbine, gas boiler, CHP, and conventional natural gas load. For the compressor inlet node, it should also include the compressor outlet flow, that is, the compressor outlet flow as the load of the inlet node, f_s is the injection flow of the gas source, and $\sum f_{ij}$ is the flow of all non-compressor branches connected with the node.

Electric Network

The power system model adopts the AC system model, and the electric load of the heating system and the natural gas system is taken into account. The balance equation of active power and reactive power is as follows:

$$\Delta P = P^G - P^l - \mathrm{Re}\{U (YU)^*\}, \tag{10}$$

$$\Delta Q = Q^G - Q^l - \mathrm{Im}\{U (YU)^*\}, \tag{11}$$

where P^G and Q^G are the active power and reactive power generated by the generator, respectively; P^l and Q^l are the active power and reactive power consumed by the load in the electric network, respectively.

Coupling Units

The coupling units of electricity, gas, and heat integrated energy systems mainly include CHP, gas boiler, gas turbine, electric compressor, and water pump.

CHP is the main coupling unit in electric, gas, and thermal systems. CHP is a kind of unit which not only generates electricity by a steam turbine but also supplies heat to thermal users by steam after power generation. The ratio of heat generation power to electricity generation power of CHP with gas turbine and reciprocating internal combustion engine in prime mover can be

regarded as a constant, and the ratio of heat to electricity can be expressed as follows:

$$c_m = \phi_{CHP}/P_{CHP}, \tag{12}$$

where P_{CHP} and ϕ_{CHP} are the power generated and thermal power of CHP, respectively, and c_m is the thermoelectric ratio of CHP.

According to the working mode, CHP can be divided into back pressure type and pumping type. The heat-power ratio of the back pressure CHP unit is constant, while the extraction–condensation CHP unit changes the heat-power ratio of the CHP unit by adjusting the amount of steam extracted, and its output is mainly related to the natural gas flow consumed, that is,

$$f_{CHP} = \frac{P_{CHP}}{q_{gas}\eta_e} + \frac{\phi_{CHP}}{q_{gas}\eta_h}, \tag{13}$$

where f_{CHP} is the natural gas flow consumed by CHP and q_{gas} is the calorific value of natural gas. η_e and η_h represent the power generation efficiency and heat generation efficiency of CHP, respectively.

The gas turbine is the equipment that consumes natural gas to generate electric energy. The relationship models between the consumed natural gas flow and the generated power are as follows:

$$f_G = a_G + b_G\phi_G + c_G\phi_G^2, \tag{14}$$

where f_G is the natural gas flow consumed by the gas turbine, P_G is the electric power generated by the gas turbine, and a_G, b_G, and c_G are consumption coefficients of the gas turbine.

MEF Model

Based on the above, an IES-oriented MEF model is constructed as follows:

$$F(x) = \begin{Bmatrix} \triangle P \\ \triangle Q \\ \triangle \Phi \\ \triangle p \\ \triangle T_s \\ \triangle T_r \\ \triangle f \end{Bmatrix} = \begin{cases} \Delta P = P^G - P^L - \mathrm{Re}\{U(YU)^*\} \\ \Delta Q = Q^G - Q^L - \mathrm{Im}\{U(YU)^*\} \\ C_p A_s m(T_s - T_o) - \Phi = 0 \\ B_h K m|m| = 0 \\ C_s T_{s,load} - b_s = 0 \\ C_r T_{r,load} - b_r = 0 \\ f_l - f_s + \sum f_{ij} = 0 \end{cases}. \tag{15}$$

In **Eq. 15**, the first row and the second row represent the active power deviation and reactive power deviation of the power system, respectively. The third to the sixth lines represent the node thermal power deviation of the thermal system, the pressure drop deviation of the heating network loop, the heating temperature deviation, and the regenerative temperature deviation, respectively. The seventh line represents the node flow deviation of the natural gas system. P^G, Q^G, Φ, and f_l are the active power, reactive power, thermal power, and natural gas load given by the system, respectively. P^L and Q^L are the total active load and reactive load, respectively. A_s is the incidence matrixes of the heating network. C_s and C_r are matrices related to the structure and flow of heating network and regenerative network, respectively, while b_s and b_r are column vectors related to heating temperature and output temperature, respectively.

It is worth noting that the power balance equation of power network includes trigonometric function, the flow balance equation of gas network involves non-convex nonlinear pipeline flow equation, and the heat network temperature balance equation includes exponential equation so that the IES-oriented MEF model is a non-convex nonlinear problem, which makes it difficult for us to solve MEF directly with traditional methods, and the calculation accuracy is difficult to be guaranteed.

Therefore, in this article, the convex optimization of the non-convex nonlinear equations will be carried out below, which can not only ensure accuracy but also greatly simplify the calculation process and shorten the calculation time.

CALCULATION METHOD OF MULTI-ENERGY FLOW IN INTEGRATED ENERGY SYSTEMS

Electric Network

Rectangular Formulation

Let Y denote the nodal admittance matrix, which has components $Y_{ij} = G_{ij} + iB_{ij}$ for each line. The complex voltage (also called voltage phasor) V_i at bus i can be expressed in the rectangular form as $V_i = e_i + if_i$.

With the above notation, the power flow conservation at each bus is given in the so-called rectangular formulation as follows:

$$P_i^G - P_i^l = G_{ii}\left(e_i^2 + f_i^2\right) + \sum_{j\epsilon\delta(i)} G_{ij}\left(e_i e_j + f_i f_j\right) - \sum_{j\epsilon\delta(i)} B_{ij}\left(e_i f_j - f_i e_j\right), \tag{16}$$

$$Q_i^G - Q_i^l = -B_{ii}\left(e_i^2 + f_i^2\right) + \sum_{j\epsilon\delta(i)} B_{ij}\left(e_i e_j + f_i f_j\right) - \sum_{j\epsilon\delta(i)} G_{ij}\left(e_i f_j - f_i e_j\right). \tag{17}$$

Generation and voltage bounds at each bus are as follows:

$$\left(V_i^{\min}\right)^2 \le e_i^2 + f_i^2 \le \left(V_i^{\max}\right)^2. \tag{18}$$

$$P_i^{\max} \le P_i^G \le P_i^{\max}, \tag{19}$$

$$Q_i^{\max} \le Q_i^G \le Q_i^{\max}. \tag{20}$$

Here, P_i^l, Q_i^l is the summary of all kinds of active and reactive load in the electric system.

Second-Order Cone Program Relaxation of Alternative Formulation

Note that the rectangular formulation of AC power flow is a non-convex quadratic optimization problem. However, quite importantly, we can observe that all the nonlinearity and non-convexity come from one of the following three forms: (1) $e_i^2 + f_i^2 = |V_i|^2$, (2) $e_i e_j + f_i f_j = |V_i||V_j|\cos(\theta_i - \theta_j)$, and (3) $e_i f_j - f_i e_j = -|V_i||V_j|\sin(\theta_i - \theta_j)$. To capture this nonlinearity, we define new variables C, S to get rid of the variable e and variable f (Kocuk et al., 2016). The new variables are defined as follows:

$$C_{ii} = e_i^2 + f_i^2, \tag{21}$$

$$C_{ij} = e_i e_j + f_i f_j, \tag{22}$$

$$S_{ij} = e_i f_j - e_j f_i. \tag{23}$$

With a change of variables, we can introduce an alternative formulation of the power flow problem in the electric system as follows:

$$P_i^G - P_i^l = G_{ii}(C_{ii}) + \sum_{j\in\delta(i)} G_{ij}(C_{ij}) - \sum_{j\in\delta(i)} B_{ij}(S_{ij}), \tag{24}$$

$$Q_i^G - Q_i^l = -B_{ii}(C_{ii}) - \sum_{j\in\delta(i)} B_{ij}(C_{ij}) - \sum_{j\in\delta(i)} G_{ij}(S_{ij}), \tag{25}$$

$$(V_i^{\min})^2 \le C_{ii} \le (V_i^{\max})^2, \tag{26}$$

$$C_{ij}^2 + S_{ij}^2 = C_{ii} C_{jj}, \tag{27}$$

$$C_{ij} = C_{ji}, \tag{28}$$

$$S_{ij} = -S_{ji}. \tag{29}$$

Through the above transformation, we convex the original Cartesian coordinate **Eqs 16–20** into **Eqs 24–29**, which is more convenient to solve.

Natural Gas Network

The original Weymouth equation, which represents the relationship between the natural gas flow with the pressure at the inlet and the outlet of a natural gas pipeline, is a non-convex and nonlinear problem and hard to solve directly. Two approximation methods are used to linearize the Weymouth equation.

Method ①: One-dimensional approximation.

From **Eq. 6**, it can be found that the right side of **Eq. 6** is a function of π_i^2 and π_j^2. By introducing variables $\varphi_i = \pi_i^2$ and $\varphi_j = \pi_j^2$, **Eq. 6** can be replaced with (Zhou, 2020) the following:

$$f_{ij} = \mathrm{sgn}(\varphi_{ij}) C_{ij} \sqrt{|\varphi_{ij}|}, \tag{30}$$

$$\varphi_{ij} = \varphi_i - \varphi_j. \tag{31}$$

In addition, the node pressure constraint can also be replaced with the following:

$$(\pi_i^{\min})^2 \le \varphi_i \le (\pi_i^{\max})^2, \tag{32}$$

$$(\pi_j^{\min})^2 \le \varphi_j \le (\pi_j^{\max})^2. \tag{33}$$

It can be seen that constraint **Eq. 30** is a one-dimensional nonlinear equation, which greatly simplifies the linearization process. The upper and lower limits of φ_{ij} can be determined by the following formula:

$$\varphi_{ij}^{\max} = (\pi_i^{\max})^2 - (\pi_j^{\min})^2, \tag{34}$$

$$\varphi_{ij}^{\min} = (\pi_i^{\min})^2 - (\pi_j^{\max})^2. \tag{35}$$

The range $[\varphi_{ij}^{\min}, \varphi_{ij}^{\max}]$ φ_{ij} can be divided into N_{ij} segments, and the nonlinear **Eq. 30** can be transformed into **Eqs. 36–39**:

$$\varphi_{ij} = \varphi_{ij0} + \sum_{p=1}^{N_{ij}} \sigma_{ij,p}. \tag{36}$$

$$f_{ij} = f_{ij0} + \sum_{p=1}^{N_{ij}} K_p^{ij} \sigma_{ij,p}, \tag{37}$$

$$z_{ij,p+1} \cdot \left(\overline{\varphi_{ij,p}} - \underline{\varphi_{ij,p}}\right) \le \sigma_{ij,p}, \tag{38}$$

$$\sigma_{ij,p} \le z_{ij,p} \cdot \left(\overline{\varphi_{ij,p}} - \underline{\varphi_{ij,p}}\right), \tag{39}$$

where p is the one-dimensional piecewise linear segment number index, $z_{ij,p}$ is the binary variable used in the one-dimensional linear approximation method, and K_p^{ij} is the constant of the one-dimensional linear equation.

Method ②: Taylor expansion approximation.

We linearize **Eq. 6** by Taylor expansion (Manshadi and Khodayar, 2015) as follows:

$$f_{ij} = C_{ij}\left(\pi_i \pi_i^0 - \pi_j \pi_j^0\right) \Big/ \sqrt{\left|(\pi_i^0)^2 - (\pi_j^0)^2\right|}, \tag{40}$$

where π_i^0 is the initial pressure value of the node i at the beginning of the optimization period and is a known quantity.

The linearization using the Taylor series is valid only if the difference in natural gas pressure between the inlet and outlet of the pipeline is assumed to be limited, that is, there is no significant pressure drop in the pipeline.

This is a reasonable assumption for the short pipelines used in microgrids. The limitation on the node pressure on the gas pipeline network guarantees the accuracy of the approximation. The Weymouth equation is linearized around the initial point procured by solving optimal energy flow within the microgrid considering no disruptions.

By Method ①, we replace the non-convex and nonlinear pipeline **Eqs 6–9** with the linear model consisting of **Eqs 36–39**. By Method ②, we transform the original Weymouth **Eq. 6** into the linear model of **Eq. 40**. Both of them are mature methods and help to solve the problem quickly.

Heating Network

The heating network model studied in this article is the radiant heat network model. The original heating network power flow in **Eqs 1–5** is a nonlinear equation. The coupling relationship between temperature and flow is strong and contains an exponential equation, making the computational complexity high so that the numerical stability is difficult to be guaranteed.

Therefore, this study adopts the method (Sun et al., 2020) based on Taylor's second-order expansion; the specific contents are as follows:

To get the flow m_i of the pipe i in **Figure 1**, we define $n_1 = m_1/m_i$, $n_2 = m_2/m_i \cdots n_{i-1} = m_{i-1}/m_i, n_i = 1$; thus,

$$\frac{T_s - T_o}{T_s - T_a} m_i^2 - \left[\frac{\frac{\lambda_1 L_1}{n_1} + \frac{\lambda_2 L_2}{n_2} + \cdots + \frac{\lambda_i L_i}{n_i}}{C_p} + \frac{\phi_i}{C_p (T_s - T_a)}\right] \times m_i + \frac{\left(\frac{\lambda_1 L_1}{n_1} + \frac{\lambda_2 L_2}{n_2} + \cdots + \frac{\lambda_i L_i}{n_i}\right)^2}{2C_P^2} = 0. \tag{41}$$

When calculating $n_1 n_2, \cdots, n_{i-1}$, the heat loss of the pipe network is ignored, and the heat energy flowing through the pipe i is set to φ_i. While to figure the pipe flow m_i into the load node, we set $n_1 \approx \frac{C_p m_1 T_1}{C_p m_i T_i} = \frac{\varphi_1}{\varphi_i}$, $n_2 \approx \frac{C_p m_2 T_2}{C_p m_i T_i} = \frac{\varphi_2}{\varphi_i} \cdots n_k \approx \frac{C_p m_k T_k}{C_p m_i T_i} = \frac{\varphi_k}{\varphi_i}$ as the temperature change of the water supply network node is small. k is

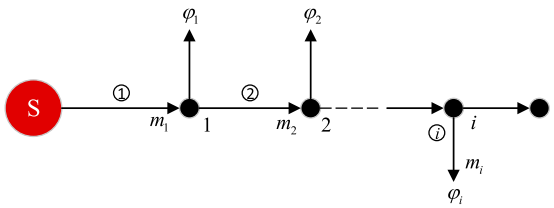

FIGURE 1 | A radial district heating network of multiple nodes.

the number of the pipe through which the flow m_i flows and φ_k is the heat energy flowing through the pipe k. Thus, we can define

$$A = \frac{T_s - T_o}{T_s - T_a}; C = \frac{\left(\frac{\lambda_1 L_1}{n_1} + \frac{\lambda_2 L_2}{n_2} + \cdots + \frac{\lambda_i L_i}{n_i}\right)^2}{2C_P^2},$$

$$B = -\left(\frac{\frac{\lambda_1 L_1}{n_1} + \frac{\lambda_2 L_2}{n_2} + \cdots + \frac{\lambda_i L_i}{n_i}}{C_p} + \frac{\phi_i}{C_p(T_s - T_a)}\right)$$

Then the **Eq. 42** can be simplified as follows:

$$Am_i^2 + Bm_i + C = 0. \quad (42)$$

The value of C is generally less than 10^{-4} orders of magnitude, then **formula (42)** can be approximated to

$$Am_i + B = 0. \quad (43)$$

In this article, we define **Eqs 42**, **Eqs 43** as model 2 and model 1, respectively.

The flow rate of each pipeline flowing into the load node can be calculated directly by **Eq. 42** or **Eq. 43**, and the supply temperature, return temperature, and pipe flow rate of each node of the heating network can be obtained according to **Eqs 1**, **3–5**.

Model 1 and model 2 decouple the water supply network and the backwater network, decouple the temperature and flow, the model is simple, the amount of calculation is small, and the derivation is based on Taylor's second-order expansion, and the solution accuracy is higher.

Through the above transformations and simplifications, the original MINLP (mixed-integer nonlinear programming) is reduced to a MICP (mixed-integer convex programming) problem, which can be effectively solved by commercial solvers.

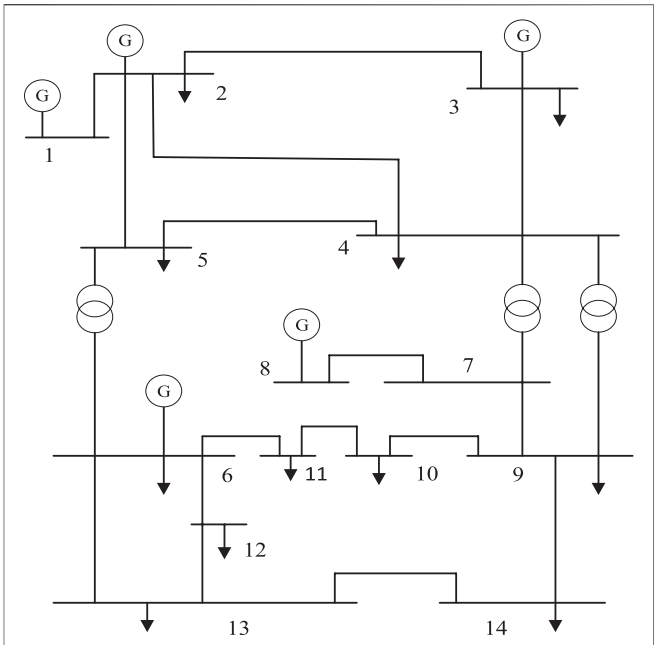

FIGURE 2 | IEEE standard 14 bus system.

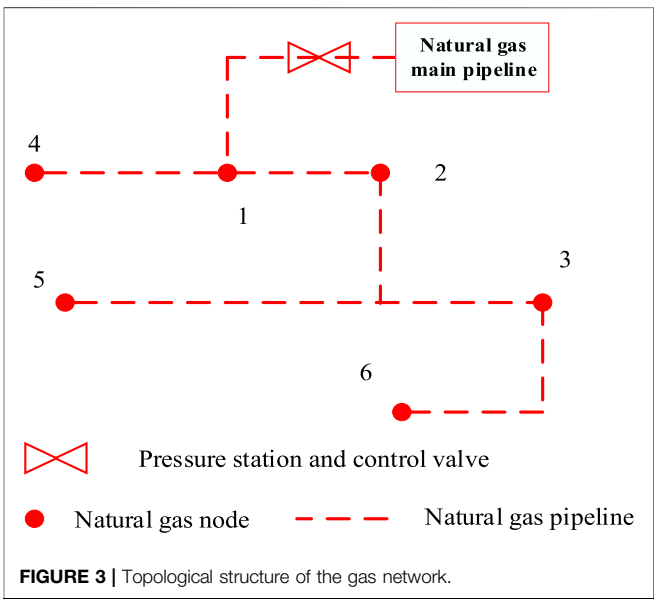

FIGURE 3 | Topological structure of the gas network.

CASE STUDIES AND ANALYSIS

Case Introduction

In the example of the integrated energy system used in this article, the power system is an IEEE standard 14-bus system (Kersting, 1991), as shown in **Figure 2**, in which the generator node is replaced by CHP. In order to match the capacity and power of CHP, the load is increased to 3.6 times, and the active load with a certain capacity is arranged at the balance node. The natural gas system is a 6-node system, and its line parameters refer to the study by Cong Liu et al. (2009).

The thermal system adopts the 23-node system in the reference Sun et al. (2020). The topological structure of each system is shown in **Figures 2–4**. In this article, the FMINCON solver is used to calculate the multi-energy flow in the MATLAB platform.

The coupling units between the power grid and the heating network mainly include the CHP units of each coupling node and the coupling unit of the power grid, the gas network includes the CHP of each coupling node and the gas turbine, and the coupling unit between the heat network and the gas network mainly includes the CHP of each coupling node. The connecting

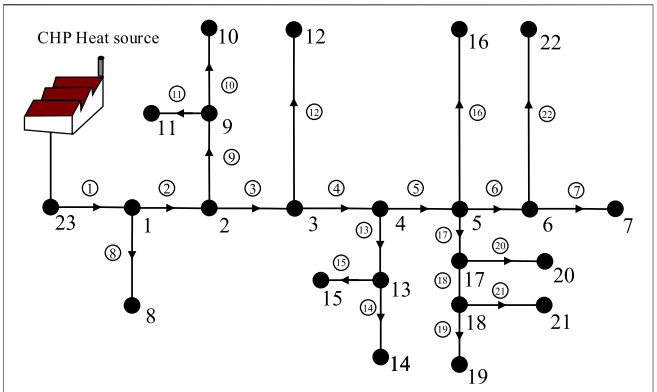

FIGURE 4 | Topological structure of the heating network.

TABLE 2 | Connecting nodes and types of coupling units.

Gas node	Electric node	Heating node	Coupling units
2	1	23	CHP
3	2	–	Gas turbine
5	6	–	Gas turbine

TABLE 3 | Parameters of CHP.

Model	Relationship	Parameters
I	$c_m = \phi_{CHP}/P_{CHP}$ $F_{CHP} = P_{CHP}/\eta_e$	$c_m = 0.6$ $\eta_e = 0.5$
II	$f_{CHP} = \frac{P_{CHP}}{q_{gas}\eta_e} + \frac{\phi_{CHP}}{q_{gas}\eta_h}$	$\eta_e = 0.5$ $\eta_h = 0.6$

nodes and types of coupling units in each network are shown in **Table 2**.

In the model of gas turbine, the model parameters of $a_G = c_G = 0, b_G = 167.1m^3/MWh$. In the model of CHP, this article considers two models: Model I is the pumping type, and Model II is the backpressure type. The parameters of CHP units are shown in **Table** 3.

Results and Analysis

In this study, we use two models to calculate the mass flow of each pipeline, water supply temperature, and return temperature of each node in the heating network. As is mentioned above, we define **Eq. 43** as Model 1 and **Eq. 42** as Model 2. Besides, we define Model 3, the control group, as the original model without linearization. The results of the heating network are shown in **Tables 4–6**.

In the process of solving, we find that the solving time of mode 1 and mode 2 is millisecond, while that of mode 3 is 21 s. In terms of solving time, the two models have the advantages of small amount of calculations and fast calculation speed.

From the above data, we can see that the maximum error of mass flow in Models 1 and 2 is 0.0058%, the maximum error of water supply temperature is 0.0075%, and return water is the same as that of Model 3. Both Models 1 and 2 have a high precision of solution. While it comes to each pipe's mass flow, Model 2 is more precise because the constant C has influence. Therefore, we use the results of Model 2 for the following calculation.

TABLE 4 | Mass flow rates of the models.

Flow (kg/s)				Error (%)	
Pipe number	**Model 1**	**Model 2**	**Model 3**	**Model 1**	**Model 2**
1	20.6611	20.6607	20.6607	0.0019	0
2	18.9458	18.9454	18.9454	0.0021	0
3	15.5065	15.5062	15.5062	0.0019	0
4	13.7888	13.7884	13.7884	0.0029	0
5	10.3437	10.3434	10.3434	0.0029	0
6	3.4499	3.4498	3.4498	0.0029	0
7	1.7268	1.7268	1.7268	0	0
8	1.7153	0.7153	0.7153	0	0
9	3.4393	3.4393	3.4393	0	0
10	1.7199	1.7199	1.7199	0	0
11	1.7194	1.7194	1.7194	0	0
12	1.7177	1.7177	1.7177	0	0
13	3.4451	3.4451	3.4451	0	0
14	1.723	1.723	1.723	0	0
15	1.7221	1.7221	1.7221	0	0
16	1.7195	1.7195	1.7194	0.0058	0.0058
17	5.1743	5.1741	5.1741	0.0039	0
18	3.4528	3.4527	3.4527	0.0029	0
19	1.7257	1.7256	1.7256	0.0058	0
20	1.7214	1.7214	1.7214	0	0
21	1.7271	1.7271	1.7271	0	0
22	1.7231	1.7231	1.7231	0	0

TABLE 5 | Water supply temperature and error of the models.

Node	T_s (°C)			Error (%)	
	Model 1	**Model 2**	**Model 3**	**Model 1**	**Model 2**
1	99.9665	99.9665	99.9666	0.0001	0.0001
2	99.929	99.929	99.9301	0.0011	0.0011
3	99.8864	99.8864	99.8871	0.0007	0.0007
4	99.8348	99.8348	99.8362	0.0014	0.0014
5	99.7681	99.7682	99.7695	0.0014	0.0013
6	99.6203	99.6203	99.6228	0.0025	0.0025
7	99.2364	99.2364	99.2389	0.0025	0.0025
8	99.7032	99.7032	99.7036	0.0004	0.0004
9	99.7978	99.7978	99.7989	0.0011	0.0011
10	99.5148	99.5148	99.5160	0.0012	0.0012
11	99.5362	99.5362	99.5370	0.0008	0.0008
12	99.6028	99.6028	99.6036	0.0008	0.0008
13	99.6635	99.6635	99.6030	0.0005	0.0005
14	99.3914	99.3914	99.3909	0.0005	0.0005
15	99.4266	99.4266	99.4280	0.0014	0.0014
16	99.5325	99.5325	99.5339	0.0014	0.0014
17	99.6893	99.6893	99.6912	0.0019	0.0019
18	99.5164	99.5164	99.5187	0.0023	0.0023
19	99.2823	99.2823	99.2845	0.0022	0.0022
20	99.4541	99.4541	99.4560	0.0019	0.0019
21	99.234	99.234	99.2266	0.0075	0.0075
22	99.3862	99.3862	99.3881	0.0019	0.0019
23	100	100	100	0	0

TABLE 6 | Water return temperature and error of the models.

Node	T_r (°C)			Error (%)	
	Model 1	Model 2	Model 3	Model 1	Model 2
1	29.8834	29.8834	29.8834	0	0
2	29.8862	29.8862	29.8862	0	0
3	29.8903	29.8903	29.8903	0	0
4	29.8958	29.8958	29.8958	0	0
5	29.9075	29.9075	29.9075	0	0
6	29.931	29.931	29.931	0	0
7	30	30	30	0	0
8	30	30	30	0	0
9	29.9393	29.9393	29.9393	0	0
10	30	30	30	0	0
11	30	30	30	0	0
12	30	30	30	0	0
13	29.9434	29.9434	29.9434	0	0
14	30	30	30	0	0
15	30	30	30	0	0
16	30	30	30	0	0
17	29.9177	29.9177	29.9177	0	0
18	29.9412	29.9412	29.9412	0	0
19	30	30	30	0	0
20	30	30	30	0	0
21	30	30	30	0	0
22	30	30	30	0	0
23	29.876	29.876	29.876	0	0

TABLE 7 | Four combinations.

Combination 1	Model I + method ①
Combination 2	Model II + method ①
Combination 3	Model I + method ②
Combination 4	Model II + method ②

the CHP unit runs in, there is a great difference between the results of Methods ① and ②, although the solving speed of both methods is in millisecond. The decisive factors of the accuracy of the two methods are different. Method ① depends on the number of segments and the value of constant K, while Method ② is only related to the initial value.

For Method ①, if we want to pursue accuracy, we need to divide more segments to achieve a higher degree of approximation. Still, at the same time, it also increases more unknowns and the amount of calculation, and the operation time becomes longer. Although Method ② is only suitable for networks with short pipeline length, it has a small amount of calculation. It involves fewer unknowns, while the natural gas network pipeline used in this study is shorter, so Method ② is more suitable for this study.

By comparing the results of combinations 1 and 2 and combinations 3 and 4, it can be seen that whichever method solving the gas system is adopted, power generated by the CHP unit is different between the two models. Model II generates more power than Model I, and at the same time, gas turbines generate less power in Model I than in Model II. Besides, when the operation mode of the CHP unit changes, the electric power generated by the CHP unit and the natural gas consumed change, which leads to the change of the power flow distribution of the power grid and the gas network, while in Model I, the electric power generated by the CHP unit depends on the thermal power generated by the CHP unit in the heating network. If the thermal power changes, the power flow distribution of the gas network, and the power grid will also be affected by it.

It can be seen that in the electric/thermal/gas integrated energy system, each network is connected into an inseparable whole through coupling units such as CHP and gas turbine, and the change of network state will affect the trend of other networks through the coupling unit.

TABLE 8 | Pressure of each node in the gas system.

Gas node	Pressure (Psig)			
	Combination 1	Combination 3	Combination 2	Combination 4
1	107.0915	109.6277	107.0289	109.0757
2	133.8886	129.5726	133.6266	131.1822
3	135.2396	129.6926	135.3875	131.966
4	137.1188	136.2581	140.8183	141.6308
5	149.556	149.2142	142.3953	143.202
6	158.1924	161.0799	161.0983	155.5046

This study considers two models of CHP units and two linearized methods of the gas network. We define the one-dimensional approximation method in the gas system as Method ① and the Taylor expansion approximation method as Method ②. So there are four running combinations in the following calculation, just as **Table 7** shows. The gas network and electric system results are shown in **Tables 8–12**, including pressure, mass flow, voltage amplitude, and voltage phase angle.

By comparing the results of combinations 1 and 3, and combinations 2 and 4, we can see that no matter which mode

CONCLUSION

To calculate the integrated energy system combined with electricity, gas, and heat more quickly and accurately, a comprehensive multi-energy flow calculation model based on convexification is proposed in this study. The model is established

TABLE 9 | Mass flow of each pipe in the gas system.

Pipeline	Flow (kcf/h)			
	Combination 1	Combination 2	Combination 3	Combination 4
2–1	4106.1	3529.9	4086.3	4066.7
4–2	1601.2	2311.5	2225.8	2288.8
5–2	2517.4	2489.9	1859.6	1946.7
5–3	2778.4	1849.2	2050.5	1783.7
6–5	2439.3	2321	3428.7	1544.3

TABLE 10 | Voltage amplitude of each node in the electric system.

Node	U			
	Combination 1	Combination 2	Combination 3	Combination 4
1	1.050461	0.942615	1.011018	0.996373
2	1.01848	1.059009	0.955131	1.0134
3	1.000828	0.995836	0.936912	0.997238
4	1.006891	0.956647	0.92582	1.002857
5	1.013993	1.016496	0.942598	0.992307
6	1.034163	0.995408	1.033986	1.004626
7	1.001988	0.978388	1.004413	1.002017
8	1.003753	1.006189	0.993287	0.999689
9	1.017289	1.040408	0.976217	0.992902
10	0.998618	0.972677	0.974783	1.008444
11	1.008466	1.009186	0.981983	0.993226
12	0.985091	1.003573	1.042348	1.003948
13	0.991417	0.992899	0.99246	0.992682
14	0.960597	1.001363	1.001352	1.003829

TABLE 11 | Voltage phase angle of each node in the electric system.

Node	Phase angle			
	Combination 1	Combination 2	Combination 3	Combination 4
1	0.839233	0.959958	0.923346	0.964182
2	0.432282	0.425692	0.479204	0.474099
3	−0.12441	−0.11958	−0.17326	−0.10111
4	0.071661	0.088176	0.06861	0.087963
5	0.180929	0.184882	0.192548	0.203757
6	−0.06562	−0.07068	−0.05942	−0.09531
7	−0.10884	−0.11696	−0.11851	−0.1062
8	−0.10884	−0.11696	−0.11851	−0.1062
9	−0.20458	−0.21788	−0.21355	−0.21123
10	−0.20352	−0.20288	−0.21466	−0.22847
11	−0.14784	−0.16606	−0.14369	−0.17439
12	−0.12905	−0.16711	−0.16322	−0.18651
13	−0.16112	−0.18464	−0.15612	−0.20356
14	−0.27028	−0.29596	−0.30276	−0.31702

TABLE 12 | Power generated by gas turbines and the CHP.

Coupling units	P (MW)			
	Combination 1	Combination 2	Combination 3	Combination 4
Gas turbine 1	0.742989	0.657478	0.858009	0.635194
Gas turbine 2	0.755985	0.701598	0.933628	0.51578
CHP	10.0983	10.9330	10.0983	10.9545

according to the different characteristics of electricity, heat, and gas networks. The natural gas network pipeline model is linearized reasonably, which greatly reduces the complexity of the model. In the heat network, two kinds of radiant heat network models that can be solved quickly are established, and the original model is transformed into the problem of solving univariate first-order equation and univariate quadratic equation, respectively; the amount of calculation of which is small, and the calculation speed is fast without any convergence problem. Considering the backpressure type and the pumping type of CHP, four running combinations combined with two models of CHP and two methods of the gas system have been established. Finally, the simulation results show that the algorithm can complete the convergence quickly, proving the algorithm's rapidity and practicability. In addition, the algorithm used in this study takes into account the interaction between different networks, which can quickly get the distribution of the comprehensive power flow of the system.

DATA AVAILABILITY STATEMENT

The original contributions presented in the study are included in the article/Supplementary Material; further inquiries can be directed to the corresponding author.

AUTHOR CONTRIBUTIONS

XB provided the overall idea. DC built the model and completed calculation of the article under the guidance of XB.

REFERENCES

Arnold, M., et al. (2008). *First International Conference on Infrastructure Systems & Services: Building Networks for A Brighter Future*, 1–6.Distributed Control Applied to Combined Electricity and Natural Gas Infrastructures.

Cong Liu, C., Shahidehpourau, M., Yong Fu, fnm., and Zuyi Li, fnm. (2009). Security-constrained Unit Commitment with Natural Gas Transmission Constraints. *IEEE Trans. Power Syst.* 24(3), 1523–1536. doi:10.1109/tpwrs.2009.2023262

Correa-Posada, C. M., and Sanchez-Martin, P. (2015). Integrated Power and Natural Gas Model for Energy Adequacy in Short-Term Operation. *IEEE Trans. Power Syst.* 30 (6), 3347–3355. doi:10.1109/tpwrs.2014.2372013

De Wolf, D., and Smeers, Y. (2000). The Gas Transmission Problem Solved by an Extension of the Simplex Algorithm. *Manag. Sci.* 46 (11), 1454–1465. doi:10.1287/mnsc.46.11.1454.12087

Geidl, M., and Andersson, G. (2007). Optimal Power Flow of Multiple Energy Carriers. *IEEE Trans. Power Syst.* IEEE 22 (1), 145–155. doi:10.1109/tpwrs.2006.888988

Geidl, M. (2007). *Integrated Modeling and Optimization of Multi-Carrier Energy Systems*. New York: Graz University of Technology.

Gu, Z., Kang, C., Chen, X., Bai, J., Cheng, L., et al. (2015). Operation Optimization of Integrated Power and Heat Energy Systems and the Benefit on Wind Power Accommodation Considering Heating Network Constraints. *Proceeding of the CSEE* 35 (14), 3596–3604.

Jia, H., Wang, D., Xu, X., Yu, X., et al. (2015). Research on Some Key Problems Related to Integrated Energy Systems. *Automation Electric Power Syst.* 38 (7), 198–207.

Kersting, W. H. (1991). Radial Distribution Test Feeders. *IEEE Trans. Power Syst.* 6 (3), 975–985. doi:10.1109/59.119237

Kocuk, B., Dey, S. S., and Sun, X. A. (2016). Strong SOCP Relaxations for the Optimal Power Flow Problem. *Operations Res.*

Liu, X. (2013). *Combined Analysis of Electricity and Heat Networks*. Cardiff: Cardiff University.

Manshadi, S. D., and Khodayar, M. E. (2015). Resilient Operation of Multiple Energy Carrier Microgrids. *IEEE Trans. Smart Grid*. IEEE 6 (5), 2283–2292. doi:10.1109/tsg.2015.2397318

Moeini-Aghtaie, M., Abbaspour, A., Fotuhi-Firuzabad, M., and Hajipour, E. (2014). A Decomposed Solution to Multiple-Energy Carriers Optimal Power Flow. *IEEE Trans. Power Syst.* 29 (2), 707–716. doi:10.1109/tpwrs.2013.2283259

OMalley, M., and Kroposki, B. (2013). Energy Comes Together: The Integration of All Systems [Guest Editorial]. *IEEE Power Energ. Mag.* 11 (5), 18–23. doi:10.1109/mpe.2013.2266594

Pan, Z., Guo, Q., and Sun, H. (2016). Interactions of District Electricity and Heating Systems Considering Time-Scale Characteristics Based on Quasi-Steady Multi-Energy Flow. *Appl. Energ.* 167, 230–243. doi:10.1016/j.apenergy.2015.10.095

Shabanpour-Haghighi, A., and Seifi, A. R. (2015). Simultaneous Integrated Optimal Energy Flow of Electricity, Gas, and Heat. *Energ. Convers. Manag.* 101, 579–591. doi:10.1016/j.enconman.2015.06.002

Sun, G., Wang, W., Wu, Y., Hu, W., Jing, J., Wei, Z., et al. (2020). Fast Power Flow Calculation Method for Radiant Electric-thermal Interconnected Integrated Energy System. *Proc. Chin. Soc. Electr. Eng.* 40 (13), 4131–4142.

Xu, F., Min, Y., Chen, L., Chen, Q., Hu, W., Zhang, W., et al. (2014). Combined Electricity-Heat Operation System Containing Large Capacity thermal Energy Storage. *Proceeding of the CSEE* 34 (29), 5063–5072.

Xu, X., Jin, X., Jia, H., Yu, X., and Li, K. (2015). Hierarchical Management for Integrated Community Energy Systems. *Appl. Energ.* 160, 231–243. doi:10.1016/j.apenergy.2015.08.134

Yang, Y., et al. (2010). Chosen Method of Optimum Cold Source Thermal-system Heater in Heat and Power Cogeneration System. *Proc. Chin. Soc. Electr. Eng.* 30 (26), 1–6.

Zhang, Y. (2005). *Study on the Methods for Analyzing Combined Gas and Electricity Networks*. Beijing: China Electric Power Research Institute.

Zhou, X. (2020). *Research on Optimal Scheduling of Gas-Electricity Interconnected Integrated Energy System Based on Piecewise Linearization of Weymouth Equation*. Nanjing Normal University.

Conflict of Interest: The authors declare that the research was conducted in the absence of any commercial or financial relationships that could be construed as a potential conflict of interest.

Publisher's Note: All claims expressed in this article are solely those of the authors and do not necessarily represent those of their affiliated organizations, or those of the publisher, the editors and the reviewers. Any product that may be evaluated in this article, or claim that may be made by its manufacturer, is not guaranteed or endorsed by the publisher.

frontiers in Energy Research

ORIGINAL RESEARCH
published: 23 August 2021
doi: 10.3389/fenrg.2021.717327

An Equivalent Rotor Speed Compensation Control of PMSG-Based Wind Turbines for Frequency Support in Islanded Microgrids

Cheng Zhong[1,2]*, *Yueming Lv*[1], *Yang Zhou*[3] *and Huayi Li*[1]

[1]Key Laboratory of Modern Power System Simulation and Control and Renewable Energy Technology (Ministry of Education), Northeast Electric Power University, Jilin, China, [2]Department of Electronic, Electrical and Systems Engineering, University of Birmingham, Birmingham, United Kingdom, [3]Weihai Power Supply Company, State Grid Shandong Electric Power Company, Weihai, China

Frequency regulation is a critical issue in the islanded microgrids, especially the integration of high penetration of the wind power generator. In order to provide inertial and primary frequency support to the wind power system, this article proposes an equivalent rotor speed compensation control scheme of PMSG for frequency support in the islanded microgrids. A new variable combining pitch angle and rotor speed is defined as the equivalent rotor speed. The equivalent rotor speed versus de-loaded power curve is designed to preserve a part of active power among the whole wind speed area. And the inertia control scheme is optimized by adding a virtual compensation variable to the equivalent rotor speed to obtain the reference of the machine-side converter control loop. Adopting the proposed scheme, the PMSG-based wind turbine can achieve a similar frequency regulation performance to synchronous generators. Simulation results demonstrate the feasibility and effectiveness of the proposed control scheme.

Keywords: the virtual compensation variable of the rotor speed, equivalent rotor speed, PMSG-based wind turbine, de-loaded control, inertial response, frequency support

OPEN ACCESS

Edited by:
Dongdong Zhang,
Guangxi University, China

Reviewed by:
Krishnakumar R. Vasudevan,
Universiti Tenaga Nasional, Malaysia
Mehdi Firouzi,
Islamic Azad University, Abhar, Iran

***Correspondence:**
Cheng Zhong
zhongcheng@neepu.edu.cn

Specialty section:
This article was submitted to Smart Grids, a section of the journal Frontiers in Energy Research

Received: *30 May 2021*
Accepted: *22 July 2021*
Published: *23 August 2021*

Citation:
Zhong C, Lv Y, Zhou Y and Li H (2021) An Equivalent Rotor Speed Compensation Control of PMSG-Based Wind Turbines for Frequency Support in Islanded Microgrids. Front. Energy Res. 9:717327. doi: 10.3389/fenrg.2021.717327

INTRODUCTION

With the rapid development of renewable energy in recent years, distributed power generation technologies such as photovoltaics (PV), wind power, and biogas have attracted more and more attention from the international community due to their cleanliness, low energy consumption, and flexible control (Li et al., 2016). At the same time, microgrids that can effectively integrate distributed energy sources have gradually become an important part of modern power grids.

Wind power is mostly connected to the grid through power electronic converters, which lack the kinetic energy (KE) of the rotor and cannot provide inertia to the grid. Wind power usually operates in the maximum power point tracking (MPPT) mode, and its output is random and volatile, which makes it unable to participate in the frequency and voltage regulation of the grid (Adam et al., 2015). Therefore, high penetration of wind powers brings about the frequency stability issue due to the reduction of the overall inertia and primary frequency capability (Zhao et al., 2019; Zhu et al., 2021a). An approach for alleviating the above problems is that wind power participates in the frequency response of the grid.

The existing approaches for variable speed wind turbines (VSWTs) can be divided into inertial control and de-loaded control. In inertial control, the VSWTs operate in MPPT mode, and the rotational kinetic energy (KE) is released to deliver temporary power for improving inertial response. Mostly, inertial control is to change the active power in proportion to the rate of change of frequency or frequency deviation or both of them (Sun et al., 2019; Zeng et al., 2019). For compromise of the frequency regulation performance and rotor speed safe operation, some adaptive gains methods were proposed (Zhang et al., 2012; Zhao et al., 2015; Wu et al., 2019; Zhao et al., 2020). In (Zhao et al., 2015), the control gains of frequency regulation schemes (FRS) under different wind speeds are adjusted based on the wind speed. In (Wu et al., 2019), the gains of additional frequency deviation loops are adaptively tuned depended on the rotor speed measurement. In (Zhao et al., 2020), time-varying gains determined based on desired frequency-response time are designed to raise frequency nadir and to eliminate frequency second drop. In (Zhang et al., 2012), an adaptive droop gain is designed, which is a function of real-time rotor speed and wind power penetration level.

For the de-loaded control, a part of the active power of VSWTs can be reserved through the pitch angle control, the overspeed control, or the combination of both (Chang-Chien et al., 2011; Margaris et al., 2012; Zertek et al., 2012; Wu et al., 2018; Luo et al., 2019; Tang et al., 2019).

Based on the de-loaded control, the droop control is adopted to akin to the synchronous generators, which can provide minutes-term primary frequency support. In (Gao et al., 2019), a comprehensive frequency regulation scheme that combines the stepwise inertial control and variable-droop control is proposed. A coordinated control scheme that flexibly switches between additional power control, tracking curve control, and pitch angle adjustment control at different start-up stages is proposed, which can effectively improve insufficient frequency support. A variable-droop control scheme that considers optional rotor KE is proposed in (Liu et al., 2019). However, the rotor KE estimation required the wind speed information and parameters of the wind turbine. Some adaptive gains methods are proposed in (Lee et al., 2016; Wu et al., 2019; Zhao et al., 2020), which introduce the additional frequency increase of inertia control into the power control loop by adjusting the parameters of the additional signal.

Due to the rotor speed limit, the overspeed de-loaded control is only adapted for low wind areas. Therefore, in (Zhang et al., 2012), three wind speed areas are defined: low wind speed area where de-loaded operation is merely by the rotor speed control; medium wind speed area where de-loaded operation is conducted by the combining pitch angle control and the rotor speed control; and high wind speed area where the modified pitch angle control is conducted alone. However, it required accurate wind speed information to determine the wind speed area, and the calculation of de-loaded power reference needs both parameters of wind turbine and wind speed. In (Chang-Chien et al., 2014), since the power output is controlled only by pitch adjustment, they continually activate the pitch regulation over the whole wind speed region. Thus, the frequent pitch activation inevitably increases pitch servo fatigue and blade stress. In (Tang et al., 2019), the strategy can make full use of the inertial response of wind turbine generators (WTGs) at all pitch positions to sustain the dispatched active power and the blade loads of wind turbines are alleviated.

Compared with doubly fed induction generator-based wind turbine generation (DFIG-WTG), permanent magnet synchronous generator-based wind turbine generation (PMSG-WTG) can provide a much stronger inertial response thanks to their full power converter, and it accommodates a wider range of rotor speed (Wu et al., 2016). In most literature, FRS are designed based on the power tracking control for DFIG-WTG. The additional power from the supplementary control loop is added to the maximum power reference or de-loaded power reference to provide frequency support.

However, for PMSG-WTG, rotor speed tracking is an alternative attractive control method that rotor speed is directly manipulated to captured wind energy. Only a few studies are focused on the FRS based on rotor speed control. An algorithm to extract the maximum KE without stalling wind turbine (WT) is proposed in (Kayikci and Milanovic, 2009), in which the electric torque is increased stepwise by increasing the rotor speed of the WT to provide virtual inertia. However, the mechanical torque was assumed constant in this study. In (LI et al., 2017), an additional reference torque is added on the torque reference of the generator-side converter to respond to the change of system frequency. In (Zhu et al., 2021b), the comprehensive coordinated control strategy containing a variable coefficient integrated inertial control and virtual capacitor control is proposed.

The purpose of this study is to investigate a new FRS for PMSG-WTG based rotor speed control during the whole wind speed area. A combined variable of rotor speed and de-loaded compensation pitch angle is defined and named "equivalent rotor speed", which helps to realize the de-loaded control during the whole wind speed area. The inertial and primary frequency response is generated through adding a virtual rotor speed deviation, which results in the rotor speed or pitch angle adjustment being coupled with grid frequency deviation to increase or decrease active power output.

The remainder of this article is organized as follows: in Section *The Traditional Frequency Regulation Scheme for PMSG-WTG*, the conventional rotor speed control structure of PMSG-WTG is introduced; in Section *The Proposed Frequency Regulation Scheme*, the basic principle of the proposed scheme is introduced in detail, including the equivalent rotor speed versus de-loaded power curve and the calculation scheme of the virtual compensation variable to change the reference rotor speed; and in Section *Case Study*, a simulation model of an islanded microgrid is built, and the proposed scheme is compared with the method in (LI et al., 2017). The effectiveness of the proposed control scheme participating in the system frequency response under various wind speed and load changes is verified. Finally, a brief conclusion is drawn in Section *Conclusion*.

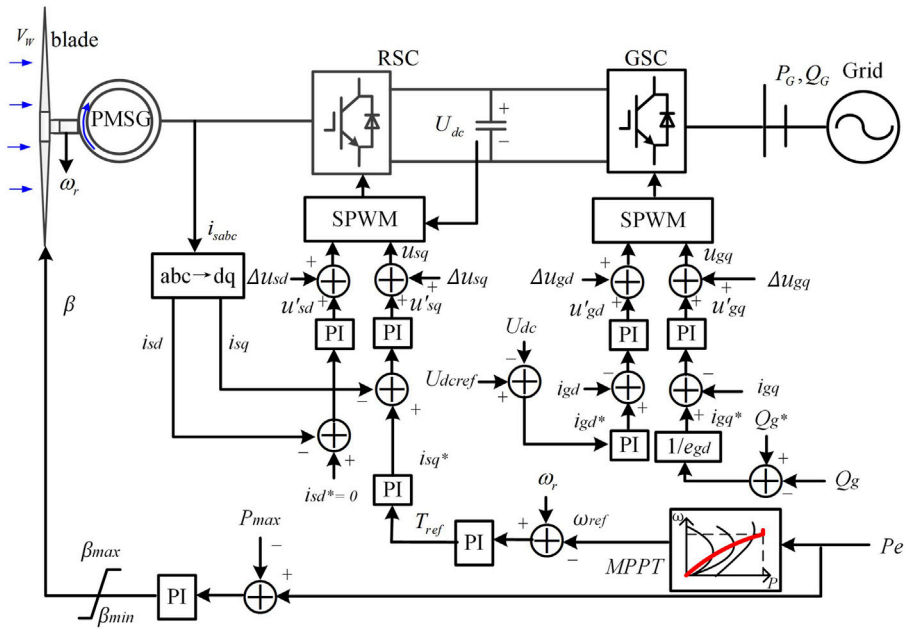

FIGURE 1 | Block diagram of a model of the PMSG based wind turbine Generators.

THE TRADITIONAL FREQUENCY REGULATION SCHEME FOR PMSG-WTG

The diagram of PMSG-WTG based rotor speed control strategy modeling (Hu et al., 2017) is shown in **Figure 1**, which is mainly composed of wind turbines, PMSG and power electronic converters. The aerodynamic rotor of the WT is directly coupled to the PMSG without any gearbox. The PMSG is connected to the grid through the machine-side converter (MSC) and the grid-side converter (GSC) to control the generator's speed and power.

The captured mechanical power from the wind, P_m, is defined by (Sun et al., 2019)

$$P_m = \frac{1}{2}\rho\pi R^2 v_w{}^3 C_p(\lambda,\beta), \tag{1}$$

where ρ is air density, R *is* radius, v_w is wind speed, λ is tip speed ratio, $\lambda = \omega_r R/v_w$, ω_r is rotor speed, β is pitch angle, and $C_p(\lambda,\beta)$ is the power coefficient.

As in (Ekanayake and Jenkins, 2004), $C_p(\lambda,\beta)$ can be expressed as

$$C_p(\lambda,\beta) = (0.44 - 0.0167\beta)sin\left[\frac{\pi(\lambda-3)}{5-0.3\beta}\right] - 0.00184(\lambda-3)\beta. \tag{2}$$

A maximum mechanical power rotor speed characteristic curve is pre-defined, and the rotor speed reference is inquired according to the electromagnetic power measurement (Sun et al., 2019). When the wind speed increases, the rotor speed of the WT accelerates due to the increase in the captured power P_m. In order to achieve the balance of the system, the electromagnetic power P_e controlled by the rotor speed controller increases. The increased P_e flows into the DC link capacitor. Then, the GSC injects the active power delivered by the MSC into the power grid to maintain a constant DC link voltage. When the wind speed continues to increase and the electromagnetic power reaches the rated power, the pitch angle control starts to act to ensure that the wind turbine runs at constant power.

However, this type of wind turbine runs in the maximum power tracking mode and cannot respond to the frequency variation of the system. In (LI et al., 2017), a typical frequency regulation scheme that the torque is adjusted according to frequency deviation is proposed, as shown in **Figure 2**.

The maximum power tracking control mode is instead of a de-loaded power tracking mode. The de-loaded rotor speed reference, ω_{de}, is provided for the speed controller, and the output of the torque T_r is obtained through the PI controller. When the grid frequency f_s deviates from the rated frequency f_n, an additional reference torque ΔT_{add} depending on the frequency deviation Δf is added on T_r. Then, the reference torque T_{ref} is obtained and transmitted to the inner control loop. The captured active power is adjusted by the inner loop response and the rotor speed tracks ω_{de}. Due to the rapid regulation effects of the GSC control system, the GSC and then the active power from MSC are immediately injected into the grid to maintain a constant DC link voltage.

The additional reference torque ΔT_{add} is determined according to the frequency deviation Δf and the droop control coefficient K_{pf}, which can be expressed as

$$\Delta T_{add} = -K_{pf}\Delta f. \tag{3}$$

However, the additional ΔT_{add} has a conflict with the speed controller. T_r from the speed controller is used to regulate the

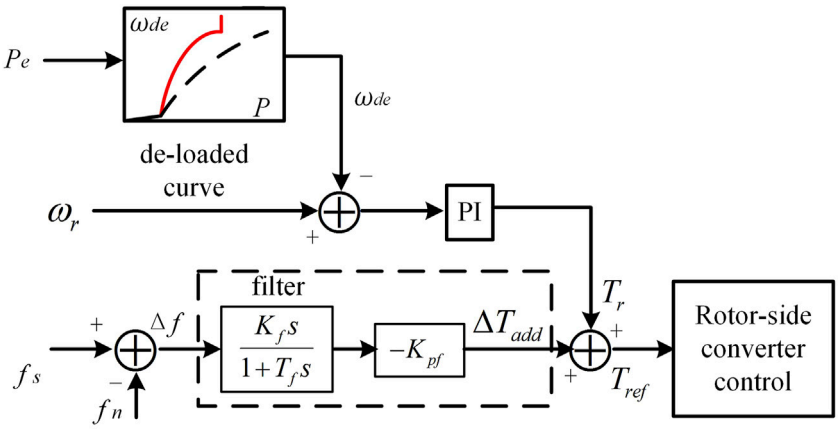

FIGURE 2 | Traditional frequency regulation control scheme.

rotor speed tracking the reference value. ΔT_{add} is dependent on the frequency deviation. This conflict influences both speed regulation and frequency support. At the same time, this scheme does not consider the coordination of the torque control and the pitch angle control. In the medium and high wind speed area, pitch angle control is necessary to regulate the active power due to the rotor speed limit. Further, K_{pf} is a fixed value, which cannot be changed adaptively under different wind speed conditions. When the wind speed is in the low area, the additional reference torque ΔT_{add} is too large, which causes the rotor speed to drop too fast. When the wind speed is in the high area, the additional reference torque ΔT_{add} for the frequency regulation will be insufficient.

THE PROPOSED FREQUENCY REGULATION SCHEME

The Block Diagram of the Proposed Frequency Regulation Scheme

The block diagram of the scheme proposed in this article is shown in **Figure 3**.

To realize the de-loaded control for PMSG during the whole wind speed range, this article defines a new variable, named equivalent rotor speed "ω_b" here, which combines the rotor speed and the de-loaded pitch angle.

$$\omega_{\mathbf{b}} = \omega_{\mathbf{de}} + \beta_{\mathbf{de}}. \tag{4}$$

ω_{de} is de-loaded rotor speed in the low wind speed area and β_{de} is the de-loaded pitch angle in the medium and high wind speed area.

Further, the equivalent rotor speed versus de-loaded power curve is obtained through the wind turbine modeling data fitting. Depending on this curve, the corresponding ω_b can be queried according to the electromagnetic power P_e. The detail is given in subsection *The Equivalent Rotor Speed-Active Power Curve* below.

To directly couple grid frequency with rotor speed, a compensation variable $\Delta\omega_b$ is obtained based on the frequency deviation. By adding the $\Delta\omega_b$ on ω_b, the reference rotor speed ω_{ref} is obtained

$$\omega_{\mathbf{ref}} = \omega_{\mathbf{b}} + \Delta\omega_{\mathbf{b}}. \tag{5}$$

Since the equivalent rotor speed ω_b contains the sum of the per-unit value of the rotor speed and pitch angle, these two values should be separated to obtain rotor speed reference or pitch angle reference for the controller. Fortunately, pitch angle act only when the rotor speed reaches ω_{max} (1. p.u in this article). Hence, a limiter is added behind the equivalent rotor speed ω_{ref}. When ω_{ref} is less than ω_{max}, ω_{ref} is directly used as the reference value of the rotor speed control loop. When ω_{ref} is larger than ω_{max}, the rotor speed reference is ω_{max}, and the pitch angle reference β_{ref} can be obtained by subtracting ω_{max} from ω_{ref}. Hence, the pitch angle can help the de-loaded control and response to frequency variation when ω_{ref} exceeds ω_{max}. How to obtain $\Delta\omega_b$ is explained in subsection *The Calculation Method of the Virtual Compensation Rotor Speed* below.

The Equivalent Rotor Speed-Active Power Curve

As in (Zhang et al., 2012), the de-loaded rotor speed and de-loaded pitch angle can be calculated by the following expressions:

$$\begin{cases} C_{\mathbf{p,de}}(\lambda_{\mathbf{de}}, 0) = (1 - d\%)C_{\mathbf{p,max}}\left(\lambda_{\mathbf{opt}}, 0\right) & v_1 < v < v_2 \\ C_{\mathbf{p,de}}\left(\lambda_{\mathbf{ref}}, \beta_{\mathbf{de}}\right) = (1 - d\%)C_{\mathbf{p,max}}\left(\lambda_{\mathbf{opt}}, 0\right) & v_2 < v < v_3 \\ C_{\mathbf{p,de}}\left(\lambda_{\mathbf{ref}}, \beta_{de}\right) = (1 - d\%)C_{\mathbf{p,rated}}\left(\lambda_{\mathbf{ref}}, \beta_0\right) & v_3 < v. \end{cases} \tag{6}$$

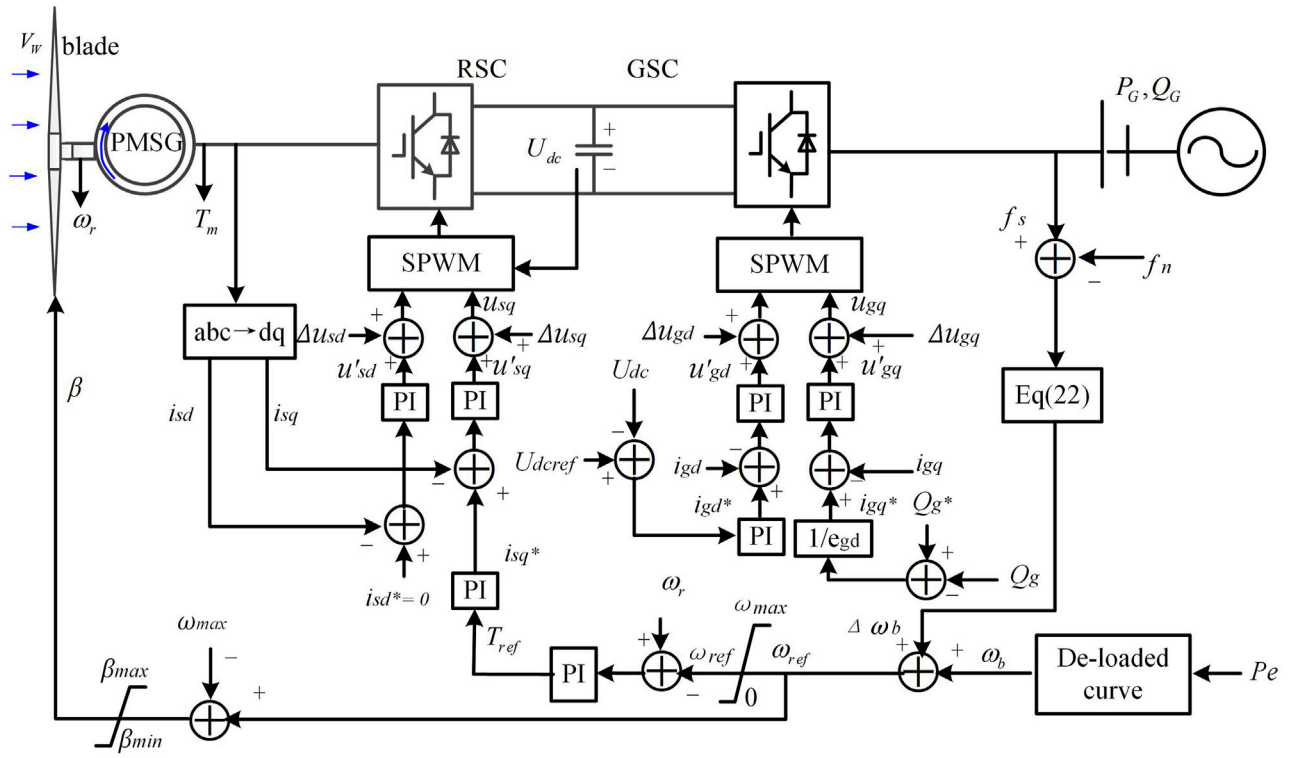

u_{sd}、u_{sq}-- d, q axis stator voltage
i_{sd}、i_{sq}-- the d and q axis stator current
i_{gd}、i_{gq}-- the d and q axis current of the grid-side converter
u'_{sd}、u'_{sq}-- voltages obtained by closed loop control of current
Δu_{sd}、Δu_{sq}-- the compensation value of cross coupling voltage
U_{dc}-- the DC capacitor voltage
ω_r -- the electrical speed of PMSG

u_{gd}、u_{gq}-- the d、q axis voltage of the grid-side converter
i_{sd}^*、i_{sq}^*-- the d,q axis stator current reference command
i_{gd}^*、i_{gq}^*-- the d,q axis stator current reference command
u'_{gd} and u'_{gq}-- voltages obtained by closed loop control of current
Δu_{gd} and Δu_{gq}-- the compensation value of cross-coupling voltage
U_{dcref}-- reference DC-linkage voltage,
e_{gd}-- the grid voltage

FIGURE 3 | The proposed frequency regulation scheme.

where v_1 is the cut-in wind speed, v_2 is the demarcation point of the wind speed between the low and medium wind speed area, v_3 is the demarcation point of the wind speed between the medium and high wind speed area, λ_{opt} is the optimal tip speed ratio, and $C_{p,max}$ is the maximum wind energy capture coefficient. λ_{de} is the tip speed ratio when de-loaded ratio is d%, λ_{ref} is the reference tip speed ratio in overspeed control and, $C_{p,rated}$ is the wind energy capture coefficient when operating at rated power, β_0 is the pitch angle reference when the wind turbines operate at the rated power, β_{de} is the de-loaded pitch angle in the de-loaded control mode, and d% is the de-loaded ratio of the wind turbine. The de-loaded ration d% is given 10% in this article.

In the low wind speed, λ_{opt} and $C_{p,max}$ can be obtained through **Eq. 2**. Hence, λ_{de} can be calculated by **Eq. 6**, and then we can calculate ω_{de} by $\lambda_{de} = \omega_{de}R/v$.

In the medium wind area, $\lambda_{ref} = \omega_{max}R/v$, λ_{opt} and $C_{p,max}$ have been obtained through **Eq. 2**. The pitch angle (β_{de}) can be calculated through **Eq. 6**.

In the high wind area, we can calculate $C_{p,rated}$ by **Eq. 1**. Then, because λ_{ref} has been known, β_0 can be obtained by **Eq. 2**. Hence, β_{de} can be obtained by **Eq. 6**.

Therefore, based on **Eq. 4** and **Eq. 6**, the offline fitting data of the de-loaded power P_{de} and ω_b under different wind speed areas can be obtained. The data and the fitting ω_b-P_{de} curve is shown in **Figure 4**.

Corresponding to wind speed area, the ω_b-P_{de} curve can be divided into three segments. The first segment is the low wind speed area, where P_{de} is less than 0.53 p.u. The pitch angle control is disabled; that is, β is 0. According to **Eq. 4**, ω_b is equal to ω_{de}. The second segment is the medium wind speed area, where the power is greater than 0.53 p.u. The third one is the high wind speed area, where P_{de} is greater than or equal to 0.9 p.u. In the second and the third segments, pitch angle control is enabled.

Considering the accuracy and complexity, the following piecewise function is employed to fit the ω_b-P_{de} curve:

$$\omega_b = \begin{cases} k_1 \sqrt[3]{P_{de}} & P_{de} \le 0.53 \text{ p.u.} \\ \dfrac{P_{de} - b_3}{k_3} & 0.53 \text{ p.u.} < P_{de} \le 0.9 \text{ p.u.} \\ \dfrac{P_{de} - b_4}{k_4} & P_{de} \ge 0.9 \text{ p.u.} \end{cases} \tag{7}$$

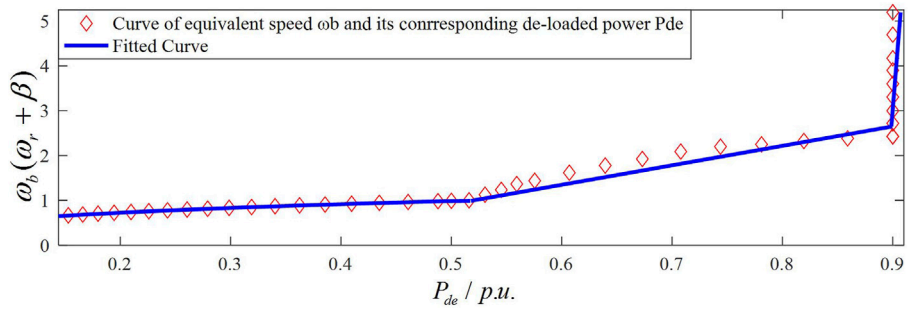

FIGURE 4 | The equivalent rotor speed ω_b active power P_{de} curve.

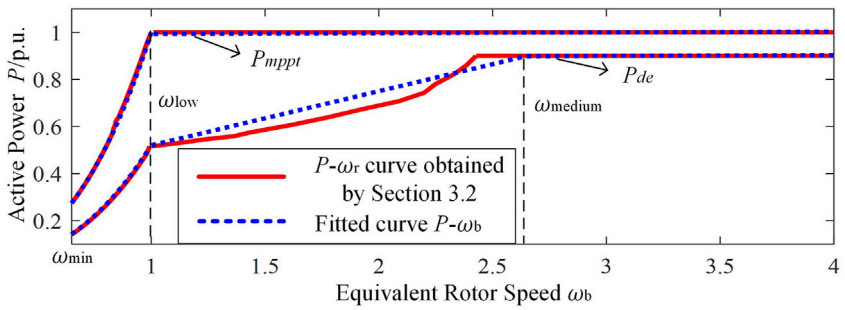

FIGURE 5 | The active power equivalent rotor speed ω_b curve in the whole wind speed area.

By using the curve fitting tool to perform linear regression on the offline data, the value of each fitting parameter in **Eq. 7** can be obtained, which are as follows: $k_1 = 0.5218$; $k_3 = 0.2393$; $b_3 = 0.29$; $k_4 = 0.003$; and $b_4 = 0.89$.

The Calculation Method of the Virtual Compensation Rotor Speed

The virtual compensation rotor speed $\Delta\omega_b$ is introduced to generate both inertial and primary frequency responses. In Section *The Equivalent Rotor Speed-Active Power Curve*, **Eq. 7** has been obtained, which describes the relationship between the de-loaded power P_{de} and the equivalent rotor speed ω_b. According to the inverse function of **Eq. 7**, we can obtain the P-ω_b curve as in

$$P_{de} = \begin{cases} k_1\omega_b^3 & \omega_{min} < \omega_b \le \omega_{blow} \\ k_3\omega_b + b_3 & \omega_{blow} < \omega \le \omega_{bmedium} \\ k_4\omega_b + b_4 & \omega \ge \omega_{bmedium}. \end{cases} \quad (8)$$

where ω_{min} is the cut-in rotor speed of the WT and ω_{blow} is the demarcation equivalent rotor speed between the low wind speed area and the medium wind speed area. The value of ω_{blow} is equal to the rated rotor speed ω_{max}, which is 1 p.u. $\omega_{bmedium}$ is the demarcation equivalent rotor speed between the medium wind speed area and the high wind speed area, and its value is 2.6 p.u.

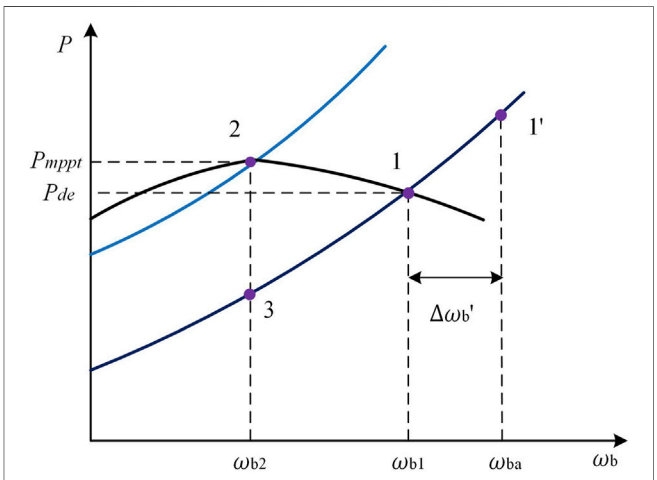

FIGURE 6 | The active power equivalent rotor speed ω_b curve in the low wind speed area.

When ω_b exceeds $\omega_{bmedium}$, the active power should be kept constant.

The maximum power curve can be approximately is give in

$$P_{mppt} = \begin{cases} k_2\omega_b^3 & \omega_{min} < \omega_b \le \omega_{blow} \\ \dfrac{k_4\omega_b + b_4}{k_4} + 0.1 & \omega_b \ge \omega_{blow} \end{cases}. \quad (9)$$

where k_2 is the maximum power coefficient, $k_2 = 0.98$.

The P_{de}-ω_b curve and P_{mppt}-ω_b curve in the low wind speed area are given in **Figure 6**. Assume that PMSG-WTG initially operates at the de-loaded stable point 1′.

Generally, the output active power of PMSG is regulated based on the frequency deviation Δf, and its expression is

$$\Delta P_e = -\frac{\Delta P_{max}}{(f_b - f_a)}\Delta f, \tag{10}$$

where ΔP_{max} is the maximum frequency regulation power, f_a and f_b correspond to the system frequency regulation interval, and ΔP_{max} is the limit frequency regulation power.

To prevent the rotor speed lower than the optimal rotor speed during the frequency regulation process, the value of ΔP_{max} is the difference between the maximum power P_{mppt} and the de-loaded power with maximum power rotor speed ω_{b2}, that is,

$$\Delta P_{\mathbf{max}} = P_{\mathbf{2}} - P_{\mathbf{3}} = k_{\mathbf{2}}\omega_{b2}^3 - k_{\mathbf{1}}\omega_{b2}^3, \tag{11}$$

where P_2 is the maximum power at operating point '2′ and P_3 is the de-loaded power with maximum power rotor speed at point '3'.

Assuming a frequency dips event occurs, the electromagnetic power P_e should increases, which is equivalent to an increase of the rotor speed $\Delta\omega_b'$

$$\begin{aligned} P_1' &= P_1 + \Delta P_{\mathbf{e}} = k_1\left(\omega_{b1} + \Delta\omega_{\mathbf{b}}'\right)^3 \\ &= k_1\left(\omega_{b1}^3 + 3\omega_{b1}^2\Delta\omega_{\mathbf{b}}' + 3\omega_{b1}\Delta\omega_{\mathbf{b}}'^{2+}\Delta\omega_{\mathbf{b}}'^3\right) \end{aligned} \tag{12}$$

Since the rotor speed regulation range is not large, $1 > \omega_{b1} >> \Delta\omega_b'$. Hence, the higher-order terms with $\Delta\omega_b'$ can be ignored, and then **Eq. 12** can be simplified

$$P_1' = P_1 + \Delta P_e \approx k_1\Delta\left(\omega_{b1}^3 + 3\omega_{b1}^2\Delta\omega_b'\right). \tag{13}$$

Combining **Eq. 13** and **Eq. 9**,

$$\Delta P_e = 3\omega_{b1}^2\Delta\omega_b' = -\frac{\Delta P_{\mathbf{max}}}{\Delta f_{\mathbf{max}}}\Delta f \tag{14}$$

The initial de-loaded power P_1 and the maximum power P_2 can be expressed as

$$P_1 = (1 - d\%)P_2. \tag{15}$$

Then, considering **Eq. 8**, **Eq. 9**, and **Eq. 15**,

$$(1 - d\%)k_2\omega_{b2}^3 = k_1\omega_{b1}^3. \tag{16}$$

From **Eq. 16**, the following expression can be derived as

$$\omega_{b2} = \sqrt[3]{\frac{k_1\omega_{b1}^3}{k_2(1 - d\%)}}. \tag{17}$$

Substitute **Eq. 17** into **Eq. 11**, the following expression can be derived:

$$\Delta P_{\mathbf{max}} = \frac{k_2k_1\omega_{b1}^3}{k_2(1 - d\%)} - \frac{k_1^2\omega_{b1}^3}{k_2(1 - d\%)}. \tag{18}$$

Further, substitute **Eq. 18** into **Eq. 10**, the following expression is obtained:

$$\Delta\omega_b' = -\frac{k_1(k_2 - k_1)\omega_{b1}}{3k_2(1 - d\%)\Delta f_{\max}}\Delta f. \tag{19}$$

Observing **Figure 6**, $\Delta\omega_b'$ is the difference between the equivalent rotor speed of the point '1′ and the equivalent rotor speed of the point '1" after the frequency regulation.

In fact, ω_{b1} is difficult to measure in engineering application. Therefore, ω_{b1} is replaced with ω_b, and **Eq. 19** can be written as

$$\Delta\omega_b = -\frac{k_1(k_2 - k_1)\omega_b}{3k_2(1 - d\%)\Delta f_{\max}}\Delta f. \tag{20}$$

ω_b is always larger than or equal to ω_{b1}. Hence, by replacing ω_{b1} with ω_b, $\Delta\omega_b$ is larger and results in releasing more active power.

In the medium wind speed area, since the adjustment range of ω_b increases, $\Delta\omega_b$' can no longer be ignored. When the frequency dips event occurs, the electromagnetic power can be expressed as

$$P_4' = P_4 + \Delta P_e = k_3\left(\omega_{\mathbf{b4}} + \Delta\omega_{\mathbf{b}}'\right) + b_3. \tag{21}$$

In the high wind speed area, ΔP_{max} is a constant value, 0.1 p.u.

Using the same analysis approach in the low wind speed area, the relationship between $\Delta\omega_b$ and Δf in the medium and high wind speed can be derived. The expression of $\Delta\omega_b$-Δf can be obtained as

$$\Delta\omega_b = \begin{cases} -\dfrac{k_1(k_2 - k_1)\omega_b}{3k_2(1 - d\%)(f_b - f_a)}\Delta f & \omega_b \le \omega_{blow} \\ -\dfrac{k_3(k_2 - k_1)\omega_b + b_3(k_2 - k_1)}{(1 - d\%)k_2k_3(f_b - f_a)}\Delta f & \omega_{blow} < \omega_b \le \omega_{bmedium} \\ -\dfrac{0.1}{k_4(f_b - f_a)}\Delta f & \omega_b > \omega_{bmedium} \end{cases}. \tag{22}$$

Dynamic Process of Frequency Regulation of the Proposed Control Scheme

The dynamic response of PMSG participating in frequency regulation when the frequency drops is illustrated in **Figure 7**. The trajectory of active power and rotor speed is shown in **Figure 8**.

In **Figure 7**, the area of S_1 between the mechanical power and the captured power by the wind turbine represents the rotational KE released by the wind turbine. It is mainly used to provide the inertial response and affects the rate of frequency change and frequency nadir. The area of S_2 represents the increase in the captured energy by the wind turbine, which is mainly used to provide primary frequency regulation and affect the steady frequency of the system.

The frequency regulation dynamic process is divided into six periods, and the dynamic process in each period is analyzed, respectively.

$t < t_1$: within this time range, P_e is equal to the captured power P_m, the rotor speed remains a constant value, and the PMSG-WTG operates in de-loaded mode.

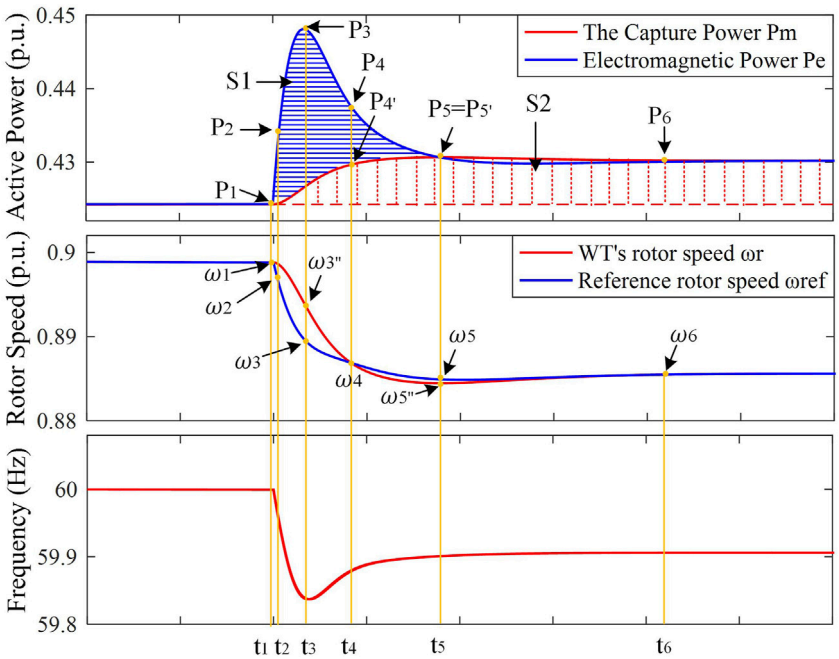

FIGURE 7 | The dynamic response process of PMSG participating in frequency regulation.

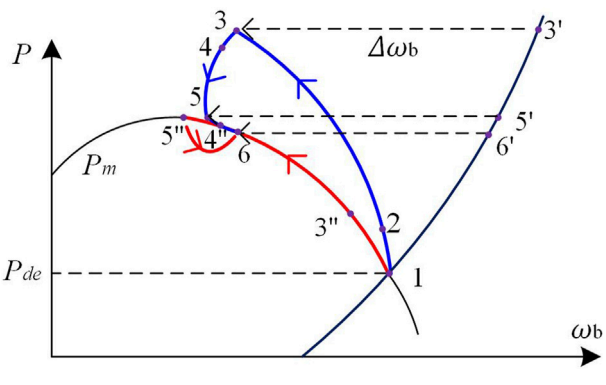

FIGURE 8 | The trajectory of active power P_e and the equivalent rotor speed ω_b.

$t_1<t<t_2$: at $t = t_1$, the load suddenly increases and the frequency drops. According to **Eq. 22**, $\Delta\omega_b$ decreases. Since the rotor speed of the PMSG decoupled with the grid frequency, the rotor speed ω_r remains unchanged at the moment. According to **Eq. 7**, ω_{ref} decreases and the deviation $\Delta\omega_e$ between ω_r and ω_{ref} increases. Therefore, through PI control, the electromagnetic torque reference T_{ref} increases. That is, P_e of the PMSG increases. According to the rotor mechanical equation, the rotor speed ω_r decreases. Due to ω_r decreasing, the capture wind power P_m increases, and its torque T_m also increases.

$t_2<t<t_3$: as P_e increases, depending on the P_{de}-ω_b curve, ω_b increases. During this period, because Δf is increasing and the change range of ω_b is small, $\Delta\omega_b$ plays a dominant role at this time, so that ω_{ref} decreases and its reduction value is larger than the reduction value of ω_r. $\Delta\omega_e$ increases. Therefore, T_{ref} increases after the PI controller, resulting in the increase of P_e. ω_r continues to decrease because of the increase of P_e. When $t = t_3$, $\Delta\omega_e$ reaches the maximum value and P_e reaches the maximum value. Based on the ω_b-P_{de} curve, ω_b also reaches its maximum value.

$t_3<t<t_4$: during this period, as the frequency starts to recovery, $\Delta\omega_b$ starts to decrease, and the change of ω_{ref} is smaller than the one of ω_r, which causes the $\Delta\omega_e$ to decrease. P_e also begins to decrease, but it is still larger than P_m. ω_b also begins to decrease with the decrease of P_e. According to **Eq. 7**, ω_{ref} will decrease. According to the rotor mechanical equation, ω_r decreases. $t_4<t<t_5$: since P_e is still larger than P_m, according to the rotor mechanical equation, ω_r and ω_{ref} continue to decrease, and the deviation $\Delta\omega_e$ continues to decrease, resulting in the decrease of T_{ref} and P_e. As ω_r decreases, P_m increases. When $t = t_5$, P_m is equal to P_e for the first time.

$t > t_5$: since the decrease of ω_r is slightly slower than ω_{ref}, P_m is slightly larger than P_e. Therefore, ω_r increases. When $t = t_6$, P_m is equal to P_e and ω_r is equal to ω_{ref}. At this time, the PMSG-WTG reaches a new steady-state operating point.

CASE STUDY

An islanded microgrid simulation model of wind power-diesel generators is built. The diagram of the islanded microgrid is shown in **Figure 9**. The rated power of the diesel unit is 70 kW. The nominal RMS voltage and frequency are 5 kV and 50 Hz, respectively.

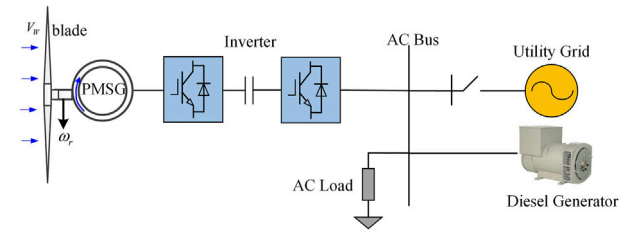

FIGURE 9 | The structure diagram of the independent microgrid model.

Various scenarios of wind speed and load changes are set to verify the effectiveness of the proposed frequency regulation scheme. The following three schemes are used to compare with the proposed control scheme.

1) The proposed frequency regulation scheme.
2) The conventional frequency regulation scheme.
3) The variable coefficient control scheme in (Zhu et al., 2021b).
4) The de-loaded control scheme (PMSG does not participate in frequency regulation).

Low Wind Speed Area

Case 1: the wind speed is set as 9 m/s; the load suddenly increases by 15 kW at 50 s.The simulation result is shown in **Figure 10**.As can be seen in **Figure 10**, when the PMSG adopts the traditional scheme, the rotor speed does not exceed the lower limiter. When the PMSG adopts the proposed scheme, the frequency nadir (FN) is 59.84 Hz, which is 0.02 Hz larger than the one of the PMSG-WTG adopting the traditional scheme, and 0.01 Hz larger than the one of the variable coefficient control scheme. The steady frequency is 59.91 Hz, which is 0.01 larger than the other two control scheme. Compared with the traditional frequency regulation scheme and the variable coefficient control scheme, the proposed scheme shows a better performance. The reason is that the active power for the frequency support increases with the increase of the wind speed, which validates that the proposed control scheme has a potential wind speed adaptability.

Case 2: the wind speed is set as 9 m/s; the load suddenly decreases by 15 kW at 50 s.The simulation result is shown in **Figure 11**.Observing the simulation results, when PMSG adopts the proposed frequency regulation scheme, the system frequency peak and deviation are smaller than those of PMSG-WTG adopting the other two control schemes, which validates that the proposed scheme has a better frequency regulation performance.

Medium Wind Speed Area

Case 3: the wind speed is set as 11 m/s; the load suddenly increases by 15 kW at 50 s.The simulation result is shown in **Figure 12**.As shown in **Figure 12A**, when the PMSG adopts the proposed scheme, the FN is 59.88 Hz, which is 0.11 Hz higher than when the PMSG does not participate in frequency regulation and 0.1 Hz and 0.09 Hz higher than those of the traditional scheme and the variable coefficient control scheme, respectively. The steady frequency is 59.92 Hz, which is 0.03 Hz larger than when the PMSG does not participate in frequency regulation, 0.019 Hz larger than that adopting the traditional scheme, and 0.019 Hz larger than the variable coefficient control scheme.As shown in **Figure 12B**, the proposed scheme's additional power is greater than that of the other frequency regulation schemes. The reduced rotor speed is used to provide inertia support. The peak power when the PMSG-WTG adopts the traditional scheme is 107.5 kW, the variable coefficient control scheme is 107.7 kW, and that of PMSG-WTG adopting the proposed scheme is 116.1 kW.During the process of frequency regulation, the PMSG-WTG operates in the safe rotor speed range, as shown in **Figure 12C**. Due to the potential self-adaption, the rotor speed of the proposed scheme converges to a lower value of 0.9739 p.u. and more KE is released during this period.As shown in **Figure 12D**, the pitch angle control is activated to provide de-loaded and frequency support control. Before the load changes, the PMSG-WTG operates in the de-loaded mode, and the pitch angle is approximately 0.094 deg.

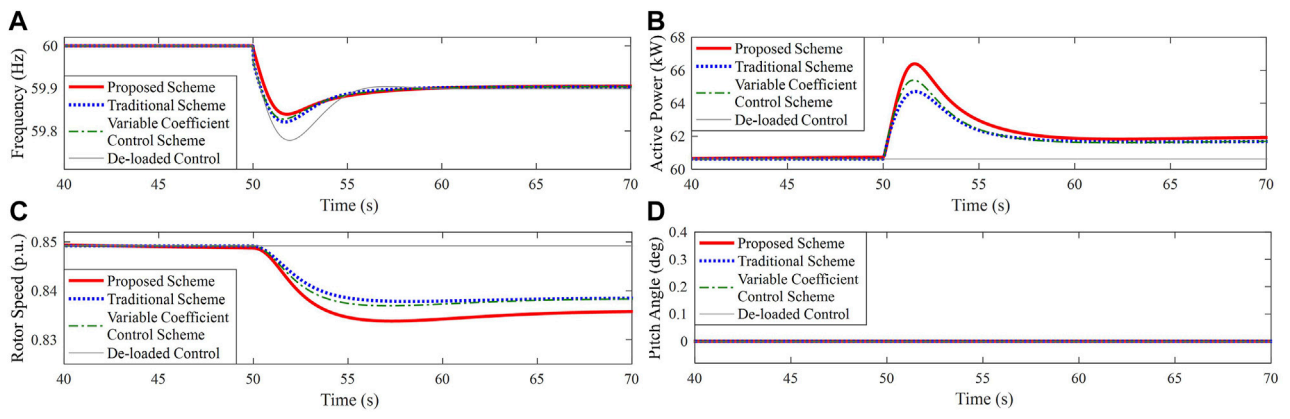

FIGURE 10 | Results for Case 1. **(A)** System frequency; **(B)** Active power of PMSG; **(C)** Rotor speed of PMSG; **(D)** Pitch angle.

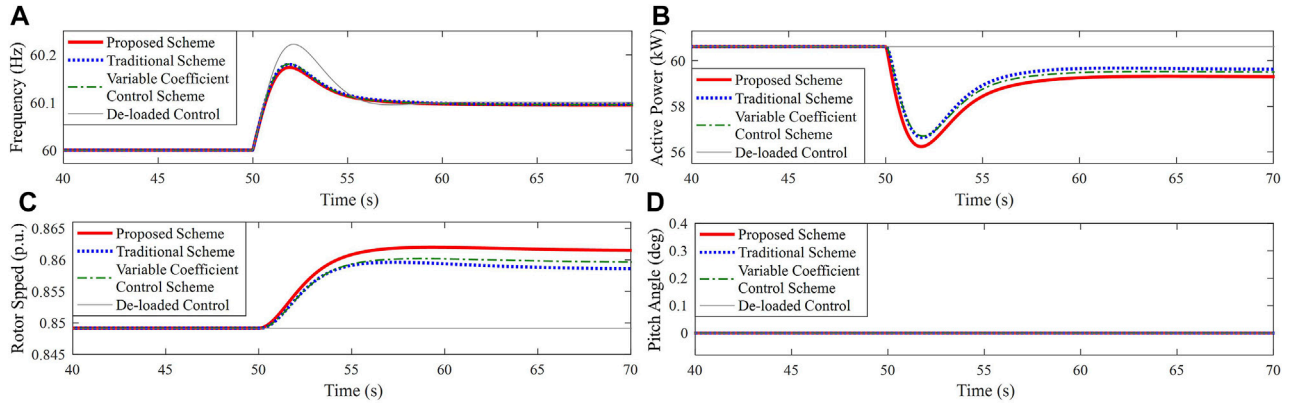

FIGURE 11 | Results for Case 2. **(A)** System frequency; **(B)** Active power of PMSG; **(C)** Rotor speed of PMSG; **(D)** Pitch angle.

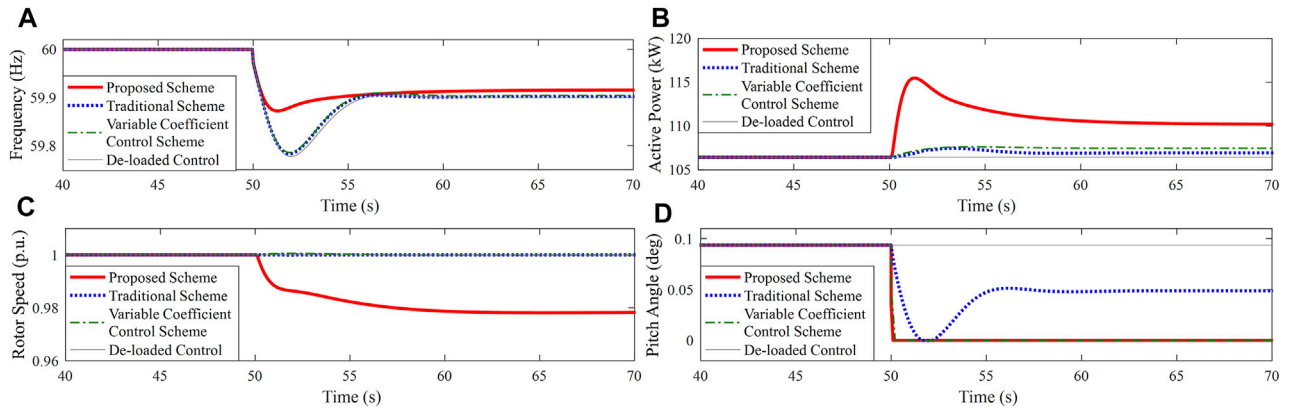

FIGURE 12 | Results for Case 3. **(A)** System frequency; **(B)** Active power of PMSG; **(C)** Rotor speed of PMSG; **(D)** Pitch angle.

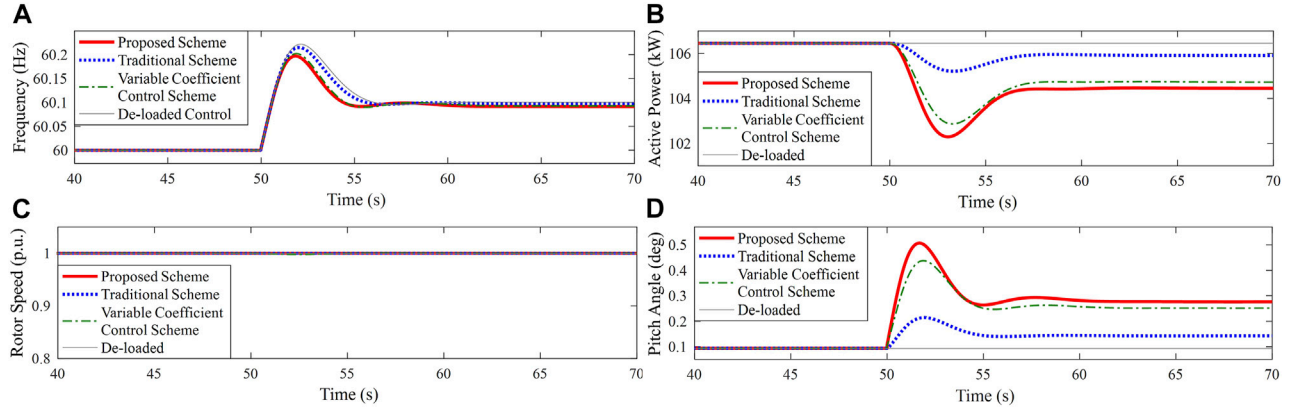

FIGURE 13 | Results for Case 4. **(A)** System frequency; **(B)** Active power of PMSG; **(C)** Rotor speed of PMSG; **(D)** Pitch angle.

After the load changes, the pitch angle is decreased to release extra power for frequency support. In fact, the pitch angle control and rotor speed control are difficult to coordinate for the other two control schemes in the medium wind speed area. When the PMSG adopts the proposed scheme, pitch angle drops deeper than that of adopting other schemes. Therefore, the proposed

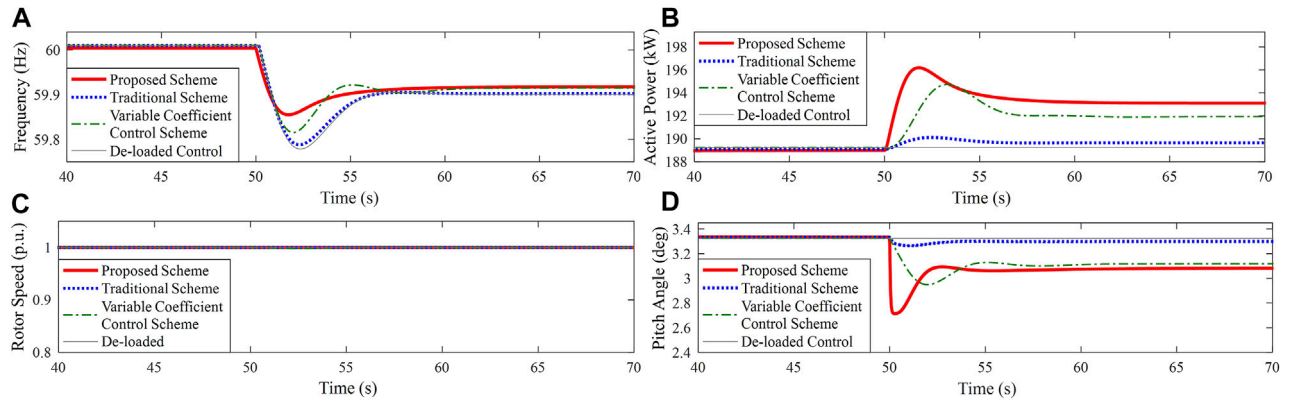

FIGURE 14 | Results for Case 5. **(A)** System frequency; **(B)** Active power of PMSG; **(C)** Rotor speed of PMSG; **(D)** Pitch angle.

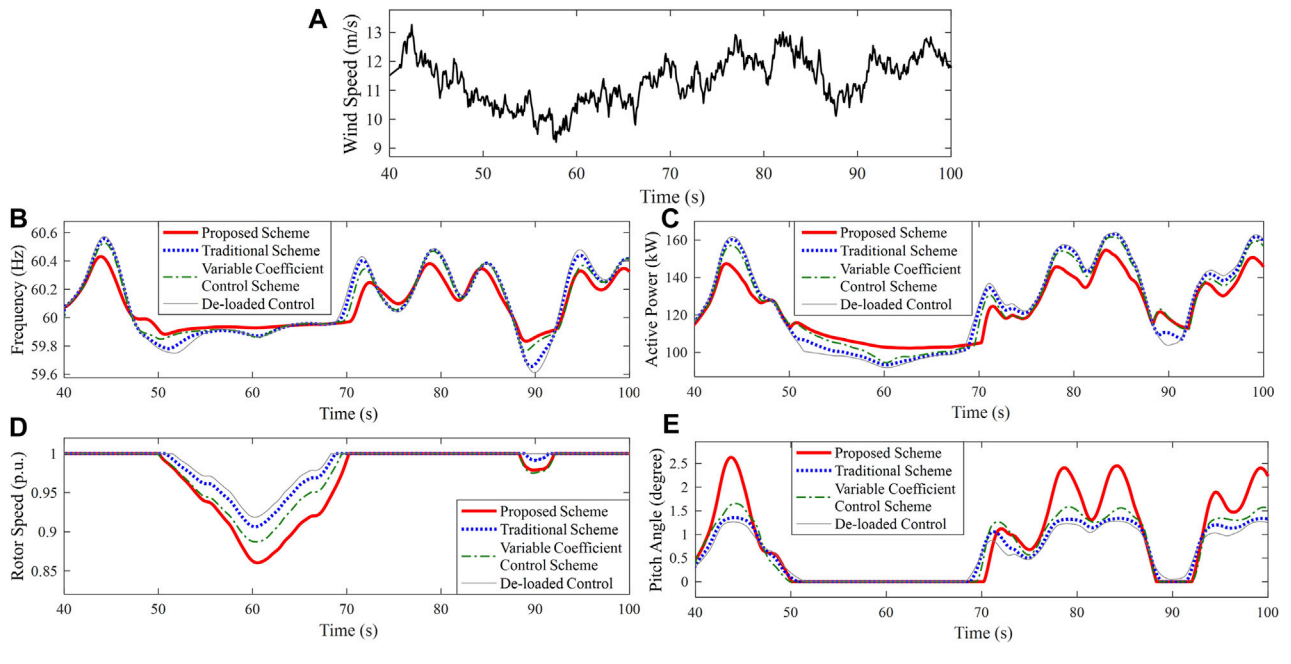

FIGURE 15 | Results for Case 6. **(A)** Random wind speed; **(B)** System frequency; **(C)** Active power of PMSG; **(D)** Rotor speed of PMSG; **(E)** Pitch angle.

scheme can better co-utilize pitch angle and rotor speed control to provide frequency support.

Case 4: the wind speed is set as 11 m/s; the load suddenly decreases by 15 kW at 50 s.The simulation result is shown in **Figure 13**. When the load decreases, if the PMSG-WTG is expected to regulate the frequency, the rotor speed should increase. However, the rotor speed has reached the maximum value during de loaded control in **Figure 13C**. Thus, the frequency deviation can be only suppressed by increasing the pitch angle, as shown in **Figure 13D**. When the PMSG adopts the proposed scheme, more active power can be released due to its potential self-adaption, as shown in **Figure 13B**. In **Figure 13A**, the peak frequency of the proposed scheme is 60.195 Hz, which is 0.01 Hz lower than the one of the variable coefficient control scheme, 0.03 Hz lower than that of the traditional scheme, and 0.04 Hz lower than that of the PMSG-WTG which does not participate in frequency regulation. The steady frequency is 60.08 Hz of the proposed scheme and variable coefficient control scheme, which is 0.02 Hz lower than that of the PMSG adopting the traditional scheme and 0.03 Hz lower than that of the PMSG which does not participate in frequency regulation.

High Wind Speed Area

Case 5: the wind speed is set as 14 m/s; the load suddenly increases by 15 kW at 50 s.The simulation result is shown in **Figure 14**.In a high wind speed area, the frequency is regulated by the pitch angle control. **Figure 14C** shows that the rotor speed

keeps 1 p.u. for all the control schemes. When the PMSG adopts the proposed scheme, there is a deeper pitch angle drop than that of the other two control scheme, as seen in **Figure 14D**.As shown in **Figure 14A**, when the PMSG adopts the proposed scheme, the FN is 59.86 Hz, More active power can be released due to potential self adaption of the proposed scheme in **Figure 14B**. Which is 0.07 Hz higher than that of the traditional scheme and 0.05 Hz higher than that of the variable coefficient control scheme. The steady frequency of the proposed scheme is 59.92 Hz, while the steady frequency of the traditional scheme and the traditional scheme is 59.9 and 59.91 Hz, respectively. Because of the adaptability of the proposed scheme, there is a deeper reduction of the pitch angle than that of other schemes.

Radom Wind Speed

Case 6: the actual measured wind speed (medium wind speed area) in Northeast China is introduced into the simulation model as seen in **Figure 15A**.Due to the change of wind speed, the output active power increases or decreases, resulting in the grid-side frequency fluctuation, as shown in **Figure 15A** and **Figure 15B**. Because of the wind turbines' participation in frequency regulation, all the traditional scheme, the variable coefficient control scheme, and the proposed scheme improve the frequency response. Compared with the other two control schemes, the proposed scheme has a potential adaptation, and additional power for frequency support adaptively changes with wind speed variation. As illustrated in **Figure 15D** and **Figure 15E**, when the PMSG adopts the proposed scheme, the rotor speed and pitch angle reduce more than other schemes, especially when wind speed is in a large section. Hence, the PMSG releases more active power. The proposed scheme provides better active power support so that the frequency fluctuation is small.The results of these cases clearly show that the proposed scheme can provide better frequency support than the other schemes for the whole wind speed range, regardless of low, medium, high, or random wind speeds. It has the potential to provide adaptive frequency support for different wind speeds.

CONCLUSION

This article proposes an equivalent rotor speed compensation control scheme of PMSG-WTG for frequency support in islanded microgrids. A new equivalent rotor speed variable of combined pitch angle and rotor speed is defined, which can find the rotor speed reference or compensation pitch angle reference according to the active power measurement. As a result, the wind turbine can simply regulate the rotor speed and pitch angle for de-loaded control during the whole wind speed area.

A virtual compensation rotor speed is provided to render PMSG-WTG rotor speed directly coupling grid frequency to generate both the inertial and primary frequency response. The virtual compensation rotor speed adaptively adjusts depending on the frequency deviation to maintain the proper torque comprising of the frequency regulation performance and wind turbine safe operation. Further, the pitch angle and torque are coordinated and regulated to provide frequency support in the medium and high wind speed area.

The simulation results under various conditions show that the proposed scheme has a potential self-adaption and provides adaptive frequency support for the whole wind area.

DATA AVAILABILITY STATEMENT

The original contributions presented in the study are included in the article/supplementary material; further inquiries can be directed to the corresponding author.

AUTHOR CONTRIBUTIONS

CZ and YL contributed to the conception and design of the study. CZ, YL, and YZ wrote the first draft of the manuscript. HL wrote sections of the manuscript. All authors contributed to manuscript revision and read and approved the submitted version.

REFERENCES

Adam, Milczarek., Mariusz, Malinowski., and Josep, M. Guerrero. (2015). Reactive Power Management in Islandedmicrogrid-Proportional Power Sharing in Hierarchical Droop Control. *IEEE Transa-ctions on Smart Grid.* 6 (4), 1631–1637. doi:10.1109/TSG.2015.2396639

Chang-Chien, L.-R., Lin, W.-T., and Yin, Y.-C. (2011). Enhancing Frequency Response Control by DFIGs in the High Wind Penetrated Power Systems. *IEEE Trans. Power Syst.* 26 (2), 710–718. doi:10.1109/tpwrs.2010.2052402

Chang-Chien, L.-R., Sun, C.-C., and Yeh, Y.-J. (2014). Modeling of Wind Farm Participation in AGC. *IEEE Trans. Power Syst.* 29 (3), 1204–1211. doi:10.1109/tpwrs.2013.2291397

Ekanayake, J., and Jenkins, N. (2004). Comparison of the Response of Doubly Fed and Fixed-Speed Induction Generator Wind Turbines to Changes in Network Frequency. *IEEE Trans. Energ. Convers.* 19 (4), 800–802. doi:10.1109/tec.2004.827712

Gao, D. W., Wu, Z., Yan, W., Zhang, H., Yan, S., and Wang, X. (2019). Comprehensive Frequency Regulation Scheme for Permanent Magnet Synchronous Generator-based Wind Turbine Generation System. *IET Renew. Power Generation.* 13 (2), 234–244. doi:10.1049/iet-rpg.2018.5247

Hu, J., Wang, S., Tang, W., and Xiong, X. (2017). Full-Capacity Wind Turbine with Inertial Support by Adjusting Phase-Locked Loop Response. *IET Renew. Power Generation* 11 (1), 44–53. doi:10.1049/iet-rpg.2016.0155

Kayikci, M., and Milanovic, J. V. (2009). Dynamic Contribution of DFIG-Based Wind Plants to System Frequency Disturbances. *IEEE Trans. Power Syst.* 24 (2), 859–867. doi:10.1109/tpwrs.2009.2016062

Lee, J., Jang, G., Muljadi, E., Blaabjerg, F., Chen, Z., and Cheol Kang, Y. (2016). Stable Short-Term Frequency Support Using Adaptive Gains for a DFIG-Based Wind Power Plant. *IEEE Trans. Energ. Convers.* 31 (3), 1068–1079. doi:10.1109/TEC.2016.2532366

Li, Shichun., Huang, Yuehua., and Wang, Lingyun., (2017). Modeling of Primary Frequency Modulation Auxiliary Control System for Doubly-Fed Wind Turbines Based on Speed Controln. *Proc. CSEE* 37 (24), 7077–7086.

Li, Xialin., Guo, Li., Wang, Chengshan., and Li, Yunwei. (2016). Overview of Research on Key Technologies of DC Microgrid. *Proc. CSEE* 36 (1), 2–17.

Liu, T., Pan, W., Quan, R., and Liu, M. (2019). A Variable Droop Frequency Control Strategy for Wind Farms that Considers Optimal Rotor Kinetic Energy. *IEEE Access* 7, 68636–68645. doi:10.1109/access.2019.2914496

Luo, H., Hu, Z., Zhang, H., and Chen, H. (2019). Coordinated Active Power Control Strategy for Deloaded Wind Turbines to Improve Regulation Performance in AGC. *IEEE Trans. Power Syst.* 34 (1), 98–108. doi:10.1109/tpwrs.2018.2867232

Margaris, I. D., Papathanassiou, S. A., Hatziargyriou, N. D., Hansen, A. D., and Sorensen, P. (2012). Frequency Control in Autonomous Power Systems with High Wind Power Penetration. *IEEE Trans. Sustain. Energ.* 3 (2), 189–199. doi:10.1109/tste.2011.2174660

Sun, C., Ali, S. Q., Joos, G., and Bouffard, F. (2019). "Improved VSG Control for Type-IV Wind Turbine Generator Considering Operation Limitations," in 2019 IEEE Energy Conversion Congress and Exposition (ECCE), 29 Sept.-3 Oct. 2019 (Baltimore, MD, USA: IEEE), 2085–2091. doi:10.1109/ecce.2019.8912663

Tang, X., Yin, M., Shen, C., Xu, Y., Dong, Z. Y., and Zou, Y. (2019). Active Power Control of Wind Turbine Generators via Coordinated Rotor Speed and Pitch Angle Regulation. *IEEE Trans. Sustain. Energ.* 10 (2), 822–832. doi:10.1109/tste.2018.2848923

Wu, Y.-K., Yang, W.-H., Hu, Y.-L., and Dzung, P. Q. (2019). Frequency Regulation at a Wind Farm Using Time-Varying Inertia and Droop Controls. *IEEE Trans. Ind. Applicat.* 55 (1), 213–224. doi:10.1109/tia.2018.2868644

Wu, Z., Gao, W., Gao, T., Yan, W., Zhang, H., Yan, S., et al. (2018). State-of-the-art Review on Frequency Response of Wind Power Plants in Power Systems. *J. Mod. Power Syst. Clean. Energ.* 6 (1), 1–16. doi:10.1007/s40565-017-0315-y

Wu, Z., Gao, W., Wang, X., Kang, M., Hwang, M., Kang, Y. C., et al. (2016). Improved Inertial Control for Permanent Magnet Synchronous Generator Wind Turbine Generators. *IET Renew. Power Generation* 10 (9), 1366–1373. doi:10.1049/iet-rpg.2016.0125

Zeng, X., Liu, T., Wang, S., Dong, Y., and Chen, Z. (2019). Comprehensive Coordinated Control Strategy of PMSG-Based Wind Turbine for Providing Frequency Regulation Services. *IEEE Access* 7, 63944–63953. doi:10.1109/access.2019.2915308

Zertek, A., Verbic, G., and Pantos, M. (2012). A Novel Strategy for Variable-Speed Wind Turbines' Participation in Primary Frequency Control. *IEEE Trans. Sustain. Energ.* 3 (4), 791–799. doi:10.1109/tste.2012.2199773

Zhang, Z.-S., Sun, Y.-Z., Lin, J., and Li, G.-J. (2012). Coordinated Frequency Regulation by Doubly Fed Induction Generator-Based Wind Power Plants. *IET Renew. Power Gener.* 6 (1), 38–47. doi:10.1049/iet-rpg.2010.0208

Zhao, Jingjing., Li, Min., and He, Xinqin. (2019). Coordinated Control Scheme of Wind Power and Energy Storage in Frequency Regulation Based on Torque Limit Control. *Trans. China Electrotechnical Soc.* 34 (23), 4982–4990.

Zhao, J., Lv, X., and Fu, Y. (2015). "Wind-solar Diesel Microgrid Frequency Adjustment Technology Based on Variable Coefficient-Based Virtual Inertia and Overspeed Control Coordination of Doubly-Fed Wind Turbines",. *J. Electrotechnical Eng.* 30 (5), 59–68. (In Chinese).

Zhao, X., Xue, Y., and Zhang, X.-P. (2020). Fast Frequency Support from Wind Turbine Systems by Arresting Frequency Nadir Close to Settling Frequency. *IEEE Open J. Power Energ.* 7, 191–202. doi:10.1109/oajpe.2020.2996949

Zhu, Xiaorong., Zheng, Li., and Meng, Fanqi. (2021). Stability Analysis of DC Microgrid Based on Different Grid Structures. *Trans. China Electrotechnical Soc.* 36 (1), 166–178.

Zhu, Y., Liu, S., and Wang, W. (2021). Comprehensive Coordinated Control Strategy of PMSG-based Wind Turbine for System Inertia Support. *IET Renew. Power Generation* 15, 1915–1926. doi:10.1049/rpg2.12115

Conflict of Interest: Author YZ was employed by State Grid Shandong Electric Power Company.

The remaining authors declare that the research was conducted in the absence of any commercial or financial relationships that could be construed as a potential conflict of interest.

Publisher's Note: All claims expressed in this article are solely those of the authors and do not necessarily represent those of their affiliated organizations, or those of the publisher, the editors, and the reviewers. Any product that may be evaluated in this article, or claim that may be made by its manufacturer, is not guaranteed or endorsed by the publisher.

frontiers in Energy Research

ORIGINAL RESEARCH
published: 26 August 2021
doi: 10.3389/fenrg.2021.717089

Optimized Placement of Voltage Sag Monitors Considering Distributed Generation Dominated Grids and Customer Demands

Ying Wang, Haishan He, Qiang Fu, XianYong Xiao and Yunzhu Chen*

College of Electrical Engineering, Sichuan University, Chengdu, China

Voltage sag causes serious economic losses to sensitive customers. However, the existing optimal placement methods of sag monitors ignore the economic needs of customers. The optimal placement model of voltage sag monitor is proposed in this paper, which considers the sag economic loss weight, realizes the redundant coverage of important customers, and reduces the risk of sag loss of them. The model is also suitable for the system with a large number of DG access. Firstly, the calculation model of exposed area based on Chebyshev iterative method is established to obtain the system exposed area quickly, and the influence of DG replacing traditional generator on exposed area and economic loss is analyzed qualitatively. Then, the economic loss is quantitatively evaluated based on the exposed area. What's more, the priority of important customers is determined accordingly, and the optimal placement model of sag monitor is proposed. Finally, simulation results show that in large-scale DG access, the customer's economic loss caused by sag will increase. Compared with traditional methods, this method can reduce the risk of loss and ensure the economic benefits of important customers.

Keywords: voltage sag, customer value, Chebyshev, optimization, economic loss, distributed generation

OPEN ACCESS

Edited by:
Dongdong Zhang,
Guangxi University, China

Reviewed by:
Ahmad Asrul Ibrahim,
National University of Malaysia, Malaysia
Narottam Das,
Central Queensland University, Australia

****Correspondence:***
Qiang Fu
fuqiang346@qq.com

Specialty section:
This article was submitted to Smart Grids, a section of the journal Frontiers in Energy Research

Received: *30 May 2021*
Accepted: *13 August 2021*
Published: *26 August 2021*

Citation:
Wang Y, He H, Fu Q, Xiao X and Chen Y (2021) Optimized Placement of Voltage Sag Monitors Considering Distributed Generation Dominated Grids and Customer Demands. Front. Energy Res. 9:717089. doi: 10.3389/fenrg.2021.717089

INTRODUCTION

Voltage sag is an event caused by a sudden large current in the system and has become a major threat to the normal and safe operation of electrical equipment in power systems. Relevant US power research institutes indicate that sags cause economic losses to customers as high as 26 billion dollars each year (Chun-Tao and Jian-Tong, 2015). Therefore, customers are paying more attention to voltage sag (Ansal, 2020). Timely and accurate monitoring of sags helps to quickly facilitate control measures, thereby minimizing the risk of customers' economic losses. However, it is difficult to install monitors at each node in the actual process due to installation cost constraints (Sun et al., 2021). The risk of customers missing sag treatment opportunities is significantly increased when sag sensitive areas are unmonitored due to failure or an insufficient number of monitors. From this point of view, the number of monitors and the risk of customers suffering sag economic losses are conflicting goals. Satisfying the power demand of customers is an important task of power grid companies. Therefore, under the constraint of sag observability, it is of great theoretical value and engineering significance to develop a multi-objective optimal placement model considering the number of monitors and the risk of customer sag economic loss. In addition, the scope of the voltage sag sensitive area is further expanded (Wang et al., 2019; Zhang et al., 2021) due to new energy grid capacity limitations and control characteristics (Fu et al., 2021a; Tian et al., 2021), which correspondingly increase the risk of

the above-mentioned missed measurement events for customers. Therefore, in a power grid dominated by distributed power generation (Du et al., 2020; Du et al., 2021), it is essential to consider the economic losses of customers in the optimal placement of monitors.

At present, much work has been done at home and abroad to optimize the placement of sag monitors. The most important research method is the Monitor Reach Area (MRA) method (Olguin et al., 2006). In this method, the sag caused by any short circuit of the line can be recognized by at least one sag monitor as a constraint condition, and the goal is to develop an optimized monitor installation plan with the minimum number of monitors (Espinosa-Juarez et al., 2009). Programming algorithms, such as genetic, particle swarm, and integer linear can be used to solve this problem (Espinosa-Juarez et al., 2009; Almeida and Kagan, 2011; Zhou and Tian, 2014). Unfortunately, in practical applications, the monitoring schemes obtained by applying these models are usually not unique, and it is difficult to select an optimal solution. The placement lacks pertinence because the existing placement process methods default to all nodes in the power system being equally important, ignoring the complexity of the actual operation process of the system. Thus, the optimization conditions are insufficient and it is difficult to find an optimal solution. Subsequent studies helped to determine an optimal placement plan solution by introducing new optimization goals, such as the largest sag observability index (Jiang et al., 2020), largest sag severity index (Ibrahim et al., 2010), largest sag weight coefficient (Šipoš et al., 2021), smallest uncertainty area index (Zhang et al., 2019), and largest immunity index (Luo et al., 2019). These studies can uniquely determine the monitoring plan for sags but mainly focus on the system side and ignore the monitoring demands of sensitive customers. In addition, the number of monitors increase in some of these studies to meet the new optimization goals.

Based on the above analysis, an optimized voltage sag monitor placement model is proposed that simultaneously considers the demands of customers and the power grid and can be used in a power grid dominated by DG. In the first step, an exposed area calculation method based on the Chebyshev iteration is proposed to solve the problem of slow convergence in the exposed area calculation process, which significantly improves the calculation efficiency. Then it is theoretically proved that the replacement of traditional generators by DG will increase the exposed area of the same sensitive node and aggravate the economic losses caused by the failure. In other words, when the total generator output remains unchanged, the severity of voltage sag increases with the increase of DG penetration rate. In the second step, a method to describe a customer's sag economic loss is proposed based on the concept of the exposed area. According to the sag economic loss, the customer nodes are classified into different important levels. Intuitively, a customer's monitoring demand for sags is to ensure that the sag can be monitored and managed in real-time to minimize their economic loss. A sag must first be monitored before it can be managed. From this point of view, the monitor should cover areas with serious economic losses. When a sag occurs, the economic loss caused by the omission of the monitor can be avoided. Therefore, in the third step, the objectives are to use the minimum number of monitors to facilitate the maximum coverage of an area with serious economic loss to customers caused by a sag. The observability of sag in the entire network is taken as the constraint to form a multi-objective optimal placement model. The fourth step is to use the IEEE 30-node system to test the proposed model. In the proposed case, the impact of different DG penetration rates on the scope of the exposed area and the customer's economic loss is analyzed. Additionally, the necessity of considering the customer's economic loss in the process of optimizing the placement is discussed. The simulation results show that the proposed model has practical application value and can reduce the risk of customers' sag economic loss while reducing the number of sag monitors and uniquely determining the monitoring plan for sags.

EXPOSED AREA CALCULATION

The key to the exposed area calculation is to find the critical position where the sag amplitude of the busbar where the sensitive load is located is lower than the set sag threshold when a short-circuit fault occurs in the line. When the fault point moves on a certain line in the system, the sag amplitude at the busbar, where the sensitive load is located, is a unimodal function with a downward opening, approximated to a quadratic function. It is possible to directly use the sag amplitude at the three positions of 0, 0.5, and 1 on the line for quadratic interpolation and form an equation with the sag threshold to solve the critical point (Park and Jang, 2007). In addition, the golden section method was proposed to improve the calculation speed and accuracy of the critical value (Ma et al., 2019). The key process for solving the exposed area is discussed in the following sections.

Calculation of Residual Voltage at Load

A short-circuit of the line in the system is the main reason for a sag of the sensitive load bus. Therefore, to solve the exposed area, it is first necessary to obtain the residual voltage of the load under different short-circuit types. The short-circuit calculation model of the power system is shown in **Figure 1**.

We suppose that m is the sensitive bus, the fault is at f in line i-j between nodes i and j, R_f is the fault resistance, and p is the normalized distance from the fault location to node i. First, the power flow calculation is performed and each sequence impedance is formed. Then, the three-phase voltage amplitude of the sensitive bus m is obtained under different fault types and the smallest absolute value is used as the sag amplitude. That is, $\left|V_m^{fault}\right| = \min\left(\left|V_{A,m}^{fault}\right|, \left|V_{B,m}^{fault}\right|, \left|V_{C,m}^{fault}\right|\right)$. The calculation formula can be found in (Buzo et al., 2021).

Branch Discriminant Matrix Calculation

After the short-circuit calculation is completed, it is necessary to form discriminant matrices $\boldsymbol{B_{sag}}$ and $\boldsymbol{L_{sag}}$ according to the calculation results in subsection A to determine the inclusion of different bus nodes and lines in the sensitive bus-exposed area.

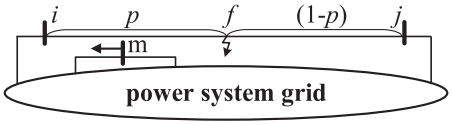

FIGURE 1 | Model of power system short-circuit calculation.

First, the sag amplitude vector $\boldsymbol{V_{sag}}$ of the bus node m is calculated, using:

$$\boldsymbol{V_{sag}} = \left[\left|V_m^{fault\_1}\right| \quad \cdots \quad \left|V_m^{fault\_u}\right| \quad \cdots \quad \left|V_m^{fault\_n}\right| \right]^{\mathrm{T}} \tag{1}$$

where $\left|V_m^{fault\_u}\right|$ denotes the sag amplitude at bus m when bus u fails, and n is the total number of buses in the system. Then, the discriminant matrices $\boldsymbol{B_{sag}}$ and $\boldsymbol{L_{sag}}$ are formed to determine the calculation lines required by the Chebyshev iteration method. The element $b_{sag,u}$ of the $\boldsymbol{B_{sag}}$ matrix is determined by the difference $\boldsymbol{\Delta V_{sag}}$ between the sag amplitude vector $\boldsymbol{V_{sag}}$ of bus m and the sag threshold vector $\boldsymbol{V_{th}}$, expressed as:

$$\boldsymbol{\Delta V_{sag}} = \left[\Delta v_{sag,1} \cdots \Delta v_{sag,u} \cdots \Delta v_{sag,n}\right]^{\mathrm{T}} \boldsymbol{V_{sag}} - \boldsymbol{V_{th}} \tag{2}$$

$$b_{sag,u} = \begin{cases} 1; \text{if} \Delta v_{sag,u} \le 0 \\ 0; \text{if} \Delta v_{sag,u} > 0 \end{cases} \tag{3}$$

If the number of lines is v, the parameter matrix $\boldsymbol{L_{sag}}$ of the line can be further determined according to the matrix $\boldsymbol{B_{sag}}$, expressed as:

$$\boldsymbol{L_{sag}} = \begin{bmatrix} l_{sag,1} \\ \vdots \\ l_{sag,v} \end{bmatrix} = \begin{bmatrix} \vdots \\ b_{sag,i} \\ \vdots \end{bmatrix} + \begin{bmatrix} \vdots \\ b_{sag,j} \\ \vdots \end{bmatrix} \tag{4}$$

where i and j represent the node numbers of the busbars at both ends of the corresponding line where they are located. When the element in $\boldsymbol{L_{sag}}$ is 0, the corresponding line i-j is not in the m-exposed area, and no subsequent calculation is required. When it is 1, the line i-j contains a critical point, and 2 denotes two critical points.

Chebyshev Iterative Method to Calculate Critical Point of the Line

The number of critical points in the line can be obtained through the discriminant matrix in *Branch Discriminant Matrix Calculation* subsection. Next, on the basis of *Branch Discriminant Matrix Calculation* Subsection, the specific position of the critical point is solved by curve fitting. When calculating the critical point of the line, the convergence speed of the dichotomy method (Park and Jang, 2007) is the same as the geometric series with a common ratio of 0.5. The golden section method (Ma et al., 2019) has two division points for each contraction interval, 0.618 and 0.382. Thus, in the worst case, the convergence speed is slower than the dichotomy method. To improve the computational efficiency, this study proposes the use of the Chebyshev iteration method with a third-order convergence rate, expressed as:

$$x_{k+1} = x_k - \frac{f(x_k)}{f'(x_k)} - \frac{f''(x_k)\left[f(x_k)\right]^2}{2\left[f'(x_k)\right]^3} \tag{5}$$

Theoretically, the Chebyshev iteration method has the fastest convergence rate among the three methods. $\boldsymbol{L_{sag}}$ must first be calculated to determine the critical point in the line. When $l_{sag,v} = 0$, line v is outside the exposed area at this time. When $l_{sag,v} = 1$, there is only one critical point on the line. First, the sag amplitude $\left|f(0.5)\right|$ of bus m at position $p = 0.5$ on the line i-j is calculated, and the sag amplitudes $\left|V_m^{fault\_i}\right|$ and $\left|V_m^{fault\_j}\right|$ of bus m at the end of the fault are combined. The quadratic curve of the sag amplitude changing with the line fault point is fitted and expressed as $f(p) = dp^2 + ep + g$, where d, e, and g are constants. Next, the Chebyshev iteration method is used to solve the critical point. The line has two critical points when $l_{sag,v} = 2$. To obtain an accurate solution, it is first necessary to solve the fault point $p_{\max}$ that maximizes the m sag amplitude in the line, which is used to preliminarily divide the range of the two solutions, p_1 and p_2. That is, $0 \le p_1 < p_{\max}$ and $p_{\max} < p_2 \le 1$. Then, the Chebyshev iteration method is used in their respective intervals to solve the exact values of the two critical points. The fitting curve f is a quadratic curve, so its first and second derivatives on (0, 1) exist and are continuous. Therefore, the initial iteration value can be 0.5 and the tangent method iteration formula can be used to quickly obtain the extreme point $p_{\max}$, expressed as:

$$x_{k+1} = x_k - \frac{f'(x_k)}{f''(x_k)} \tag{6}$$

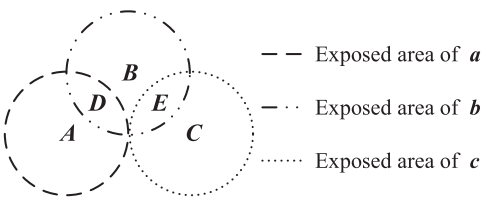

FIGURE 2 | Schematic diagram of economic losses caused by short circuits in different areas.

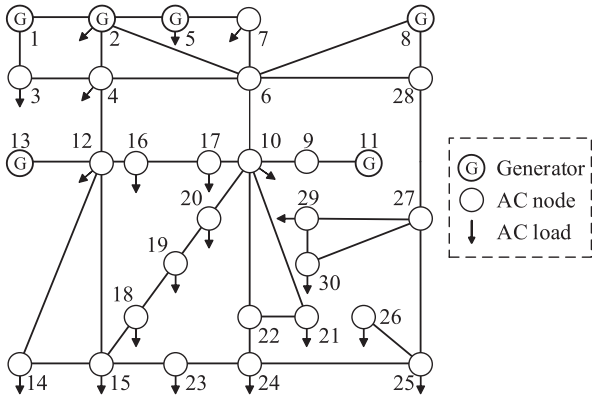

FIGURE 3 | Schematic diagram of IEEE 30-node system.

The condition for the end of the above iteration is $f^{'}(x_k) < \varepsilon$, where $\varepsilon > 0$ represents the calculation accuracy. The extreme point $p_{\max}$ is obtained from the solution and combined with the endpoint value, and the quadratic curve is fitted again. Then, the exact solution can be obtained using the Chebyshev iteration method in the respective intervals of the two solutions. The lines in the system are traversed and the calculation process is repeated to obtain the exposed area of bus node *m*.

Impact of Distributed Generator (DG) Replacement of Ordinary Generator on the Scope of the Exposed Area

This subsection qualitatively analyzes the impact of replacing the original ordinary generator of the system with DG on the exposed area of load node. *Calculation of Residual Voltage at Load*, *Branch Discriminant Matrix Calculation*, and *Chebyshev Iterative Method to Calculate Critical Point of the Line* Subsections provide quantitative calculation methods for this scene. The original ordinary generator is used as PV node in the system, and the replaced DG is used as PQ node in the system (Fu et al., 2021b). The proportion of DG to the total active capacity of all generators in the system is taken as the proportion of DG. After the short circuit, PQ node's voltage support capacity is weaker than that of PV node (Kumar et al., 2020a; Kumar et al., 2020b), so the higher the proportion of DG, the lower the sag amplitude of load node and the higher the vulnerability of voltage sag.

In order to study the change of voltage before and after short circuit when PV node is replaced by PQ node with the same active power, it is assumed that the same node in the system switches between PQ and PV. When there is no short circuit in the system, the other nodes outside PQ (PV) node can be equivalent to an impedance Z_s, which is $R_s + jX_s$. The admittance form of impedance is $Y_s = G_s + jB_s$. G_s and B_s are their conductance and admittance respectively.

$$\begin{cases} G_s = \dfrac{R_s}{R_s^2 + X_s^2} \\ B_s = \dfrac{X_s}{R_s^2 + X_s^2} \end{cases} \tag{7}$$

For PQ node, the equation is as follows:

$$\begin{cases} G_s\left(e_{s1}^2 + f_{s1}^2\right) = P_1 \\ B_s\left(e_{s1}^2 + f_{s1}^2\right) = Q_1 \\ e_{s1}^2 + f_{s1}^2 = \left(P_1 + jQ_1\right)/Y_s \end{cases} \tag{8}$$

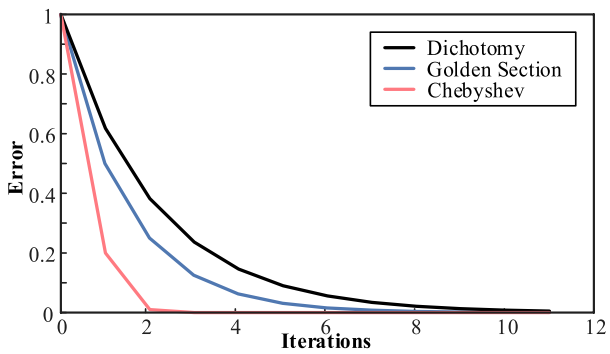

FIGURE 4 | Comparison chart of the relationship between error and number of iterations.

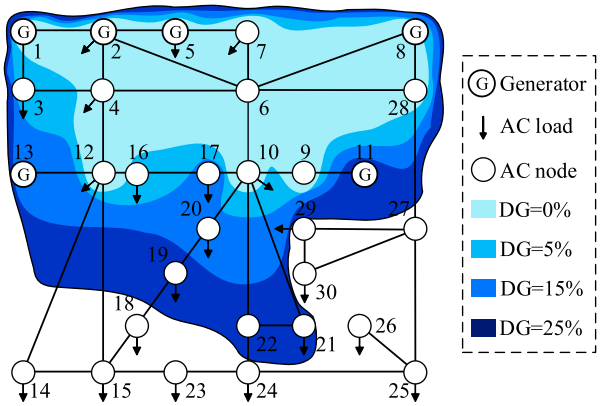

FIGURE 5 | Exposed area under different DG penetration rate.

e_{s1} and f_{s1} are the real and imaginary parts of voltage U_{s1} at PQ node, P_1 and Q_1 are the active and reactive power flowing through PQ node respectively. For PV nodes, the equation is as follows:

$$\begin{cases} G_s\left(e_{s2}^2 + f_{s2}^2\right) = P_2 \\ e_{s2}^2 + f_{s2}^2 = U_{s2} \\ e_{s2}^2 + f_{s2}^2 = \left(P_2 + jQ_2\right)/Y_s \end{cases} \tag{9}$$

Among them, e_{s2} and f_{s2} are the real and imaginary parts of the voltage U_{s2} at the PV node, P_2 and Q_2 are the active and reactive power flowing through the PV node respectively.

During normal operation, make the two operating states consistent, that is, $P_1 = P_2$, $Q_1 = Q_2$, $U_{s1} = U_{s2}$. When the short-circuit fault occurs, the equivalent impedance Z_s decreases due to the parallel connection of short-circuit impedance. The absolute values of resistance and reactance change are respectively: ΔR_s and ΔX_s. The equivalent conductance and equivalent reactance after short circuit can be obtained by **Eq. 7** can be expressed as follows:

$$\begin{cases} G_s' = \dfrac{R_s - \Delta R_s}{\left(R_s - \Delta R_s\right)^2 + \left(X_s - \Delta X_s\right)^2} \\ B_s' = \dfrac{X_s - \Delta X_s}{\left(R_s - \Delta R_s\right)^2 + \left(X_s - \Delta X_s\right)^2} \end{cases} \tag{10}$$

It can be obtained from **Eq. 7** and **Eq. 10**

$$\begin{cases} \Delta G_s = G_s' - G_s > 0 \\ \Delta B_s = B_s' - B_s > 0 \end{cases} \tag{11}$$

When PQ node is short circuited, it can be concluded from **Eq. 8** and **Eq. 10** that under constant active power control, the node voltage U_{s1}' satisfies the following relation:

$$U_{s1}'^2 = \frac{P_1}{\left(G_s + \Delta G_s\right)} = \frac{P_1 + jQ_1}{\left(G_s + \Delta G_s\right) + j\left(B_s + \Delta B_s\right)} \tag{12}$$

① Assuming that the upper limit of reactive power output of PV node after short circuit is greater than the reactive power required by the support voltage, the PV node voltage U_{s2}' does not change.

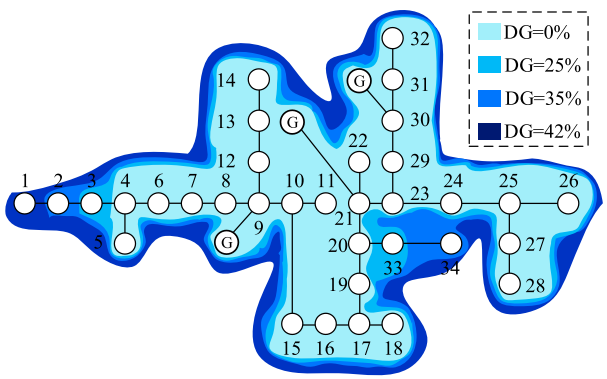

FIGURE 6 | Exposed area under different DG penetration rate.

TABLE 1 | Placement plan obtained by traditional method.

Plan number	Node number	Plan number	Node number
1	2,24	10	5,27
2	2,25	11	5,29
3	2,26	12	5,30
4	2,27	13	7,24
5	2,29	14	7,25
6	2,30	15	7,26
7	5,24	16	7,27
8	5,25	17	7,29
9	5,26	18	7,30

$$U_{s2}'^2 = U_{s2}^2 = \frac{P_2}{G_s} = \frac{P_1}{G_s} > U_{s2}'^2 \tag{13}$$

② Assuming that the upper limit of reactive power output of PV node is lower than the reactive power required by support voltage after short circuit, PV node can provide partial reactive power, reactive power Q_2' to the upper limit of reactive power output Q_{m} ($Q_{\mathrm{m}} > Q_1$), voltage U_{s2}' will be less than U_{s2}.

$$U_{s2}'^2 = \frac{P_2 + jQ_{\mathrm{m}}}{(G_s + \Delta G_s) + j(B_s + \Delta B_s)} > U_{s2}'^2 \tag{14}$$

It can be concluded from **Eq. 13** and **Eq. 14**: when the original ordinary generator of the system is replaced by DG controlled by constant active power of the same active capacity, the depth of voltage sag will intensify, which will lead to the expansion of exposed area and increase the economic loss of sag, and further clarify the necessity of considering the economic loss of voltage sag in the Grid dominated by distributed generation.

OPTIMIZED PLACEMENT OF VOLTAGE SAG MONITORS

Calculation of Customer Sag Economic Loss Based on Exposed Area

The exposed area is a concept for a bus node. In the actual operation of a power system, customers must be distributed on multiple buses and the exposed areas of multiple busbar nodes can be simultaneously calculated. The more severe the overlap of the exposed areas, the more sensitive customers will be affected by the short circuit of the busbar nodes, subsequently causing more serious economic losses. This phenomenon is shown in **Figure 2**.

TABLE 2 | Customers' economic losses caused by the sag.

Business	Sag annual economic loss/ten thousand yuan
cotton textiles	200
tobacco products	350
Biopharmaceutical	50
electronic product processing	400
government affairs data center	100
logistics processing	250
food additives	270
health products	80
man-made board	220

We assume that *a, b*, and *c* are three busbars randomly selected from the system and their exposed areas intersect to create five areas, *A, B, C, D,* and *E*, as shown in **Figure 2**. Now a new concept Sag Risk Level (SRL) is introduced to further characterize the sag sensitive area in the system. SRL is corresponding to the redudancy or intersections of exposed areas. For example, the SRL values of areas D and E in **Figure 2** are the same. (See *Analysis of Customer Sag Economic Loss* and **Appendix A** for details). If the influence of the remaining busbars and lines are temporarily ignored, then the three bus-exposed areas are independently short-circuited and cause their own sags. The economic losses to customers are originally ll_a, ll_b, and ll_c. Subsequently, the economic losses to customers caused by faults in the five areas are ll_a, ll_b, ll_c, $ll_a + ll_b$, and $ll_b + ll_c$. (See **Appendix A** for details). From this point of view, the economic losses to customers caused by short circuits in different exposed areas, or even different areas in the same exposed area in the system, are also different. The monitor placement should consider the sag in the entire power grid. This will reduce the risk of economic loss to customers caused by failures in exposed areas that are not monitored in real-time and facilitate corrective measures. Monitoring redundancy should also be improved in the exposed areas that could cause higher economic losses during a fault.

First, to reflect the economic losses caused by independent failures in each busbar exposed area, the vector $\boldsymbol{LE}$ is introduced as:

$$\boldsymbol{LE} = \begin{bmatrix} le_1 & le_2 & \cdots & le_n \end{bmatrix}^{\mathrm{T}} \tag{15}$$

where n represents the number of busbar nodes in the system and the element $le_x, x \in [1, n]$ represents the economic loss to customers when a short circuit occurs independently in the exposed area of node x. The economic loss of customers is obtained through investigation, and the unit of economic loss is yuan. Second, a binary matrix $\boldsymbol{LC}$ is formed according to the calculation result of the exposed area to reflect whether the line is included in the exposed area of the bus, expressed as:

$$\boldsymbol{LC} = \begin{bmatrix} lc_{11} & lc_{12} & \cdots & lc_{1l} \\ lc_{21} & lc_{22} & \cdots & lc_{2l} \\ \vdots & \vdots & lc_{cd} & \vdots \\ lc_{n1} & lc_{n2} & \cdots & lc_{nl} \end{bmatrix} \tag{16}$$

where the subscript n represents the number of system nodes, l represents the total number of system lines, and when the system determines, l is also determined. Its element lc_{cd} obtains a value according to the following formula:

$$lc_{cd} = \begin{cases} 1; \text{line } d \text{ is in the exposed area of bus } c \\ 0; \text{Other situations} \end{cases} \tag{17}$$

Assuming that the failure probability of each line is equal, the vector $\boldsymbol{LO}$ reflecting a customer's economic loss caused by a sag can be obtained using:

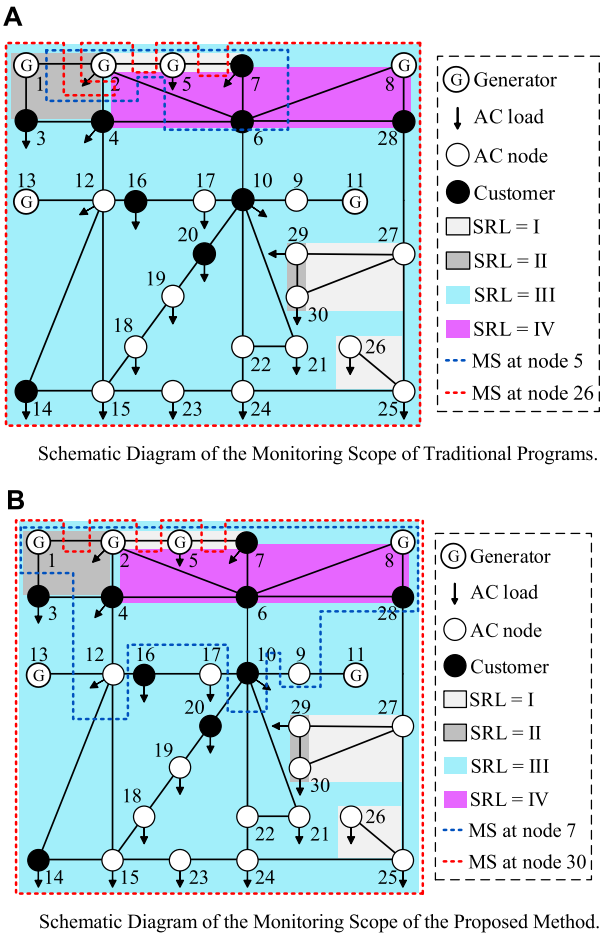

FIGURE 7 | Comparison of the monitoring scope of the two schemes.

$$\boldsymbol{LO} = \frac{\boldsymbol{LC} \cdot (\boldsymbol{LC})^{\mathrm{T}} \cdot \boldsymbol{LE}}{l} \tag{18}$$

The above formula is the case for a single fault type. The element value of vector $\boldsymbol{LO}$ represents the expected value of economic loss to customers monitored by different nodes. However, the matrix $\boldsymbol{LC}$ is different for different fault types. Finally, to comprehensively consider the four types of faults, the $\boldsymbol{LO}$ needs to be modified as follows:

$$\boldsymbol{LO} = \lambda_1 \boldsymbol{LO}^1 + \lambda_2 \boldsymbol{LO}^2 + \lambda_3 \boldsymbol{LO}^3 + \lambda_4 \boldsymbol{LO}^4 \tag{19}$$

where $\boldsymbol{LO}^1$, $\boldsymbol{LO}^2$, $\boldsymbol{LO}^3$, and $\boldsymbol{LO}^4$ represent the customer's economic loss vector for three-phase, single-phase, two-phase, and two-phase grounding short circuits, respectively, and the coefficients $\lambda_1, \lambda_2, \lambda_3$, and λ_4 represent the respective probability of occurrence of these types of faults.

Monitor Reach Area Matrix Calculation

A sag caused by a short circuit is random, and the key to the placement of the sag monitor is whether it can accurately identify a sag event caused by any short-circuit fault. The observability of the voltage sag of the system can be reflected by the MRA matrix. Assuming that the number of nodes in the system is n and the number of line segments is s, the MRA matrix $\boldsymbol{M}^w$ under any short-circuit fault type can be expressed as:

$$\boldsymbol{M}^w = \begin{bmatrix} m_{11}^w & m_{12}^w & \cdots & m_{1s}^w \\ m_{21}^w & m_{22}^w & \cdots & m_{2s}^w \\ \vdots & \vdots & m_{ab}^w & \vdots \\ m_{n1}^w & m_{n2}^w & \cdots & m_{ns}^w \end{bmatrix} \tag{20}$$

where w represents four types of faults, and its values 0, 1, 2, and 3 represent the three-phase, single-phase grounding, two-phase, and two-phase grounding short circuits, respectively. $\boldsymbol{M}^w$ is a binary matrix, expressed as:

$$m_{ab}^w = \begin{cases} 1 & V_{ab} \le V_{th} \\ 0 & V_{ab} > V_{th} \end{cases} \tag{21}$$

where $a = 1, 2, \cdots n$, $b = 1, 2, \cdots s$, V_{ab} represents the sag amplitude at node b when the line section a is short-circuited, and V_{th} represents the sag threshold set by the sag monitor. When the element $m_{ab} = 1$ in the matrix, it

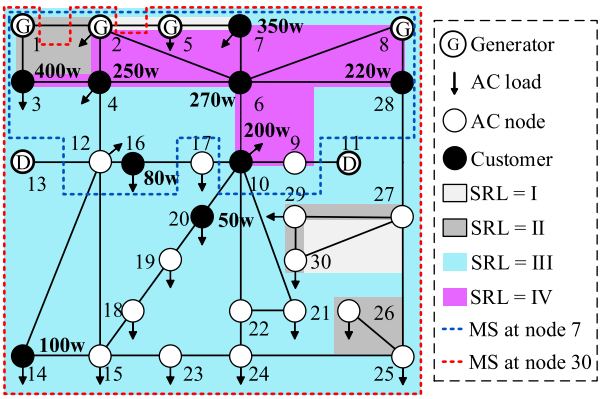

FIGURE 8 | Monitoring scope of case B2.

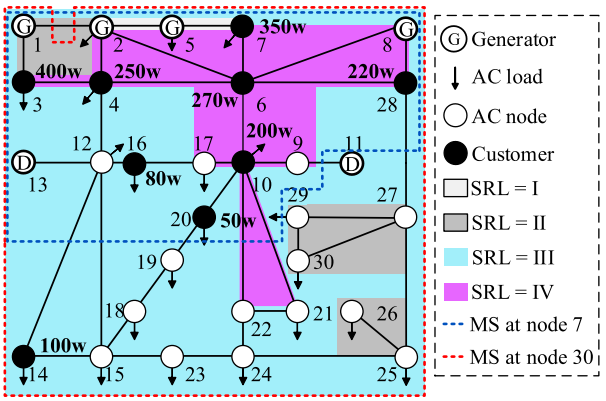

FIGURE 9 | Monitoring scope of case B3.

means that a short circuit in line segment a will cause node b to sag and will be monitored. Conversely, a value of 0 means that it cannot be monitored. If some nodes can be determined and the union of the monitoring scopes can cover the entire power system, it is not necessary to place monitors at all nodes to observe considerable sags in the entire grid. This is because the rows in the $\boldsymbol{M}^{w}$ matrix represent the sag monitoring scope of the corresponding node.

Multi-Objective Optimization Placement of Voltage Sag Monitors That Considers the Number of Monitors and Risk of Customer Sag Economic Loss

This section forms an optimal placement model based on the calculation results of sections A and B. Assuming a total of n nodes in the system, the decision vector for configuring the sag monitors can be expressed as:

$$\boldsymbol{X} = \begin{bmatrix} x_1 & x_2 & \cdots & x_n \end{bmatrix} \tag{22}$$

$\boldsymbol{X}$ is a binary vector, and its elements are obtained according to:

$$x_i = \begin{cases} 1; \text{ if monitor is needed at } i \\ 0; \text{ if monitor is not needed at } i \end{cases} \tag{23}$$

where $i = 1, 2, \cdots n$. The sag in the entire power grid is considered as a constraint. Thus, the basic principle is that the sag caused by any fault can be recorded by at least one monitor, expressed as:

$$\sum_{i=1}^{n} x_i m_{ij} \geq 1 \tag{24}$$

Considering the high cost of monitors in practical applications, the placement of a minimum number of monitors is the first-level goal, expressed as:

$$\min\ f_1 = \sum_{i=1}^{n} x_i \tag{25}$$

The above placement method defaults to all nodes being equally important. In addition, insufficient optimization conditions result in a non-unique placement scheme. For a long time, the primary task of electric power companies was to meet the electricity demand of customers. However, the sag monitor should now be placed with an emphasis on reducing the risk of economic loss for sensitive customers. Using the economic loss vector shown in **Eq. 19**, the secondary target is ensuring that the monitor covers the maximum scope of the area where the customer's economic loss is the most serious. This is expressed as:

$$\max\ f_2 = \sum_{i=1}^{n} x_i \cdot lo_i \tag{26}$$

To facilitate the solution, it needs to be deformed according to the actual characteristics of the two objective functions. By introducing a priority factor to **Eq. 25**, the two goals can be transformed into the following equation:

$$\min\ f = \alpha \sum_{i=1}^{n} x_i - \sum_{i=1}^{n} x_i \cdot lo_i \tag{27}$$

To determine the value of α, a sensitivity analysis is performed on **Eq. 26**. The number of sag monitors is changed by one, expressed as:

$$\Delta \sum_{i=1}^{N} x_i = 1 \tag{28}$$

Then, the secondary target change amount is expressed as:

$$\Delta f_2 = \left(\Delta \sum_{i=1}^{n} x_i \cdot lo_i \right) \in \left[0, \sum_{i=1}^{n} le_i \right] \tag{29}$$

Therefore, **Eq. 27** becomes:

$$\Delta f = \alpha \Delta \sum_{i=1}^{n} x_i - \Delta \sum_{i=1}^{n} x_i \cdot lo_i = \alpha - \beta, \beta \in \left[0, \sum_{i=1}^{n} le_i \right] \tag{30}$$

To ensure that the first-level target is satisfied before the second-level target, $\alpha \gg \beta$. That is, $\alpha \gg \sum_{i=1}^{n} le_i$ needs to be satisfied. If

target two is divided by $\sum_{i=1}^{n} le_i$, the optimal placement model can be expressed as:

$$\begin{cases} \min\ f = \alpha \sum_{i=1}^{N} x_i - \dfrac{\sum_{i=1}^{n} x_i \cdot le_i}{\sum_{i=1}^{n} le_i}, \alpha \gg 1 \\ \text{s.t.}\ \ \sum_{i=1}^{n} x_i m_{ij} \geq 1 \end{cases} \tag{31}$$

CASE ANALYSIS

Calculation Efficiency Analysis of Exposed Area

The IEEE 30-node method was used to verify the feasibility and effectiveness of the proposed method. The system structure was composed of 37 lines connected to 30 bus nodes, similar to the system in (Wang et al., 2021), as shown in **Figure 3**.

We consider the single-phase grounding short-circuit fault on the line between buses 2 and 4 as an example and calculate its critical point. As $l_{sag,v} = 2$, there are two critical points on the line. First, the Chebyshev iteration method is used to calculate the maximum value of the sag amplitude with coordinates $p_{\max} = (0.247, 0.8465\ \text{p.u.})$. This is then combined with the line endpoint coordinates (0.247, 0.813 p. u.) and (0.247, 0.721 p.u.) for quadratic interpolation fitting. The interpolation equation is $U\text{th} = -0.6314\ p^2 + 0.4461\ p + 0.7746$, and the convergence condition was set to $\varepsilon = 0.0001$. The dichotomy (Zhang et al., 2019), golden section (Luo et al., 2019), and Chebyshev methods are used to calculate the critical points. The relationship between the calculation errors of the three methods and the number of iterations is shown in **Figure 4**.

When the sag threshold was set to 0.84, the solution critical points were 0.2076 and 0.4989. The dichotomy, golden section, and Chebyshev methods required 11, 9, and 3 iterations to meet the accuracy requirements, respectively, as shown in **Figure 5**. This shows that the Chebyshev iteration method can reduce the calculation time and occupied resources in practical applications, which is of great significance to the optimization of calculations.

Some cases are now proposed to demonstrate the performance of the proposed optimization model and analyze the scope of the exposed area under different DG penetration levels. The IEEE 30-node test system (a mesh power network) was used and it was assumed that the voltage sags were caused by single-phase short-circuit faults. The considered scenarios of DG penetration are:

Case A1. Base case. The data used is provided from (Wang et al., 2021), which means that there is no DG. The capacities of generators 1, 2, 5, 8, 11, and 13 are 100, 80, 50, 20, 20, and 20 MW, respectively.

Case A2. The DG penetration rate is 5%. The generator at node 11 in Case A1 is replaced with DG with capacity of 20 MW.

Case A3. The DG penetration rate is 15%. The generators at nodes 11, and 13 in Case A1 are replaced with DGs with capacities of 20 and 20 MW, respectively.

Case A4. The DG penetration rate is 25%. The generators at nodes 5 and 11 in Case A1 are replaced with DGs with capacities of 50, and 20 MW, respectively.

In all cases, the DG replaced the generators in the original IEEE 30-node system and used a constant power control method. The exposed area of the node under the four cases were calculated using node 7 as an example, as shown in **Figure 5**.

Since IEEE 34 node itself is not connected to ordinary generator, some modifications are made to the system in order to analyze the impact of replacing existing ordinary generator with DG on sag. The modified IEEE 34-node system (a radial distributed power network) was used and it was assumed that the voltage sags were caused by single-phase short-circuit faults. The considered scenarios of DG penetration are:

Case A5. Base case. The data used is provided from (Niknam et al., 2003), which means that there is no DG. The active power capacity of generators at nodes 9, 21 and 30 are 90, 120 and 150 kW respectively.

Case A6. The DG penetration rate is 25%. The generator at node 9 in Case A5 is replaced with DG with capacity of 90 kW.

Case A7. The DG penetration rate is 35%. The generator at node 21 in Case A5 is replaced with DG with capacity of 120 kW.

Case A8. The DG penetration rate is 42%. The generator at node 30 in Case A5 is replaced with DG with capacity of 150 kW.

In all cases, the DG replaced the generators in the original IEEE 34-node system and used a constant power control method. The exposed area of the node under the four cases were calculated using node 4 as an example, as shown in **Figure 6**.

As the penetration rate of DG increased, the scope of the exposed area gradually expanded, as shown in **Figure 5** and **Figure 6**. Additionally, the hazard degree of the sag became more serious and the resulting economic loss was greater. Therefore, it is necessary to consider the customers' economic losses caused by sags in a grid dominated by DG.

Analysis of Customer Sag Economic Loss

First, the sag threshold was set to 0.9 p. u. Then, the traditional placement model shown in **Eq. 24** and **Eq. 25** was solved and the placement plan to realize the observability of the voltage sag in the entire power grid was obtained, as shown in **Table 1**. It can be seen from the table that the scheme meeting the minimum number of monitors is not unique.

Field investigations in a certain city were conducted during the process of optimizing the placement of the sag monitor to consider the sag economic loss to different types of customers. The relevant data are shown in **Table 2**.

A simulation calculation was carried out in the IEEE 30-node system, and the distribution of various system customers was artificially and randomly assumed. The distribution of different

customers in the system is shown as a black solid circle in **Figures 6–8**, and the sag annual economic loss is marked in bold black font. At this time, we can obtain the vector $\boldsymbol{LE}$ = (0, 0, 400, 250, 0, 270, 350, 0, 0, 200, 0, 0, 0, 100, 0, 80, 0, 0, 0, 50, 0, 0, 0, 0, 0, 0, 0, 220, 0, 0). Then, the calculation results of the exposed area of all buses are used to form the matrix $\boldsymbol{LC}$ and vector $\boldsymbol{LO}$ from **Eq. 19**. Subsequently, the optimization model shown in **Eq. 31** can be used to obtain the optimal placement scheme.

Some additional cases are proposed to consider the influence of DG permeability. The scenarios considered for DG penetration are as follows:

Case B1. Base case. The data used is provided from Ref. (Wang et al., 2021), which means that there is no DG. The capacities of generators 1, 2, 5, 8, 11, and 13 are 100, 80, 50, 20, 20, and 20 MW, respectively.

Case B2. The DG penetration rate is 5%. The generator at node 11 in Case B1 is replaced with DG with capacity of 15 MW.

Case B3. The DG penetration rate is 15%. The generators at nodes 11, and 13 in Case B1 are replaced with DGs with capacities of 25 and 20 MW, respectively.

Case B4. The DG penetration rate is 25%. The generators at nodes 5 and 11 in Case B1 are replaced with DGs with capacities of 50, and 20 MW, respectively.

The monitoring scheme for Case B1 is to place a monitor at nodes 7 and 30. To illustrate the effectiveness of the proposed method, a group of schemes, such as 5 and 26, were randomly selected from the placement schemes obtained by the traditional method for comparison with schemes 7 and 30 that were obtained with the proposed method.

The sag monitoring scope for the proposed method and traditional programs (Zhou and Tian, 2014) are based on the calculation results of the exposed area, as shown in **Figure 7**.

a) Schematic Diagram of the Monitoring Scope of Traditional Programs.
b) Schematic Diagram of the Monitoring Scope of the Proposed Method.

MS is the abbreviation of monitoring scope, as shown in **Figure 7**. The MS of the sag monitor at the node refers to the range that can monitor the sag, which is equal to the exposed area under the node setting threshold. The scopes of different monitors are represented by dotted lines of different colors. Lines or nodes with different risk levels are represented by different colored areas according to the following division rules. The total number of occurrences of lines or nodes in all exposed areas can be divided into four intervals representing four different SRL: (0, 7), (Du et al., 2021; Šipoš et al., 2021), (Zhang et al., 2019; Kumar et al., 2020a), and (24, 30). For example, the number of times a line appears in the exposed area of different nodes in the system at the same time is 10, $10 \in [8, 16]$, so the SRL of the line is 2. Only the case of a single-phase short-circuit fault is listed here, but the results under other faults are similar. First, it can be seen from the figure that both monitoring schemes can cover the entire system, indicating that both schemes can achieve the observability of voltage sags in the entire power grid. However, fewer monitors were used by the proposed method. Second, the monitoring program used by the proposed method could simultaneously monitor a wider range of sag sensitive areas. Third, assuming that the failure probability of each line is the same, the $\boldsymbol{X}^{*}\boldsymbol{LC}^{*}(\boldsymbol{LC})^{\mathrm{T}}$ values of the traditional and proposed schemes can be calculated by rewriting **Eq. 18** and **Eq. 26**, respectively, as:

$$[2, 5, 12, 17, 4, 13, 12, 5, 24, 29, 1, 26, 2, 29, 29, 29, 29, 29, 29, 29, 30, 31, 32, 33, 33, 33, 33, 18, 33, 33] \tag{32}$$

$$[2, 7, 20, 25, 4, 21, 20, 10, 31, 37, 1, 33, 2, 37, 37, 37, 37, 37, 37, 37, 38, 39, 40, 41, 41 , 41, 41, 26, 41, 41] \tag{33}$$

The traditional and proposed schemes monitor and obtain the total economic loss $\boldsymbol{X}^{*}\boldsymbol{LC}^{*}(\boldsymbol{LC})^{\mathrm{T}}{}^{*}\boldsymbol{LE}/l$ caused by the sag to customers as 8.97 and 13.12 million yuan, respectively. The results show that the proposed method can effectively improve the monitoring reliability and redundancy in areas that have a serious impact on customer losses when sags occur. Additionally, the proposed method reduces the risk of missing voltage sags due to the failure of a monitor. This facilitates timely governance measures, improves the quality of the power supply to customers, and fundamentally reduces the economic loss of customers.

The monitoring schemes of Cases B2 and B3 are the same, with monitors placed at nodes 7 and 30. In Case B4, only one monitor was installed at node 30. The monitoring scopes for Cases B2 and B3 are shown in **Figure 8** and **Figure 9**, respectively.

The monitoring scope gradually expands and the sag risk level of the line rises with an increase in DG permeability, as seen in **Figures 7–9**. The total economic losses to customers caused by the sag are monitored at 14.19 and 15.26 million yuan, as seen in **Figures 8**, **9**, respectively. This again shows that the economic loss caused by the voltage sag in a DG-dominated power grid is more serious. Therefore, to meet the power demand of customers, it is necessary to consider the optimal placement of monitors to reduce the risk of customers' economic loss. The results show that when the DG penetration rate increases to 25%, the installation of a monitor at node 30 can achieve observability of the sag in the entire system, as shown in Case B4. At this time, the total economic loss to customers caused by the sag is monitored at 8.29 million yuan.

CONCLUSION

Starting from the primary task of power grid company to meet the power demand of customers, this paper proposes the optimal placement model of sag monitor considering the economic loss of customers, which realizes the redundant coverage of important customers and ensures the economic benefits of them. The main conclusions are as follows:

① The Chebyshev iterative method is used to calculate the exposed area. The Chebyshev iterative method has the advantage of third-order convergence speed, which

effectively improves the efficiency of solution. ② The derivation proves that the use of DG to replace the original ordinary generators in the system will result in the expansion of exposed area, thus increasing the economic losses suffered by customers. It verifies the necessity of considering the economic losses of customers in the Grid dominated by distributed generation. ③ Based on the exposed area, a method to calculate the economic loss of customers is proposed. ④ Considering the weight of customer's economic loss, the optimal placement model of sag monitor is proposed, and the placement scheme with low monitoring cost and high monitoring ability for important customers is obtained, which reduces the risk of customer's economic loss.

DATA AVAILABILITY STATEMENT

Publicly available datasets were analyzed in this study. This data can be found here: https://pan.baidu.com/s/1tcx_GEVFSJI0uT05RKHggg password:6fda.

AUTHOR CONTRIBUTIONS

YW contributed to conception and design of the study. QF organized the database. YC performed the statistical analysis. HH wrote the first draft of the manuscript. XX wrote sections of the manuscript. All authors contributed to manuscript revision, read, and approved the submitted version.

REFERENCES

Almeida, C., and Kagan, N. (2011). Using Genetic Algorithms and Fuzzy Programming to Monitor Voltage Sags and Swells. *IEEE Intell. Syst.* 26, 46–53. doi:10.1109/mis.2011.2

Ansal, V. (2020). ALO-optimized Artificial Neural Network-Controlled Dynamic Voltage Restorer for Compensation of Voltage Issues in Distribution System. *Soft Comput.* 24, 1171–1184. doi:10.1007/s00500-019-03952-1

Buzo, R. F., Barradas, H. M., and Leão, F. B. (2021). A New Method for Fault Location in Distribution Networks Based on Voltage Sag Measurements. *IEEE Trans. Power Deliv.* 36, 651–662. doi:10.1109/tpwrd.2020.2987892

Chun-Tao, M., and Jian-Tong, L. (2015). "Allocation of Voltage Sag Monitoring Based on Improved S-Transform and Exposed Area," in 2015 Fifth International Conference on Instrumentation and Measurement, Computer, Communication and Control (IMCCC), Qinhuangdao, China, September 18–20, 2015, 1898–1903. doi:10.1109/IMCCC.2015.403

Du, W., Wang, Y., Wang, H., Yu, J., and Xiao, X. (2020). Collective Impact of Multiple Doubly Fed Induction Generators with Similar Dynamics on the Oscillation Stability of a Grid-Connected Wind Farm. *IEEE Trans. Power Deliv.*, 1. doi:10.1109/TPWRD.2020.3030645

Du, W., Wang, Y., Wang, Y., Wang, H., and Xiao., X. (2021). Analytical Examination of Oscillatory Stability of a Grid-Connected Pmsg Wind Farm Based on the Block Diagram Model. *IEEE Trans. Power Syst.*, 1. doi:10.1109/TPWRS.2021.3077121

Espinosa-Juarez, E., Hernandez, A., and Olguin, G. (2009). An Approach Based on Analytical Expressions for Optimal Location of Voltage Sags Monitors. *IEEE Trans. Power Deliv.* 24, 2034–2042. doi:10.1109/tpwrd.2009.2028777

Fu, Q., Du, W., Wang, H. F., and Ren, B. (2021). Analysis of Small-Signal Power Oscillations in MTDC Power Transmission System. *IEEE Trans. Power Syst.* 36, 3248–3259. doi:10.1109/TPWRS.2020.3043041

Fu, Q., Du, W., Wang, H., Ren, B., and Xiao, X. (2021). Small-signal Stability Analysis of a VSC-MTDC System for Investigating Dc Voltage Oscillation. *IEEE Trans. Power Syst.*, 1. doi:10.1109/TPWRS.2021.3072399

Ibrahim, A. A., Mohamed, A., and Shareef, H. (2010). "Optimal Placement of Voltage Sag Monitors Based on Monitor Reach Area and Sag Severity index," in IEEE Student Conference on Research and Development (SCOReD 2010), Kuala Lumpur, Malaysia, December 13–14, 2010. 1, 467–470. doi:10.1109/scored.2010.5704055

Jiang, H., Xu, Y., and Liu, Z. (2020). A BPSO-Based Method for Optimal Voltage Sag Monitor Placement Considering Un-certainties of Transition Resistance. *IEEE Access* 8, 1. doi:10.1109/access.2020.2990634

Kumar, N. M., Chopra, S. S., Malvoni, M., Elavarasan, R. M., and Das, N. (2020). Solar Cell Technology Selection for a PV Leaf Based on Energy and Sustainability Indicators-A Case of a Multilayered Solar Photovoltaic Tree. *Energies* 13, 6439. doi:10.3390/en13236439

Kumar, S., Sarita, K., Vardhan, A. S. S., Elavarasan, R. M., Saket, R. K., and Das, N. (2020). Reliability Assessment of Wind-Solar Pv Integrated Distribution System Using Electrical Loss Minimization Technique. *Energies* 13, 5631. doi:10.3390/en13215631

Luo, S. S., Sun, H. T., and Du, X. T. (2019). Research on Optimal Configuration Method of Monitoring Points Considering Sag Positioning and Anti-disturbance Index[J]. *Power Capacitors and Reactive Power Compensa-tion* 40, 119–125.

Ma, M., Xu, B. Y., and Wang, Y. (2019). A Hybrid Identifi-Cation Method of Voltage Sag Region Based on Critical point Method. *Power Supply and Consumption* 36, 50–55.

Niknam, T., Ranjbar, A. M., and Shirani, A. R. (2003). "Impact of Distributed Generation on volt/Var Control in Distribution Networks," in 2003 IEEE Bologna Power Tech Conference Proceedings, Bologna, Italy, June 23–26, 2003. 7.

Olguin, G., Vuinovich, F., and Bollen, M. H. J. (2006). An Optimal Monitoring Program for Obtaining Voltage Sag System Indexes. *IEEE Trans. Power Syst.* 21, 378–384. doi:10.1109/tpwrs.2005.857837

Park, C.-H., and Jang, G. (2007). Stochastic Estimation of Voltage Sags in a Large Meshed Network. *IEEE Trans. Power Deliv.* 22, 1655–1664. doi:10.1109/tpwrd.2006.886795

Šipoš, M., Klaić, Z., and Nyarko, E. K. (2021). Determining the Optimal Location and Number of Voltage Dip Monitoring Devices Using the Binary Bat Algorithm. *Energies* 14, 255. doi:10.3390/en14010255

Sun, R., Ma, J., and Yang, W. (2021). Transient Synchronization Stability Control for Lvrt with Power Angle Estimation. *IEEE Trans. Power Electron.* 36, 10981–10985. doi:10.1109/tpel.2021.3070380

Tian, S. X., Li, K. P., and Wei, S. R. (2021). Distribution Network Security Situation Awareness Method Based on Synchronous Phasor Measuring Device. *Proc. Chin. Soc. Electr. Eng.* 41, 617–632.

Wang, Y., Luo, H., and Xiao, X.-Y. (2019). Voltage Sag Frequency Kernel Density Estimation Method Considering protection Characteristics and Fault Distribution. *Electric Power Syst. Res.* 170, 128–137. doi:10.1016/j.epsr.2019.01.009

Wang, Y., Luo, H., and Xiao, X. (2021). Joint Optimal Planning of Distributed Generations and Sensitive Users Considering Voltage Sag. *IEEE Trans. Power Deliv.*, 1. doi:10.1109/tpwrd.2021.3053996

Zhang, L., Tong, B., Wang, Z., Tang, W., and Shen, C. (2021). Optimal Configuration of Hybrid AC/DC Distribution Network Considering the Temporal Power Flow Complementarity on Lines. *IEEE Trans. Smart Grid*, 1. doi:10.1109/TSG.2021.3102615

Zhang, Y., Lin, Y. Y., and Shao, Z. G. (2019). Multi-objective Optimal Placement of Positioning Monitoring Points under the Constraints of Considerable Voltage Sag. *Trans. Chin. Soc. Electr. Eng.* 34, 2375–2383. doi:10.19595/j.cnki.1000-6753.tces.180647

Zhou, C., and Tian, L. J. (2014). Optimal Configuration of Voltage Sag Monitoring Points Based on Particle Swarm Optimiza-Tion Algorithm. *J. Electrotechnical Technol.* 29, 181–187. doi:10.19595/j.cnki.1000-6753.tces.2014.04.024

Conflict of Interest: The authors declare that the research was conducted in the absence of any commercial or financial relationships that could be construed as a potential conflict of interest.

Publisher's Note: All claims expressed in this article are solely those of the authors and do not necessarily represent those of their affiliated organizations, or those of the publisher, the editors and the reviewers. Any product that may be evaluated in this article, or claim that may be made by its manufacturer, is not guaranteed or endorsed by the publisher.

APPENDIX A

When a short circuit fault occurs in the intersection of the exposed areas of different load nodes, it will cause the sag of these load nodes at the same time and increase the economic loss of Sag (greater than that of a single load node). The intersection of exposed areas of n ($n \geq 2, n \geq Z$) load nodes is called redundant area and the redundancy of the redundant area is n. If the sag is not monitored and managed in time, the greater the redundancy is, the greater the economic loss will be suffered by customers, that is, the risk of economic loss will increase with the increase of redundancy. This phenomenon can be explained by **Figure 2** in the manuscript. In addition, for the convenience of reviewers, the detailed explanation is as follows:

1) As shown in **Figure A1**, it is assumed that load node a has x customers, and the exposed area of load node a does not intersect with the exposed area of any other node, that is, the area redundancy represented by the exposed area of load node a is 1.

Then the total economic loss caused to the customers of node a can be calculated as

$$\text{loss} = \text{loss}_1 + \text{loss}_2 + \ldots + \text{loss}_o + \ldots + \text{loss}_x \quad \text{(A1)}$$

Where loss_o represents the economic loss of the oth ($o\varepsilon[0, x]$) customer.

2) As shown in **Figure A2**, suppose that load node a has x customers and load node b has y customers, and the exposed area of load node a intersects with that of load node b, the redundancy of the intersection is 2, and the redundancy of the blue and purple areas outside the intersection is 1.

When a fault occurs at any position in the intersection, it will cause economic losses to the customers of node a and b. the total loss can be calculated as:

$$\begin{aligned}\text{loss} = {} & \text{loss}_1 + \text{loss}_2 + \ldots + \text{loss}_o + \ldots + \text{loss}_x \\ & + \text{lloss}_1 + \text{lloss}_2 + \ldots + \text{lloss}_p + \ldots + \text{lloss}_y\end{aligned} \quad \text{(A2)}$$

Among them, loss_o represents the economic loss of the oth ($o\varepsilon[0, x]$) customer of node a, and lloss_p represents the economic loss of the pth ($p\varepsilon[0, y]$) customer of node b. The calculation method of the total economic loss caused by the failure in the area with redundancy of 1 is shown in **Eq. A1**.

3) As shown in **Figure A3**, assume that load node a has x customers, load node b has y customers, and load node c has z customers, and the exposed areas of load nodes a, b, and c intersect each other. The common intersection of a, b and c is shown in red, and its redundancy is 3, the redundancy of gray area is 2, and the redundancy of other areas is 1.

When any location in the red area fails, it will cause economic losses to the customers of nodes a, b and c. The total loss can be calculated as:

$$\begin{aligned}\text{loss} = {} & \text{loss}_1 + \text{loss}_2 + \ldots + \text{loss}_o + \ldots + \text{loss}_x \\ & + \text{lloss}_1 + \text{lloss}_2 + \ldots + \text{lloss}_p + \ldots + \text{lloss}_y \\ & + \text{llloss}_1 + \text{llloss}_2 + \ldots + \text{llloss}_q + \ldots + \text{llloss}_z\end{aligned} \quad \text{(A3)}$$

Among them, loss_o represents the economic loss of the oth ($o\varepsilon[0, x]$) customer of node a, lloss_p represents the economic loss of the pth ($p\varepsilon[0, y]$) customer of node b, and llloss_q represents the economic loss of the qth ($q\varepsilon[0, z]$) customer of node c. The calculation method of the total economic loss caused by the failure in the area with redundancy of 1 and 2 respectively is shown in **Eq. A1** and **Eq. A2**. The calculation formula of the sag economic loss increases with the increase of redundancy, and so on.

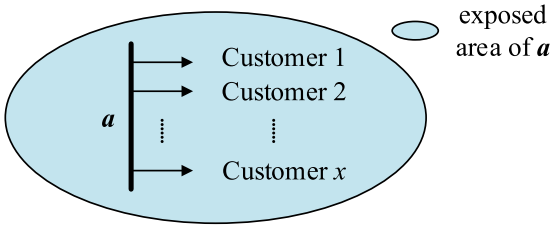

FIGURE A1 | Calculation of Economic Loss of Voltage Sag.

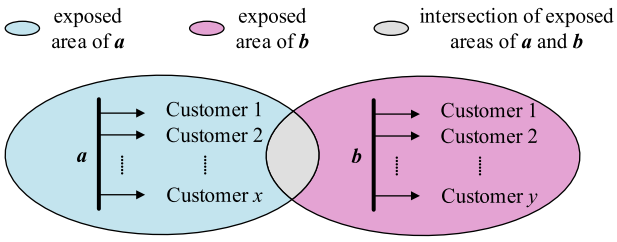

FIGURE A2 | Calculation of Economic Loss of Voltage Sag.

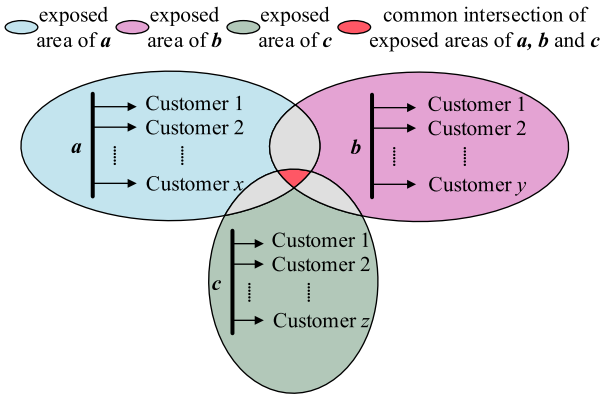

FIGURE A3 | Calculation of Economic Loss of Voltage Sag.

frontiers in Energy Research

ORIGINAL RESEARCH
published: 26 August 2021
doi: 10.3389/fenrg.2021.718859

A Weak-Consistency–Oriented Collaborative Strategy for Large-Scale Distributed Demand Response

Yu Liu[1], Tian Gao[1], Xiaolong Sun[2], Zexin Yang[1], Yujia Zhang[1], Shan Gao[1] and Xueliang Huang[1]*

[1]School of Electrical Engineering, Southeast University, Nanjing, China, [2]Guodian Nanjing Automation Co., Ltd., Nanjing, China

Large-scale distributed demand response is a hotspot in the development of power systems, which is of much significance in accelerating the consumption of new energy power generation and the process of clean energy substitution. However, the rigorous distributed algorithms utilized in current research studies are mostly very complicated for the large-scale demand response, requiring high quality of information systems. Considering the electrical features of power systems, a weak-consistency–oriented collaborative strategy is proposed for the practical implementation of the large-scale distributed demand response in this study. First, the basic conditions and objectives of demand response are explored from the view of system operators, and the challenges of large-scale demand response are discussed and furthermore modelled with a simplification based on the power system characteristics, including uncertainties and fluctuations. Then, a weakly consistent distributed strategy for demand response is proposed based on the Paxos distributed algorithm, where the information transmission is redesigned based on the electrical features to achieve better error tolerance. Using case studies with different information transmission error rates and other conditions, the proposed strategy is demonstrated to be an effective solution for the large-scale distributed demand response implementation, with a robust response capability under even remarkable transmission errors. By integrating the proposed strategy, the requirement for the large-scale distributed systems, especially the information systems, is highly eased, leading to the acceleration of the practical demand response implementation.

Keywords: demand side management, distributed control, large-scale collaboration, slacked control, weak consistency

OPEN ACCESS

Edited by:
Dongdong Zhang,
Guangxi University, China

Reviewed by:
Guangchao Geng,
Zhejiang University, China
Haixiang Zang,
Hohai University, China

****Correspondence:***
Yu Liu
yuliu@seu.edu.cn

Specialty section:
This article was submitted to Smart Grids, a section of the journal Frontiers in Energy Research

Received: *01 June 2021*
Accepted: *27 July 2021*
Published: *26 August 2021*

Citation:
Liu Y, Gao T, Sun X, Yang Z, Zhang Y, Gao S and Huang X (2021) A Weak-Consistency–Oriented Collaborative Strategy for Large-Scale Distributed Demand Response. Front. Energy Res. 9:718859. doi: 10.3389/fenrg.2021.718859

INTRODUCTION

Energy transition has become a key issue for sustainable economic and social development. The world urgently needs to transform energy production, allocation, and consumption methods today, so evolutions are emerged in both generation and consumption sides (Heffron et al., 2020). Developing and utilizing clean energy instead of the traditional fossil fuel are welcomed in the power production side, while much attention should also be paid to the intelligent interaction of power loads in the consumption side (Hoggett, 2014). Wind power, photovoltaic power generation, and other intermittent new energy sources and new controllable loads have been integrated to the grid on a large scale, leading to the new features of power system operations (Kolhe, 2012).

In spite of the electricity contribution, the high penetration of renewable generations brings some challenges. On the one hand, the uncertainties of the renewable power generation will make the

power output and electricity flow in the grid fluctuate more seriously (Dvorkin et al., 2015), which would influence the safe and stable operation of the system. On the other hand, the proportion of conventional power generation is decreasing, which will significantly weaken the dynamic voltage and power regulation capability of the grid (Zheng et al., 2015). Based on these problems caused on the generation side, the consumption side is highly expected to help with the situation. Hence, demand response (DR) emerges. DR emphasizes the direct interaction between the power users and systems via the electricity market or other patterns featuring faster response action, lower cost, better environmental protection, and high potential to increase the system's flexibility (Huang et al., 2019), which is desired by users and utilities, resulting in a fast development in recent years (Ribó-Pérez et al., 2021).

There has been a lot of research on the utilization of demand-side resources. Among the loads that can participate in demand response, the resident load has high potential. A resident-side demand response energy management model can be established to analyze and evaluate the flexibility from the demand side and to optimize the entire response system (D'hulst et al., 2015). Considering real-time electricity prices, a kind of demand-side energy management controller based on dynamic pricing for residential power usage can be used to reasonably dispatch electrical equipment to maximize user satisfaction and benefit (Chen et al., 2021). The air conditioning load as a kind of thermostatically controlled load, which would account for more than half of the total electricity demand in summer, can become the main control resource in the DR process (Mahdavi and Braslavsky, 2020), realizing an adaptive control mode according to the index of ambient temperature and human comfort (Perez et al., 2016). Considering the small capacity of scattered air conditioning loads, the practical demand response usually requires the participation of quantities of residents through aggregation technology to achieve efficient utilization (Gao et al., 2017), leading to a large-scale problem.

The coordination strategy is extremely important for the large-scale systems, which is also the research hotspot for demand response. Currently, there are three majorly investigated strategies, i.e., centralized control, decentralized control, and distributed control. Through the centralized control, the power consumption of loads is controlled directly using a utility or by a system operator, which features fast response speed and concise control volume (Chen and Liu, 2017). However, this control method depends largely on the information transmitted between the operator and the loads, which issues a higher requirement on the accuracy of information transmission (Tang et al., 2018). It depends on an information platform based on the coupled cyber-physical power system to achieve the coordination between the operator and the user, which requires particularly solid robustness to secure information transmission process (Qi et al., 2017). Although with desired performance, the centralized control requires a process center and a complete information system, which is not economic at all. Hence, the decentralized control combines local control strategy and centralized display, which can avoid the problem of information delay and the high cost to build a strictly robust information transmission system (Bahrami et al., 2018). Although many methods and theories have been proposed to improve the time-delay systems, it is found difficult to keep the balance between small delay and good control precision (Zhu and Fridman, 2020). As can be seen, the response performance is comparatively poor with that of decentralized control strategy, while the over-response and under-response cannot be avoided. For the sake of combining the advantages of the abovementioned control strategies, the distributed control is proposed, which is based on centralized management and distributed control (Burns, 2018). It has been widely used in the IoT industry for its interoperability, scalability, and dependability, which are the key features of many distributed systems (Iwanicki, 2018). Different algorithms and control strategies are widely studied and adopted to improve the efficiency of the distributed control (Xiao et al., 2019) and its natural features of error tolerance (Raynal, 2018). Specific algorithms have been used, including clock synchronization theories (Dalwadi and Padole, 2017) and self-stabilization algorithm (Altisen et al., 2019), to ensure the information consistency and control stability, which are very precise and complicated to realize in some real scenarios as for controllable power loads. Therefore, the distributed control strategy is prominent in large-scale collaborations at the current stage. Meanwhile, the existing demand response process has certain challenges, where the reliability of the physical information system is highlighted (Ming et al., 2018). In the reviewed demand response system, the coordinated and stable status of the information and physical system is the basis of the reliable implementation of demand response (Huang et al., 2019). However, practically speaking, based on the power system features, the power system–demand response does not need these tight conditions, such as the rigorous control algorithm or the extremely reliable information systems. First, the demand response objective value can be flexible around the target since the system state is time-varying. Second, the response individuals do not need the accurate system information all the time, while the focus of the system is the final objective and their focus is their own behaviors. These characteristics provide a potential way to simplify the large-scale distributed demand response implementation.

Based on abovementioned observations, a weak-consistency–oriented distributed control algorithm is proposed in this study to tackle the large-scale demand response problem in a practical way. At the first stage, the air conditioning model and demand response structure are presented and the severe impacts of information errors are extensively discussed. Then, by revising the transmitted information format, the consistency requirement is slacked, resulting in a weak-consistency distributed algorithm. By implementing the proposed algorithm, the demand response performance of large-scale systems is highly improved, especially with a high rate of information errors. The contributions of this study are as follows. First, a weak-consistency–oriented distributed algorithm is proposed based on the features of demand-side resources and the structure of DR in power systems. Then, a specific DR strategy is proposed and proved valid to realize the demand response under the control structure, which is of much robustness especially to solve the problem of

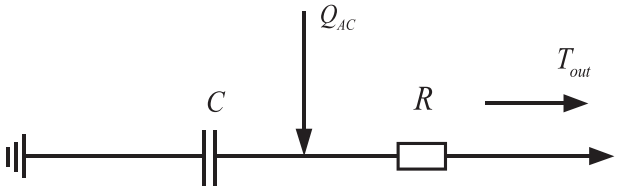

FIGURE 1 | The first-order equivalent thermal parameter model.

errors in the information transmission process, improving the performance of large-scale systems.

AIR CONDITIONING–BASED DEMAND RESPONSE FORMULATION

Model of Air Conditioners for Demand Response

The air conditioning load is a kind of TCL. The modeling of the air conditioning load consists of building a thermodynamic model and the air conditioning unit electromechanical transformation model (Shen et al., 2019).

Thermodynamic Model of Buildings

The thermodynamic model of a house usually adopts an equivalent thermal parameter model. In order to simplify the calculation, only the change process of the indoor temperature is considered (Lu, 2012). In this study, the first-order equivalent thermal parameter model is used, as shown in **Figure 1**.

The model equation is shown as follows:

$$\frac{dT_{in}(t)}{dt} = -\frac{1}{RC}T_{in}(t) + \frac{T_{out}(t)}{RC} + \frac{Q_{AC}(t)}{C}, \tag{1}$$

where $T_{in}(t)$ and $T_{out}(t)$ are, respectively, the indoor and outdoor temperatures at time t, whose unit is ˚C; R is the equivalent thermal resistance, whose unit is ˚C/W; C is the heat capacity of the indoor air, whose unit is J/˚C; and $Q_{AC}(t)$ is the air conditioning cooling capacity at time t, whose unit is W.

Assuming that the outdoor temperature $T_{out}(t)$ remains constant during the period of time $[t_k, t_{k+1}]$, we use $T_{in}(t_k)$ as the initial value to solve **Eq. 1** in order to obtain the indoor temperature at time t_{k+1}:

$$T_{in}(t_{k+1}) = T_{out}(t_k) - Q_{AC}(t_k)R - [T_{out}(t_k) - Q_{AC}(t_k) R - T_{in(}(t_k)] \cdot e^{-\frac{\Delta t}{RC}}. \tag{2}$$

Electromechanical Transformation Model of Air Conditioners

The electromechanical transformation model of air conditioners describes the relationship between the air conditioning power and the cooling (heat) quantity, that is, the energy efficiency ratio. The energy efficiency ratio of fixed-frequency air conditioners is a constant value, while the energy efficiency ratio of inverter air conditioners is related to the working frequency.

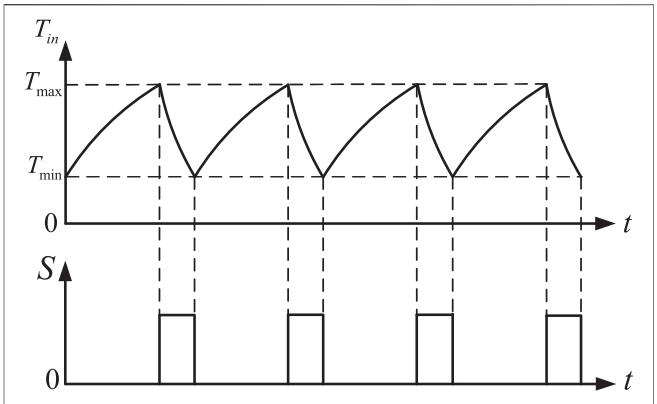

FIGURE 2 | Working characteristics of the fixed-frequency air conditioning compressor.

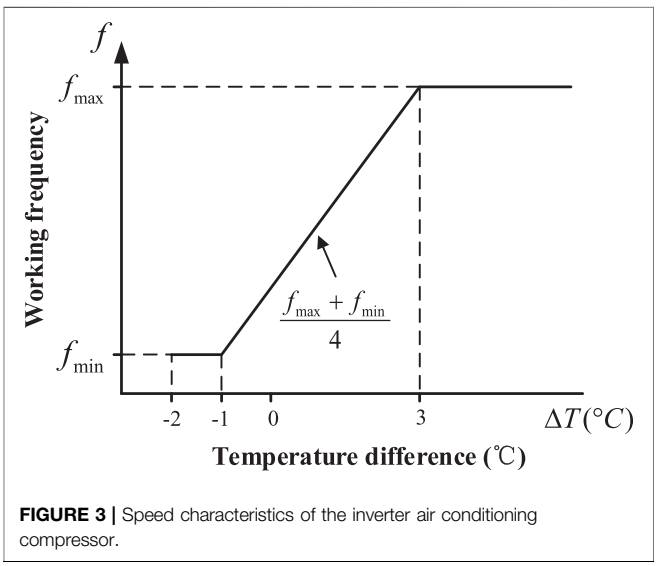

FIGURE 3 | Speed characteristics of the inverter air conditioning compressor.

The fixed-frequency air conditioner adopts a fixed-speed compressor to control ON and OFF states according to the temperature T_{set}, which is set by the user, so that the room temperature is ranging within a certain threshold near T_{set} and the upper and lower temperature limits, T_{max} and T_{min} are, respectively, $T_{set} \pm \delta/2$ as shown in **Figure 2**. δ is the parameter that characterizes the control accuracy of the thermostat controller.

The compressor start–stop state is represented by *S*. *S* is denoted by 0 to indicate that the compressor is in a stopped state, and *S* is denoted by 1 to indicate that the compressor is in a constant-speed operation state. The relationship between the indicator *S* and the indoor temperature can be expressed as

$$S(t_k) = \begin{cases} 1 & ' \quad T_{in}(t_k) \geq T_{max} \\ 0 & ' \quad T_{in}(t_k) \leq T_{min} \\ S(t_{k-1}) & ' \quad T_{min} < T_{in}(t_k) < T_{max} \end{cases}. \tag{3}$$

Therefore, the relationship between the indicator *S* and the electric power of the air conditioner, $P_{AC}(t_k)$, can be expressed as

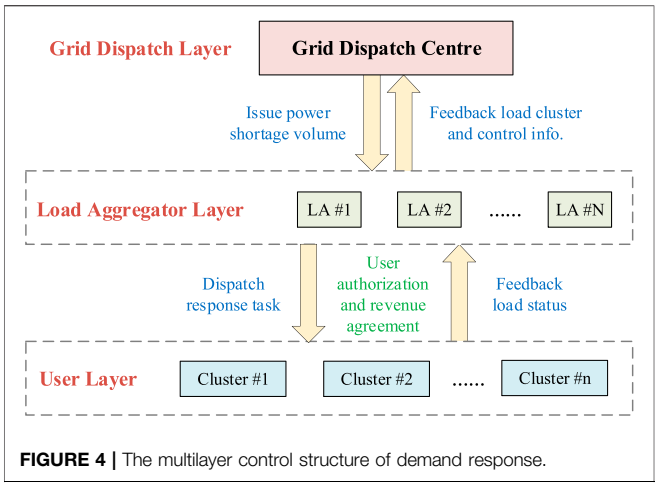

FIGURE 4 | The multilayer control structure of demand response.

$$P_{AC}(t_k) = P_{rated}(t_k)S(t_k), \tag{4}$$

where $P_{rated}(t_k)$ is the electric power of the air conditioner, whose unit is W.

The inverter air conditioner uses a frequency converter to drive the compressor and continuously controls the cooling capacity by adjusting the working frequency and changing the compressor speed (Zhou et al., 2015). As shown in **Figure 3**, the frequency setting is related to the difference between the actual indoor temperature and the set temperature, which can be expressed by ΔT:

$$f = \begin{cases} 0 & \Delta T < -2^{\circ}C \\ f_{min} & -2^{\circ}C \le \Delta T \le -1^{\circ}C \\ f_{min} + \dfrac{(\Delta T + 1)(f_{max} + f_{min})}{4} & -1^{\circ}C \le \Delta T \le 3^{\circ}C \\ f_{max} & \Delta T > 3^{\circ}C \end{cases}, \tag{5}$$

where f_{max} and f_{min}, respectively, represent the allowable maximum and minimum operating frequencies of the inverter air conditioner.

Structure of Demand Response

The research in this work is based on a hierarchical distributed control architecture based on load aggregators. As shown in **Figure 4**, the entire control system is divided into grid dispatch layer, load aggregator layer, and user layer. Continuous information exchange between the layers realizes overall load control (Samad et al., 2016).

On the one hand, the load aggregator layer needs to receive power control instructions from the grid dispatch center, as well as integrate and analyze load types, operating status, adjustable capacity, whether or not it can participate in DR, and other information of the scattered flexible load within its jurisdiction, in order to evaluate the response potential and reaction time which will be fed back to the dispatch center. On the other hand, the load aggregator layer allocates the power adjustment tasks issued by the power grid to users in the area and receives information feedback after participating in the response process. In such a multilevel control structure, the information transmitted can be divided into information control signals, power reduction signals, control decision signals, price signals, and so on.

Impacts of Information Errors

It can be seen that if there are errors in the information transmission between different layers, the results of regional demand response will be highly influenced. For example, there are 2500 air conditioner users in a certain area who can participate in demand response. The ratio of fixed-frequency air conditioners to inverter air conditioners is 1:1, and their rated maximum operating power is 1500 and 2100 W, respectively. The total response task issued by the load aggregator is 500 kW. When there are errors in information transmission between users, the overall response effect will be considerably affected. The result is shown in **Supplementary Table S1** and **Figure 5**.

This study defined an index of response rate (%) in order to describe the effect of demand response process. If the response rate is more than 90%, the demand response process can be anticipated as a successful one. It can be calculated by the following function, where P_{dem} refers to the demand issued by the load aggregators and P_{res} refers to the actual response power of the cluster:

$$R\% = \frac{P_{dem} - P_{res}}{P_{res}} \times 100\%. \tag{6}$$

It can be seen from **Supplementary Table S1** and **Figure 5** that when the information transmission process is correct, the response result met the response task well; when the information error rate is increasing, the number of users who can normally participate in the response is obviously reduced and the response rate index drops to 27%. Meanwhile, as shown in **Figure 6**, operation results under 1% information error rate fluctuated in a large range and the average response volume of 50 rounds of operation has quite a large gap to the demand.

The purpose of this study is to optimize the response rate index, combined with the distributed theory and Paxos algorithm, proposing a weakly consistent distributed strategy for demand response, which can effectively avoid the corresponding consequences caused by the problem of information error in the process of demand response, by which the demand response process could achieve a better effect.

A WEAK-CONSISTENCY–ORIENTED DISTRIBUTED ALGORITHM

Paxos Algorithm

In a distributed computing environment, solving the problems of data synchronization between nodes and distributed resource competition and autonomous recovery of single-node failures is the basic guarantee for the correctness and reliability of the system (Shi and Li, 2012). Paxos algorithm is a consensus algorithm based on message passing and high fault tolerance (Lamport, 2006; Rao et al., 2011). In the algorithm, different

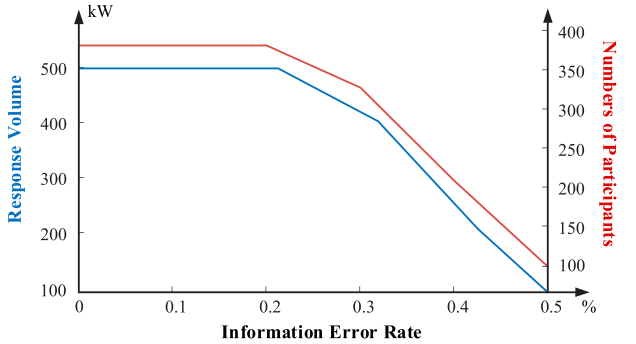

FIGURE 5 | Result distribution of different information error rates.

nodes are represented by three roles: Proposer, Accepter, and Learner (Marzullo et al., 2011). Among them, the Proposer submits a proposal to the Accepter and the proposal contains a resolution; the Accepter approves the proposal; and the Learner obtains and knows the resolution contained in the approved proposal. A node plays multiple roles. The consistency problem of the distributed theory can be simply described as follows: in a distributed system, each node as a participant can propose a plan and the consensus algorithm ensures that only one of these proposals can be selected, while other nodes should also be aware of the proposal which is selected. As a result, all participants will reach only one agreement.

According to the abovementioned Paxos algorithm, the process of air conditioning load participating in demand response can be illustrated. It is assumed that the load aggregator issues power adjustment instructions to users within a certain range, and five users A, B, C, D, and E can participate in the demand response. To simplify the analysis, the order of participation priority of these five users is arranged in an alphabetical order. The response process is shown in **Figure 7**. The load aggregator releases a power shortage task to each user as 100, and the load capacities that users A, B, C, D, and E can respond to are 20, 30, 30, 40, and 50, respectively. The specific process is as shown in **Figure 7**.

The rectangle box in **Figure 7** represents the information sent by a certain user after participating in the demand response and the round box represents the information received by a certain user. The number format is "response amount; remaining demand amount." Before user E responds, the remaining demand received is 0, and hence, there is no need for user E to participate in this demand response.

Weak-Consistency Control Strategy

The weak-consistency control strategy is carried out on the basis of ensuring that the information sent or received by each user is correct. However, in the actual response process, there is a certain bias in information transmission between users. This study believes that demand response objective value can be flexible around the target since the system state is time-varying and the inconsistent state of data in the process will not affect the overall availability and the response performance of the system. There is no need for a strong data consistency, so a weak-consistency distributed strategy and a new kind of information format for demand response are proposed as follows.

First, the responding users could be considered as the nodes in the Paxos distributed algorithm. Then, in the process, the responding user, the Proposer in Paxos, transmits two sets of information to the system pool instead of one, including the load response information of the current user and of the previous one, which is received before the response takes place. The next responding user, the Accepter, could check the two sets of information received and correct errors in the information transmission process, in order to confirm whether the proposal has passed and decide whether to proceed with the next response action. The response process after adopting this strategy is shown in **Figure 8**. If the information is transmitted correctly, the response is normal.

If information errors exist in the process, the errors could be corrected in some occasions. It is assumed that there is no error in the information transmission between the first two users who participated in the response to ensure that the subsequent

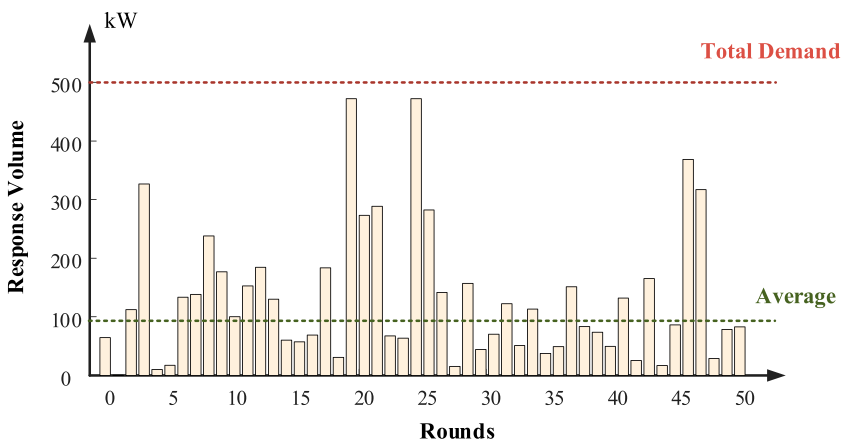

FIGURE 6 | Result distribution of the 50 rounds of operation with 1% information error rate.

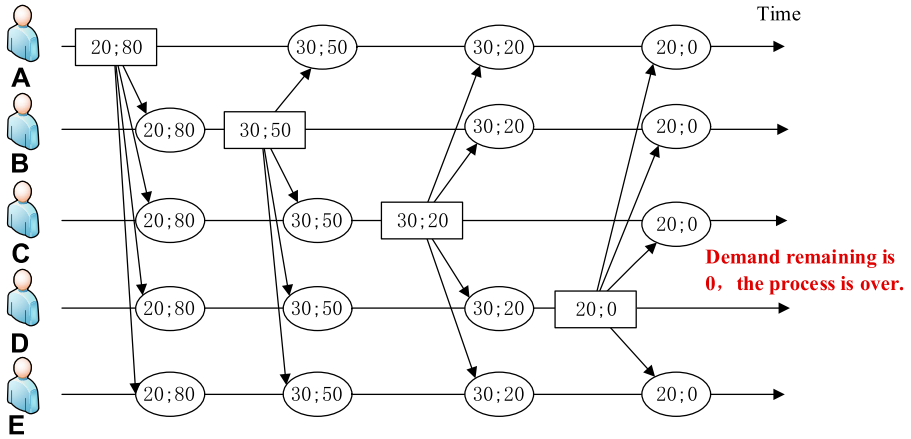

FIGURE 7 | Illustration of user participation in the demand response process.

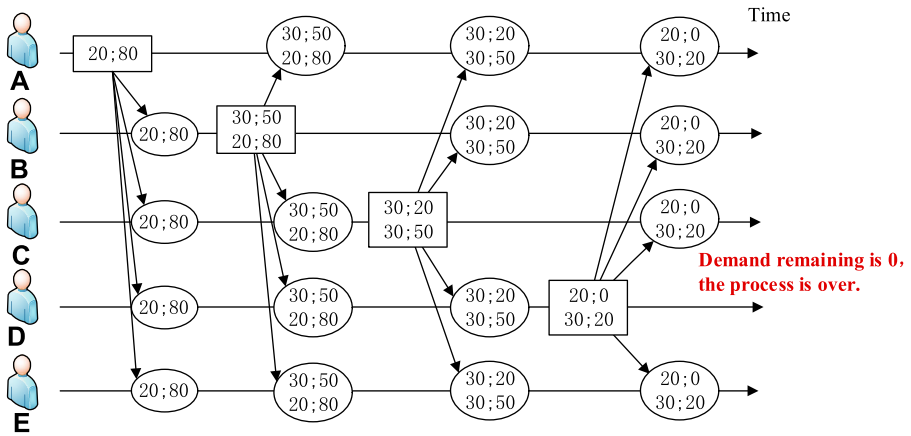

FIGURE 8 | Illustration using the weak-consistency strategy when the information is correct.

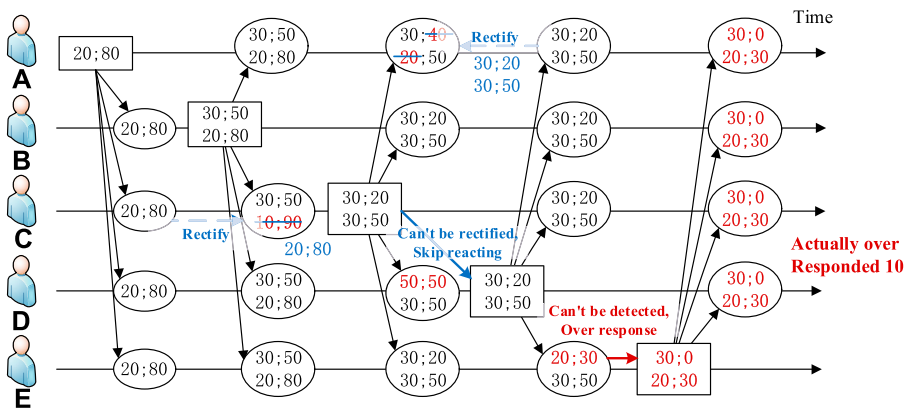

FIGURE 9 | Implementation using the weak-consistency strategy when the information is incorrectly transmitted.

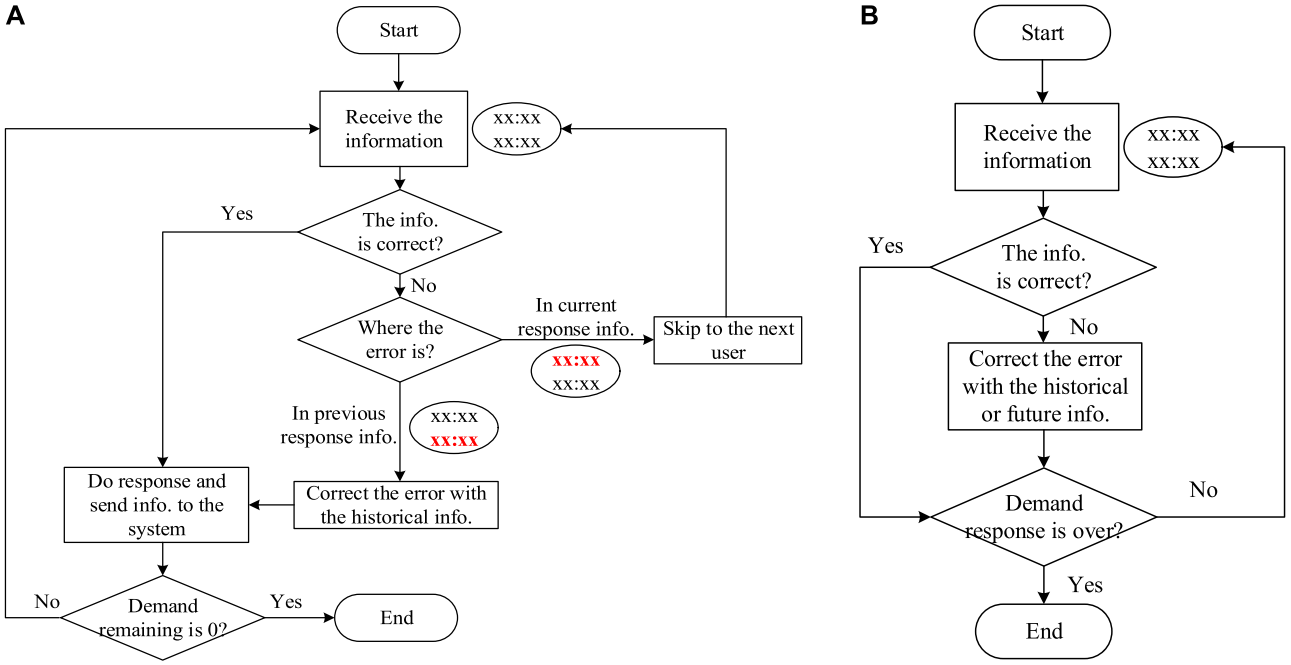

FIGURE 10 | Response strategy of (a) an Accepter and (b) a Learner.

response process can proceed normally; otherwise, there will be surplus errors in the subsequent process and the demand response cannot be performed normally.

As shown in **Figure 9**, there are four possible kinds of information errors in the response process:

1) A Learner, user A for example, has errors in the information received after other's response, which can be corrected based on the two sets of data received before and after.
2) An Accepter receives incorrect information after the former participant responded. It can only be judged and rectified by previous response information, the current response user's adjustable capacity, and other conditions. There can be three possible situations:

a) The error occurs in the response information of the previous participant, which can be rectified by the information previously received. In **Figure 9**, "10; 90" in red can be corrected to "20; 80."
b) The error occurs in the response information of the current participant, but it can be judged but cannot be corrected only, depending on the previous information and the capacity index. Hence, in order to avoid errors in the subsequent response process, the next participant, user C in **Figure 9** for example, should give up participation and send the same response signal as B to the system pool.
c) The error occurs in the response information of the current participant, which cannot even be detected because it coincides with the capacity and other information. It may finally cause some over- or under-response problems, which is 10 in the implementation, and its proportion in the whole demand would be smaller if more users participate in the process. So, this kind of error could be ignored.

Method Flow

After analyzing different possible information errors, a control strategy which can effectively solve the DR problem can be proposed, which is shown in **Figure 10**.

1) Each user sends two sets of load information to the system pool when participating in demand response: the information of the current responding user and of the previous user.

TABLE 1 | Maximum response volume of different numbers of users with different type ratios.

Number of users		1,000	2,000	3,000	5,000	10,000	20,000
Maximum response volume (kW)	1:1	1327.0	2645.3	3959.4	6588.1	13254.1	26433.7
	1:2	1500.0	3000.0	4500.0	7500.0	15000.0	30000.0
	1:3	1234.2	2478.6	3701.8	6182.7	12358.1	24669.3

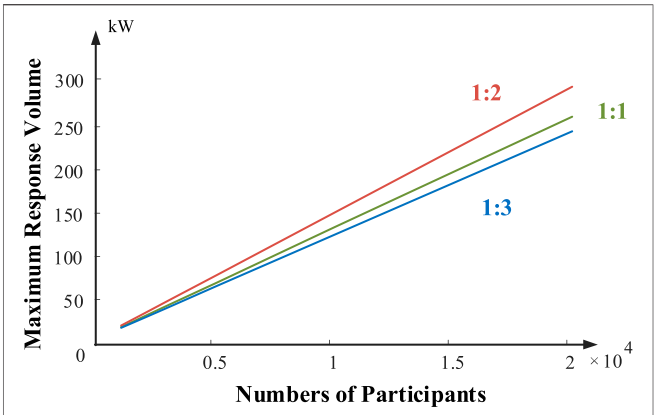

FIGURE 11 | Maximum response volume of different numbers of users with different type ratios.

2) It should be ensured that there is no error in the information transmission between the first two users, so that the process can continue correctly
3) Starting from the second user, it is necessary to verify each time whether the information received is correct. If correct, the information is updated according to the received information and passed on to other users. If not, when the error takes place in the previous response information, it should be corrected based on the historical information and the process could be continued. However, when the error takes place in the current response information, the user should skip the current response period without conducting a response action and the process could start directly from the next user to continue responding.
4) After the current user information is updated, the demand remaining needs to be judged to determine whether the response process is over.
5) For the information received by all the learners, it can be verified based on the information received before and after and the wrong information should be corrected as much as possible without affecting the final response result.

CASE STUDIES

This section uses multiple cases to explore the probability distribution of the response degree when the response strategy proposed in this study is fully adopted, or not. It is assumed that the demand response process takes place on summer days of 34°C outside and the rated maximum operating power of the fixed-frequency air conditioners and the inverter air conditioners is, respectively, 1500 and 2100 W. The simulation is based on the MATLAB 2020 platform, and the computer is configured as Intel(R) Core (TM) i5-8400 2.80 GHz with 8 Gb memory.

Response Capability Analysis

When ratio of fixed-frequency and inverter air conditioners is 1:1 and the information error rate is 0, different numbers of users could meet the demand of different power adjustment tasks.

TABLE 2 | Maximum response volume of different numbers of users with different type ratios and different information error rates.

Number of users	Ratio of fixed-frequency and inverter air conditioners	Information error rate (%)	Maximum response volume (kW)
1,000	1:1	0	131.1
		5	125.1
		10	119.2
	1:2	0	150.0
		5	142.7
		10	134.0
	1:3	0	123.4
		5	117.3
		10	113.6
2,000	1:1	0	2631.0
		5	2463.5
		10	2372.5
	1:2	0	3000.0
		5	2859.0
		10	2713.5
	1:3	0	2467.6
		5	2341.8
		10	2221.0
5,000	1:1	0	6576.5
		5	6330.5
		10	5902.5
	1:2	0	7500.0
		5	7115.0
		10	6721.5
	1:3	0	6104.3
		5	5869.3
		10	5568.4

TABLE 3 | Cases set for analysis and discussion.

	Number of users	Ratio of fixed-frequency and inverter air conditioners	Response task (kW)
Case 1	2,000	1:2	3,000
Case 2	4,000	1:3	5,000

TABLE 4 | Implementation results of different information error rates in Case 1.

Information error rate (%)	Actual response volume (kW)		Number of actual participants		Response rate (%)	
	With the strategy	Without the strategy	With the strategy	Without the strategy	With the strategy	Without the strategy
0.0	3000.0	3000.0	2000	2000	100.0	100.0
0.1	3000.0	2678.6	2000	1786	100.0	89.3
0.2	3000.0	1975.3	2000	1317	99.9	65.8
0.3	3000.0	884.6	2000	590	99.9	29.5
0.4	3000.0	817.7	2000	546	99.6	27.3
0.5	3000.0	474.7	2000	317	99.6	15.8

TABLE 5 | Implementation results of different information error rates in Case 2.

Information error rate (%)	Actual response volume (kW)		Number of responsive users		Response rate (%)	
	With the strategy	Without the strategy	With the strategy	Without the strategy	With the strategy	Without the strategy
0.0	4932.3	4947.6	4000	4000	98.646	98.952
0.1	4930.8	3378.7	4000	2269	98.616	67.574
0.2	4918.5	2591.4	4000	1336	98.37	51.828
0.3	4894.2	1181.2	4000	975	97.884	23.624
0.4	4901.9	709.4	4000	759	98.038	14.188
0.5	4896.6	372.5	4000	305	97.932	7.45

Under the same responding conditions, more participants or smaller demand volume would lead to higher success rate of demand response. That is to say, the total response volume is restricted by the whole capacity of the cluster, and if the task volume is within the capacity, the response would be close to success. The maximum response load that the air conditioning load cluster can afford is positively proportional to the number of users. The actual response volume when the information error rate is 0 can be approximately considered as the maximum response capacity of the whole cluster, which is shown in **Table 1** and **Figure 11**.

With the development of technology in air conditioners, additional inverter air conditioners are used, replacing fixed-frequency ones, because of their convenience, low cost, and easy maintenance. In **Table 1** and **Figure 11**, the comparison between different ratios of fixed-frequency and inverter air conditioners participating in demand response is shown, which illustrates that the ratio of air conditioner types could influence response capacity. Under different numbers of users and information error rates, the response capacity also changes by the change in type ratio, which shows a peak when the ratio is about 1:2. The next three groups of results are listed in **Table 2** to analyze the reason behind this.

The two types of air conditioners taking part in the simulation are of different rated power outputs. As shown in **Table 2**, no matter what the information error rate is, the response result of 1:2 ratio is the best correspondingly. The rated maximum operating power of the fixed-frequency air conditioner and the inverter air conditioner, is respectively, 1500 and 2100 W, while the former one works with a fixed-speed compressor and the ON–OFF strategy and the working power of the latter one is related to ΔT, the difference between the actual indoor temperature and the temperature set by the user. That is to say, the actual power of fixed-frequency air conditioners which can take part in the response is constantly 1500W, having the ability to provide more response capacity with less number of air conditioners. Also, the actual power of inverter air conditioners changes between 755W and 2100 W according to ΔT, which is randomly emerged in the process to simulate the real working situation. It is of better flexibility to provide power when the inverter ones are comparatively more. However, when the ratio comes to 1:3, the decrease in the number of fixed-frequency ones will lead to a drop in the overall response capacity.

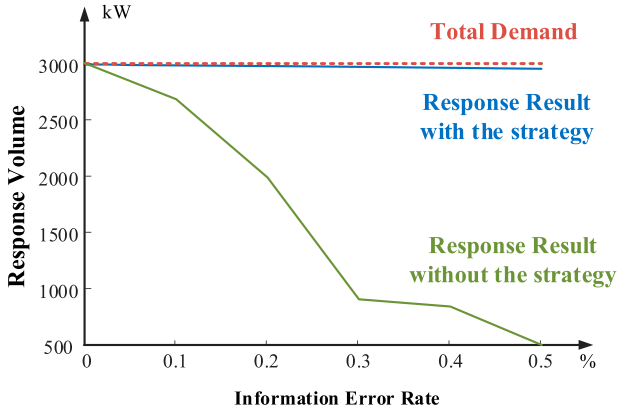

FIGURE 12 | Comparison between adopting the strategy or not in Case 1.

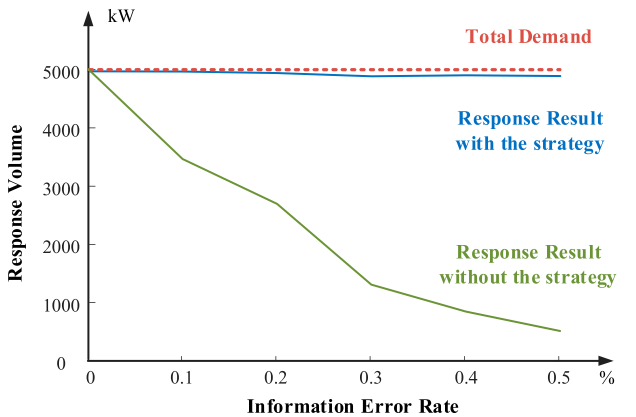

FIGURE 13 | Comparison between adopting the proposed strategy or not in Case 2.

Discussion on Demand Response Implementation

In this section, several cases are set in **Table 3** in order to discuss the difference in the performance of demand response with or without the strategy proposed and the performance under different information error rates of the strategy proposed in order to test and prove the robustness of it. The information error rate is set from 0 to 0.5%. The results are listed in **Tables 4**, **5** for comparison.

As shown in **Tables 4**, **5**, and **Figure 12**, **Figure 13**, if the information error rate increases, the number of users who cannot take part in the response will increase correspondingly. With the strategy, when the response demand is comparatively small, the information error will not affect the final response result and the system response requirements can still be reached. Although there are data inconsistencies caused by information transmission errors in the response process, this intermediate state does not affect the availability and final consistency of the overall system. It illustrates the fault tolerance characteristic of the distributed system. Through the comparison among the corresponding rows of **Table 4** and **Table 5**, a significant difference occurred in the response situation between adopting the demand response strategy proposed in this study or not, which could convincingly illustrate that the strategy is of high validity and good fault tolerance feature.

In order to test the robustness of the system with the strategy proposed, we set different information error rates to the response process to observe the consistency of the response result with the method of repeated trials.

As shown in **Figure 14**, where information error rate is set to 5 and 10% under Case 1, if we perform 50 rounds of response process, it will illustrate that when adopting the strategy, the response rate can mostly reach the requirement of 90% under information error rates even up to 10%. The response rate of 50 rounds is listed in **Supplementary Table S2**. However, without the strategy, when the security and correctness of information transmission are ignored in the demand response process, the response rate will be extremely poor, which drops to 39% in average when the information error rate is only 0.1%. In addition, when performing 50 rounds of response process, the

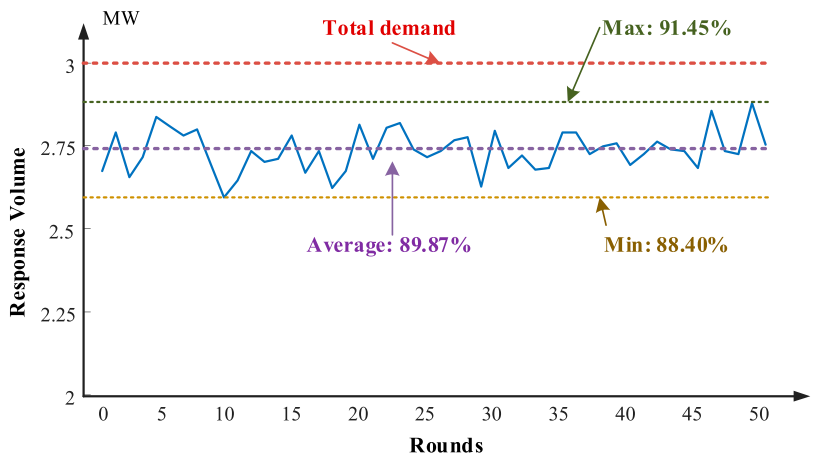

FIGURE 14 | Response results of 50 rounds with the strategy.

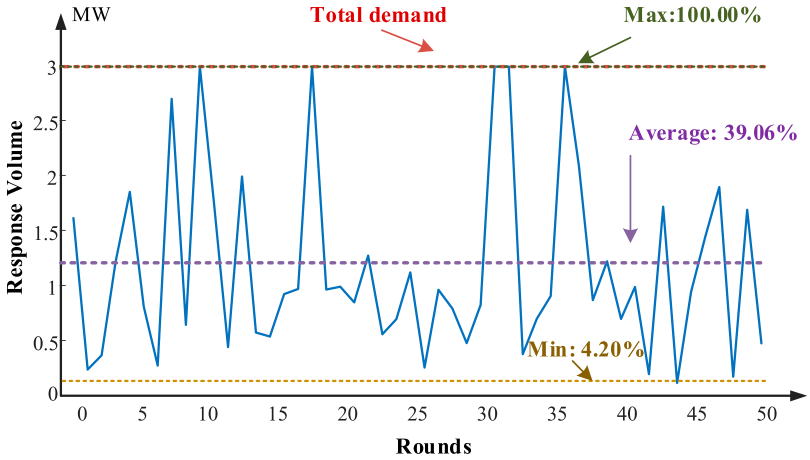

FIGURE 15 | Response results of 50 rounds without the strategy.

response amount and response rate vary greatly, but there is no obvious regulation, as shown in **Figure 15** and **Supplementary Table S3**. The phenomenon, on the one hand, can illustrate the significant influence of information transmission error on the response result and, on the other hand, prove the necessity to adopt a strategy to prevent or avoid the problem. The strategy proposed can effectively improve fault tolerance ability and stabilize the result when the errors exist.

CONCLUSION

This study considers the possible errors in information transmission when large-scale loads participate in demand response. Based on the information format modification and the Paxos distributed algorithm, a weakly consistent demand response strategy considering information collation and correction is proposed, targeting the practical DR implementation with robustness. Through the analysis of specific demand response cases of residential air conditioning loads under different conditions, the proposed strategy is demonstrated to be effective in information self-inspection and furthermore the robust demand response implementation. Specifically, the proposed approach is especially applicable to the large-scale systems, while the error tolerance range is increased to 10%. The proposed distributed algorithm provides a reliable and robust scheme for the implementation of large-scale demand response, which is a strong foundation of the future smart-grid development.

DATA AVAILABILITY STATEMENT

The original contributions presented in the study are included in the article/**Supplementary Material**; further inquiries can be directed to the corresponding author.

AUTHOR CONTRIBUTIONS

YL: Conceptualization, Writing–original draft, Funding acquisition. TG: Software, Validation. XS: Project administration. ZY: Formal Analysis. YZ: Writing–review and editing. SG: Conception, Methodology. XH: Supervision.

FUNDING

This work was supported in part by the National Nature Science Foundation of China under Grant 51907024.

SUPPLEMENTARY MATERIAL

The Supplementary Material for this article can be found online at: https://www.frontiersin.org/articles/10.3389/fenrg.2021.718859/full#supplementary-material

REFERENCES

Altisen, K., Devismes, S., Dubois, S., and Petit, F. (2019). Introduction to Distributed Self-Stabilizing Algorithms. *Synth. Lectures Distributed Comput. Theor.* 8 (1), 1–165. doi:10.2200/s00908ed1v01y201903dct015

Bahrami, S., Amini, M. H., Shafie-Khah, M., and Catalao, J. P. S. (2018). A Decentralized Renewable Generation Management and Demand Response in Power Distribution Networks. *IEEE Trans. Sustain. Energ.* 9 (4), 1783–1797. doi:10.1109/tste.2018.2815502

Burns, B. (2018). *Designing Distributed Systems: Patterns and Paradigms for Scalable, Reliable Services*. Boston, MA: O'Reilly Media, Inc. doi:10.1109/aspdac.2018.8297270

Chen, L., Yang, Y., and Xu, Q. (2021). Retail Dynamic Pricing Strategy Design Considering the Fluctuations in Day-Ahead Market Using Integrated Demand Response. *Int. J. Electr. Power Energ. Syst.* 130, 106983. doi:10.1016/j.ijepes.2021.106983

Chen, S., and Liu, C.-C. (2017). From Demand Response to Transactive Energy: State of the Art. *J. Mod. Power Syst. Clean. Energ.* 5 (1), 10–19. doi:10.1007/s40565-016-0256-x

D'hulst, R., Labeeuw, W., Beusen, B., Claessens, S., Deconinck, G., and Vanthournout, K. (2015). Demand Response Flexibility and Flexibility Potential of Residential Smart Appliances: Experiences from Large Pilot Test in Belgium. *Appl. Energ.* 155, 79–90. doi:10.1016/j.apenergy.2015.05.101

Dalwadi, N. N., and Padole, C. M. (2017). Comparative Study of Clock Synchronization Algorithms in Distributed Systems. *Adv. Comput. Sci. Technol.* 10 (6), 1941–1952.

Dvorkin, Y., Lubin, M., Backhaus, S., and Chertkov, M. (2015). Uncertainty Sets for Wind Power Generation. *IEEE Trans. Power Syst.* 31 (4), 3326–3327. doi:10.1109/TPWRS.2015.2476664

Gao, Y., Sun, Y., Wang, X., Chen, F., Ehsan, A., Li, H., et al. (2017). Multi-objective Optimized Aggregation of Demand Side Resources Based on a Self-Organizing Map Clustering Algorithm Considering a Multi-Scenario Technique. *Energies* 10 (12), 2144. doi:10.3390/en10122144

Heffron, R., Körner, M.-F., Wagner, J., Weibelzahl, M., and Fridgen, G. (2020). Industrial Demand-Side Flexibility: A Key Element of a Just Energy Transition and Industrial Development. *Appl. Energ.* 269, 115026. doi:10.1016/j.apenergy.2020.115026

Hoggett, R. (2014). Technology Scale and Supply Chains in a Secure, Affordable and Low Carbon Energy Transition. *Appl. Energ.* 123, 296–306. doi:10.1016/j.apenergy.2013.12.006

Huang, W., Zhang, N., Kang, C., Li, M., and Huo, M. (2019). From Demand Response to Integrated Demand Response: Review and prospect of Research and Application. *Prot. Control. Mod. Power Syst.* 4 (1), 1–13. doi:10.1186/s41601-019-0126-4

Iwanicki, K. (2018). "A Distributed Systems Perspective on Industrial IoT," in 2018 IEEE 38th International Conference on Distributed Computing Systems, Vienna, Austria, July 2–6, 2018 (Vienna, Austria: ICDCS), 1164–1170.

Kolhe, M. (2012). Smart Grid: Charting a New Energy Future: Research, Development and Demonstration. *Electricity J.* 25 (2), 88–93. doi:10.1016/j.tej.2012.01.018

Lamport, L. (2006). Fast Paxos. *Distributed Comput.* 19 (2), 79–103.

Lu, N. (2012). An Evaluation of the HVAC Load Potential for Providing Load Balancing Service. *IEEE Trans. Smart Grid* 3 (3), 1263–1270. doi:10.1109/TSG.2012.2183649

Mahdavi, N., and Braslavsky, J. H. (2020). Modelling and Control of Ensembles of Variable-Speed Air Conditioning Loads for Demand Response. *IEEE Trans. Smart Grid* 11 (5), 4249–4260. doi:10.1109/tsg.2020.2991835

Marzullo, K., Meling, H., and Mei, A. (2011). "Brief Announcement: When You Don't Trust Clients: Byzantine Proposer Fast Paxos," in International Symposium on Distributed Computing, Macau, China, January 1, 2012, 143–144.

Ming, N., Qian, C., Manli, L., Qi, W., and Yi, T. (2018). A Frequency Control Model for Cyber Physical Power System Considering Demand Response Strategy. *Energ. Proced.* 145, 38–43. doi:10.1016/j.egypro.2018.04.008

Perez, K. X., Baldea, M., and Edgar, T. F. (2016). Integrated HVAC Management and Optimal Scheduling of Smart Appliances for Community Peak Load Reduction. *Energy and Buildings* 123, 34–40. doi:10.1016/j.enbuild.2016.04.003

Qi, L., Zhang, X., Dou, W., and Ni, Q. (2017). A Distributed Locality-Sensitive Hashing-Based Approach for Cloud Service Recommendation from Multi-Source Data. *IEEE J. Select. Areas Commun.* 35 (11), 2616–2624. doi:10.1109/jsac.2017.2760458

Rao, J., Shekita, E. J., and Tata, S. (2011). *Using Paxos to Build a Scalable, Consistent, and Highly Available Datastore*. arXiv preprint arXiv, 1103.2408.

Raynal, M. (2018). *Fault-Tolerant Message-Passing Distributed Systems*. Cham, Switzerland: Gewerbestrasse, 459.

Ribó-Pérez, D., Larrosa-López, L., Pecondón-Tricas, D., and Alcázar-Ortega, M. (2021). A Critical Review of Demand Response Products as Resource for Ancillary Services: International Experience and Policy Recommendations. *Energies* 14, 846. doi:10.3390/en14040846

Samad, T., Koch, E., and Stluka, P. (2016). Automated Demand Response for Smart Buildings and Microgrids: The State of the Practice and Research Challenges. *Proc. IEEE* 104 (4), 726–744. doi:10.1109/JPROC.2016.2520639

Shen, C., Bao, Y. Q., Ji, T. Z., Zhang, J. L., and Wang, Z. (2019). "A Robust Control Strategy for Air Conditioner Group to Participate in Power System Frequency Regulation," in *2019 IEEE Innovative Smart Grid Technologies-Asia*. (Chengdu, China: ISGT Asia), 678–682.

Shi, W. C., and Li, J. P. (2012). "Research on Consistency of Distributed System Based on Paxos Algorithm," in 2012 International Conference on Wavelet Active Media Technology and Information Processing, Chengdu, China, December 17, 2012 (Chengdu, China: ICWAMTIP), 257–259.

Tang, R., Wang, S., and Yan, C. (2018). A Direct Load Control Strategy of Centralized Air-Conditioning Systems for Building Fast Demand Response to Urgent Requests of Smart Grids. *Automation in Construction* 87, 74–83. doi:10.1016/j.autcon.2017.12.012

Xiao, F., Zhang, Z., and Abawajy, J. (2019). Workflow Scheduling in Distributed Systems under Fuzzy Environment. *Ifs* 37 (4), 5323–5333. doi:10.3233/jifs-190483

Zheng, W., Wu, W., Zhang, B., Sun, H., and Liu, Y. (2015). A Fully Distributed Reactive Power Optimization and Control Method for Active Distribution Networks. *IEEE Trans. Smart Grid* 7 (2), 1021–1033. doi:10.1109/TSG.2015.2396493

Zhou, R., Zhang, Z., Liu, X., Ju, P., Qin, C., and Chen, Q. (2015). "November). Simulation and Modeling of Blended Constant-Frequency and Variable-Frequency Air-Conditioner," in 2015 5th International Conference on Electric Utility Deregulation and Restructuring and Power Technologies, Changsha, China, November 26–29, 2015 (Chengdu, China: DRPT), 269–273.

Zhu, Y., and Fridman, E. (2020). Decentralized Predictor Output Feedback for Large-Scale Systems with Large Delays. *IFAC-PapersOnLine* 53 (2), 7527–7532. doi:10.1016/j.ifacol.2020.12.1346

Conflict of Interest: Author XS is employed by Guodian Nanjing Automation Co., Ltd.

The remaining authors declare that the research was conducted in the absence of any commercial or financial relationships that could be construed as a potential conflict of interest.

Publisher's Note: All claims expressed in this article are solely those of the authors and do not necessarily represent those of their affiliated organizations, or those of the publisher, the editors and the reviewers. Any product that may be evaluated in this article, or claim that may be made by its manufacturer, is not guaranteed or endorsed by the publisher.

frontiers in Energy Research

ORIGINAL RESEARCH
published: 30 September 2021
doi: 10.3389/fenrg.2021.718916

Non-Intrusive Load Monitoring Based on Unsupervised Optimization Enhanced Neural Network Deep Learning

Yu Liu, Jiarui Wang, Jiewen Deng, Wenquan Sheng and Pengxiang Tan*

School of Electrical Engineering, Southeast University, Nanjing, China

Non-intrusive load monitoring has broad application prospects because of its low implementation cost and little interference to energy users, which has been highly expected in the industrial field recently due to the development of learning algorithms. Targeting at the investigation of practical and reliable load monitoring in field implementations, a non-intrusive load disaggregation approach based on an enhanced neural network learning algorithm is proposed in this article. The presented appliance monitoring approach establishes the neural network model following the supervised learning strategy at first and then utilizes the unsupervised learning based optimization to enhance the flexibility and adaptability for diverse scenarios, leading to the improvement of disaggregation performance. By verifications on the REDD public dataset, the proposed approach is demonstrated to be with good performance in non-intrusive load monitoring. In addition to the accuracy enhancement, the proposed approach is also with good scalability, which is efficient in recognizing the newly added appliance.

Keywords: unsupervised learning, NILM, neural network, BP – back propagation algorithm, electricity consumption behavior analysis, k-means clustering

OPEN ACCESS

Edited by:
Dongdong Zhang,
Guangxi University, China

Reviewed by:
Xuguang Hu,
Northeastern University, China
Bo Liu,
King Fahd University of Petroleum and Minerals, Saudi Arabia

****Correspondence:***
Yu Liu
yuliu@seu.edu.cn

Specialty section:
This article was submitted to Smart Grids, a section of the journal Frontiers in Energy Research

Received: *01 June 2021*
Accepted: *06 August 2021*
Published: *30 September 2021*

Citation:
Liu Y, Wang J, Deng J, Sheng W and Tan P (2021) Non-Intrusive Load Monitoring Based on Unsupervised Optimization Enhanced Neural Network Deep Learning. Front. Energy Res. 9:718916. doi: 10.3389/fenrg.2021.718916

INTRODUCTION

In the context of the carbon neutrality plan proposed by China in the late 2020 (President of the People's, 2020), the energy related industry is with high expectation to contribute to the realization while the power system is highlighted. For better and efficient operation, the power grid is designed to be smart, among which the transparency, that is, knowing small-grained operating data including the status of various electrical appliances, is of high value. By knowing the operation information of single appliances, energy users can understand the insights of appliance operations and help them conduct energy conservation. In addition, the power companies may extract valuable information through electric appliance data mining and introduce corresponding measures, leading to saving electricity up to 14% (Ehrhardt et al., 2010). Therefore, providing users with appliance status information and furthermore the energy saving and cost reduction solutions has become one of the important business models in the future. This is the challenge and also opportunity for power companies and many integrated energy service providers in the context of energy digitization and information transformation. The detailed appliance monitoring is one of the effective means to support such revolution (Guo et al., 2021).

There are two implementation methods for appliance monitoring, namely, the intrusive appliance monitoring (ILM) and the non-intrusive appliance monitoring (NILM). The former focuses on the

hardware by installing sensors and chips on each appliance to monitor each device separately. Meanwhile, NILM focuses on software algorithms using power data from the service panel to analyze the resident's internal appliance operating status (HART, 1992). Considering that the sensor-based monitoring scheme is expensive, NILM is highly welcomed by energy users and becomes the research front in both academic and industrial fields.

NILM was put forward in the 1990's by professor Hart G. W. from MIT (HART, 1992). Since the initial NILM has a high computational complexity and low accuracy, it did not attract much attention at that time. In recent years, due to the rapid development of computer science, especially the widespread use of deep learning for pattern recognition, NILM has now regained the attention of scholars and has become a research hotspot. Currently, non-intrusive appliance monitoring is mainly divided into two categories based on diverse sampling rates, that is, low-frequency and high-frequency. The information utilized in low-frequency data mainly includes current, voltage, power, etc. Because of the simplicity, the low-frequency data may lead to some problems such as inaccurate performance. Meanwhile, the high-frequency data usually contain more information, such as current harmonics, voltage–current trajectories, and high-frequency transient waveforms (Cox et al., 2006). Although the results of high-frequency data analysis are usually more accurate, the high requirements for monitoring equipment show a cost disadvantage in comparison with low-frequency data analysis. From the view of practical applications, the low-frequency data–based solutions become more and more attractive considering the industrial aspect and therefore are focused in our work.

For valid applications of NILM technology, the credible load disaggregation is the premise. To address the reliable appliance monitoring, various NILM solutions have been proposed. First, some mathematical models have been explored, such as fuzzy model (Lin and Tsai, 2014), graph signal processing (He et al., 2018), linear programming model and (Liu et al., 2020). The fuzzy model obtains the membership degree of each sample signal to all appliance centers by optimizing the objective function, thereby determining the appliance category of sample signals to achieve the purpose of automatically identifying sample data (Lin and Tsai, 2014). Meanwhile, graph signal processing first establishes an undirected graph based on the signal simple, then groups the on/off events for appliances, and finally defines an optimization problem to find the signal with a minimum variation (He et al., 2018). Linear programming model treats NILM problem as an optimization and forms a multi-feature objective function to realize appliance decomposition and recognition for different electrical appliances (Liu et al., 2020). Although some achievements have been realized by mathematical model-based research studies, there still exist some limitations. The most prominent is that most of these explorations are optimization based, resulting in the low scalability of the formulation and the high dependency of the algorithms. Therefore, the disaggregation performance is highly scenario dependent, and the model is required to be tuned for the practical applications. However, the rise of deep learning algorithms has provided some effective ways to overcome these obstacles, and hence, a number of research studies have been investigated. The hidden Markov model (HMM) (Kolter and Jaakkola, 2012) is a typical category of these studies, where a double random process combing the appliance states and explicit random functions is utilized to establish the operation series. Furthermore, neural networks (NNs) have been combined with HMMs in a study by Yan et al. (2019), where the emission probabilities of the HMM are modeled by a Gaussian distribution for the state representing the single appliance and by a DNN for the state representing the aggregated signal. By the above investigations, the high potential of deep learning approaches in the NILM problem is demonstrated.

At present, deep learning in non-intrusive appliance monitoring learning algorithms can be roughly divided into three categories, that is, supervised algorithms (Liu et al., 2019a), unsupervised algorithms (Li and Dick, 2019), and semi-supervised algorithms (Zoha et al., 2012). Supervised algorithms can learn from training data or can establish a model and then speculate a new instance based on this model. It has the advantages of simple implementation, fast calculation speed, small storage space, and high accuracy of analysis results (Liu et al., 2019a). However, there are some problems. For example, when the spatial characteristics are large, the logistic regression performance is poor. There are also some disadvantages such as under-fitting or over-fitting and poor self-learning ability. The unsupervised algorithm refers to a data processing method that classifies samples through data analysis of many samples of the research object without category information. It has strong self-learning ability and new data can be directly added to the data set without retraining, but it also has the disadvantages of low accuracy of analysis results (Kelly and Knottenbelt, 2015). Semi-supervised learning uses a large amount of unlabeled data and simultaneously uses labeled data for pattern recognition, and hence, it is considered as the most promising learning algorithm branch. However, the research on semi-supervised regression problems is relatively limited.

Among all the reviewed deep learning approaches, the neural networks are highlighted due to their outstanding performance. In addition to Bonfigli et al. (2018) where NNs are employed for the improvement of NILM performance, there are many research publications discussing the advantages of neural networks in enhancing NILM. The literature Andrean et al. (2018) is an early literature to solve the NILM by using NNs, where the studies named neural NILM are proposed at the first stage and the related research studies are inspired. Bonfigli et al. (2018) proposed a neural network-based approach for non-intrusive harmonic source identification. In this approach, NNs are trained to extract important features from the input current waveform to uniquely identify various types of devices using their distinct harmonic signatures. In order to be suitable for a specific problem, some NN approaches are modified for diverse NILM applications. An additional optimization is proposed by Faustine and Pereira (2020) to be embedded into the NILM formulation, forming the noise reduction self-encoding method. As research studies go further, more and more investigations have been reported in neural NILM problems.

(Tan et al., 2011) proposed the convolutional neural network (CNN)-based multi-label learning approach, which links multiple appliances to an observed aggregate current signal. The approach applies the Fryze power theory to decompose the current features into active and non-active components and use the Euclidean distance similarity function to transform the decomposed current into an image-like representation, which achieves remarkable progress. (Liu et al., 2019b) proposed a general appliance recognition model based on the convolutional neural network. The parameters do not depend on the appliances category, and a time series of 0 and 1 can be obtained to represent the switching state of a single appliance. In a study by Monteiro et al. (2021), the problem of identifying the electrical loads connected to a house is investigated, and a system capable of extracting the energy demand of each individual device is proposed. The whole study is NILM based, and the disaggregation is CNN formulated, achieving the simultaneous detection and classification. Although proved by so many studies, CNN-based solutions have certain disadvantages that the model is usually complicated, leading to the decreased practicability. Meanwhile, the recurrent neural network (RNN) is also widely concerned in NILM, such as (Xue and Guo, 2016), where an RNN model is utilized to extract the appliance characteristics of the steady-state section as the model input for identification after the event is detected. However, in the process of large sample data training, the RNN model shows a limitation defined as a phenomenon of "gradient disappearance". To overcome the difficulties of RNN in learning long-term dependencies, a 1D CNN-based approach is proposed in a study by Figueiredo et al. (2014), and the NILM problem is solved by considering the electrical current signals and using Long Short-Term Memory (LSTM) neural networks. Although a better performance is achieved, the high complexity infers to the impossibility of applying in field measurements by these approaches. As seen, the neural NILM is highlighted by building a multi-layer perceptron with multiple hidden layers. Through layer-by-layer training, the signal features of each layer are extracted, and finally, the underlying features are combined to form more abstract high-level features to realize the prediction and classification of data objects (Zhou et al., 2018). The only disadvantage is the algorithmic complexity. Understanding this, some investigations focusing on complexity reduction have been conducted, such as Ciancetta et al., (2021), where the simplest neural network, that is, back propagation neural network (BPNN), is used to realize load identification using the sudden change value of active power and corresponding odd harmonics only. By verifying the effectiveness of BPNN in NILM problems, it is possible to deploy such a deep learning approach for practical applications.

However, toward the practical applications of NILM, multiple new concerns emerge in addition to the high accuracy requirements. First, the deployed approach is expected to be with self-learning ability, that is, it is capable of adapting to diverse scenarios. Second, the algorithm complexity of the applied approach should be acceptable, which is possible to be allocated on smart meters. Last but not least, it would be really practical if the newly added appliance can be addressed with guaranteed performance.

In order to address the above problems, this article utilizes the unsupervised learning-based optimization to enhance the supervised learning-based NN-NILM model, while the corresponding solution is proposed to address the newly added appliance. First, the basic appliance disaggregation model is established based on the clustering oriented BPNN learning framework, where both adaptability and simplicity are achieved. Considering the deficient samples of newly added appliance, an unsupervised learning-based optimization scheme is proposed, which combines the large samples of original appliances and small samples of unknown appliance to reconstruct the learning network to achieve the reliable disaggregation. By implementing the proposed approach, the inherent problems of neutral networks, such as insufficient fitting, over-fitting, and insufficient promotion capabilities, are all alleviated, leading to the improvement of NILM with high accuracy and flexible scalability. The comprehensive verifications are investigated on the REDD public dataset, and the results demonstrate the effectiveness of our work. In addition to addressing the newly added appliance, the proposed approach also provides a reliable NILM solution with high precision and robustness, leading to the practical NILM applications.

The main contribution of this study is the presentation of a practical NILM solution with reliable accuracy, adaptive flexibility, and high scalability. In other words, the presented NILM approach can be adaptive to diverse practical application scenarios, even addressing the newly added appliance without sufficient information. Such contribution fills a research gap in related field. Detailed technical contributions can be summarized as follows:

- A practical and adaptive NILM formulation model is established based on the BP neural network, of which the parameter settings are following the supervised learning scheme.
- An unsupervised learning based optimization is utilized on the presented NILM model to improve the scalability and robustness of the approach.
- Combining the unsupervised learning based optimization with the supervised BPNN model, the proposed NILM solution is able to identify the newly added appliances, while an important research gap is filled.
- The presented model and method are verified *via* a public dataset. In addition to the high precision of load disaggregation, all the proposed potentials are demonstrated to be valid.

The rest of this article is organized as follows. The methodologies are discussed in the Methodology section, including the supervised NILM model based on BPNN and unsupervised optimization based enhancement. The Results and Discussions section illustrates our results and discussions in detail. Conclusions are drawn in the Conclusion section.

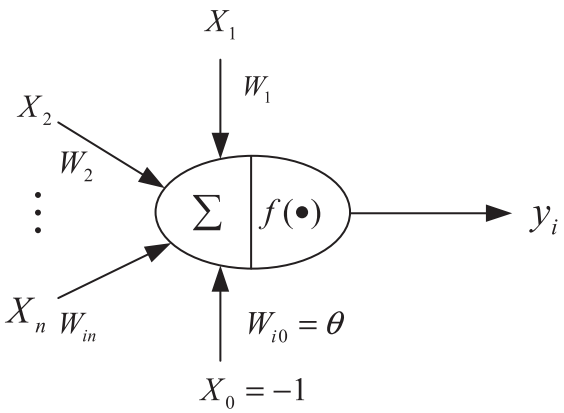

FIGURE 1 | The principle of the artificial neuron model.

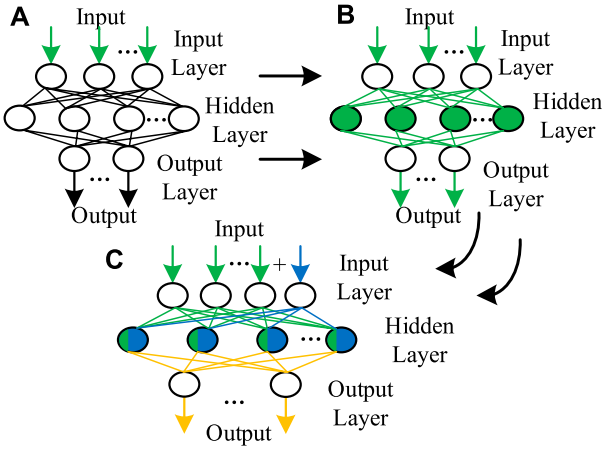

FIGURE 2 | Three-layer BP neural network model and enhancement: **(A)** Typical model, **(B)** NILM featured model, **(C)** Enhanced NILM model addressing newly added appliance.

METHODOLOGY

Basic Principles of Neural Networks

Artificial Neuron Model

Artificial neuron is the basic element of a neural network, and its principle can be represented by **Figure 1**. The neuron model in the **Figure 1** is called the MP model (McCulloch–Pitts Model), also known as a processing element (PE) of the neural network.

In **Figure 1**, $x_1 - x_n$ are the input signals coming from the other neurons. W_{ij} denotes the connected weights expressed from neuron j to neuron i. θ is the threshold value, usually known as a bias. Then, the relationship between the output and input of neuron i can be expressed as follows:

$$net_i = \sum_{j=1}^{n} W_{ij} x_j - \theta, \tag{1}$$

where net_i is the net activation of the neuron i.

If the threshold is regarded as the weight W_{i0} of an input x_0 of neuron i, the above formula can be simplified to

$$net_i = \sum_{j=0}^{n} W_{ij} x_j. \tag{2}$$

If $\boldsymbol{X}$ is used to represent the input vector and $\boldsymbol{W}$ is used to represent the weight vector, that is,

$$\boldsymbol{X} = [x_0, x_1, x_2, \cdots, x_n],$$
$$\boldsymbol{W} = [W_{i0}, W_{i1}, W_{i2}, \cdots, W_{in}]^{\mathrm{T}},$$

then the output of the neuron can be expressed in the form of vector multiplication as

$$net_i = \boldsymbol{X}\boldsymbol{W}. \tag{3}$$

By applying a so-called activation function or transfer function $f(.)$ on net_i, the final output y_i can be expressed as

$$y_i = f(net_i) = f(\boldsymbol{X}\boldsymbol{W}). \tag{4}$$

If the net activation *net* of a neuron is positive, the neuron is said to be in an activated state or in a state of fire. If the net activation *net* is negative, it is said that the neuron is in an inhibited state.

Neural Network Models

A neural network is a network composed of many interconnected neurons, of which the feed-forward network is widely used. This kind of network only has a feed signal during the training process, and during the classification process, the data can only be sent forward until it reaches the output layer. There is no backward feedback signal between the layers, so it is called a feed-forward network. The perceptron and BP neural network belong to this type.

For a three-layer feed-forward neural network, if $\boldsymbol{X}$ is used to represent the input vector of the network, $\boldsymbol{W}_1$, $\boldsymbol{W}_2$, and $\boldsymbol{W}_3$ represent the connection weight vectors of each layer of the network, and $\boldsymbol{F}_1$, $\boldsymbol{F}_2$, and $\boldsymbol{F}_3$ represent the activation functions set of the three layers of the neural network, then the output vector $\boldsymbol{Y}_1$ of the first layer of neurons in the neural network is

$$\boldsymbol{Y}_1 = \boldsymbol{F}_1(\boldsymbol{X}\boldsymbol{W}_1). \tag{5}$$

The output of the second layer $\boldsymbol{Y}_2$ is

$$\boldsymbol{Y}_2 = \boldsymbol{F}_2(\boldsymbol{F}_1(\boldsymbol{X}\boldsymbol{W}_1)\boldsymbol{W}_2). \tag{6}$$

The output of the final layer $\boldsymbol{Y}_3$ is

$$\boldsymbol{Y}_3 = \boldsymbol{F}_3(\boldsymbol{F}_2\boldsymbol{F}_1(\boldsymbol{X}\boldsymbol{W}_1)\boldsymbol{W}_2)\boldsymbol{W}_3. \tag{7}$$

If the activation functions are all linear functions, then the output $\boldsymbol{Y}_3$ of the neural network will be a linear function of the input $\boldsymbol{X}$. However, the NILM problem leads to the approximation of higher order functions; therefore, an appropriate nonlinear function should be selected as the activation function.

The BP network has a strong nonlinear mapping ability, and theoretically, a three-layer BP neural network can approximate any nonlinear function. So BPNN is extremely appropriate for our NILM problem. The typical three-layer BP neural network model is shown in **Figure 2A**.

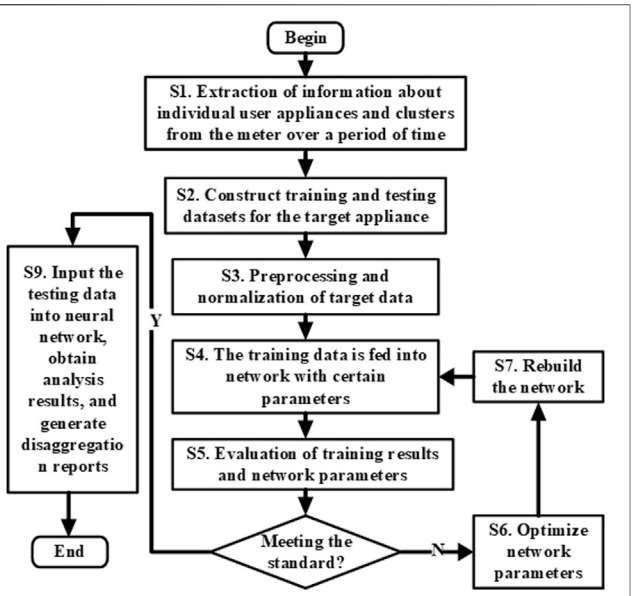

FIGURE 3 | Method flow of BPNN based NILM.

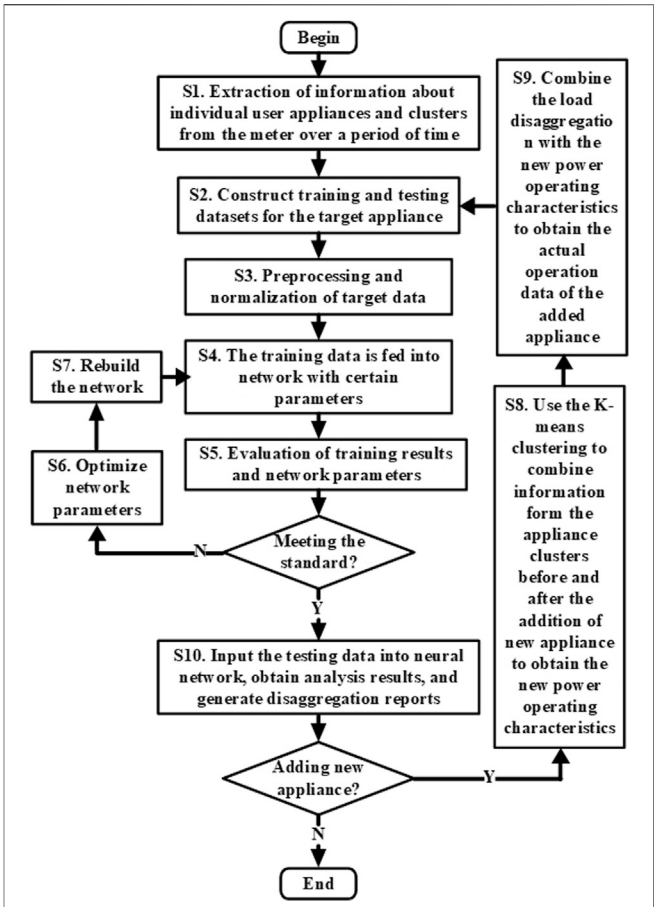

FIGURE 4 | The method flow of enhanced NILM with newly added appliance.

NILM Algorithm by Enhanced Neural Network

The Basic Model of NILM

The main idea of the NILM system is to identify the power consumption of individual appliances in a house based on the analysis of the aggregated data measured from a single meter. The whole formulation can be expressed as

$$P = \sum_{i=1}^{n} P_i + e_0, \tag{8}$$

where P is the aggregated data measured from a meter, P_i is the load signature of ith appliance, and e_0 is the error generated. Note that the data from smart meter can be real power, reactive power, harmonics, or the combination of these electric features. Since we are targeting the practical applications, only real power and reactive power are utilized in the following discussions, that is, P denotes power. Nevertheless, the proposed approach is compatible with other feature utilizations.

BPNN Based NILM

For preparation of integrating the BPNN model into NILM formulation, the first step is to convert the measured data from a smart meter to be adequate for the BPNN input. Therefore, a normalization is required for the power matrix obtained from the entrance meter,

$$\boldsymbol{P}_{\text{norm}} = (\boldsymbol{P} - P_{\min})/(P_{\max} - P_{\min}), \tag{9}$$

where $\boldsymbol{P}$ is the power matrix containing all the measured power from the meter. $\boldsymbol{P}_{\text{norm}}$ is the normalized power matrix of $\boldsymbol{P}$ and also the input of BPNN. $P_{\min}$ and $P_{\max}$ are, respectively, the minimum power and the maximum power after traversing the measured power matrix.

Originally, we have a typical BP neural network with three layers as seen in **Figure 2A**. Once the processed data matrix enters the neural network as a training matrix, a non-intrusive load monitoring network following supervised learning is established, as illustrated in **Figure 2B**. To be specific, the network error square is used as the objective function, and the gradient descent method is used to optimize the problem. The parameters of the learning algorithm are adjusted by the validation set or cross-validation. The detailed implementations of constructing the adaptive BPNN for NILM are shown in **Figure 3**. After implementing the procedures, the internal parameters of the BP neural network, especially the hidden layer, have been changed and also customized with the diverse input data. Therefore, the proposed model is highly adaptive to the input data, and such a supervised learning scheme is welcomed by a practical NILM problem, where the deployed monitoring can be self-adapting to diverse household scenarios.

Enhanced BPNN Based NILM

Even using a successfully trained neural network for appliance monitoring, the problem of network failure occurs due to the newly added appliances. Because there are new appliance features in the appliance clusters that have not been learned by the

TABLE 1 | Results of BPNN without unsupervised optimization for dataset A.

	App1	App2	App3	App4	App5	App6	App7	App8
PRE	0.1825	0.2998	0.1286	0.1367	0.2316	0.2781	0.2571	NA*
REC	0.9989	0.9999	0.9978	0.9988	0.9997	0.9749	0.9999	NA
F1	0.3086	0.4613	0.2279	0.2405	0.3760	0.4351	0.4090	NA
MAE	0.9468	1.1474	1.1123	1.1179	0.9769	1.1423	1.1224	NA

NA: Not applicable for the appliance.

TABLE 2 | Results of BPNN with unsupervised optimization for dataset A.

	App1	App2	App3	App4	App5	App6	App7	App8
PRE	0.9895	0.9976	0.9781	0.9999	0.9882	0.9999	0.9999	0.9562
REC	0.9932	0.9999	0.9898	0.9998	0.9782	0.9999	0.9999	0.9678
F1	0.99997	0.9998	0.9999	0.9992	0.9899	0.9999	0.9999	0.9799
MAE	0.0364	0.0406	0.1411	0.0652	0.0083	0.1735	0.0064	0.1334

TABLE 3 | Results of BPNN with unsupervised optimization for dataset B.

	App1	App2	App3	App4	App5	App6
PRE	0.5222	0.5988	0.3875	0.4961	0.4670	0.4544
REC	0.9992	0.9898	0.9673	0.9719	0.9999	0.9999
F1	0.6861	0.7490	0.5586	0.6632	0.6367	0.6249
MAE	0.5132	0.4782	0.7488	0.4824	0.5541	0.5929

supervised neural network, the unsupervised learning-based scheme is required to explore the signatures of new features based on the insufficient samples. Here, the adaptive *K*-means clustering algorithm is used to iteratively address the newly added appliance for each target clustering center. First, the algorithm selects *K* points from the given dataset, where each point represents the initial cluster center. Then, calculate the Euclidean distance of each remaining sample to these cluster centers, and classify it into the cluster closest to it. Finally, recalculate the average value of each cluster. The whole process is repeated until the square error criterion function reaches the smallest (Wang et al., 2019). The square error criterion is defined as

$$\min E = \min \sum_{i=1}^{K} \sum_{j=1}^{t_i} \left\| x_j - m_i \right\|^2, \tag{10}$$

where K is the number of clusters, t_i is the number of samples in the ith category, and m_i is the mean of the samples in the ith category. The *K*-means clustering algorithm is a typical distance-based clustering algorithm. The distance between points is used as the similarity evaluation index, that is, the closer the distance between two objects, the greater the similarity. So the Euclidean distance between diverse points in one cluster is expected to be as small as possible,

$$\min \sum_{i=1}^{K} \sum_{x \in m_i} dist\,(m_i, x)^2, \tag{11}$$

where dist(m,x) is the Euclidean distance function, calculating the Euclidean distance between point m and x. $x \in m_i$ refers to the points x clustered into ith category.

As seen from **Eq. 11**, this algorithm considers that clusters are composed of objects that are close to each other, so it makes the final goal to obtain compact and independent clusters. For practical implementation, it is important to determine the number of centers *K*. In our NILM problem, the method for determining the initial *K* value is as follows. Assume that the original *N* appliances are operating independently, and there are *M* appliances that may operate at the same time. Once we have a newly added appliance, the number of cluster centers is

$$1 + N + \sum_{i=1}^{M} C_M^i. \tag{12}$$

In the newly added clusters, the cluster center with the lowest power value is the rated feature center of the newly added appliance. Consistently, the *K*-means clustering algorithm can also obtain the new appliance action time stamp and then reconstitute the training data, including the electric features, switching action, and timestamp. In order to guarantee the effectiveness of the rated feature center, the following verification is conducted:

$$\text{find}\left\{ m_{o,i} \in \boldsymbol{M_o} \middle| m_{o,i} = m_{n,j} - m_{na} \right\}, \forall m_{n,j} \in \boldsymbol{M_n}, \tag{13}$$

where $\boldsymbol{M_o}$ and $\boldsymbol{M_n}$ are, respectively, the original cluster sets and newly added cluster sets. m_{na} is the rated feature center of the newly added appliance. $m_{o,i} \in \boldsymbol{M_o}$ refers to the specific center $m_{o,i}$ belonging to the original cluster sets, and $m_{n,j} \in \boldsymbol{M_n}$ refers to the specific center $m_{n,j}$ belonging to the newly added clusters. By such a closed loop check, we can obtain the reliable load signature of the newly added appliance. However, if **Eq. 13** is violated during the checking period, it is suggested to fine-tune the value of K based on **Eq. 12**. Such operations can be conducted multiple times until final results meet all constraints.

Following the above strategies, the detailed procedures addressing the newly added appliance are illustrated in **Figure 4**. By introducing a larger closed loop feedback as shown on the right, the approach handling the newly added appliance is embedded into the BPNN framework. The key

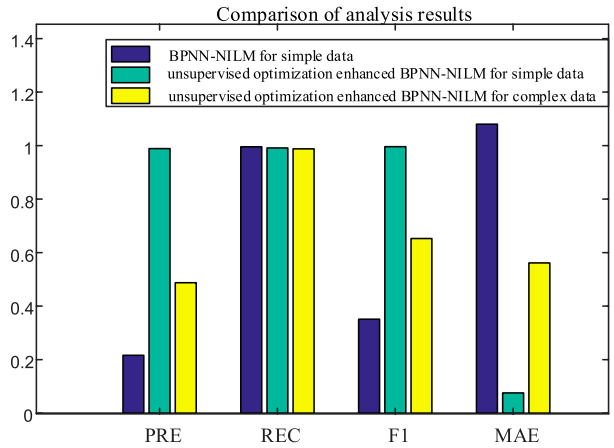

FIGURE 5 | Comparison of analysis results.

change of the neural network is shown in **Figure 2C**. By modifying the training matrix to change the constraints of the neural network and reconstruct it, the neural network can learn the rated features of the newly added appliance by itself. Specifically, the internal structure of the BP neural network is enhanced from two aspects. First, the input layer is supplemented with new neurons to handle the newly added appliance. Second, the parameters of the hidden layer are totally tuned based on the additional information by the newly added appliance. Correspondingly, the data flow after the hidden layer changes to take the new appliance feature into consideration. Based on the above analysis, the BPNN performs well even with insufficient data of newly added appliance. Such a strategy follows an unsupervised strategy and uses the *K*-means algorithm as the basic approach, so defined as *K*-means based unsupervised optimization. By enhancing the BPNN through *K*-means based unsupervised optimization, the scalability of the neural network NILM method has been improved. Besides, *via* the evolution process as shown from (a), (b), and (c) in **Figure 2**, it is clearly seen that the key ideas and solutions of incorporating the concerned problems in the BPNN-based NILM formulations.

RESULTS AND DISCUSSIONS

Data Preparation

In order to verify the effectiveness of the proposed strategy and approach, this article uses the data set generated based on the REDD data to conduct case studies. The data composition of the REDD low-frequency dataset is the power under 1 Hz for integral signals and 0.2–0.3 Hz for individual appliances. To be consistent, the data for individual appliances are complemented to be 1 Hz. Considering the different operating states and the possible power fluctuations, two scenarios with different complexities are prepared to analyze the proposed study. Dataset A is with a relatively simple appliance operating condition. It runs for 21 days and has seven independent appliances under a regular operation mode, as well as one newly added appliance. Dataset B is considering a more complicated operation situation, also running for a total of 21 days and with six independent appliances, as well as one newly added appliance. However, the appliances are operating randomly with more than 60 different operation combinations.

General NILM Results

In order to fully evaluate the performance of the study, this article selects four metrics, that is, precision, recall rate, *F*1 score, and average absolute error as evaluation indicators. The specific calculation of metrics (Barsim et al., 2014) is as follows:

$$PRE = \frac{TP}{TP + FP}, \tag{14}$$

$$REC = \frac{TP}{TP + FN}, \tag{15}$$

$$F1 = 2 \times \frac{PRE \times REC}{PRE + REC}, \tag{16}$$

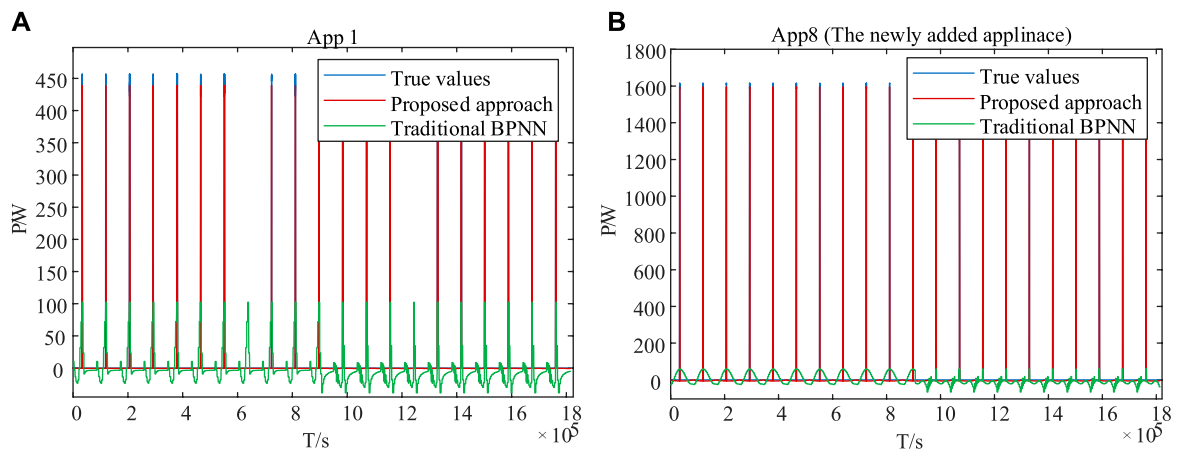

FIGURE 6 | Energy disaggregation results by diverse approaches **(A)** App1, **(B)** App8 (the newly added appliance).

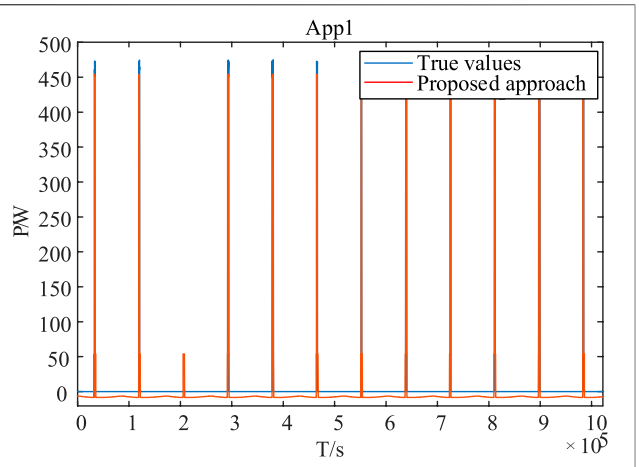

FIGURE 7 | Energy disaggregation results of App1 from dataset B.

$$MAE = \frac{1}{T_1 - T_0} \sum_{t=T_0}^{T_1} \text{abs}\left(\frac{\tilde{y}_t - y_t}{y_t}\right), \tag{17}$$

where *PRE* represents the precision. *REC* represents the recall rate. *F*1 represents the *F*1 score, also known as the balanced *F* score. *TP* represents the total number of the sequence points that the electrical appliance is actually working and the disaggregation result is also working. *FP* represents the number of sequence points that the electrical appliance is actually working but the result is in a non-working state. *FN* represents the total number of sequence points, which indicate that the electrical appliance is actually not working but the model decomposition result is in the working state. y_t represents the true power of the electrical appliance at a time t. $\tilde{y}_t$ represents the disaggregated power at time t, and *MAE* represents the average absolute error of the power disaggregation in the time period from T_0 to T_1. The *PRE*, *REC*, and *F*1 scores can reflect the accuracy of the model in judging whether the electrical appliance is in a working state and are the basic indicators of the non-intrusive load disaggregation. *MAE* can reflect the accuracy of the disaggregated power value at each time period. The lower the value, the higher the accuracy of the power decomposed value.

First, results and discussions are provided focusing on the dataset A. Through multiple experiments for the dataset A, the disaggregation results without the consideration of the newly added appliance are shown in **Table 1**, while **Table 2** shows the results by the complete strategy and approach proposed in this study. As seen, after the new appliance is added, the new network obtained by the proposed algorithm has good performance in accuracy, recall rate, and balanced F1 score. Comparing with the approach that BPNN without unsupervised optimization, we can see the remarkable enhancement by the proposed study. The load disaggregation results are reliable and desired with a new appliance considered in the household.

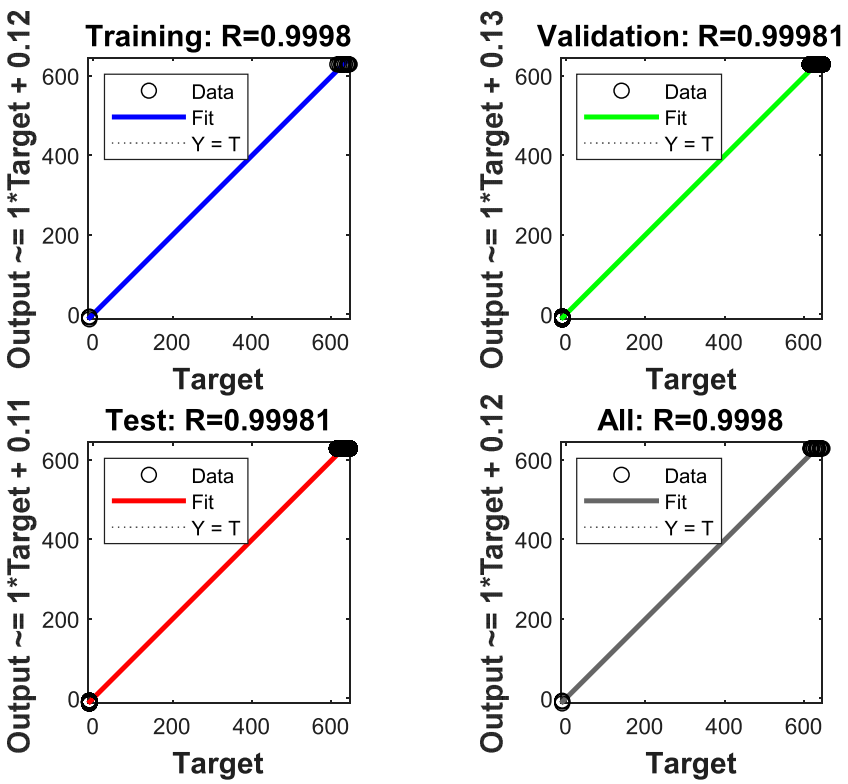

FIGURE 8 | The training results of the neural network.

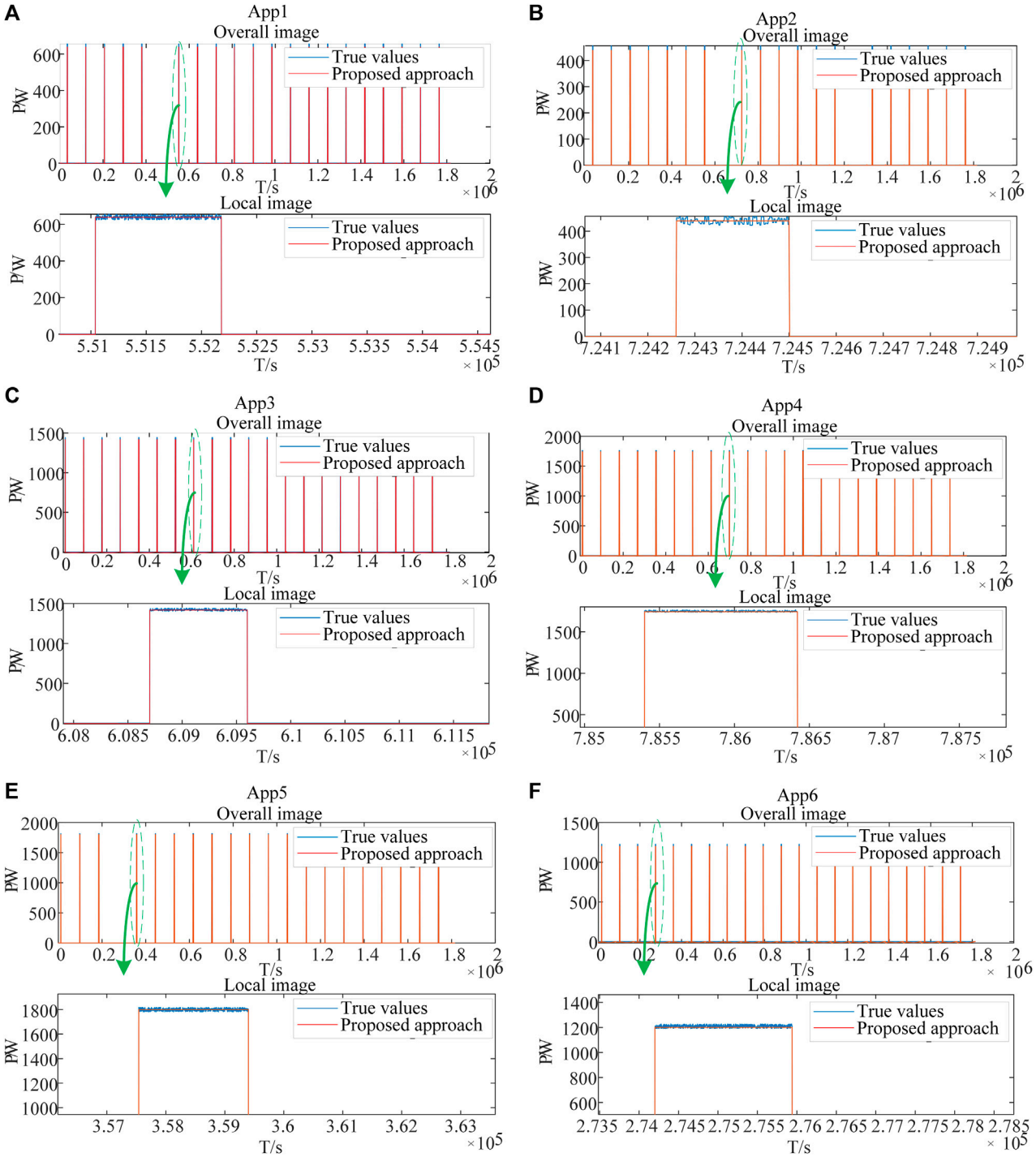

FIGURE 9 | Load disaggregation performance of the trained neural network for dataset A: **(A)** App1, **(B)** App2, **(C)** App3, **(D)** App4, **(E)** App5, and **(F)** App6.

Because the appliance operation mode of dataset A is relatively simple, the parameters calculated in the BPNN have a good degree of fit. To test the robustness of the algorithm, data set B with complex appliance operation mode is used for analysis again. **Table 3** illustrates the disaggregation performance for dataset B by implementing our approach. Although the precision, F1 score, and MAE parameters have been reduced to a certain extent, the proposed approach is still effective in recognizing the newly added appliance. In detail, the recall rates keep in a high level, while the balanced F1 scores are almost all over 0.6. Such results are desirable since we only take real and reactive power as our load signatures and try to disaggregate the appliances under complicated operation modes. As to the power error, **Table 1** shows that the traditional BPNN method has a

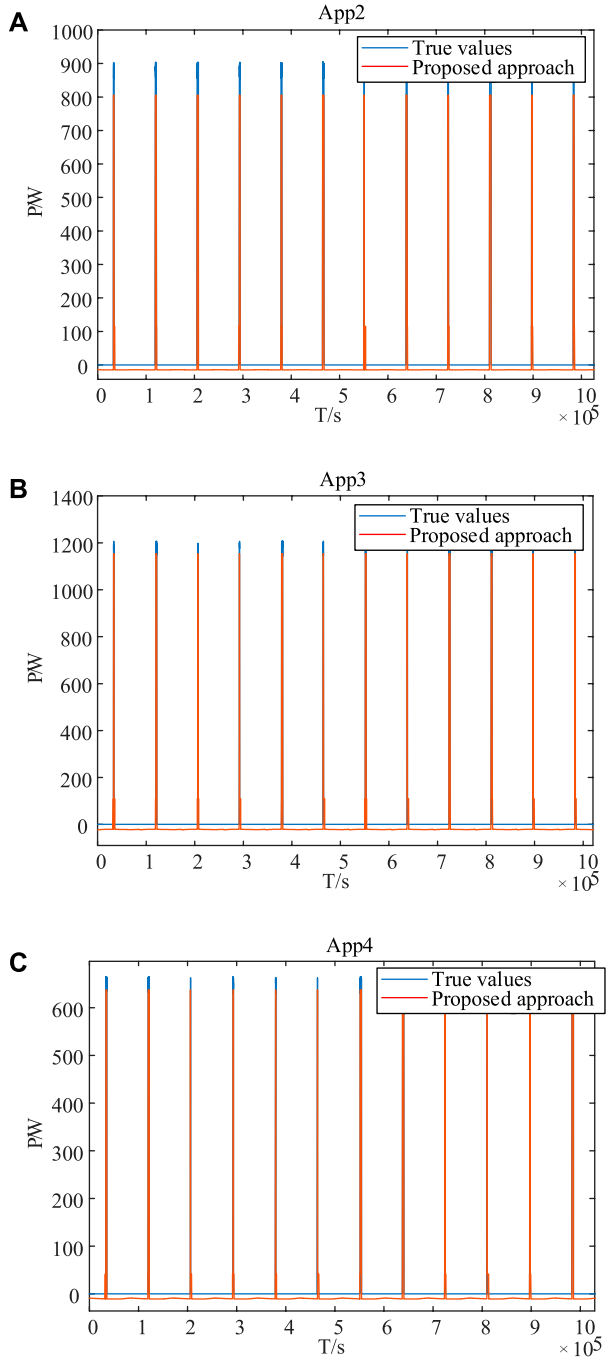

FIGURE 10 | Load disaggregation performance of the trained neural network for dataset B: **(A)** App2, **(B)** App3, and **(C)** App4.

large MAE. By introducing the enhancement in **Table 2**, the MAE becomes very small, indicating the effectiveness of energy consumption monitoring. Such efficiency, although reduced, can still be found for complicated operation scenarios, as the results seen in **Table 3**.

Combining **Table 1**, **2**, and **3**, the average metrics for different scenarios are visualized in **Figure 5**. It can be seen that the

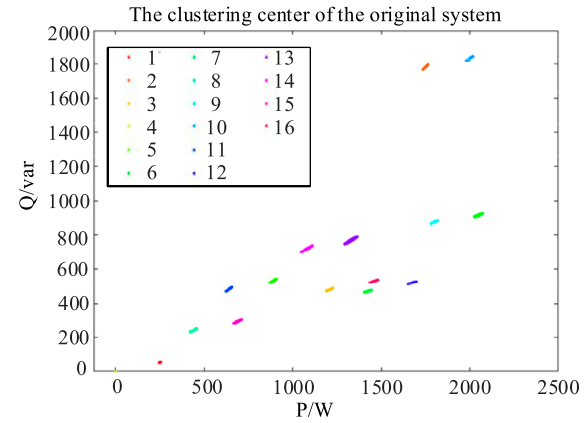

FIGURE 11 | The appliance clustering feature center of the original system.

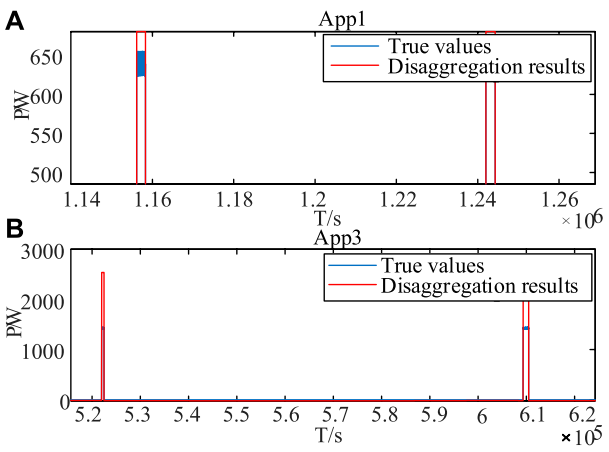

FIGURE 12 | Disaggregation errors with original cluster centers: **(A)** App1 **(B)** App3.

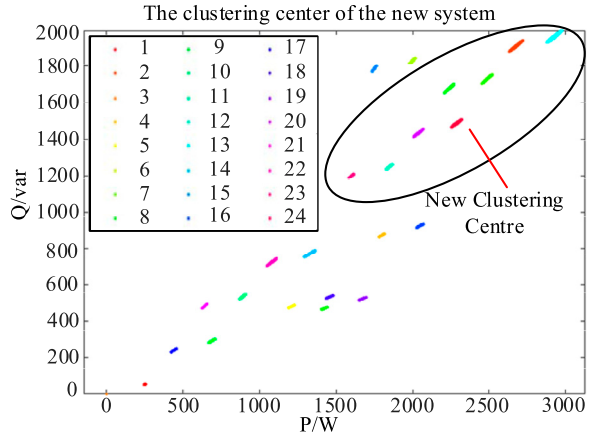

FIGURE 13 | The new system cluster centers.

TABLE 4 | The results of the *K*-means clustering algorithm.

Cluster center of the original system			Cluster center of the new system after adding a new appliance			New tags from the comparison of clustering features		
No	P (W)	Q (var)	No	P (W)	Q (var)	No	P (W)	Q (var)
1	249.4101	50.6449	1	249.41	50.6449	1	0	0
2	1.7495e+03	1.7848e+03	2	2.679e+03	1.9168e+03	2	2.6790e+03	1.9168e+03
3	1.2087e+03	477.7206	3	0	0	3	0	0
4	0	0	4	1.799e+03	871.5186	4	0	0
5	888.9645	530.3280	5	1.2087e+03	477.7206	5	0	0
6	2.0488e+03	922.1552	6	1.9990e+03	1.8356e+03	6	0	0
7	1.4246e+03	468.2964	7	2.4884e+03	1.7299e+03	7	2.4884e+03	1.7299e+03
8	439.4848	237.2088	8	1.4246e+03	468.2694	8	0	0
9	1.7994e+03	871.5186	9	2.2400e+03	1.6800e+03	9	2.2400e+03	1.6800e+03
10	1.999e+03	1.8356e+03	10	688.8953	287.8055	10	0	0
11	639.5707	479.6780	11	888.9653	530.3429	11	0	0
12	1.6739e+03	518.8563	12	1.8489e+03	1.2502e+03	12	1.8489e+03	1.2502e+03
13	1.3283e+03	767.5381	13	2.9287e+03	1.9677e+03	13	2.9287e+03	1.9677e+03
14	1.0796e+03	717.2861	14	1.3277e+03	767.0841	14	0	0
15	688.9235	287.8703	15	1.7495e+03	1.7848e+03	15	0	0
16	1.4577e+03	528.2045	16	2.0488e+03	922.1552	16	0	0
			17	439.5427	237.2400	17	0	0
			18	1.4577e+03	528.2040	18	0	0
			19	1.6739e+03	518.8563	19	0	0
			20	2.0384e+03	1.4364e+03	20	2.0384e+03	1.4364e+03
			21	639.3944	479.5458	21	0	0
			22	1.0797e+03	717.4234	22	0	0
			23	1.5997e+03	1.1998e+03	23	1.5997e+03	1.1998e+03
			24	2.2886e+03	1.4876e+03	24	2.2886e+03	1.4876e+03

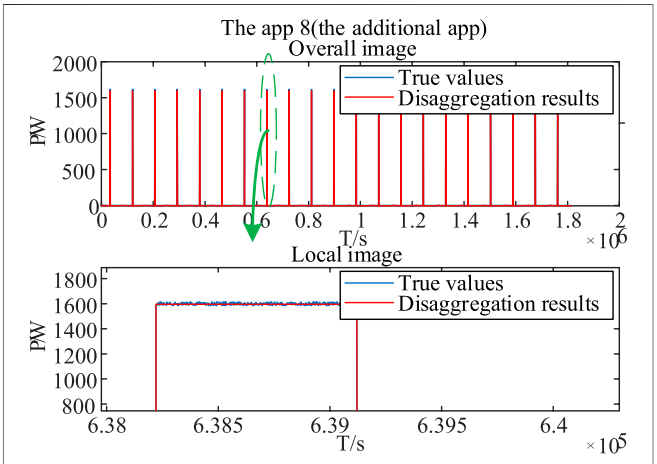

FIGURE 14 | The disaggregation results of the new appliance by the newly constructed network.

traditional BPNN without unsupervised optimization performs worst. The proposed BPNN solution with unsupervised optimization is compatible of handling both datasets A and B. Although a slight decrease is seen *via* some metrics, the disaggregation results are reliable from the view of whole household energy consumption.

To give a comprehensive illustration of our study, some appliances are selected for extended discussions. Energy disaggregation results for App1 and App8 from dataset A are illustrated in **Figure 6**. As shown by the green line, when the BPNN without unsupervised optimization encounters the appliance clusters with the new appliance, the analysis performance will be greatly reduced. As shown by the red line, the BPNN with unsupervised optimization in this article has the better capability to analyze all the appliances, including the newly added appliance.

Energy disaggregation results of App1 from dataset B is also selected for illustration, as shown in **Figure 7**. We can see that the algorithm still has a certain analytical ability and can clearly distinguish the operating time of each appliance and the approximate operating information.

NN Model Performance

In order to investigate the insights of NN performance in our study, details are explored. In above cases, the initial neuron number of the hidden layer is 3, the initial learning rate is 0.001, and the maximum number of failures is fixed at 10. In addition, for the part of network training, the elastic gradient descent method is used. After the training stage, the established network is compared with the required error to determine the whether it is valid. If not satisfied, the coordinate axis descent method is activated to optimize the network parameters, rebuild the network for retraining, and analyze the training results again until the accuracy requirements are met. In our NILM problem, the training results are shown in **Figure 8**.

Using this network to decompose each appliance data, we can get the operation status of each appliance. We draw the disaggregation diagram of each appliance obtained through neural network analysis with the real data of each appliance in a chart for comparison, as shown in **Figure 9** for dataset A, and

we can see that the disaggregated results are now very close to the true values. The illustrated results suggest the effectiveness of the established network.

Since applying a more complex appliance running dataset is an effective way to test the generalization and robustness of the algorithm, the load disaggregation performance of the trained neural network for dataset B is analyzed and shown in **Figure 10**. Although there is a certain error for the appliance power tracking, it is acceptable within a small range. Therefore, the neural network has strong generalization ability and good robustness, even for complex appliance operation data, which is desired in the NILM problems.

Handling the Newly Added Appliance

Extensive discussions on dataset A are presented here to show how the proposed approach handles the newly added appliance. Originally, there are seven appliances in the household system, while the App7 is a long-run appliance. By training, the clustered operation feature centers are illustrated in **Figure 11**, where there are total 16 clusters for these household operations.

When a new appliance is added, the function of the original network will fail. As a result, the disaggregation results will differ remarkably from the true operating power. For example, **Figure 12** shows the large disaggregation errors of App1 and App3 under a certain time period.

Considering the newly added App8, through the calculations by **Eqs 10–13**, **Figure 13** below shows the clustering results of the new system, where there are total 24 cluster centers and eight of them are the new centers.

The corresponding clustering centers are digitized in **Table 4**, where the new centers are listed on the right. As seen, **Eq. 13** not only provides an indicator to check the validity of the rated feature of the newly added appliance but also helps to determine the optimal clustering centers. It plays a vital role in the proposed unsupervised learning enhancement.

By extracting the newly added appliance information from **Table 4**, the rated operating power of the new appliance in the new system can be calculated, and the new BPNN-based NILM system can be constructed. **Figure 14** below shows the disaggregation results of the new appliance by the newly constructed network.

As seen from **Figure 14**, by implementing the proposed approach, the newly added appliance can be accurately tracked under the NILM framework. However, if there are two or more new appliances, following discussions can be noticed. If the new appliances are added one by one, our system is still effective in recognizing them, since after a period of time the newly added appliance will change to be the conventional appliance. If they are added together, our approach can only tell that multiple electrical appliances have been added but cannot build the learning model for each in the neural networks. This is indeed the true challenge we will focus on in the future. Nevertheless, such a scenario does not affect our contribution because current NILM studies are mostly targeting at the residential power monitoring, where the total number of monitored appliances is limited. It is very unusual for a house to add two new household appliances at the same time, so such a capability does not influence our contribution to the practical NILM applications.

CONCLUSION

Toward the practical non-intrusive load disaggregation in field measurements, especially to tackle the newly added appliance with deficient samples in the NILM field, the BPNN-based solution is thoroughly investigated and improved in this article. Specifically, a deep learning-based NILM approach is proposed, where the model is established based on the supervised BP neural network and enhanced by the unsupervised optimization, and the solution is provided with adaptive scalabilities. By the joint optimization design based on large samples of original appliances and small samples of newly added appliances, the brand new features of unknown appliances are effectively handled by the enhanced BPNN model, leading to the capability of recognizing the out-of-range appliance. In addition to the desired accuracy, the proposed approach is demonstrated to be with high reliability and scalability, proving to be a feasible solution in the future practical NILM applications.

DATA AVAILABILITY STATEMENT

The raw data supporting the conclusions of this article will be made available by the authors, without undue reservation.

AUTHOR CONTRIBUTIONS

YL: conceptualization, writing—review and editing, funding acquisition, and supervision. JW: writing—original draft, writing—review and editing. JD: software and validation. WS: formal Analysis. PT: methodology.

FUNDING

This work was supported in part by the National Natural Science Foundation of China under Grant 51907024.

REFERENCES

Andrean, V., Zhao, X.-H., Teshome, D. F., Huang, T.-D., and Lian, K.-L. (2018). A Hybrid Method of Cascade-Filtering and Committee Decision Mechanism for Non-intrusive Load Monitoring. *IEEE Access* 6, 41212–41223. doi:10.1109/access.2018.2856278

Barsim, K. S., Wiewel, F., and Yang, B. (2014). On the Feasibility of Generic Deep Disaggregation for Single-Load Extraction. In The 4rd International Workshop on Non-intrusive Load Monitoring. Washington, America, 1–5.

Bonfigli, R., Felicetti, A., Principi, E., Fagiani, M., Squartini, S., and Piazza, F. (2018). Denoising Autoencoders for Non-intrusive Load Monitoring: Improvements and Comparative Evaluation. *Energy and Buildings* 158, 1461–1474. doi:10.1016/j.enbuild.2017.11.054

Ciancetta, F., Bucci, G., Fiorucci, E., Mari, S., and Fioravanti, A. (2021). A New Convolutional Neural Network-Based System for NILM Applications. *IEEE Trans. Instrumentation Meas.* 70, 1501112. doi:10.1109/tim.2020.3035193

Cox, R., Leeb, S. B., and Shaw, S. R. (2006). Transient Event Detection for Nonintrusive Load Monitoring and Demand Side Management Using Voltage Distortion. In Twenty-First Annual IEEE Applied Power Electronics Conference and Exposition. Dallas, TX, USA: IEEE.

Ehrhardt, K., Donnelly, K., and Lait, J. A. (2010). *Advanced Metering Initiatives and Residential Feedback Programs: A Meta-Review for Household Electricity-Saving Opportunities*. Washington DC, United State: American Council for an Energy-Efficient Economy.

Faustine, A., and Pereira, L. (2020). Multi-Label Learning for Appliance Recognition in NILM Using Fryze-Current Decomposition and Convolutional Neural Network. *Energies* 13, 4154. doi:10.3390/en13164154

Figueiredo, M., Ribeiro, B., and de Almeida, A. (2014). Electrical Signal Source Separation via Nonnegative Tensor Factorization Using on Site Measurements in a Smart home. *IEEE Trans. Instrum. Meas.* 63 (2), 364–373. doi:10.1109/TIM.2013.2278596

Guo, H., Lu, J., and Yang, P. (2021). Review on Key Techniques of Non-intrusive Load Monitoring. *Electric Power Automation Equipment* 41 (1).

Hart, G. W. (1992). Nonintrusive Appliance Load Monitoring. *Proc. IEEE* 80 (12), 1870–1891. doi:10.1109/5.192069

He, K., Stankovic, L., Liao, J., and Stankovic, V. (2018). Non-Intrusive Load Disaggregation Using Graph Signal Processing. *IEEE Trans. Smart Grid* 9 (3). doi:10.1109/tsg.2016.2598872

Kelly, J., and Knottenbelt, W. (2015). Neural NILM. In Proceedings of the 2nd ACM International Conference on Embedded Systems for Energy-Efficient Built Environments. New York, NY, USA: Association for Computing Machinery, 55–64. doi:10.1145/2821650.2821672

Kolter, J. Z., and Jaakkola, T. (2012). " Approximate Inference in Additive Factorial HMMS with Application to Energy Disaggregation", in Proceedings of the 15th International Conference on Artificial Intelligence and Statistics, Journal of Machine Learning Research. La Palma, Spain 22, 1472–1482.

Li, D., and Dick, S. (2019). Residential Household Non-intrusive Load Monitoring via Graph-Based Multi-Label Semi-supervised Learning. *IEEE Trans. Smart Grid* 10 (4), 4615–4627. doi:10.1109/tsg.2018.2865702

Lin, Y.-H., and Tsai, M.-S. (2014). Non-Intrusive Load Monitoring by Novel Neuro-Fuzzy Classification Considering Uncertainties. *IEEE Trans. Smart Grid* 5 (5), 2376–2384. doi:10.1109/tsg.2014.2314738

Liu, H. Y., Shi, S. B., and Xu, H. X. (2019). A Non-intrusive Load Identification Method Based on RNN Model. *Power Syst. Prot. Control.* 47 (13), 162–170.

Liu, Q., Kamoto, K. M., Liu, X., Sun, M., and Linge, N. (2019). Low-Complexity Non-intrusive Load Monitoring Using Unsupervised Learning and Generalized Appliance Models. *IEEE Trans. Consumer Electron.* 65 (1), 28–37. doi:10.1109/tce.2019.2891160

Liu, S., Liu, Y., Gao, S., Guo, H., Song, T., Jiang, W., et al. (2020). Non-intrusive Load Monitoring Method Based on PCA-ILP Considering Multi-Feature Objective Function. *IEEE Trans. Consumer Elect.* 2020, 1000–7229.

Monteiro, R. V. A., de Santana, J. C. R., Teixeira, R. F. S., Bretas, A. S., Aguiar, R., and Poma, C. E. P. (2021). Non-intrusive Load Monitoring Using Artificial Intelligence Classifiers: Performance Analysis of Machine Learning Techniques. *Electric Power Syst. Res.* 198, 107347. doi:10.1016/j.epsr.2021.107347

President of the People's Republic of China (2020). Carrying on the Past and Opening up a New Journey of Global Response to Climate Change. Available at: http://www.gov.cn/gongbao/content/2020/content_5570055.htm.

Tan, P. N., Steinbach, M., and Kumar, V. (2011). *Introduction to Data Mining. FAN Ming, FAN Hongjian*. Beijing: People Post Press.

Wang, K., Zhong, H., Yu, N., and Xia, Q. (2019). Nonintrusive Load Monitoring Based on Sequence-To-Sequence Model with Attention Mechanism. *Proc. CSEE* 2019, 0258–8013.

Xue, F. X., and Guo, D. Z. A Survey on Deep Learning for Natural Language Processing. *Acta Automatica Sinica*, 2016, 42(10): 1445–1465.

Yan, X., Zhai, S., Wang, F., and He, G. (2019). Application of Deep Neural Network in Non-intrusive Load Disaggregation. *Automation Electric Power Syst.* doi:10.7500/AEPS20180629004

Zhou, M., Song, X., and Tu, J. (2018). Residential Electricity Consumption Behavior Analysis Based on Non-intrusive Load Monitoring. *Power Syst. Tech.* 42 (10), 3268–3274.

Zoha, A., Gluhak, A., Imran, M., and Rajasegarar, S. (2012). Non-intrusive Load Monitoring Approaches for Disaggregated Energy Sensing: a Survey. *Sensors* 12 (12), 16838–16866. doi:10.3390/s121216838

Conflict of Interest: The authors declare that the research was conducted in the absence of any commercial or financial relationships that could be construed as a potential conflict of interest.

Publisher's Note: All claims expressed in this article are solely those of the authors and do not necessarily represent those of their affiliated organizations, or those of the publisher, the editors and the reviewers. Any product that may be evaluated in this article, or claim that may be made by its manufacturer, is not guaranteed or endorsed by the publisher.

frontiers in Energy Research

ORIGINAL RESEARCH
published: 21 October 2021
doi: 10.3389/fenrg.2021.734801

A Distributed Two-Stage Economic Dispatch for Virtual Power Plant Based on An Improved Exact Diffusion Algorithm

Yingxuan Zheng, Zhen Wang, Ping Ju and Hao Wu*

College of Electrical Engineering, Zhejiang University, Hangzhou, China

To manage a large scale of distributed energy resources (DERs) dispersed geographically and reduce the impact of DER uncertainties, this paper proposes a distributed two-stage economic dispatch for virtual power plant (VPP) to track a specified VPP schedule curve. In the look-ahead stage, a distributed economic dispatch strategy is proposed to optimally allocate the scheduled power among DERs. In the real-time stage, a distributed VPP schedule curve tracking problem is modeled to balance the fluctuation of wind farms and/or PV stations. The two-stage distributed optimization problems are solved by an improved exact diffusion algorithm which is proved to be robust to local communication failure. Case studies validate the performance of the algorithm proposed.

Keywords: distributed energy resources, virtual power plant, distributed economic dispatch, multi-agent, communication failure

OPEN ACCESS

Edited by:
Ningyi Dai,
University of Macau, China

Reviewed by:
Xiaoqing Bai,
Guangxi University, China
Xiaohe Yan,
North China Electric Power University, China

****Correspondence:***
Zhen Wang
eezwang@ieee.org

Specialty section:
This article was submitted to Smart Grids, a section of the journal Frontiers in Energy Research

Received: *01 July 2021*
Accepted: *23 September 2021*
Published: *21 October 2021*

Citation:
Zheng Y, Wang Z, Ju P and Wu H (2021) A Distributed Two-Stage Economic Dispatch for Virtual Power Plant Based on An Improved Exact Diffusion Algorithm. Front. Energy Res. 9:734801. doi: 10.3389/fenrg.2021.734801

INTRODUCTION

In recent years, the penetration rate of renewable energy especially for wind and solar power is rapidly increasing. However, the power fluctuation of wind and solar power pose great challenges for the operation and control of the evolving power system, such as frequency control and peak-load regulation (Bouffard and Galiana 2008). In reality, there are large number of DERs including wind farms and PV parks, micro turbine generator, storage, different types of flexible demand resources like EV, thermal pump load, air-conditioner, etc. (DING Yi 2016), dispersed geographically to provide flexible power supply. To manage these DERs, the virtual power plant (VPP) is introduced as an aggregator to manage and dispatch these DERs to achieve an resource sharing and overall benefit target, which has attracted great attention in power industry (Koraki and Strunz 2018).

Usually, VPP manages DERs in two modes: centralized and distributed. In centralized way, DERs in VPP are managed and dispatched by a central system operator (CSO). In this way, the most challenging issue for the CSO is how to manage uncertainties from various DERs. There have been massive efforts devoted to this issue. For example, in (Baringo, Baringo, and Arroyo 2019), a combination of scenario-based stochastic programming and adaptive robust optimization is developed for VPP to participate in the day-ahead energy and reserve electricity market, where the wind power uncertainty is represented by confidence bounds. In (Vahedipour-Dahraie et al., 2021) a two-stage risk-averse stochastic framework is proposed for optimal schedule of energy and reserve services for VPP, in which a Monte Carlo method is developed considering the probability distribution of the market prices, renewable energy power, flexible loads as well as the reserve requirement. In addition to the uncertainty issue, due to the user privacy, some DER information cannot be shared with CSO and thus how to model flexible loads with incomplete information and

conduct decision-making is another issue in this centralized framework. To overcome this problem, in (Zhou et al., 2021) each DER is represented by an automatic response model based on Markov decision process and an event-driven stimulus-feedback control scheme is proposed to guide DERs with limited information *via* self-approaching optimization. However, since DERs are dispersed geographically, so in the centralized mode there always exist some risk of communication failure and transfer delay considering large scale of DER communication network.

On the other hand, in a distributed VPP each DER has limited information exchange with neighboring DERs and is less dependent on communication compared with the centralized VPP, and thus the VPP communication burden can be decreased. In distributed VPP, a basic issue is how to realize each DER's distributed economic dispatch (DED) operation. In existing works, there are mainly three strategies to solve the DED problem (Yuan et al., 2019a): 1) the consensus strategy, 2) the diffusion strategy and 3) the alternating direction method of multipliers (ADMM). In these DED strategies, each DER exists an independent iteration process to approach its own optimal solution. The main differences are as follows: In the consensus strategy, in each iteration every DER will exchange information with neighboring DERs and then its incremental cost is updated, and finally all DERs will reach consensus with a common the incremental cost (Nedic and Ozdaglar 2009). In comparison, in the diffusion strategy, the incremental cost is first updated and then followed by the information exchange, i.e., the difference is mainly on the procedure order, which has proved to be more stable and effective (Tu and Sayed 2012). Furthermore, an improved diffusion algorithm called the exact diffusion algorithm (the standard EDA) is proposed in (Yuan et al., 2019a) which can accelerate the convergence speed and can approach to the exact optimal solution. A common point for the former two methods is that each DER will finally approach to the equal increment principle (EIP) consensus in mechanism. On the other hand, the algorithm mechanism of ADMM is different from the former two, in which the DER optimization problem is decomposed into several subproblems including some primal and dual problems, which are solved in sequence and coordinated to find a global solution (Boyd 2010). (Xia et al., 2019) presented a distributed hierarchical framework based on ADMM to manage multiple DERs in an economic way.

The main contribution of this paper is summarized as follows:

1) A distributed two-stage economic dispatch is proposed to track the generation schedule curve. During the economic dispatch, DERs make determinations independently only with the limited information from their neighboring DERs, which can protect user privacy. The proposed two-stage distributed economic dispatch can well adapt to the future power system dispatch framework considering the rolling ultra-short-term forecasting of renewable generation.
2) Local communication failure is carefully considered and the treatment proposed enables each agent to react to the communication failure independently and the algorithm can still converge to the optimal point without interrupting the optimization process. Compared with the existing works that consider the communication failure treatment in system-level, the treatment proposed is more practical in distributed optimization.
3) An improved EDA is developed to solve the distributed problem, which can accelerate the convergence speed with the penalty term and reduce the communication burden compared with the standard EDA. The penalty term only involves the information from neighboring DERs which doesn't need extra effort to achieve global information and can increase convergence efficiency.

The remaining part of the paper is organized as follows: *The Dispatch Framework of Virtual Power Plant* introduces the framework of VPP's dispatch framework and its topology; in *The Two-Stage Distributed Economic Dispatch for VPP* a distributed two-stage economic dispatch optimization model for VPP is formulated and an improved EDA is developed; *Case Study* includes the case study to validate the effectiveness of the algorithm proposed; *Conclusion* concludes the paper.

THE DISPATCH FRAMEWORK OF VIRTUAL POWER PLANT

VPP is a network of decentralized, medium-scale DERs such as wind farms, PV stations, micro turbine and flexible loads (residential, commercial and industrial) and storage systems, etc. The objective of introducing VPP is to relieve the load requirement/capacity of the individual units during periods of power generation shortage. In short, VPP can aggregate DERs dispersed in various areas as a whole virtual generator unit dispatched by the power system.

VPP is responsible for the generation scheduling and benefit allocation among each DER. To reduce the impact of DER uncertainty, the following two-stage VPP dispatch is considered: 1) In the look-ahead dispatch, the initial VPP schedule curve will be determined by the VPP aggregator firstly and then be submitted to CSO. After executing the system-level economic dispatch, CSO will issue the corrected VPP schedule curve (considering transmission congestion, VPP capacity limits, etc.) to VPP. Finally, VPP will allocate the scheduled VPP power among all dispatchable DERs based on the forecasting wind and solar power; 2) In the real-time stage, VPP can further adjust each dispatchable DER power if there is any update of wind and solar power information from the ultra-short-term forecasting (i.e., the real-time forecasting) so that the look-ahead VPP schedule curve can be well tracked.

For the purpose of managing a large scale of DERs dispersed geographically and dealing with the uncertainty of DERs, in this study the DER power schedule will be determined by a distributed two-stage economic dispatch in a multi-agent communication framework.

Multi-Agent Communication Framework

The distributed optimization of DERs in VPP in this study is implemented in a multi-agent communication framework, as

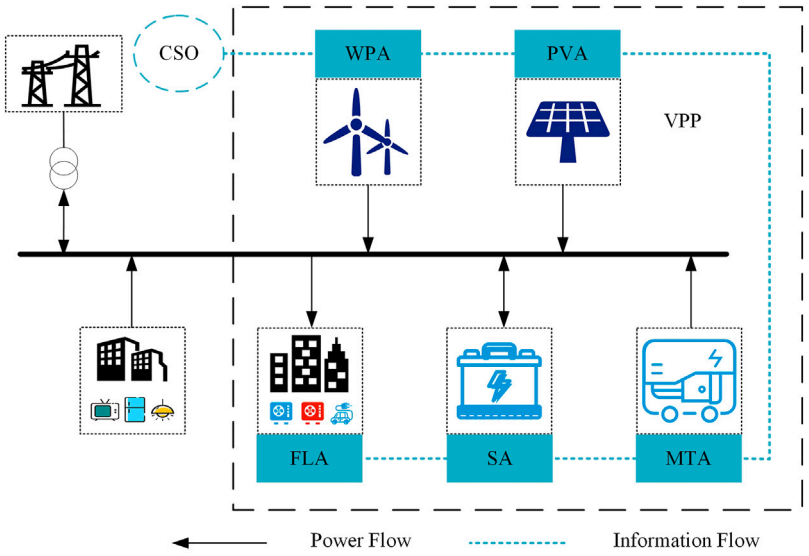

FIGURE 1 | VPP system schematic diagram.

illustrated in **Figure 1**. Each DER is assigned to an agent who is responsible for communication with the other agent, controlling the DER power, and detecting the measurement changes (e.g., power deviation, changes in temperature). In this study, only five kinds of DER/agents are considered, but the proposed method can be easily extended to other DERs if any: wind power agent (WPA), photovoltaic agent (PVA), micro turbine agent (MTA), storage agent (SA), flexible load agent (FLA). What's more, among the agents mentioned above, one agent with reliable communicate connection with CSO is specified as the connection agent who takes extra responsibility for external communication and internal information publishing.

For simplicity, in this paper the agent index system is identical to the DER index system, i.e., each DER has the same index as its corresponding DER agent as described below. The communication network of the agents can be described using an undirected graph $G = \{\phi_N, \phi_E, \phi_W\}$, which is consisting of three types of elements: 1) an agent index set $\phi_N = \{1, 2, \cdots n\}$, and the 1st agent represents the connection agent 2) an edge set ϕ_E where each edge $(i, j) \in \phi_E$ is an unordered pair of distinct agents, and 3) the topology graph $\phi_W = \{w_{ij} | i, j \in \phi_N\}$ and w_{ij} is the edge weight. If agent i and agent j can communicate with each other, i.e. $(i, j) \in \phi_E$, then $w_{ij} > 0$, and they are considered neighboring. If $(i, j) \notin \phi_E$, then $w_{ij} = 0$. In this study, w_{ij} is given by (Lin and Boyd 2003):

$$w_{ij} = \begin{cases} \dfrac{1}{\max\left(n_i, n_j\right)}, & (i,j) \in \phi_E, i \neq j \\ 1 - \sum\limits_{(i,j) \in \phi_E} w_{ij}, & (i,j) \in \phi_E, i = j \end{cases} \tag{1}$$

where n_i and n_j denotes the number of the neighboring agents of agent i and agent j, respectively.

In the communication framework above, the agents have the following characteristics (McArthur et al., 2007):

1) n agents in above definition means there are n DERs in VPP, vice versa.
2) Each dispatchable DER is a controlled unit and assigned to an agent that is responsible for communication and control. The agents of non-dispatchable DERs (wind farms or PV stations) only have the duty of communication.
3) Each agent has the functions of bidirectional communication, self-determination and sensing the environment. All the agents in VPP can coordinate and control DER through mutual communication to achieve the optimization goal of the whole system.

DER Economy Model

For the three typical dispatchable DERs in VPP mentioned above, the classic quadratic function is adopted to define the DER operation costs:

$$\begin{gathered} C_{MT}\left(P_{MT}^t\right) = a_{MT} P_{MT}^{t^2} + b_{MT} P_{MT}^t + c_{MT}, \\ \underline{P}_{MT} \le P_{MT}^t \le \overline{P}_{MT} \end{gathered} \tag{2a}$$

$$C_S\left(P_S^t\right) = a_S\left[P_S^t + 3\overline{P}_S\left(1 - SOC^t\right)\right]^2 + b_S\left[P_S^t + 3\overline{P}_S\left(1 - SOC^t\right)\right] + c_S,$$

$$\underline{P}_S \le P_S^t \le \overline{P}_S \tag{2b}$$

$$\begin{gathered} C_{FL}\left(P_{FL}^t\right) = a_{FL}\left(P_{FL}^{B,t} - P_{FL}^t\right)^2 + b_{FL}\left(P_{FL}^{B,t} - P_{FL}^t\right) + c_{FL}, \\ \underline{P}_{FL} \le P_{FL}^t \le \overline{P}_{FL}, \end{gathered} \tag{2c}$$

$$\begin{gathered} SOC^{t+1} = SOC^t - \eta \cdot \frac{P_S^t \Delta t}{S}, \\ \underline{SOC} \le SOC^t \le \overline{SOC} \end{gathered} \tag{2d}$$

In above economy models, the variable subscripts "MT," "S," and "FL" denote the micro turbine, storage and flexible loads,

respectively; $C(\cdot)$ is the cost function; P^t is the power output or consumption at time t; a, b and c denote the coefficients of quadratic cost function; $\overline{P}$ and $\underline{P}$ represent the upper and the lower limits of the power; SOC^t is the storage state of charge; $\overline{SOC}$ and $\underline{SOC}$ are its upper and the lower limits; S represents the storage capacity; η is the discharge and charge efficient; Δt is the time interval between t and $t+1$; $P_{FL}^{B,t}$ is the baseline load. In **Eq. 2c**, the incentive cost is adopted here for flexible load adjustment cost which is the function of the load power change (Wang et al., 2019).

The Two-Stage Dispatch Framework

To accommodate renewable power integration and reduce the impact of prediction error, a multiple time-scale rolling dispatch framework is adopted (Li et al., 2015), which includes the following two stage process: 1) the look-ahead dispatch, which will execute VPP dispatch in a receding horizon every 1 h in the upcoming 4 h, with a time resolution of 15 min and 2) the real-time dispatch, which will perform in a receding horizon every 5 min in the upcoming 1 h, with a time resolution of 5 min.

THE TWO-STAGE DISTRIBUTED ECONOMIC DISPATCH FOR VPP

According to the VPP framework discussed in *The Dispatch Framework of Virtual Power Plant*, a look-ahead and real-time two-stage distributed economic dispatch is developed in this section.

The Look-Ahead Economic Dispatch Model

In the look-ahead dispatch, VPP is responsible for allocating the 4 h VPP power schedule with a time resolution of 15 min issued by CSO to each DER based on the look-ahead forecasting wind and solar power.

The Look-Ahead CED Model

The wind and solar power are non-dispatchable DERs whose cost are regarded as constant, so only the overall VPP cost minimization of micro turbine, storage and flexible loads is considered:

$$\min \sum_{i=1}^{n} C_{MT,i}\left(P_{MT,i}^t\right) + C_{S,i}\left(P_{S,i}^t\right) + C_{FL,i}\left(P_{FL,i}^t\right) \tag{3a}$$

where n is the number of DER; $P_{MT,i}^t$, $P_{S,i}^t$ and $P_{FL,i}^t$ are the power of micro turbines, storage and flexible loads, respectively (Note: an uniform DER index is used and i denotes the ith DER, $P_{S,i}^t = P_{FL,i}^t = 0$, and the storage DER and flexible load DER follow the similar rule). For clean expression, the symbol t is omitted when there is no confusion in the context.

The constraints in the look-ahead stage include:

(1) Flexible load power limits:

$$\underline{P}_{FL,i} \le P_{FL,i} \le \overline{P}_{FL,i} \tag{3b}$$

The minimum and maximum power limits of all flexible loads are considered constant values in this paper. It should be noted that the limits in **Eq. 3b** can be adjusted with the real environment parameters in different periods, such as temperature, air pressure, etc. (Lu 2012)

2) Storage power and SOC limits:

$$\begin{aligned} \underline{P}_{S,i} \le P_{S,i} \le \overline{P}_{S,i} \\ \underline{SOC}_i \le SOC_i \le \overline{SOC}_i \end{aligned} \tag{3c}$$

3) Micro turbine power limits:

$$\underline{P}_{MT,i} \le P_{MT,i} \le \overline{P}_{MT,i} \tag{3d}$$

4) Power flow limits:

$$\underline{P}_l \le P_l \le \overline{P}_l \ (l = 1, 2 \ldots m) \tag{3e}$$

where P_l is the power flow in line l; $\overline{P}_l$ and $\underline{P}_l$ represent the power flow limits of line l; m is the number of lines. Based on DC power flow, P_l can be transformed to a linear combination of DERs power (Christie et al., 2000).

$$P_l = \sum_{i=1}^{n} \rho_{li}\left(P_{MT,i} + P_{S,i} + P_{FL,i} + P_{W,i}^{lk} + P_{V,i}^{lk}\right)$$

where ρ_{li} is the sensitivity of power injection at DER i to the power flow on line l. Denote $D \triangleq [\rho_{li}] \in \mathbb{R}^{m \times n}$, D is the power transfer distribution factor matrix, which can be obtained as follows (Šošić et al., 2014):

$$D = B^f B_r^{-1}$$

where B^f is the matrix of branch network susceptances; B_r is the matrix of nodes' susceptances.

(5) Power balance:

$$\sum_{i=1}^{n} P_{MT,i} + P_{S,i} + P_{FL,i} + P_{W,i}^{lk} + P_{V,i}^{lk} = P_{VPP} \tag{3f}$$

where $P_{W,i}^{lk}$ and $P_{V,i}^{lk}$ are the wind and PV look-ahead forecasting power, respectively; P_{VPP} is the scheduled VPP power output.

The optimization model **(3a)**–**(3f)** is called a typical centralized economic dispatch (CED) for VPP. To derive the DED model, the dual counterpart of **(3a)**–**(3f)** is further organized as:

$$\begin{aligned} \max_{\lambda, \overline{z}_l, \underline{z}_l} L_d\left(\lambda, \overline{z}_l, \underline{z}_l\right) = & \sum_{i=1}^{n}\left[C_{MT,i}\left(P_{MT,i}^*\right) + C_{S,i}\left(P_{S,i}^*\right) + C_{FL,i}\left(P_{FL,i}^*\right)\right] \\ & -\lambda\left[\sum_{i=1}^{n}\left(P_{MT,i}^* + P_{S,i}^* + P_{FL,i}^* + P_{W,i}^{lk} + P_{V,i}^{lk}\right) - P_{VPP}\right] \\ & + \sum_{l=1}^{m} \overline{z}_l\left[\sum_{i=1}^{n} \rho_{li}\left(P_{MT,i}^* + P_{S,i}^* + P_{FL,i}^* + P_{W,i}^{lk} + P_{V,i}^{lk}\right) - \overline{P}_l\right] \\ & + \sum_{l=1}^{m} \underline{z}_l\left\{\underline{P}_l - \sum_{i=1}^{n} \rho_{li}\left(P_{MT,i}^* + P_{S,i}^* + P_{FL,i}^* + P_{W,i}^{lk} + P_{V,i}^{lk}\right)\right\} \end{aligned} \tag{4a}$$

$$\begin{aligned} P_{MT,i}^* &= S\left[\frac{\lambda - b_{MT} - \sum \rho_{li}\left(\overline{z}_l - \underline{z}_l\right)}{2a_{MT}}\right], P_{FL,i}^* = S\left[P_{FL}^B - \frac{\lambda - b_{FL} - \sum \rho_{li}\left(\overline{z}_l - \underline{z}_l\right)}{2a_{FL}}\right] \\ P_{S,i}^* &= S\left[\frac{\lambda - b_S - \sum \rho_{li}\left(\overline{z}_l - \underline{z}_l\right)}{2a_S} - 3\overline{P}_S(1 - SOC)\right] \end{aligned} \tag{4b}$$

where λ, $\overline{z_l} \geq 0$ and $\underline{z_l} \geq 0$ are the Lagrangian multipliers; the notation $S[\cdot]$ denotes the constraint projection operator, which can bound the argument within the constraint $[\underline{P}, \overline{P}]$.

The Look-Ahead DED Model

To transform the centralized model into the distributed model (Mateos-Nunez and Cortes 2017), the Lagrangian multiplier λ in **Eq. 4a** is separated as following:

$$\lambda\left[\sum_{i=1}^{n}\left(P_{MT,i}^{*}+P_{S,i}^{*}+P_{FL,i}^{*}+P_{W,i}^{lk}+P_{V,i}^{lk}\right)-P_{VPP}\right]$$
$$=\sum_{i=1}^{n}\lambda_i\left(P_{MT,i}^{*}+P_{S,i}^{*}+P_{FL,i}^{*}+P_{W,i}^{lk}+P_{V,i}^{lk}\right)-\lambda_1 P_{VPP} \quad (5a)$$
$$\lambda_i=\lambda_j\,(i,j)\in\phi_E \quad (5b)$$

where λ_i is the Lagrangian multiplier of the ith DER, $\lambda = [\lambda_1, \cdots \lambda_n]$.

For a communication-connected system, **Eq. 5b** means that all multipliers are equal, which makes (5a) holds. In **Eq. 5a**, since P_{VPP} is not the power output of any DER, here the connection agent's Lagrangian multiplier λ_1 will be used for P_{VPP}. $\overline{z_l}$ and $\underline{z_l}$ can be separated similarly to become $\overline{z_l} = [\overline{z_{l,1}}, \cdots, \overline{z_{l,k}}, \cdots \overline{z_{l,n}}]$ and $\underline{z_l} = [\underline{z_{l,1}}, \cdots, \underline{z_{l,k}}, \cdots \underline{z_{l,n}}]$. $\overline{z_{l,k}}$ and $\underline{z_{l,k}}$ are the Lagrangian multiplier of line l at kth DER. And in terms of power flow constraints, and are used for and in (6a) $\overline{z_{l,1}}$, $\underline{z_{l,1}}$ are used for $\overline{P_l}$ and $\underline{P_l}$. In this way, all DERs can be decoupled with each other so that the centralized model is transferred into a distributed model. Finally, the distributed model of the look-ahead economic dispatch is formed:

$$\max_{\boldsymbol{\lambda},\overline{\mathbf{z}},\underline{\mathbf{z}}} L_d\left(\boldsymbol{\lambda},\overline{\mathbf{z}},\underline{\mathbf{z}}\right)=\max\sum_{i=1}^{n}L_d\left(\lambda_i,\overline{z_{l,i}},\underline{z_{l,i}}\right)$$
$$s.t.\ \lambda_i=\lambda_j,\overline{z_{l,i}}=\overline{z_{l,j}},\ \underline{z_{l,i}}=\underline{z_{l,j}}\quad (\mathrm{i},\mathrm{j})\in\varphi_E$$
$$L_d\left(\lambda_1,\overline{z_{l,1}},\underline{z_{l,1}}\right)=C_{MT,1}\left(P_{MT,1}^{*}\right)+C_{S,1}\left(P_{S,1}^{*}\right)+C_{FL,i}\left(P_{FL,1}^{*}\right)$$
$$-\lambda_1\left(P_{MT,1}^{*}+P_{S,1}^{*}+P_{FL,1}^{*}+P_{W,1}^{lk}+P_{V,1}^{lk}-P_{VPP}\right)$$
$$+\left[\sum\rho_{li}\left(\overline{z_{l,1}}-\underline{z_{l,1}}\right)\cdot\left(P_{MT,1}^{*}+P_{S,1}^{*}+P_{FL,1}^{*}+P_{W,1}^{lk}+P_{V,1}^{lk}\right)\right.$$
$$\left.-\overline{z_{l,1}}\cdot\overline{P_l}+\underline{z_{l,1}}\cdot\underline{P_l}\right]\quad (i=1) \quad (6a)$$

$$L_d\left(\lambda_i,\overline{z_{l,i}},\underline{z_{l,i}}\right)=C_{MT,i}\left(P_{MT,i}^{*}\right)+C_{S,i}\left(P_{S,i}^{*}\right)+C_{FL,i}\left(P_{FL,i}^{*}\right)$$
$$+\left[\sum\rho_{li}\left(\overline{z_{l,i}}-\underline{z_{l,i}}\right)-\lambda_i\right]\cdot\left(P_{MT,i}^{*}+P_{S,i}^{*}+P_{FL,i}^{*}+P_{W,i}^{lk}+P_{V,i}^{lk}\right)$$
$$(i=2,3\ldots,n) \quad (6b)$$

The Real-Time Economic Dispatch Model

In the real-time stage, VPP will adjust DER power through rolling optimization if there is any update of wind and solar power information from the ultra-short-term/real-time forecasting to track the look-ahead VPP schedule curve in a receding horizon every 5 min in the upcoming 1 h.

The Real-Time CED Model

In the real-time stage, suppose at each timer interval t, the look-ahead VPP schedule curve can be completely tracked, the following minimum cost objective function is considered **(3a)**–**(3f)**:

$$\min\sum_{i=1}^{n}C_{MT,i}\left(P_{MT,i}\right)+C_{S,i}\left(P_{S,i}\right)+C_{FL,i}\left(P_{FL,i}\right)$$
$$\mathrm{s.t}\,(3b)-(3e)$$
$$\sum_{i=1}^{n}\left(P_{FL,i}-P_{FL,i}^{lk}+P_{S,i}-P_{S,i}^{lk}+P_{MT,i}-P_{MT,i}^{lk}\right)$$
$$=\Delta P_{\mathrm{GOAL}}=\sum_{i=1}^{n}\left(-\Delta P_{W,i}-\Delta P_{V,i}\right)$$
$$\Delta P_{W,i}=P_{W,i}^{\mathrm{real}}-P_{W,i}^{lk},\ \Delta P_{V,i}=P_{V,i}^{\mathrm{real}}-P_{V,i}^{lk} \quad (7)$$

where $P_{MT,i}^{lk}$, $P_{S,i}^{lk}$ and $P_{FL,i}^{lk}$ are the latest look-ahead scheduled power of micro turbines, storage and flexible loads respectively; ΔP_{GOAL} represents the expected regulation of VPP to track the VPP schedule curve; $P_{W,i}^{\mathrm{real}}$ and $P_{V,i}^{\mathrm{real}}$ are the real-time forecasting power of wind and PV; $\Delta P_{W,i}$ and $\Delta P_{V,i}$ are the power deviation of wind and solar, respectively.

The Expected Regulation Correction

In reality, the expected regulation ΔP_{GOAL} should also consider the VPP regulation limits and dead zone for further corrections:

$$\Delta P_{\mathrm{GOAL}}=\begin{cases}0, & \left|\sum\left(\Delta P_{W,i}+\Delta P_{V,i}\right)\right|<M_{\mathrm{vpp}}\\ \sum\Delta P_{\mathrm{up},i}, & 0\leq\sum\Delta P_{\mathrm{up},i}\leq-\sum\left(\Delta P_{W,i}+\Delta P_{V,i}\right)\\ \sum\Delta P_{\mathrm{down},i}, & 0\leq\sum\Delta P_{\mathrm{down},i}\leq\sum\left(\Delta P_{W,i}+\Delta P_{V,i}\right)\\ -\sum\left(\Delta P_{W,i}+\Delta P_{V,i}\right), & \text{else}\end{cases}$$
$$\Delta P_{\mathrm{up},i}=\overline{P}_{MT,i}-P_{MT,i}^{lk}+\overline{P}_{S,i}-P_{S,i}^{lk}+\overline{P}_{FL,i}-P_{FL,i}^{lk}$$
$$\Delta P_{\mathrm{down},i}=P_{MT,i}^{lk}-\underline{P}_{MT,i}+P_{S,i}^{lk}-\underline{P}_{S,i}+P_{FL,i}^{lk}-\underline{P}_{FL,i} \quad (8)$$

where $\Delta P_{up,i}$ is the up-regulation capacity of ith DER; $\Delta P_{\mathrm{down,i}}$ is the down-regulation capacity; M_{VPP} is the regulation dead-zone. In **Eq. 8**, two particular cases related to wind/solar power uncertainty are considered: 1) If the total real-time forecasting power is less than the total look-ahead forecasting values i.e., $\sum\left(\Delta P_{W,i}+\Delta P_{V,i}\right)<0$, the dispatchable DERs need to increase their power up to $\sum\Delta P_{\mathrm{up},i}$ to correct the deviation; 2) On the other hand, the real-time forecasting power is higher than the total look-ahead one, i.e., $\sum\left(\Delta P_{W,i}+\Delta P_{V,i}\right)>0$, the dispatchable DERs need to reduce their power down to $\sum\Delta P_{\mathrm{down,i}}$.

The Real-Time DED Model

Like the look-ahead DED model, the real-time DED model is constructed as follows:

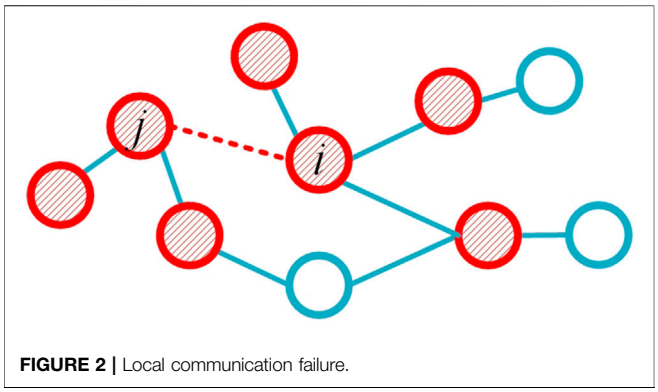

FIGURE 2 | Local communication failure.

$$\begin{aligned}
&\max_{\lambda,\overline{z_l},\underline{z_l}} L_d(\lambda,\overline{z},\underline{z}) = \max \sum_{i=1}^{n} L_d\left(\lambda_i,\overline{z_i},\underline{z_i}\right)\\
&\text{s.t.}\overline{\lambda_i} = \lambda_j, \overline{z_i} = \overline{z_j}, \underline{z_i} = \underline{z_j}\ (i,j) \in \phi_E,\\
&L_r\left(\lambda_i,\overline{z_i},\underline{z_i}\right) = C_{MT,i}\left(P^*_{MT,i}\right) + C_{S,i}\left(P^*_{S,i}\right) + C_{FL,i}\left(P^*_{FL,i}\right)\\
&+\lambda_i\left(P^*_{FL,i} - P^{lk}_{FL,i} + P^*_{S,i} - P^{lk}_{S,i} + P^*_{MT,i} - P^{lk}_{W,i} - \frac{\Delta P_{\mathrm{GOAL}}}{n}\right)\\
&+\sum \rho_{li}\left(\overline{z_{l,i}} - \underline{z_{l,i}}\right)\cdot\left(P^*_{MT,i} + P^*_{S,i} + P^*_{FL,i} + P^{\mathrm{real}}_{W,i} + P^{\mathrm{real}}_{V,i}\right) \quad (9)
\end{aligned}$$

It is noted that **Eq. 9** doesn't mean the expected regulation of each DER is $\Delta P_{\mathrm{GOAL}}/n$. It only reflects the total regulation requirement for VPP. Since ΔP_{GOAL} is the VPP-level regulation, for each agent how to achieve $\Delta P_{\mathrm{GOAL}}/n$ based on the local information is an important concern, which will be discussed in *The Real-Time DED Procedure*.

The two-stage DED problems **Eqs 6, 9** are convex optimization problems with equality constraint, which can be solved by the method explained below.

Solution Methodology Based on the Improved Exact Diffusion Algorithm

To solve the distributed optimization problems above, an improved EDA is developed.

The Standard Exact Diffusion Algorithm

In the distributed convex optimization problems **Eqs 6, 9**, the three Lagrangian multipliers λ, $\overline{z_l}$ and $\underline{z_l}$ are independent and they can be updated alternatively in each iteration (Mateos-Nunez and Cortes 2017). Taking λ as example, the standard EDA in **(10a)**-**(10c)** can be applied for updating the Lagrangian multipliers (Yuan et al., 2019a), $\overline{z_l}$ and $\underline{z_l}$ can be done similarly:

$$\phi_i(k+1) = \lambda_i(k) + \mu\cdot\partial L(\lambda_i)/\partial\lambda_i \quad (10a)$$

$$\varphi_i(k+1) = \phi_i(k+1) + \lambda_i(k) - \phi_i(k) \quad (10b)$$

$$\lambda_i(k+1) = \sum w_{ij}\varphi_j(k+1) \quad (10c)$$

where for the ith DER at iteration k, $\lambda_i(k)$ represents a Lagrangian multiplier and can be regarded as the incremental cost of the ith DER to be updated; μ is the step size, which is set to 0.1 in the study; $\phi_i(k)$ represents the local incremental cost by a gradient-descent type iteration, similar to consensus iteration; $\varphi_i(k)$ is the local incremental cost considering bias correction (Yuan et al., 2019a); $\mathrm{L}(\lambda_i)$ stands for $\mathrm{L}_d(\lambda_i)$ in the look-ahead DED and $\mathrm{L}_r(\lambda_i)$ in the real-time DED, respectively; w_{ij} is the edge weight introduced in **Eq. 1**. More explanations about **(10a)**-**(10c)** are added as follows:

1) In **Eq. 10a**, usually the gradient at optimal point λ^* of each DER is not zero (for instance, $\partial L_d(\lambda)/\partial\lambda_i$ is the power output of ith DER which is not zero in general). It will cause oscillation when λ_i reaches near the optimal point and slow down the convergence. A correction term $\lambda_i(k) - \phi_i(k)$ is added in **Eq. 10b** to remove the bias incurred by the gradient item, as is proved by **Eq. 11**. When λ_i converge to λ^*:

$$\begin{aligned}
&\varphi_i(k+1) = \lambda_i(k) + \lambda_i(k) - \lambda_i(k-1) + \mu\left[\left.\frac{\partial L}{\partial\lambda_i}\right|_{\lambda_i=\lambda_i(k)} - \left.\frac{\partial L}{\partial\lambda_i}\right|_{\lambda_i=\lambda_i(k-1)}\right] \quad (11)\\
&= \lambda^*(k) + \lambda^*(k) - \lambda^*(k-1) = \lambda^*
\end{aligned}$$

2) In **Eq. 10c**, information exchange between the neighboring agents occurs. Each agent will exchange its $\varphi_i(k)$ with all neighbors and the weighted average cost in **Eq. 10c** is used to evaluate the next incremental cost $\lambda_i(k+1)$. During the whole iteration, the incremental cost of any DER will be diffused to other communication-connected DERs through **Eq. 10c** and $\lambda_i(k)$ will finally converge and reach the global optimal point (Yuan et al., 2019b).

The Improved Exact Diffusion Algorithm

Convex Penalty Term

To increase the cost for the equality constraints violation of $\lambda_i = \lambda_j$ and accelerate the convergence speed, a convex penalty term $\sum_{(i,j)\in\phi_E}\beta(\lambda_i - \lambda_j)^2$ is added to the DED objective function **Eqs 6, 9**, β is the penalty parameter, which is set to 0.7 in the study. And the exact-diffusion-based formulas to be updated in each iteration become:

$$\begin{aligned}
&\phi_i(k+1) = X_i(k) + \mu\cdot\left[\frac{\partial L}{\partial\lambda_i}, \frac{\partial L}{\partial\overline{z_i}}, \frac{\partial L}{\partial\underline{z_i}}\right]^T\\
&\varphi_i(k+1) = \phi_i(k+1) + X_i(k) - \phi_i(k)\\
&X_i(k+1) = \sum w_{ij}\varphi_j(k+1)
\end{aligned} \quad (12)$$

where

$$X_i(k) = \left[\lambda_i(k), \overline{z_i}(k), \underline{z_i}(k)\right]^T \quad (13)$$

The designed penalty term only involves the information from neighboring DERs which doesn't need extra effort to achieve global information during the iterations and can increase convergence efficiency, while the ADMM need the information of the whole VPP (Xia et al., 2019).

Information Exchange Relief and Stop Criteria

Each agent will exchange the following information with its neighbors: 1) $\varphi_i(k+1)$; 2) $X_i(k)$; 3) the agent status, any of these three types (Normal, Idle, or Failure) (as explained in *The Look-Ahead DED Procedure*).

TABLE 1 | Pseudo-code of the look-ahead DED for each agent.

Preparation: Calculate the power transfer distribution factor matrix *D*
1. Initialization: Let $k = 0$, $X_i(0) = \phi_i(0) = 0$, set the status of agent i and all its neighbors as Normal
2. While (agent i and its neighbors are not Idle)
{
2.1 $\overline{z_i}(k) = \max\{0, \overline{z_i}(k)\}$, $\underline{z_i}(k) = \max\{0, \underline{z_i}(k)\}$
2.2 Apply (4b) and (12) to update P_i^*, $\phi_i(k+1)$ and $\varphi_i(k+1)$
2.3 If (14) is satisfied, then set agent i as Idle
2.4 If the data-transfer waiting time of agent j is greater than 3 ms {
Set the status of agent j as Failure;}
Else {
Set the status of agent j as Normal
Send $X_i(k)$, $\varphi_i(k+1)$ and the agent status to agent j and receive agent j updated information; }
2.5 Traverse agent status of agent i and all the neighbors
2.4.1 If agent j is Failure [$n_j = n_j - 1$ and recalculate (1);]
2.4.2 If agent j is Idle {
set $X_j(k) = X_j(k-1)$, $\varphi_j(k+1) = \varphi_j(k)$; }
2.6 Apply (10c) to update $X_i(k+1)$
2.7 $k = k + 1$
}
3. End

TABLE 2 | Pseudo-code of the real-time DED.

1. Initialization: Let $k = 0$, calculate $D_i(0)$ with real-time forecasting and real-time measurement data and set agent status of agent i as Normal
2. While (agent i and its neighbors are not Idle)
{
2.1 Apply (**15b**) to update $\delta_i(k+1)$
2.2 Handling information exchange, communication failure and conditional communication if any
2.3 Apply (**15c**) to update $D_i(k+1)$
2.4 k = k + 1
}
3. Set ΔP_{GOAL} based on (8) from the final $D_i(k)$ according to **(15d)–(15e)**
4. Early algorithm termination evaluation
4.1 If ΔP_{GOAL} equals zero; then stop and end
4.2 If $\Delta P_{GOAL}$is equal to its upper or lower limits, {
Set the dispatchable DERs power equal to their limit values
Stop and end;}
5. Execute the real-time DED similar to Step 1–2 in the look-ahead DED

To reduce the information exchange burden of communication during the distribution optimization process, the following conditional communication rule in **Eq. 14** will be applied when there is minor incremental cost difference between consecutive iterations:

$$\sum_{j=1}^{n} w_{ij} \left\| \varphi_j(k+1) - \varphi_j(k) \right\| < \varepsilon, k > 2 \tag{14}$$

Thus, the conditional communication rule becomes:

If **Eq. 13** is satisfied, then $X_i(k) = X_i(k-1)$, $\varphi_i(k+1) = \varphi_i(k)$

When the conditional communication rule is satisfied with a pre-specified accuracy level ε (10^{-5} in the study), agent i will stop information exchange and set the agent status Idle, and accordingly the agents that receive Idle from agent j will update X with the last φ_j and X_j they received from agent j. It should be noted that when agent i and its neighbors are all Idle, agent i will stop the iteration.

Local Communication Failure Treatment

In distributed communication network, the information transfer distance is short, and the impact of delay and bit errors is limited compared with communication failures. So, the treatment of local communication failures is studied in this paper.

When there is local communication failure happened (the dotted line in **Figure 2**) and provided that the communication network keeps connected, the proposed algorithm still works according to the following treatment **Eqs 1–3**:

1) If agent i and agent j cannot receive the next updated information from each other within the maximum data-transfer waiting time, they will set the agent status Failure.

2) Then in the next iteration, the number of the neighboring agents for the involved agent i and agent j (i.e., the shadowed agents in **Figure 2**) will be less one in **Eq. 14** and then **Eq. 1** will be recalculated to update w_{ij}.

$$n_i = n_i - 1,$$
$$n_j = n_j - 1$$

3) When the communication recovers, agent i and agent j can receive information from each other, and the agent status will be set to Normal, and update n_i, n_j and w_{ij} similarly.

It is worth mentioning that the proposed algorithm also has some error tolerance for communication delay, when the data-transfer time exceeds the maximum waiting time, then the algorithm iteration will turn to above local communication failure treatment **Eqs 1–3**. In addition, the proposed improved EDA is robust to occasional bit errors. The false data due to bit errors can be regarded as another new initial data and the algorithm can still reach convergence as long as the remaining data is correct during the iterations, since one advantage of EDA is that its convergence performance is insensitive to the initialization setting (Yuan et al., 2019b).

The DED Solution Procedure

The Look-Ahead DED Procedure

For each agent, the look-ahead DED algorithm in pseudo-code form is summarized in **Table 1**, in which 2.2 represents the conditional communication strategy, 2.3 represents information exchange and 2.4 represents the communication failure treatment, respectively. The maximum data-transfer waiting time is set to 3 ms in the study.

The Real-Time DED Procedure

As mentioned in *The Expected Regulation Correction*, in the real-time stage how to evaluate the expected regulation $\Delta P_{GOAL}/n$ based on the local information should be finished before executing the improved EDA. For each agent, the local information given includes: 1) The forecasting power deviation

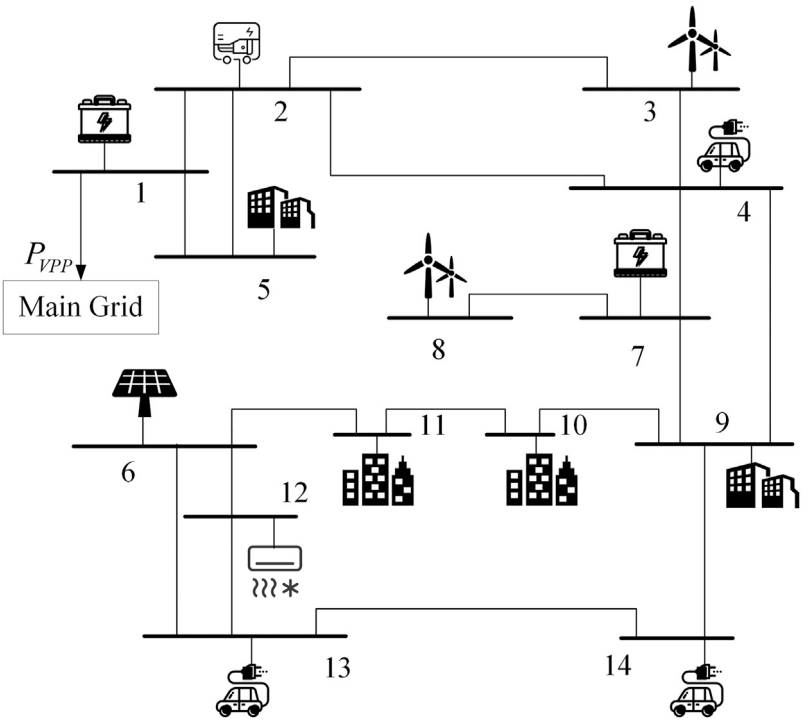

FIGURE 3 | Diagram of the 14-DERs VPP.

TABLE 3 | DERs parameters.

Bus	DER type	$\overline{P}$(kW)	$\underline{P}$(kW)	Cost function coefficients		
				a	b	c
1	battery storage	15	−15	0.065	1.5	400
2	micro turbine	30	0	0.1	4.8	600
4	flexible loads	−25	−45	0.035	8	350
5	flexible loads	−13	−20	0.032	6.5	300
7	battery storage	10	−10	0.065	1.5	400
9	flexible loads	−20	−40	0.03	8	300
10	flexible loads	−15	−25	0.038	7	400
11	flexible loads	−12	−24	0.035	7.5	350
12	flexible loads	−28	−45	0.04	8	450
13	flexible loads	−14	−25	0.035	7	350
14	flexible loads	−25	−45	0.032	8	300

TABLE 4 | Battery storage parameters.

Parameter	S	η	SOC^0	$\overline{SOC}$	$\underline{SOC}$
Value	50 kWh	0.8	0.5	0.9	0.1

$\Delta P_{W,i} + \Delta P_{V,i}$, for the DER without any wind or solar power, $\Delta P_{W,i} + \Delta P_{V,i} = 0$; 2) The regulation capacity $\Delta P_{\mathrm{up},i}$ and $\Delta P_{\mathrm{down},i}$, for non-dispatchable DERs, $\Delta P_{\mathrm{up},i} = 0$ and $\Delta P_{\mathrm{down},i} = 0$.

The information diffusion strategy in (de Azevedo et al., 2017) is adopted for each agent to get the global information in **Eq. 8**, which can be regarded as an algorithm preparation for the improved DEA to solve the real-time DED problem, here some important procedures are explained below.

TABLE 5 | Parameters in the algorithm.

Parameter	μ	β	ϵ	M_{vpp}
Value	0.1	0.7	10^{-5}	1kW

1) Define the regulation vector $D_i(k) = [d_{1,i}(k)\ \ d_{2,i}(k)\, d_{3,i}(k)]^T$, which is initialized according to **Eq. 15a** and updated iteratively with **(15b)**–**(15c)**.

$$D_i(0) = \left[\left(\Delta P_{W,i} + \Delta P_{V,i}\right)\Delta P_{\mathrm{up},i}\Delta P_{\mathrm{down},i}\right]^T \tag{15a}$$

$$\delta_i(k+1) = D_i(k) + 0.65 \cdot [D_i(k) - D_i(k-1)] \tag{15b}$$

$$D_i(k+1) = \sum w_{ij}\delta_j(k+1) \tag{15c}$$

In **(15b)**–**(15c)**, the information diffusion iteration can be regarded as a specific form of the standard EDA iteration where $D_i(k)$, $0.65D_i(k)$ and $\delta_i(k)$ correspond to $\lambda_i(k)$, $\phi_i(k)$ and $\varphi_i(k)$ in **(10a)**-**(10c)**, respectively. In this way, the similar information exchange, stop criteria and local communication failure treatment in *The Improved Exact Diffusion Algorithm* and *Local Communication Failure Treatment* can be applied.

2) When the algorithm converges and let $D_i(\infty)$ denotes the final regulation vector, thus each agent can achieve the global information as follows:

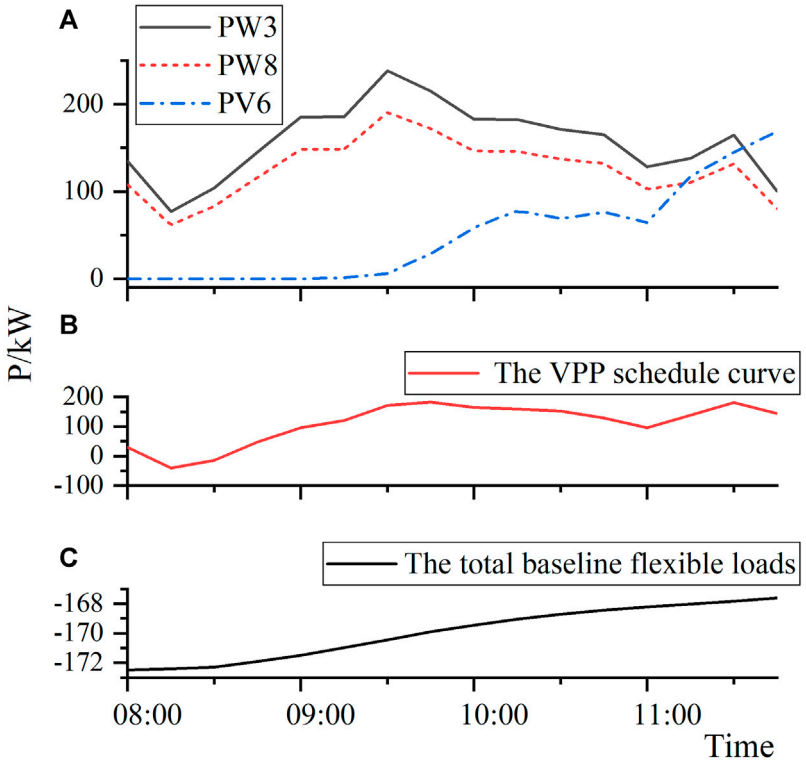

FIGURE 4 | VPP data: **(A)** The look-ahead forecasting curve **(B)** The VPP schedule curve **(C)** The total baseline flexible loads.

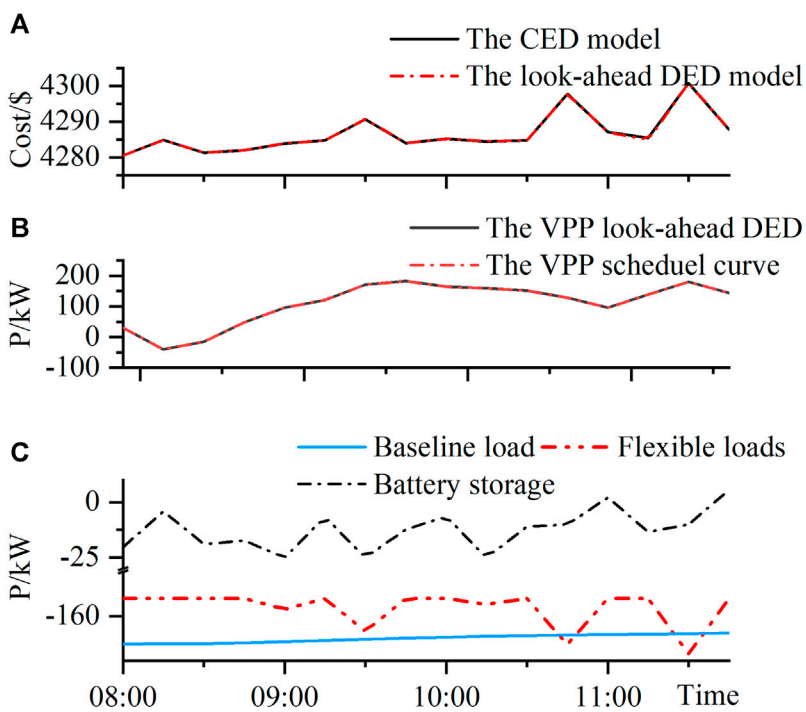

FIGURE 5 | The look-ahead DED performance analysis **(A)** Total cost **(B)** Tracking performance **(C)** Flexible loads and battery storage power.

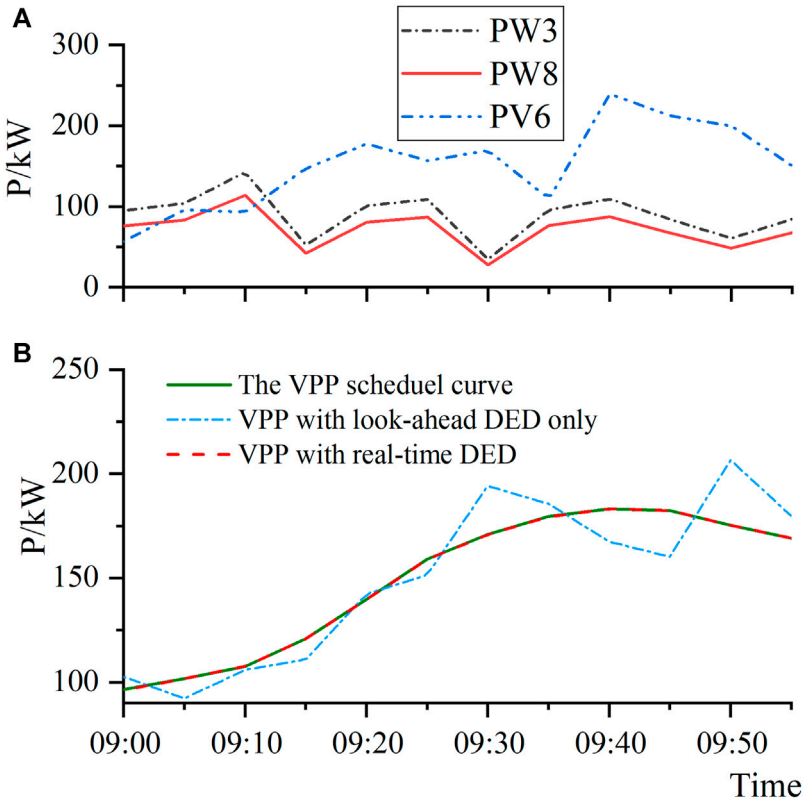

FIGURE 6 | (A) The real-time forecasting power **(B)** The VPP real-time DED performance.

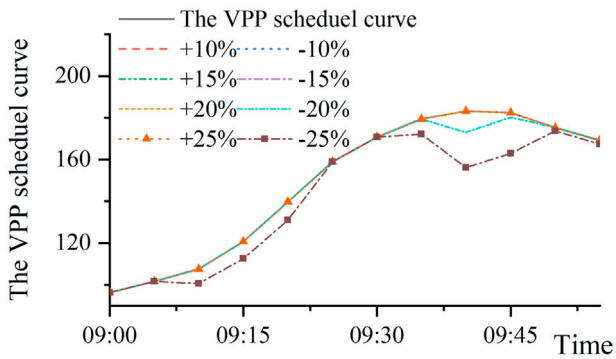

FIGURE 7 | Look-ahead DED performance with prediction error.

$$D_i(\infty) = \left[d_{1,i}(\infty) d_{2,i}(\infty) d_{3,i}(\infty)\right]^T \tag{15d}$$

$$\frac{\sum \Delta P_{W,i} + \Delta P_{V,i}}{n} = d_{1,i}(\infty),$$

$$\frac{\sum \Delta P_{\mathrm{up},i}}{n} = d_{2,i}(\infty), \tag{15e}$$

$$\frac{\sum \Delta P_{\mathrm{down},i}}{n} = d_{3,i}(\infty)$$

3) Each agent can achieve the average expected regulation of VPP $\Delta P_{\mathrm{GOAL}}/n$ using **Eq. 8**.

For each agent, the whole real-time DED algorithm including the expected regulation evaluation is summarized in **Table 2**, in which the details of the information exchange and communication failure treatment is similar to those in the look-ahead DED procedure, Step 1-3 represents the information diffusion strategy for algorithm preparation.

CASE STUDY

To validate the performance of the algorithm proposed above, we use a modified IEEE 14-bus topology to represent the VPP internal topology, as illustrated in **Figure 3**. There are 14 DERs deployed separately in the system. Two wind farms are deployed at bus 3 and bus 8, respectively, one PV station at bus 6 and the rest buses are deployed with dispatchable DERs. The dispatchable DERs data are given in **Table 3**, where the positive value means the power is injected and the negative value means the power is absorbed. The power flow constraints are excluded in the case. As mentioned in *Multi-Agent Communication Framework*, the bus indices in **Table 3** are used to represent the DER indices and each DER agent has the same index as its corresponding DER; and the connection agent is located at bus 1 which is connected to the main grid. The communication network topology is identical to the physical network topology. The battery storage parameters and the improved EDA parameters are summarized in **Table 4** and **Table 5**, respectively.

TABLE 6 | The mean absolute tracking error.

Prediction error	+10%	−10%	+15%	−15%	20%	−20%	25%	−25%
Tracking error/kW	0.043	0.041	0.042	0.042	0.042	2.927	0.043	8.576

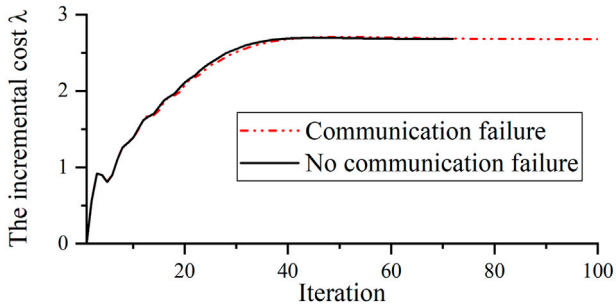

FIGURE 8 | The convergence process of bus 1.

Suppose the look-ahead VPP dispatch is executed at t = 8:00 and the corresponding real-time VPP dispatch is executed at t = 9:00. **Figure 4A** gives the 4 h look-ahead forecasting data from 8:00 to 12:00, including the wind power at bus 3 (PW3) and bus 8 (PW8), the solar power at bus 6 (PV6). **Figure 4B** shows the VPP schedule curve issued by CSO, in which the negative value means VPP need to absorb power, considering some specific operation scenario that the wind and solar power is low. **Figure 4C** gives the total baseline flexible loads profiles initially (before dispatch).

Dispatch Results

The look-ahead DED is finished based on the improved EDA in *Solution Methodology Based on the Improved Exact Diffusion Algorithm*. For comparison purpose, the CED model **(3a)**–**(3f)** is also solved. The total cost of each dispatchable DER from the DED solution and the CED overall cost are presented in **Figure 5A**, it is very clear that the total DED cost is very close to the CED overall cost, which can confirm the effectiveness of the DED model. Further, the resultant time-series VPP power exchange with the main grid is plotted in **Figure 5B** which can well track the VPP schedule curve in **Figure 4B**. The resultant total battery storage power and the total flexible loads after the look-ahead dispatch is shown in **Figure 5C**. The micro turbine doesn't provide any power output in the look-ahead dispatch due to its high cost.

The real-time tracking performance of VPP from 9:00–10:00 is shown in **Figures 6A,B**. Due to the deviation between the look-ahead forecasting and the real-time forecasting, there exists obvious tracking errors, comparing the VPP power output (the dot dash line) with the VPP schedule curve (the solid line) in **Figure 6B**. In addition, the real-time DED can further correct the deviation (the dash line) and improve the tracking performance.

Analysis on the Effect of Prediction Error

To analyze the effect of prediction error on dispatch performance, the look-ahead dispatch according to four prediction error level, ± 10, ± 15, ± 20, and ±25% are presented in **Figure 7**, where the real-time wind and solar power data here is represented by the look-ahead prediction plus prediction error. Based on the above two-stage dispatch, the tracking standard deviation from the schedule curve during 9:00–10:00 is used to measure the tracking effect is presented in **Table 6**.

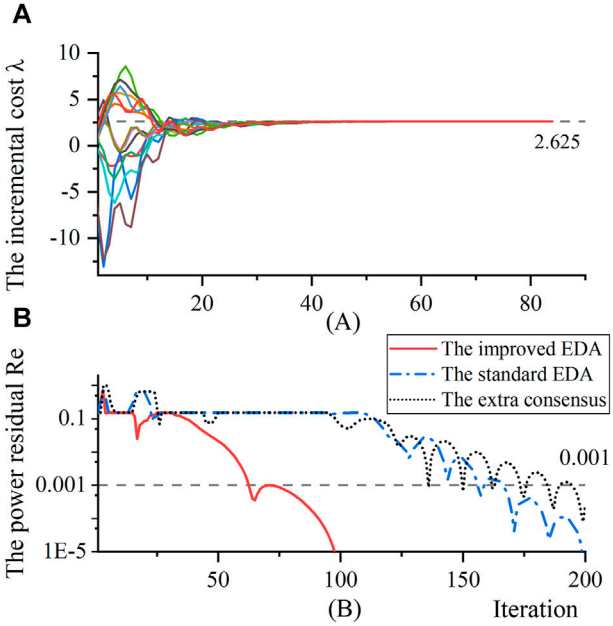

FIGURE 9 | (A) The convergence process **(B)** The power residual evolution.

It is observed that when the prediction error is within ± 20%, the VPP power output in this test system can well track the schedule curve. Nevertheless, the tracking performance will become worse when the prediction error is enlarged, because the total up-regulation capacity is not enough in this case. On the other hand, the dispatch performance can be satisfied when there is enough adjustment capacity in the real-time stage to compensate for the deviation.

Communication Robustness

To verify the algorithm robustness, it is supposed that the communication line between agent 1 and agent 2 fails at 9:15 during the real-time DED. The whole convergence process of agent 1 (at bus 1) for the 9:15–9:20 time interval with and without communication failure is plotted in **Figure 8**:

It can be seen from **Figure 8**, when the local communication failure occurs, the proposed improved EDA still has enough robustness to converge to the same optimal solution without

communication-failure, only with the convergence speed lightly slowed down.

Algorithm Performance Verification

To measure the accuracy and convergence performance of the improved EDA, a power residual based performance index *Re* is introduced (Tang, Hill, and Liu 2018):

$$Re = \|\boldsymbol{P}(k) - \boldsymbol{P}^*\|_2 / \|\boldsymbol{P}(0) - \boldsymbol{P}^*\|_2$$

where $\boldsymbol{P}(k) = \left[P_1(k), P_2(k) \cdots P_n(k)\right]$ is the kth iteration DER power vector; $P_i(k)$ is the power of the ith DER at iteration k; $\boldsymbol{P}^*$is the optimal power obtained by the CED method; the less is the *Re* value, the more accurate will the method be.

For comparison purpose, here the look-ahead dispatch at 8:00 is performed using the proposed improved EDA, the standard EDA and the consensus-based algorithm (Tang, Hill, and Liu 2018). The results are given in **Figure 9**, where the convergence processes of all DERs are presented in **Figure 9A** and the power residual evolution comparison is presented in **Figure 9B**. It is very clear that the incremental cost of all DERs converge to the consensus value $\lambda = 2.625$. **Figure 9B** also verifies the improved EDA have better accuracy and convergence performance than the standard EDA and the consensus-based algorithm. For the real-time DED, the improved EDA has similar observation and conclusion.

CONCLUSION

A distributed two-stage economic dispatch for VPP based on the improved exact diffusion algorithm is proposed in this paper to manage a large scale of DERs dispersed geographically and deal with the uncertainty of DERs. The centralized look-ahead dispatch and real-time tracking models are transformed to distributed ones by constructing dual problems and separating the Lagrange multipliers. The exact diffusion algorithm is improved by adding a convex penalty term and a conditional communication strategy. Case studies based on a modified IEEE 14-bus system validate that VPP power output can track the VPP schedule curve well and balance the power deviation using the improved exact diffusion algorithm with certain robustness against local communication failure.

DATA AVAILABILITY STATEMENT

The original contributions presented in the study are included in the article/supplementary material, further inquiries can be directed to the corresponding author.

AUTHOR CONTRIBUTIONS

YZ and ZW conceptualized the study; YZ and ZW performed the analysis; YZ, ZW, and HW performed investigations; ZW and PJ acquired resources; ZW and PJ acquired funding; YZ and ZW wrote the original draft; PJ and HW reviewed and edited the manuscript. All authors agree to be accountable for the content of the work.

FUNDING

This work was supported by the National Nature Science Foundation of China (No. 51837004).

REFERENCES

Baringo, A., Baringo, L., and Arroyo, J. M. (2019). Day-Ahead Self-Scheduling of a Virtual Power Plant in Energy and Reserve Electricity Markets under Uncertainty. *IEEE Trans. Power Syst.* 34 (3), 1881–1894. doi:10.1109/tpwrs.2018.2883753

Bouffard, F., and Galiana, F. D. (2008). Stochastic Security for Operations Planning with Significant Wind Power Generation. *IEEE Trans. Power Syst.* 23 (2), 306–316. doi:10.1109/TPWRS.2008.919318

Boyd, S. (2010). Distributed Optimization and Statistical Learning via the Alternating Direction Method of Multipliers. *Foundations Trends® Machine Learn.* 3 (1), 1–122. doi:10.1561/2200000016

Christie, R. D., Wollenberg, B. F., and Wangensteen, I. (2000). Transmission Management in the Deregulated Environment. *Proc. IEEE* 88 (2), 170–195. doi:10.1109/5.823997

de Azevedo, R., Mehmet Hazar, C., Tan, Ma., Osama, A., and Mohammed (2017). Multiagent-Based Optimal Microgrid Control Using Fully Distributed Diffusion Strategy. *IEEE Trans. Smart Grid* 8 (4), 1997–2008. doi:10.1109/tsg.2016.2587741

Ding, Y., Jia, H., Song, Y., Li, Y., and Jin, W. (2016). Review of Reliability Evaluation Methods for the Smart Grid Considering the Interaction between Wind Power and Flexible Demand Resources. *Proc. CSEE* 36 (6), 1517–1526. (in Chinese). doi:10.13334/j.0258-8013.pcsee.2016.06.007

Koraki, D., and Strunz, K. (2018). Wind and Solar Power Integration in Electricity Markets and Distribution Networks through Service-Centric Virtual Power Plants. *IEEE Trans. Power Syst.* 33 (1), 473–485. doi:10.1109/tpwrs.2017.2710481

Li, Z., Wu, W., Zhang, B., and Wang, B. (2015). Adjustable Robust Real-Time Power Dispatch with Large-Scale Wind Power Integration. *IEEE Trans. Sustainable Energ.* 6 (2), 357–368. doi:10.1109/tste.2014.2377752

Lin, X., and Boyd, S. (2003). Fast Linear Iterations for Distributed Averaging." in Proceeding of the 42nd IEEE International Conference on Decision and Control. Maui, HI: IEEE. December 9–12, 2003, Maui, HI, USA.

Lu, N. (2012). An Evaluation of the HVAC Load Potential for Providing Load Balancing Service. *IEEE Trans. Smart Grid* 3 (3), 1263–1270. doi:10.1109/tsg.2012.2183649

Mateos-Nunez, D., and Cortes, J. (2017). Distributed Saddle-Point Subgradient Algorithms with Laplacian Averaging. *IEEE Trans. Automatic Control.* 62 (6), 2720–2735. doi:10.1109/tac.2016.2616646

McArthur, S. D. J., Davidson, E. M., Catterson, V. M., Dimeas, A. L., Hatziargyriou, N. D., Ponci, F., et al. (2007). Multi-Agent Systems for Power Engineering Applications—Part I: Concepts, Approaches, and Technical Challenges. *IEEE Trans. Power Syst.* 22 (4), 1743–1752. doi:10.1109/TPWRS.2007.908471

Nedic, A., and Ozdaglar, A. (2009). Distributed Subgradient Methods for Multi-Agent Optimization. *IEEE Trans. Automatic Control.* 54 (1), 48–61. doi:10.1109/tac.2008.2009515

Šošić, D., Škokljev, N, and Pokimica, N., 2014. Features of Power Transfer Distribution Coefficients in Power System Networks, *INFOTEH-JAHORINA* 13, 86–90.

Tang, Z., Hill, Dd. J., and Tao, . (2018). A Novel Consensus-Based Economic Dispatch for Microgrids. *IEEE Trans. Smart Grid* 9 (4), 3920–3922. doi:10.1109/tsg.2018.2835657

Tu, S-Y., and Ali, S. (2012). Diffusion Strategies Outperform Consensus Strategies for Distributed Estimation over Adaptive Networks. *IEEE Trans. Signal Process.* 60 (12), 6217–6234. doi:10.1109/TSP.2012.2217338

Vahedipour-Dahraie, M., Rashidizadeh-Kermani, H., Shafie-Khah, M., and Catalão, J. P. S. (2021). Risk-Averse Optimal Energy and Reserve Scheduling for Virtual Power Plants Incorporating Demand Response Programs. *IEEE Trans. Smart Grid* 12 (2), 1405–1415. doi:10.1109/TSG.2020.3026971

Wang, B., Hu, X., Gu, W., Li, Y., and Kong, L. (2019). Hierarchical Control Architecture and Decentralized Cooperative Control Strategy for Large Scale Air Conditioning Load Participating in Peak Load Regulation. *Proc. CSEE* 39 (12), 3514–3528. (in Chinese). doi:10.13334/j.0258-8013.pcsee.172444

Xia, S., Bu, S., Wan, C., Lu, Xi., Chan, K. W., and Zhou, B. (2019). A Fully Distributed Hierarchical Control Framework for Coordinated Operation of DERs in Active Distribution Power Networks. *IEEE Trans. Power Syst.* 34 (6), 5184–5197. doi:10.1109/tpwrs.2018.2870153

Yuan, K., Ying, B., Zhao, X., and Sayed, A. H. (2019a). Exact Diffusion for Distributed Optimization and Learning—Part I: Algorithm Development. *IEEE Trans. Signal Process.* 67 (3), 708–723. doi:10.1109/tsp.2018.2875898

Yuan, K., Ying, B., Zhao, X., and Sayed, A. H. (2019b). Exact Diffusion for Distributed Optimization and Learning—Part II: Convergence Analysis. *IEEE Trans. Signal Process.* 67 (3), 724–739. doi:10.1109/tsp.2018.2875883

Zhou, H., Wang, Fen., Li, Z., Jiang, L. I. U., Li, Z., and He, G. (2021). Load Tracking Control Strategy for Virtual Power Plant via Self-Approaching Optimization. *Proceedings of the CSEE* (in Chinese), 1–17. doi:10.13334/j.0258-8013.pcsee.202005

Conflict of Interest: The authors declare that the research was conducted in the absence of any commercial or financial relationships that could be construed as a potential conflict of interest.

Advantages of publishing in Frontiers

OPEN ACCESS
Articles are free to read for greatest visibility and readership

FAST PUBLICATION
Around 90 days from submission to decision

HIGH QUALITY PEER-REVIEW
Rigorous, collaborative, and constructive peer-review

TRANSPARENT PEER-REVIEW
Editors and reviewers acknowledged by name on published articles

Frontiers
Avenue du Tribunal-Fédéral 34
1005 Lausanne | Switzerland

Visit us: www.frontiersin.org
Contact us: frontiersin.org/about/contact

REPRODUCIBILITY OF RESEARCH
Support open data and methods to enhance research reproducibility

DIGITAL PUBLISHING
Articles designed for optimal readership across devices

FOLLOW US
@frontiersin

IMPACT METRICS
Advanced article metrics track visibility across digital media

EXTENSIVE PROMOTION
Marketing and promotion of impactful research

LOOP RESEARCH NETWORK
Our network increases your article's readership